UC San Diego

UC San Diego Electronic Theses and Dissertations

Title

Observations and modeling of shallow fault creep along the San Andreas Fault System

Permalink

https://escholarship.org/uc/item/5dw410rg

Author

Wei, Meng

Publication Date

2011

Peer reviewed|Thesis/dissertation

eScholarship.org Powered by the California Digital Library
University of California

UNIVERSITY OF CALIFORNIA, SAN DIEGO

Observations and Modeling of Shallow Fault Creep Along the San Andreas Fault System

A dissertation submitted in partial satisfaction of the requirements for the degree of

Doctor of Philosophy

in

Earth Sciences

by

Meng Wei

Committee in charge:

Professor David T. Sandwell, Chair
Professor Kevin Brown
Professor Yuri Fialko
Professor John Goodkind
Professor Glenn Ierley

2011

© Copyright

Meng Wei, 2011

All Rights Reserved

The Dissertation of Meng Wei is approved, and it is acceptable in quality and form for publication on microfilm and electronically:

_____

_____

_____

_____

_____

Chair

University of California, San Diego

2011

DEDICATION

To my wife Ying Zhang

To my son Brian

To my parents Jiliang Wei and Wenhua Liu

TABLE OF CONTENTS

LIST OF FIGURES

LIST OF TABLES

ACKNOWLEDGMENTS

This dissertation is not possible without the committee's help. As my advisor, professor David Sandwell supported me both intellectually and financially. His door is always open and my questions are welcomed. He is also very fast on revising my papers. He always encouraged me to attend meetings, even though some of them are expensive, such as the ALOS meeting at Hawaii in 2010. His hands-off style helped me to do research and think freely and independently. His enthusiasm and dedication to science and life has enormous influence on me. I consider it an honor to work with Dave.

Besides my advisor, I want to thank my other committee members. Professor Yuri Fialko helped me in several projects and is a co-author of three of my papers. His insights always make the project more interesting and successful. His ability to explain complex things with simple words impressed me so many times that I believe I will be very glad if I can be even half as good as him. Professor Kevin Brown provided me a different angle from a geologist's point of view, which is crucial to the success of my projects. He is always positive and smiling, making me feel delighted. Professor Glenn Ierley helped me from a mathematic perspective. He saved me a lot of time by solving my problems using the software Mathematics or Maple. The conversation with him is also always positive and constructive. I thank Professor John Goodkind for being on my committee and attending committee meetings several times along the way. His perspective as a Physicist improved the quality my thesis greatly.

I would also like to acknowledge the members of the Sandwell's lab. Bridget Smith-Konter helped me a lot for my English writings and provided me with suggestions

on scientific career development. We still work together sometime during her visit to the lab from Texas, where she is a professor now. Karen Luttrell also helped me on English writings and revising my papers. She is also a good friend of mine during off-hours. Conversations with her have been always pleasant. Xiaopeng Tong helped me on several projects regarding InSAR processing. I thank Karen Scott for handling all my travel reimbursements.

I am also greatly indebted to Debi Kilb, who has been so helpful. She reviewed all my papers before I submitted them to journals. My papers look much better with her comments.

I want to thank the students who came to Scripps the same year as I did, Leah Ziegler, Danny Brothers, Robin Matoza, Fan Yang and Todd Hanson. We spent the first two years as officemate at Keller. I think my experience of working with those guys on class projects and exams was fantastic. Different background but same dedication makes life much enjoyable and easier.

The other faculty members and students in our department are also being helpful and nice, which makes my life here much easier. Professor Peter Shearer answered my questions about seismology all the time. Professor Duncan Agnew helped me on GPS surveys. Professor Yehuda Bock and his lab helped me processed GPS data from our surveys. Sylvain Barbot is very helpful on several projects. I feel lucky to be in such a supportive environment and thank all who have helped and encouraged me.

Last, but not least, I want to thank my family. I share the credit of my work with my wife, who is with me for the entire six years of my graduate student life. She supported me with love, care, and constructive suggestions. I feel very fortunate to have

her as my wife. I am heartily thankful to my parents for raising me up and supporting my education through college.

Text of Chapter 2, 3, 5, 6, and 8, in full, are reprints of the material as it appears in the Journal of Geophysical Research, Geophysical Research Letters, IEEE Transaction on Geoscience and Remote Sensing, Advance in Space Science, and Tectonophysics, respectively. Text of Chapter 4, in part is currently being prepared for submission for publication of the material. The dissertation author was the primary investigator and author of these papers.

VITA, PUBLICATIONS AND FIELD OF STUDY

Nov. 30, 1981	Born, Xiangfan, Hubei Province, China
2004	B.S., Geophysics, Peking University, China
2004-2010	Research assistant, Scripps Institution of Oceanography, University of California, San Diego
2011	Ph.D., University of California, San Diego

Wei, M., D. T. Sandwell, Y. Fialko, and R. Bilham (2011), Slip on faults in the Imperial Valley triggered by the 4 April 2010 Mw 7.2 El Mayor-Cucapah earthquake revealed by InSAR, Geophysical Research Letters, 38, L01308, doi:10.1029/2010GL045235.

Wei, M., D. T. Sandwell, and B. Smith-Konter (2010), Optimal Combination of InSAR and GPS for Measuring Interseismic Crustal deformation, *Advances in Space Research*, 99, 1-11, doi: 10.1016/j.asr.2010.03.013.

Wei, M. and D. T. Sandwell (2010), Decorrelation of ALOS and ERS interferometry over vegetated areas in California", *IEEE Geoscience and Remote Sensing*, 10.1109/TGRS.2010.2043442.

Wei, M., D. T. Sandwell and Y. Fialko (2009), Creep event on the Superstition Hills fault, Southern California, *JGR Solid Earth*, 114, B07402, doi: 10.1029/2008JB006135.

Wei, M. and D. T. Sandwell (2006) Reply to comment on: Estimates of Ridge-Axis Heat Flow from Depth and Age Data, *Tectonophysics* 428 101-103. doi:10.1016/j.tecto.2006.08.007.

Wei, M. and D. T. Sandwell (2006), Estimates of Ridge-Axis Heat Flow from Depth and Age Data, *Tectonophysics* 417 325-335. doi:10.1016/j.tecto.2006.02.004

Studies in Geodynamics

Professer John Yongshun Chen, Peking University

Studies in Crustal Deformation

Professor David Sandwell

ABSTRACT OF THE DISSERTATION/THESIS

Observations and Modeling of Shallow Fault Creep Along the

San Andreas Fault System

by

Meng Wei

Doctor Of Philosophy in Earth Sciences

University of California, San Diego, 2011

Professor David T. Sandwell, Chair

This dissertation focuses on observations and modeling of fault creep in California aiming to understand the relationship between creep and earthquakes and assess the earthquake hazards in California. Chapter 1 gives an introduction of fault creep research in California, geodetic methods used to measure fault creep, and mechanism of fault creep. Chapter 2 documents an investigate on a creep event on the Supersitition Hills Fault in Southern California and the spatial and temporal variations in slip history between 1992 and 2008 using ERS, and Envisat Satellite data confirming

that the fault creep is confined within the sediments layer and is probably due to the low normal stress in unconsolidated sediments. Chapter 3 presents a study on triggered slip on faults in the Salton Trough by the 2010 El Mayor-Cucapah Mw 7.2 earthquake. Chapter 4 compiles geodetic data and investigates the relationship between shallow stress accumulating rate and creep rate. Chapter 5 and 6 explores two technical projects related to fault creep observations in California. Chapter 5 analyzes decorrelation of L-band and C-band interferograms in California with implications for future fault creep study. Chapter 6 proposes an optimal way to combine GPS and InSAR to measure interseismic deformation, including fault creep. The proposed method is compared with other method and the improvements are observed. Chapter 7 presents the conclusions of the previous six chapters.

Chapter 8 presents my work in the first two years in graduate school, which is not related to fault creep. We compute global maps of surface minus basal heat flow that show qualitative agreement with heat flow based on the inverse square root of age relation.

In the beginning of each chapter, I provide you an earthquake safety tip. I borrowed them from an interesting website for your safety and interests. Hopefully it could be one more motivation to read through my thesis. I didn't bother to invent them, as Ralph Waldo Emerson noted "All my best thoughts were stolen by the ancients."

1. CHAPTER 1: Introduction

Earthquake safety tip 1:

To minimize loss and damage in a quake, try not to own things.

(All the jokes used in this thesis are retrieved on December 20, 2010 from the following website: http://www.unwind.com/jokes-funnies/miscjokes/earthquake.shtml)

1.1 Fault creep in California

Many large earthquakes occur on the continental strike-slip faults, such as the San Andreas Fault in California. In geology, a fault is a planar fracture in a volume of rock, across which has been significant displacement. Because of the friction on fault surfaces, rocks that meet along a fault do not slide freely past each other, but are instead locked for long periods. Over decades to thousands of years, stress builds up within the rocks that are separated by the fault as their movement is prevented by along-fault friction. At some point, the amount of stress exceeds the frictional forces that are preventing slip. The fault ruptures and rocks on either side of the fault slide rapidly as the energy is relieved, which we call earthquakes. The earthquake cycle is frequently referred to as a "stick-slip" process - long periods of "stick" are followed by a short period of "slip", and the process then repeats itself. The term "cycle" does refer to the repeating nature of earthquakes. However, it does not mean that earthquakes are a periodic or regularly repeating event. Actually, earthquakes usually occur irregularly. Otherwise, predicting earthquakes will be a much easier job.

My research is motivated by simple models of the earthquake cycle that incorporate an empirical theory for rock friction. The seismic cycle can be divided into

three periods, consisting of inter-seismic, co-seismic, and post-seismic slip (Figure 1-1, 2). The inter-seismic period refers to the period of slow accumulation of elastic strain that coincides with frictional locking of a fault between earthquakes, ranging from decades to thousands of years. The co-seismic period refers to the moment an earthquake occurs, usually lasting a few seconds to a few minutes. The post-seismic period refers to a short time period (a few years to decades) immediate after an earthquake occurred. Over a period of many earthquake cycles, the cumulative displacement is uniform at all depths such that the sum of the co-seismic, post-seismic, and inter-seismic deformation is equal to the geologic displacement. At intermediate depth, sliding is episodic and generates earthquakes because the static coefficient of fault friction is greater than the dynamic coefficient of friction (Figure 1-3). At shallower and greater depths, slip is at steady state and does not generate seismic waves because the strength of the fault increases with sliding velocity (Figure 1-3). Such deformation mode, slipping without generating seismic waves, is defined as fault creep, which can be continuous or transient. Please note that although creep can be either shallow or deep, we refer fault creep to only shallow fault creep in the entire thesis because the focus of this thesis is on shallow fault creep.

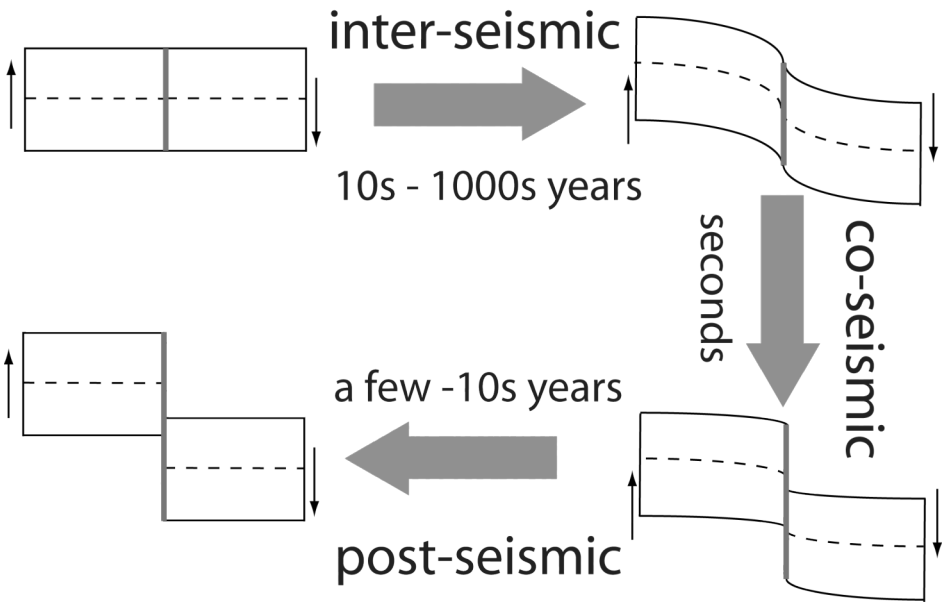

Figure 1-1. Elastic rebound theory of earthquake cycle on strike-slip fault environment. Two rectangle blocks represent two plates. Gray line is the fault trace. Relative motion between the two creates stress near the boundary, a fault zone.

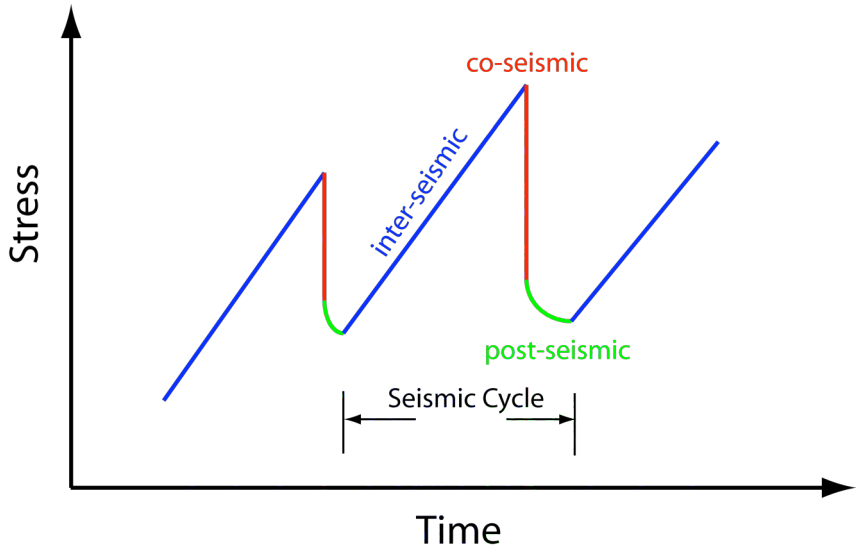

Figure 1-2. Stress change with time during different period of seismic cycle.

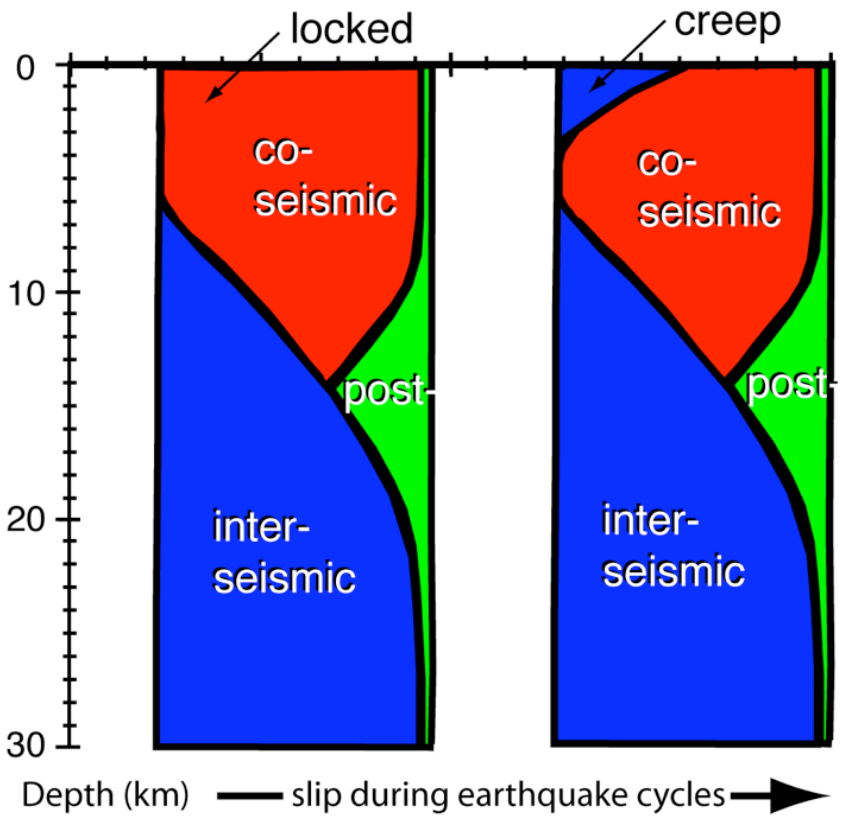

Figure 1-3. Fault slips in different period of seismic cycle. (left) no shallow fault creep. (right) with shallow fault creep. The x-axis represents the area of slip.

There are a number of fault segments that creep in California and around the world (Figure 1-4, Table 1-1). The creeping section of the San Andreas Fault in central California is the most famous one and has the highest creep rate (~30 mm/yr). Fault creep shows a variety of behaviors and can be classified based on different criteria. First, depending on the creep rate, fault creep can be classified as fast creep fault or slow creep fault. The rate of fault creep in California ranges from a few mm/year to about 30 mm/year. Generally, creep is faster in the Northern and Central California whereas creep is slower in Southern California. For example, fault creep on the central San Andreas Fault is 30 mm/yr whereas creep rate on the southern San Andreas Fault is only about 3

mm/yr. Second, depending on the temporal nature, fault creep can be continuous or abrupt. For example, on the Hayward fault, many observations show steady creep for decades, whereas in the Salton Trough, creep mostly occurred as a series of small events. Third, depending on the phase of earthquake cycle, creep can also be classified as interseismic, post-seismic and precursory. For example, post-seismic creep or afterslip was observed on the Superstition Hills Fault after the 1987 earthquake. Finally, creep can be classified as triggered or non-triggered. For example, triggered creep can be seen in the Salton Trough where creep was triggered by nearby earthquakes [*Rymer et al.*, 2002], or in the central San Andreas Fault where creep was triggered by precipitation [*Roeloffs*, 2001].

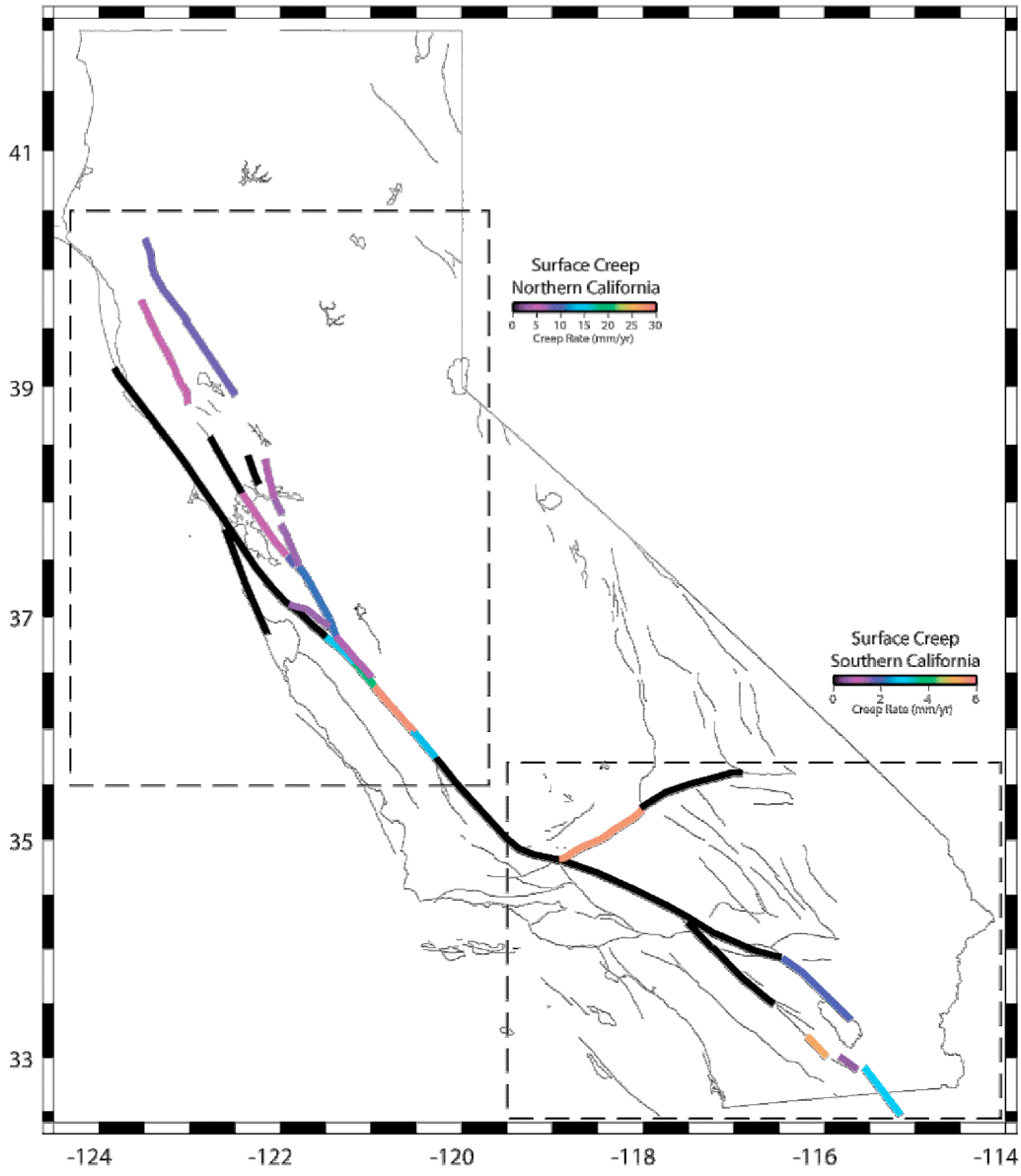

Figure 1-4. Fault creep in California. This figure is from *Wisely et al.* 2008. Color solid lines are faults with documented fault creep. Black solid lines are faults without documented fault creep. Please note that the color bar is different for southern and northern California.

Table 1-1. Faults that creep in California and around the world.

Fault	Country or Region	Reference
California		
Maacama	North	Galehouse and Lienkaemper (2003)
Rodgers Creek	North	Galehouse and Lienkaemper (2003)
Bartlett Springs	North	Galehouse and Lienkaemper (2003)
West Napa	North	Galehouse and Lienkaemper (2003)
Hayward	North	Galehouse and Lienkaemper (2003)
Calaveras	North	Galehouse and Lienkaemper (2003)
Concord	North	Galehouse and Lienkaemper (2003)
Green Valley	North	Galehouse and Lienkaemper (2003)
Sargent	North	Prescott and Burford (1976)
Imperial	South	Louie et al. (1985)
San Andreas	Central, South	Galehouse and Lienkaemper (2003), Louie et al. (1985)
Superstition Hills	South	Louie et al. (1985), Bilham and Behr (1992), Wei et al. (2009)
Coyote Creek	South	Louie et al. (1985)
Asia		
Xianshuihe	China	Allen et al. (1991)
Haiyuan	China	Cavalie et al. (2008)
Nahan	Himalaya	Sinvhal et al. (1973)
Dasht e Bayaz	Iran	King et al. (1975)
North Anatolian	Turkey	Ambraseys (1970), Cakir et al. (2005), Kutoglu and Akcin (2006), Kutoglu et al. (2008)
Chaman	Afghanistan	Furuya and Satyabala (2008)
Chihshang	Chinese Taiwan	Lee et al. (2003)
Longitudinal Valley	Chinese Taiwan	Hsu and Burgmann (2006)
	Philippines	Duquesnoy et al. (1994), Prioul et al. (2000)
Europe		
Pernicana	Italy	Azzaro et al. (2001)
Unknown	Italy	Bella et al. (1995)
Unknown	Georgia	Bella et al. (1995)
Central or South America		
	Guatemala	Bucknam et al. (1978)
	Mexico	Glowacka (1996)

Table 1-1. Continued

Africa		
	Algeria	Mahsas et al. (2008)
Australia		
Alpine	New Zealand	Walcott (1978)

Why do we care about fault creep? Although fault creep is slow (< 30 mm/yr), it is important for earthquake hazard assessment. Shallow creep was once regarded as a possible earthquake precursor [*Bakun and Lindh*, 1985], when a couple anomalies were noted during the 1966 Parkfield earthquake. About 9 hours before the 1966 M_L 6.0 Parkfield earthquake, a pipeline 2 km northwest of the main rupture broke. Furthermore, a fresh crack was observed in the fault zone near the rupture zone 12 days before the 1966 main shock. The broken pipeline and fresh crack might have formed as a result of aseismic slip in the rupture zone. One interpretation is that a detectable aseismic slip occurred before the earthquake and could be used as a tool to predict future earthquakes. Inspired by this apparent precursor in 1966, a large geodetic network, mostly creepmeters and alignment arrays, was built to detect precursory creep before large earthquakes. Unfortunately, after 38 years of waiting, a similar precursor was not detected for the 2004 M_w 6.0 Parkfield earthquake [*Bakun et al.,* 2005], even though the instrument array in Parkfield is the densest in the U.S. In addition, between 1966-2004, researchers studied the relationship between creep events and moderate earthquakes using the data collected by the network and seismometers. Although correlation was found between creep events and moderate earthquakes, the false alarm rate (> 90%) was so high that using creep events as a precursor to earthquake is not reliable [*Thurber and*

Sessions, 1998]. Therefore, the future of short-term earthquake prediction using creep signals remains unclear. Based on a review of previous studies of earthquake prediction, Geller concluded that it is impossible to reliably issue warnings of imminent large earthquakes [*Geller,* 1997].

Although the predictable value of creep is small, the long-term rate of creep is still valuable for earthquake hazard assessment [*Galehouse and Lienkaemper*, 2003]. Generally, a fault that creeps has a lower probability for generating large earthquakes than a fault that does not creep [*Field*, 2007]. This is because the area of slip in future earthquake is smaller on faults that creep (Figure 1-3). Another way of looking at this is that fault creep may partially relieve stress buildup along faults, thereby reducing the magnitude of future large earthquakes. Thus, estimation of the depth of creep can be used to forecast the magnitude of future earthquakes. Also, the temporal changes in creep rate may reflect stress changes on the fault as a result of local or regional earthquakes. These stress changes may either advance or retard future earthquakes. For these reasons, fault creep is an important research topic.

1.2 Mechanism of fault creep

Why do some faults creep at a shallow depth is still unclear. One explanation is that the fault material prefers creep to rapid sliding at shallow depth at certain conditions. This is supported by lab experiments and the theory developed based on them (Figure 1-5). Rate-and-state theory is an empirical theory that Dieterich and Ruina have developed since the late 1970's [*Dieterich,* 1979; *Ruina,* 1983; *Marone,* 1998]. There are two main observations in the lab experiment. First, the static friction increases

logarithmically with the holding time. *Dieterich* interpreted this effect as the contact area increases with time [*Dieterich,* 1994]. Second, the dynamic friction jumps immediately after the slip rate increased an order of magnitude and decreases to a new steady state after certain displacement. The dynamic friction depends logarithmically on sliding velocity.

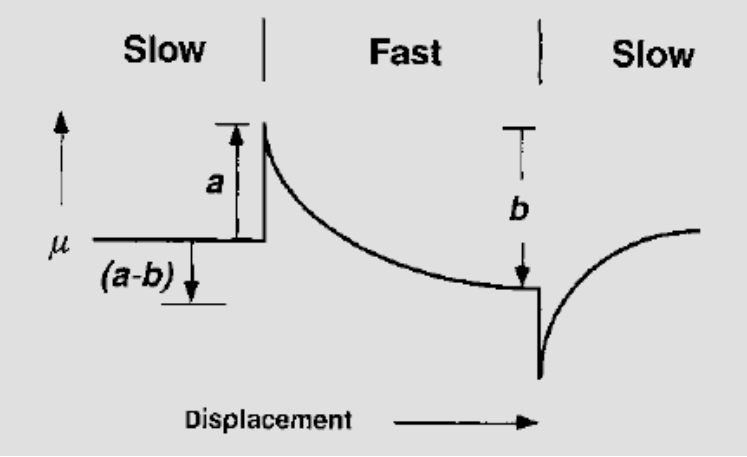

Figure 1-5. Simplified illustration of experiment result of lab friction result. As two blocks slides with each other, the friction coefficient changes with sliding speed. Reproduced from Scholz, 1998.

Based on these observations, *Dieterich and Ruina* developed a constitution friction formula, states that friction μ depends on the instantaneous sliding velocity V and a time-dependent state variable θ:

$$\mu(V,\theta) = \mu_o + a\ln(\frac{V}{V_o}) + b\ln(\frac{V_o\theta}{D_c})$$

in which the state variable θ evolves as follows:

$$\dot{\theta} = 1 - (\frac{V\theta}{D_c})$$

where D_c is the critical slip distance, μ_o is the friction coefficient at sliding velocity V_o. Applying the rate-and-state friction theory to a simple spring-slider system, both continuous stable sliding and stick-slip behavior are observed [*Ruina*, 1983; *Gu and Rice,* 1983]. In the real world, stable sliding corresponds to fault creep whereas stick-slip corresponds to earthquakes. The stability of the system depends on the parameter $(a-b)$. If $a-b \geq 0$, which is defined as velocity-strengthening, the system is intrinsically stable. If $a-b<0$, which is defined as velocity-weakening, the system can be either stable or unstable depends on the effective normal stress. For higher values of normal stress, the system is unstable. For lower values of normal stress, the system is stable. Parameter $(a-b)$ is a material property. If the rock on both sides of the fault has positive $(a-b)$, the fault will creep. For example, the existence of fault creep in the Salton Trough, Southern California is associated with the unconsolidated sediments at shallow depth.

Even rate-and-state friction is consistent with observation; there are some difficulties of applying this theory to the real world. First, there is a scaling problem. The size of the sample used in lab experiment is much smaller than the rocks sliding in the real world. How to project the value of parameters determined in lab experiments to the real world is an issue. Second, which rock exactly explains the existence of fault creep is still unclear. Previously, serpentinite is commonly considered as the cause of the creep and the low strength of the creeping section of the San Andreas Fault. However, the frictional strength of serpentine minerals is too high and not consistent with fault strength of the San Andreas Fault, and these minerals also have the potential for unstable slip under some conditions. The recent discovery of talc in the SAFOD samples can

explain both the low strength and stable sliding in the creeping section of the San Andreas Fault [*Moore and Rymer,* 2007]. Yet it cannot be concluded that there is an abundance of talc in the fault zone due to the limited sample and heterogeneity of the fault.

1.3 Geodetic methods for measuring creep

As described in the first section of the introduction, it is important to estimate the magnitude and extent of fault creep. We do this by measuring ground deformation caused by fault creep using geodetic instruments such as creepmeter, alignment array, GPS, and Interferometric Synthetic Aperture Radar (InSAR). In this section, I will introduce these geodetic methods and discuss each method's strength and weakness. InSAR is by far the best tool to estimate the depth of fault creep as it provides deformation away from the fault in high spatial sampling interval. However, InSAR has its own disadvantages. So when multiple data sets are available, the best strategy is combining them.

Soon after the discovery of fault creep in 1956 in California, a program of creepmeter measurements using theodolites and dial gauges instruments was initiated to quantify the slow aseismic movement of surface faults [*Bilham et al.,* 2004]. Twenty-one of these early creepmeters are still in use and data are assembled at the USGS Menlo Park office. Creepmeters provide high quality time series of fault movement, which can be used to study the dynamics of fault creep. The timing of creep events is also important information to study the triggering mechanism of creep events.

Even though creepmeter is designed to measure creep, it has disadvantages. The typical length of a creepmeter is between 3-200 meters. If creep signal is spreading over a greater distance from the fault, creepmeter will underestimate the creep rate. In contrast, alignment array, trilateration, and leveling usually span the entire fault zone, thus giving accurate measurements. However, these methods require frequent field surveys. So the temporal resolution of these instruments depends on how often surveys are taken and often varies from months to years. In addition, leveling can only measure the vertical deformation, thus no sensitivity to strike-slip fault motion.

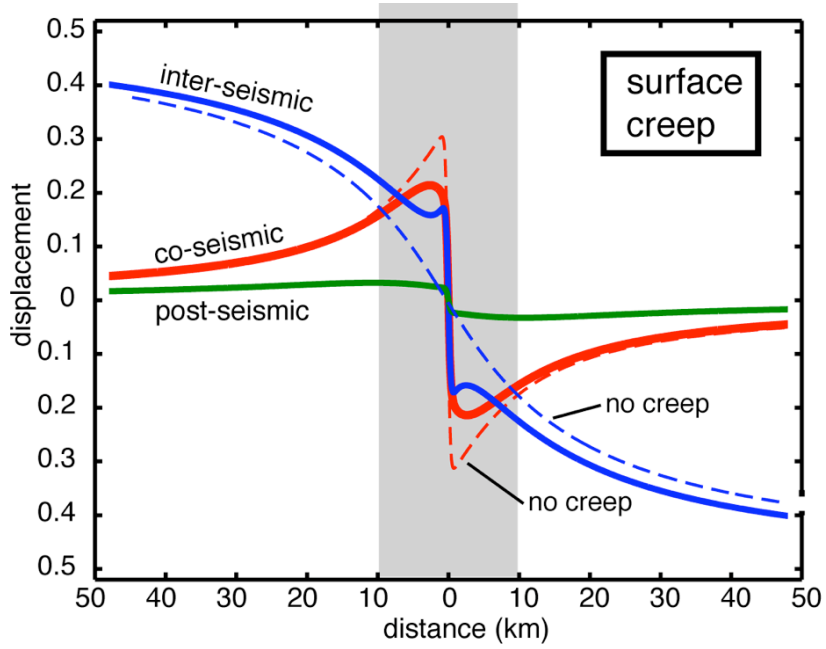

Figure 1-6. Deformation profile across a strike-slip fault system such as the San Andreas Fault during different seismic cycles. Dashed lines are signal on fault with shallow fault creep whereas the solid lines are not. InSAR is useful to get data near the fault zone (gray rectangle), where the most fault creep signal exists.

The latest developments in geodetic technique in the last 30 years are GPS and InSAR. GPS and InSAR are highly complementary methods for measuring surface deformation. GPS data provides high precision (mm/yr) vector displacements at high temporal sampling rate and a moderate spatial sampling (10 km). The main weakness of using only GPS array data is that the spacing of monitoring stations. For example, the continuous GPS stations (CGPS) of the EarthScope Plate Boundary Observatory (PBO) project, is not adequate for resolving high velocity gradients (i.e., areas of high strain rate) which usually occur near active faults. Alternatively, InSAR data has sub-cm precision, a moderate temporal sampling rate (10–50 days) and a high spatial sampling (100 m), so theoretically it could provide the short spatial scale information currently lacking in CGPS data. InSAR can reveal the distribution of slip with distance from the fault on the earth surface and thus can be used to infer the slip distribution with depth.

Table 1-2. Main geodetic methods to measure fault creep

	Temporal Sampling	Spatial Sampling	Spatial Coverage
Cultural offset	10 years	Limited	Limited
Alignment array	Month-Year	10-20 km	Very limited
Trilateration	Month-Year	100 meter	Very limited
Leveling (vertical)	Month-Year	100 meter	Very limited
Creepmeter	Seconds	3-200 meter	1 point per km along the fault
GPS	Seconds	10 km	0.1 point/square km
InSAR	10-50 days	100 meter	100 point/square km

Since InSAR is the main source of data used in my thesis, here I introduce the principle of InSAR briefly. The products of InSAR are satellite images showing ground deformation in high precision and broad areas. The principle of InSAR is making interference image between two radar observations. As satellites or airplanes pass over earth, electric magnetic waves are sent to the ground. The antenna on board records the backscatter from the ground. Each radar image is a 2D array of complex numbers. Assuming range between satellite and the ground target for two observations are ρ_1 and ρ_2, the phase difference between these two measurements is

$$\phi = \varphi_2 - \varphi_1 = \frac{4\pi}{\lambda}(\rho_2 - \rho_1)$$

After construct the interference image, we can link the surface deformation to the phase observation. In this manner, surface deformation map can be constructed after the effect of topography is removed. There are a number of review papers about the principles and applications of InSAR, including *Bamler and Hartl* [1998], *Massonnet and Feigl* [1998], *Rosen et al.* [2000], *Burgmann et al.* [2000], and *Hanssen* [2001]. Please refer to these papers for details of InSAR.

1.4 What I do in this thesis

In this thesis, I study fault creep in three different directions. First, I focused on creep on faults in the Imperial Valley, Southern California, especially on the Superstition Hills Fault (SHF). This part consists of two major components, a creep event on the SHF in 2006 and triggered slip on many faults in this area by the 4 April 2010 El Mayor-

Cucapah earthquake. The main conclusion is that the depth of fault creep is similar to sediment depth, being consistent with the rate-and-state theory. Second, I studied the relationship between fault creep rate and shallow stressing rate. High correlation exist between the two and it provided us a tool to estimate creep depth on faults that no good InSAR data available. Third, I did two technique papers on the method to study fault creep, including the optimal way to combine GPS and InSAR, and quantitatively estimate the improvement of InSAR measurements over vegetated area for L-band interferometry compared to C-band.

Important questions about fault creep and the hypothesis:

1. Is fault creep actually more widespread than it is currently thought? (Yes, there are more fault creep than we currently thought.)
2. Is rate-and-state model correct? (Hypothesis: creep depth is shallower than sediments depth.)
3. What is the creeping depth for fault segments in California? (Most segments are shallow, 1-5 km.)
4. What is the mechanism of shallow fault creep? (stressing rate controls the creep rate)
5. Which area can InSAR make a better creeping rate map? (Maacama Fault in Northern California.)
6. Can we estimate the depth extent of shallow creep based on strain rate and creep rate? (Yes, we can estimate creep depth from strain rate and creep rate. See chapter 4.)

1.5 References

Allen, C. R., Zhuoli, L., Hong, Q., Xueze, W., Huawei, Z., and Weishi, H. (1991). Field study of a highly active fault zone; the Xianshuihe Fault of Southwestern China. *Bulletin of the Geological Society of America, 103*(9), 1178-1199.

Ambraseys, N. N. (1970). Some characteristic features of the Anatolian fault zone. *Tectonophysics*, *9*, 143-165.

Azzaro, R., Mattia, M., and Puglisi, G. (2001). Fault creep and kinematics of the eastern segment of the Pernicana fault (Mt. Etna, Italy) derived from geodetic observations and their tectonic significance. *Tectonophysics*, *333*(3-4), 401-415.

Bakun, W. H., Aagaard, B., Dost, B., and Ellsworth, W. L. (2005). Implications for prediction and hazard assessment from the 2004 Parkfield earthquake. *Nature*, *437*, 969-974.

Bakun, W. H., and Lindh, A. G. (1985). The Parkfield, California, earthquake prediction experiment. *Science*, *229*, 619-624.

Bamler, R., and Hartl, P. (1998). Synthetic aperture radar interferometry. *Inverse problems*, *14*(4), 1-54.

Beavan, J., Moore, M., Pearson, C., Henderson, M., Parsons, B., Bourne, S. et al. (1999). Crustal deformation during 1994-1998 due to oblique continental collision in the central Southern Alps, New Zealand, and implications for seismic potential of the Alpine fault. *Journal of geophysical research*, *104*(B 11), 25233-25255.

Bella, F., Biagi, P. F., Caputo, M., Dellamonica, G., Ermini, A., Manjgaladze, P. V. et al. (1995). Possible Creep-Related Tilt Precursors Obtained in the Central Apennines (Italy) and in the Southern Caucasus (Georgia). *Pure and Applied Geophysics*, *144*(2), 277-300.

Bilham, R., and Behr, J. (1992). A two-layer model for aseismic slip on the Superstition Hills fault, California. *Bulletin of the Seismological Society of America*, *82*(3), 1223-1235.

Bilham, R., and Suszek, N. (2004). California creepmeters. *Seismological Research Letters*, *75*(4), 481-492.

Bucknam, R. C., Plafker, G., and Sharp, R. V. (1978). Fault movement (afterslip) following the Guatemala earthquake of February 4, 1976. *Geology*, *6*(3), 170.

Burgmann, R., Rosen, P. A., and Fielding, E. J. (2000). Synthetic aperture radar interferometry to measure Earth's surface topography and its deformation. *Annual Review of Earth and Planetary Sciences*, *28*, 169-209.

Cakir, Z., Akoglu, A. M., Belabbes, S., Ergintav, S., and Meghraoui, M. (2005). Creeping along the ismetpasa section of the North Anatolian fault (Western Turkey): Rate and extent from InSAR. *Earth and Planetary Science Letters*, *238*(1-2), 225-234.

Cavalie, O., Lasserre, C., Doin, M. P., Peltzer, G., Sun, J., Xu, X. et al. (2008). Measurement of interseismic strain across the Haiyuan fault (Gansu, China), by InSAR. *Earth Planet Sc Lett*, *275*(3-4), 246-257.

Dieterich, J. H. (1978). Time-dependent friction and the mechanics of stick-slip. *Pure and applied geophysics*, *116*(4), 790-806.

Dieterich, J. H., and Kilgore, B. D. (1994). Direct observation of frictional contacts: New insights for state-dependent properties. *Pure and Applied Geophysics*, *143*(1), 283-302.

Duquesnoy, T., Barrier, E., Kasser, M., Aurelio, M., Gaulon, R., Punongbayan, R. S. et al. (1994). Detection of creep along the Philippine Fault: first results of geodetic measurements on Leyte island, central Philippine. *Geophysical Research Letters*, *21*(11), 975-978.

Field, E. H. (2007). A summary of previous working groups on California earthquake probabilities. *Bulletin of the Seismological Society of America*, *97*(4), 1033-1053.

Furuya, M., and Satyabala, S. P. (2008). Slow earthquake in Afghanistan detected by InSAR. *Geophys. Res. Lett*, *35*, L06309.

Galehouse, J. S., and Lienkaemper, J. J. (2003). Inferences drawn from two decades of alinement array measurements of creep on faults in the San Francisco Bay Region. *Bulletin of the Seismological Society of America*, *93*(6), 2415-2433.

Geller, R. J. (1997). Earthquake prediction: a critical review. *Geophysical Journal International*, *131*, 425-450.

Glowacka, E., and Nava, F. A. (1996). Major earthquakes in Mexicali Valley, Mexico, and fluid extraction at Cerro Prieto geothermal field. *Bulletin of the Seismological Society of.*, *86*, 93-105.

Gu, J. C., Rice, J. R., Ruina, A. L., and Tse, S. T. (1984). Slip motion and stability of a single degree of freedom elastic system with rate and state dependent friction. *J. Mech. Phys. Solids*, *32*(3), 167-196.

Hanssen, R. F. (2001). Radar Interferometry: Data Interpretation and Error Analysis. *Kluwer Academic Publishers,* Dordrecht.

Hsu, L., and Burgmann, R. (2006). Surface creep along the Longitudinal Valley fault, Taiwan from InSAR measurements. *Geophys. Res. Lett*, *33*, L06312.

King, G. C. P., Bilham, R. G., Campbell, J. W., and McKenzie, D. P. (1975). Detection of elastic strainfields caused by fault creep events in Iran. *Nature*, *253*, 420-423.

Kutoglu, H. S., and Akcin, H. (2006). Determination of the 30-year creep trend on the Ismetpasa segment of the North Anatolian Fault using an old geodetic network. *Earth Planets and Space*, *58*(8), 937-942.

Kutoglu, H. S., Akcin, H., Kemaldere, H., and Gormus, K. S. (2008). *Triggered creep rate on the Ismetpasa segment of the North Anatolian Fault* (8(6)).

Lee, J. C., Angelier, J., Chu, H. T., Hu, J. C., Jeng, F. S., and Rau, R. J. (2003). Active fault creep variations at Chihshang, Taiwan, revealed by creep meter monitoring, 1998-2001. *Journal of Geophysical Research-Solid Earth*, *108*(B11), 2528.

Louie, J. N., Allen, C. R., Johnson, D. C., Haase, P. C., and Cohn, S. N. (1985). Fault slip in southern California. *Bulletin of the Seismological Society of America*, *75*(3), 811-833.

Mahsas, A., Lammali, K., Yelles, K., Calais, E., Freed, A. M., and Briole, P. (2008). Shallow afterslip following the 2003 May 21, Mw= 6.9 Boumerdes earthquake, Algeria. *Geophysical Journal International*, *172*(1), 155-166.

Marone, C. (1998). Laboratory-derived Friction Laws and Their Application to Seismic Faulting. *Annual Reviews in Earth and Planetary Sciences*, *26*, 643-696.

Massonnet, D., and Feigl, K. L. (1998). Radar interferometry and its application to changes in the Earth's surface. *Rev. Geophys*, *36*(4), 441–500.

Moore, D. E., and Rymer, M. J. (2007). Talc-bearing serpentinite and the creeping section of the San Andreas fault. *Nature*, *448*(7155), 795-797.

Prescott, W. H., and Burford, R. O. (1976). Slip on the Sargent fault. *Bulletin of the Seismological Society of America,* 1013-1016.

Prioul, R., Cornet, F. H., Dorbath, C., Dorbath, L., Ogena, M., and Ramos, E. (2000). An induced seismicity experiment across a creeping segment of the Philippine fault. *Journal of geophysical research*, *105*(B6), 13595.

Roeloffs, E. A. (2001). Creep rate changes at Parkfield, California 1966-1999: Seasonal, precipitation induced, and tectonic. *Journal of Geophysical Research-Solid Earth*, *106*(B8), 16525-16547.

Rosen, P. A., Hensley, S., Joughin, I. R., Li, F. K., Madsen, S. N., Rodriguez, E. et al. (2000). Synthetic aperture radar interferometry. *Proceedings of the IEEE*, *88*(3), 333-382.

Ruina, A. (1983). Slip instability and state variable friction laws. *Journal of Geophysical Research-Solid Earth*, *88*(B12).

Rymer, M. J., Boatwright, J., Seekins, L. C., Yule, J. D., and Liu, J. (2002). Triggered surface slips in the Salton Trough associated with the 1999 Hector Mine, California, earthquake. *Bulletin of the Seismologenical Society of America*, *92*(4), 1300-1317.

Sinvhal, H., Agrawal, P. N., King, G. C. P., and Gaur, V. K. (1973). Interpretation of measured movement at a Himalayan (Nahan) thrust. *Geophysical Journal of International*, *34*(2), 203-210.

Thurber, C., and Sessions, R. (1998). Assessment of creep events as potential earthquake precursors: application to the creeping section of the San Andreas fault, California. *Pure and Applied Geophysics*, *152*(4), 685-705.

Walcott, R. I. (1978). Present tectonics and late Cenozoic evolution of New Zealand. *Geophysical Journal of the Royal Astronomical Society*, *52*(1), 137-164.

Wei, M., and Sandwell, D. (2009). A silent Mw 4.7 slip event of October 2006 on the Superstition Hills fault, southern California. *Journal of Geophysical Research*, *114*, B07402.

Wisely, B. A., and Schmidt., D. A. (2008). Appendix P: Compilation of Surface Creep on California Faults and Comparison of WGCEP 2007 Deformation Model to Pacific-North American Plate Motion. *USGS Open File Report*, *2007-1437p*.

2. CHAPTER 2: A Silent M4.8 Slip Event of October 3-6, 2006, on the Superstition Hills Fault, Southern California.

Earthquake safety tip 2:

Look out your window often. If you see a large, zig-zag-shaped crevasse moving rapidly from the horizon toward your home, step either to the right or the left.

2.1 Abstract

During October of 2006, the 20-km long Superstition Hills fault (SHF) in the Salton Trough, Southern California, slipped aseismically producing a maximum offset of 27 mm as recorded by a creepmeter. We investigate this creep event as well as the spatial and temporal variations in slip history since 1992 using ERS and ENVISAT satellite data. During a 15-year period, steady creep is punctuated by at least three events. The first two events were dynamically triggered by the 1992 Landers and 1999 Hector Mine earthquakes. In contrast, there is no obvious triggering mechanism for the October 2006 event. Field measurements of fault offset after the 1999 and 2006 events are in good agreement with the InSAR data indicating that creep occurred along the 20 km-long fault above 4 km depth with most of the slip occurring at the surface. The moment released during this event is equivalent to a M_w 4.7 earthquake. This event produced no detectable aftershocks and was not recorded by the continuous GPS stations that were 9 km away. Modeling of the long-term creep from 1992 to 2007 creep using stacked ERS interferograms also shows a maximum creep depth of 2-4 km

with slip tapering with depth. Considering that the sediment thickness varies between 3 km and 5 km along the SHF, our results are consistent with pervious studies suggesting that shallow creep is controlled by sediment depth, perhaps due to high pore pressures in the unconsolidated sediments.

2.2 Introduction

Aseismic creep refers to fault slip that does not produce seismic radiation. Both geological and geodetic observations document evidence of creep along many fault segments in California [*Steinbrugge and Zacher*, 1960; *Tocher*, 1960; *Nason*, 1971; *King et al.*, 1973; *Burford and Harsh*, 1980; *Prescott et al.*, 1981; *Schulz et al.*, 1982; *Wesson*, 1988; *Burgmann et al.*, 2000; *Lyons et al.*, 2002; *Lyons and Sandwell*, 2003a]. Fault creep releases elastic strain and reduces the hazard from future earthquakes [*Mavko*, 1982; *Burgmann et al.*, 2000; *Toda and Stein*, 2002; *Schmidt et al.*, 2005; *Fialko*, 2006; *Lienkaemper et al.*, 2006], making it an important part of seismic hazard estimation.

The Superstition Hills Fault (SHF) is located on the southern extent of the San Jacinto fault zone (Figure 1). This fault has a well documented history of surface creep, most of which is triggered by nearby earthquakes as seen in 1951, 1968, 1987, 1989, 1992 and 1999 [*Allen et al.,* 1972; *Hudnut and Sieh*, 1989; *Bodin et al.*, 1994; *Rymer et al.*, 2002]. The 1987 M_s 6.6 earthquake was the largest event on this segment in 300 years and was extensively investigated in a number of seismic and geodetic studies [*Bilham*, 1989; *Boatwright et al.*, 1989; *Hudnut and Clark*, 1989; *Hudnut et al.*, 1989a;

Hudnut et al., 1989b; *Hudnut and Sieh*, 1989; *Klinger and Rockwell*, 1989; *Lindvall et al.*, 1989; *Mcgill et al.*, 1989; *Sharp*, 1989; *Sharp et al.*, 1989; *Sharp and Saxton*, 1989; *Williams and Magistrale*, 1989]. During the 11 years before the 1987 earthquake, the average rate of surface creep was 0.5 mm/yr [*Louie et al.*, 1985]. A creepmeter installed after the 1987 earthquake [*Bilham and Behr*, 1992] showed afterslip at an average rate of 28 mm/yr consisting of episodic creep events super-imposed on a slow quasi-steady slip of 2.4 mm/yr through 1991. No creepmeter data are available between 1991 and 2004. A new creepmeter was installed in March 2004 and recorded steady creep at a rate of 1.35 mm/year through October 2006. Dextral creep events occurred on 11 Aug 2005 with an amplitude of 0.5 mm and on 20 January 2006 with an amplitude of 0.35 mm. Starting on 3 October 2006, creep events occurred with an amplitude of more than 27 mm over the next 14 days, with 85% of the amplitude manifested in the first 3 days (Figure 2). For the 2006 creep event there was no obvious triggering event. The 2006 creep event was not detected seismically nor was it observed on the closest continuous GPS station 9 km from the fault. A better understanding of the poorly recorded creep history of the SHF has implications not only for the earthquake hazard assessment in the Imperial Valley area, but also for the general understanding of the physical mechanisms of fault slip and the depth-dependent transition from velocity-strengthening to velocity-weakening in the shallow part of the seismogenic zone [*Marone and Scholz*, 1988].

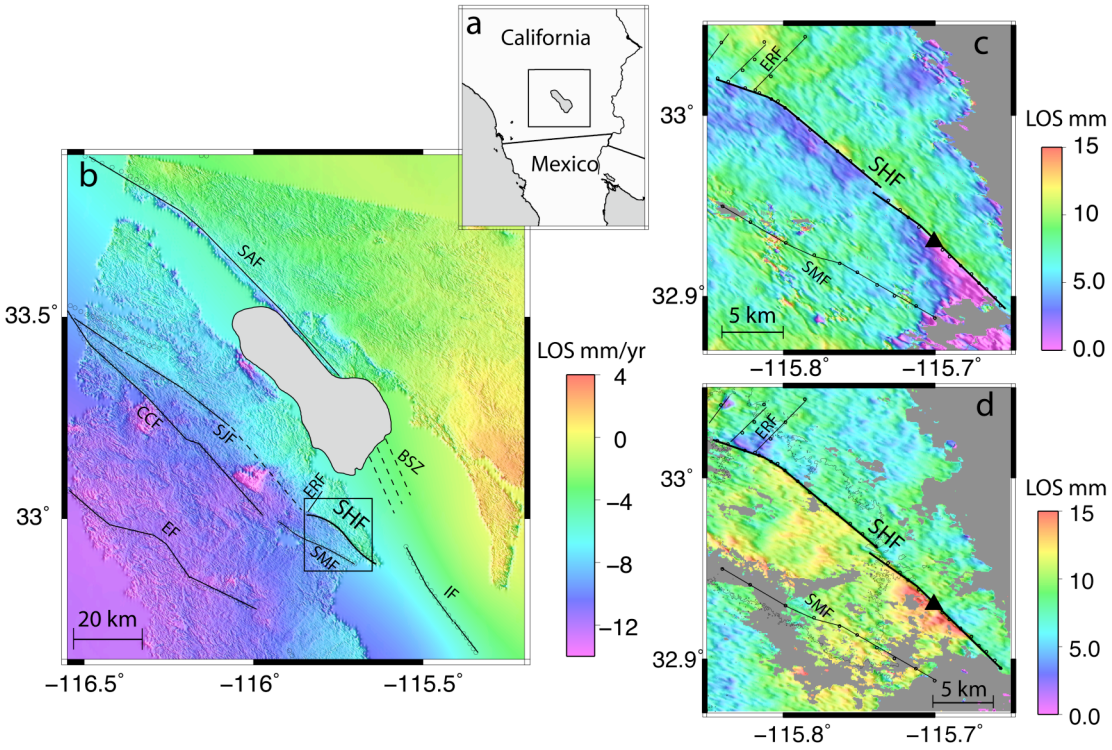

Figure 2-1. (a) Research area in southern California. The square box is the location of figure 1b. (b) Stacked 13 interferograms of 15 years ERS1/2 data (Track 356 Frame 2925/2943). The square box on the mid-bottom is the area of figure 1c and 1d. (c) Stacked 7 descending interferograms of ENVISAT data (Track 356 Frame 2943) that span the 2006 creep event. The black dots trace the SHF fault, the Elmore Ranch fault and the Superstition Mountain fault. The black triangle is the location of a creepmeter. (d) Stacked 2 ascending interferograms of ENVISAT data (Track 77 Frame 657) that span the 2006 creep event. Faults names are abbreviated as follows: SAF, San Andreas fault; SJF, San Jacinto fault; EF, Elsinore fault; SHF, Superstition Hills fault; SMF, Superstition Mountains fault; IF, Imperial fault; ERF, Elmore Ranch fault; BSZ, Brawley Seismic Zone; CCF, Coyote Creek fault.

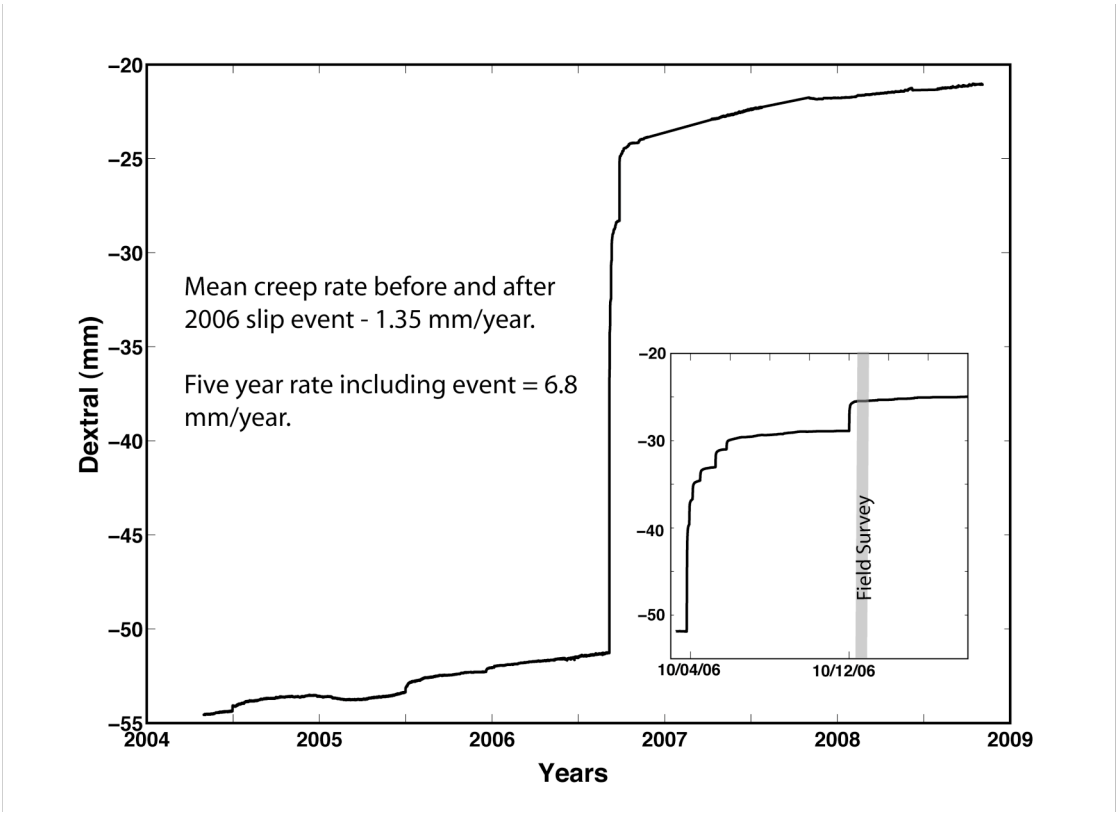

Figure 2-2. Creepmeter data from a new creepmeter installed by Roger Bilham beginning in 2004. It recorded 1.35 mm/year before and after the 2006 events during 2004-2009 (least squares fit). Compared to the ~ 27 mm creep event, the signal-to-noise level in the instrument is >1000:1. The small figure on the right-bottom corner is a zoom-in of slip during the 2006 events. The second field survey is on 10/12/2006, after the creep events ended. No slip was triggered on the Superstition Hills or San Andreas Fault (SAF) following a magnitude 4.5 earthquake 3 Nov 06 41.7 km to the southwest of the creepmeter.

While creepmeters can provide excellent temporal coverage of fault slip [*Bilham et al.*, 2004], they do not reveal the spatial variations in displacement that are needed to infer the along-strike and down-dip variations in slip. Field measurements of the surface offset can provide information on along-strike variations due to creep events [*Rymer et al.*, 2002] although they are not always performed or are often incomplete. It is possible that the ground cracking can be distributed across a fault zone so that a portion of slip

can be overlooked. Moreover, neither field measurements nor sparse GPS measurements (>10 km spacing) can record the variations in cross-fault displacement that are needed to infer the slip distribution with depth [*Lorenzetti and Tullis*, 1989; *Thatcher*, 1990; *Savage and Lisowski*, 1993; *Fialko et al.*, 2001; *Simpson et al.*, 2001; *Wyss*, 2001; *Malservisi et al.*, 2005; *Schmidt et al.*, 2005; *Funning et al.*, 2007]. Repeat-pass radar interferometry [*Massonnet and Feigl*, 1998] is a valuable tool for measuring spatial variations in fault slip at length scales greater than about 50 m. The main limitations of InSAR are the poor temporal coverage (e.g. given large repeat interval) and lack of phase correlation in vegetated areas [*Rosen et al.*, 1996]. Fortunately, a large section of the SHF is located in arid desert and hence well correlated in the interferometric images (Figure 1). To our knowledge, this is the first time that both extensive field measurements and InSAR interferograms are available for multiple creep events in this area.

There are three goals of this paper. The first is to estimate the magnitude and depth of creep along the SHF associated with the October 2006 creep event. The creepmeter measurements provide excellent temporal coverage of the 2006 event at a single point. To extend the spatial coverage, we use stacks of ascending and descending ENVISAT InSAR imagery. This combination of data is used (i) to demonstrate that the creep is localized on a narrow fault trace, (ii) to measure the along-strike variations in fault creep, and (iii) to invert for the depth extent of creep. The amount of moment released by aseismic creep can be used for seismic hazard assessment of the SHF and improving understanding of the relation between creep and earthquakes.

The second goal is to document the slip history of the SHF over a longer time interval spanning 1992 to 2007 and compare these InSAR measurements with field measurements of the long-term creep record. A similar analysis has been performed by *Van Zandt and Mellors* [manuscript in preparation, 2008]. In addition, the magnitude and depth of the accumulated shallow creep is estimated and compared with the 2006 event.

The third goal is to test the two-layer creep model for aseismic slip on the SHF proposed by *Bilham and Behr* [1992]. Creepmeter measurements following the Ms 6.6 1987 earthquake demonstrate that the time averaged slip rate decreases as a power law [*Bilham and Behr*, 1992]. The 3-year average creep rate between 1989 and 1991 was 28 mm/yr while the average creep rate is about 6.8 mm/yr between 2004-2006 based on creepmeter data. The creepmeter data show that long-term shallow creep consists of slow steady creep punctuated by accelerated creep events. Between 1989 and 1991 the creep rate during the events was about 10 times greater than the average creep rate between events. Based on this 10-1 ratio, *Bilham and Behr* [1992] proposed a two-layer model for aseismic slip on the SHF. During periods of the long-term shallow steady creep, the slip extends from the surface to a depth of about 300 m. During the creep events the slip extends 10 times deeper to a depth of about 3 km. The estimate of 3 km for the depth of the creep events was based on the abrupt increase in aftershock seismicity below approximately 3 km depth which also corresponds to the base of the sediments in the region [*Kohler and Fuis*, 1986]. Bilham and Behr speculated that the transition depth is sensitive to applied fault-normal stresses and suggest that the ratio of stable-sliding to episodic-slip velocities may provide an indication of secular variations

in tectonic stress. Using InSAR data we attempt to test the hypothesis that the depth of the long-term shallow steady creep is systematically smaller than the depth of the creep events. We find that the average shallow creep depth between 1992 and 2007 is similar to the depth of the 2006 event, both about 2-4 km. If this observation is correct then the slip is dominated by creep events from 1992 to 2007 and we can't discriminate the depth of the shallow steady creep from the depth of the creep events using InSAR.

2.3 Data

Following the observation of the SHF creep event starting on October 6, 2006 [*Roger Bilham*, personal communication], we performed two field surveys: an initial reconnaissance survey on October 8 and a second more detailed survey in collaboration with *Rob Mellors* and *Afton Van Zandt* from San Diego State University on October 12, 2006. Because small surface cracks associated with creep can be degraded quickly by wind and especially rain, it was important to make measurements soon after the event [*Rymer et al.*, 2002]. Fortunately, the cracks were visible on the surface for more than 3 months following the event due to the lack of rain. In this region, the surface is arid and the creep amplitude was substantial (5-27 mm) making the surface cracks easy to trace for 8 km (Figure 3). The southernmost end of the rupture was located. But the northern end was not completely mapped because of time limitations. A typical surface offset is shown in Figure 3d. Strike-slip displacement was measured along the trace of the rupture at approximately 100 m intervals.

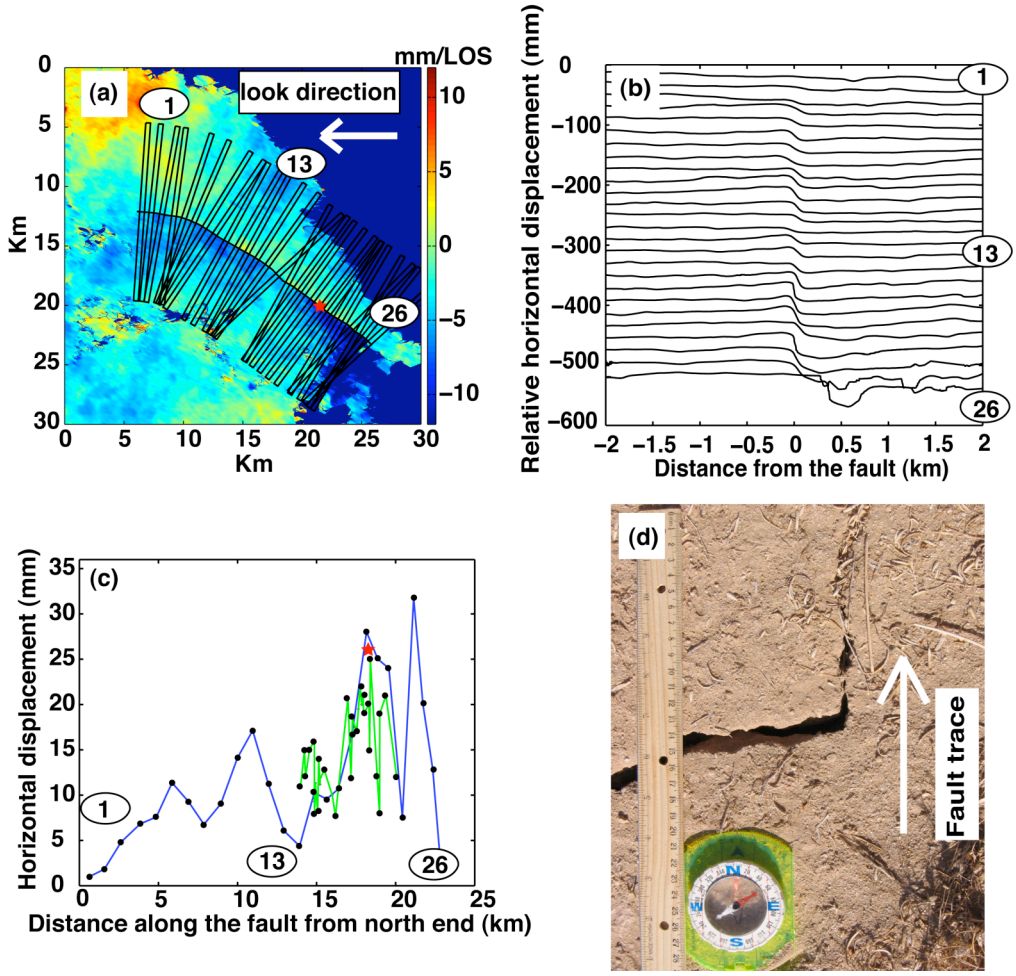

Figure 2-3. (a) Stack of 7 ENVISAT interferograms spanning the October 5, 2006 creep event on the Superstition Hills segment of the San Jacinto Fault zone. This event was measured/monitored on a creepmeter (red star) maintained by *Roger Billham*, but this event was not detected by the sparse continuous GPS array nor nearby seismometers. (b) Line of sight (LOS) deformation along 26 profiles across the fault trace reveals a sharp step. (c) Peak-to-trough LOS deformation (blue) from interferometry compared with field measurements (green) made by students and faculty from UCSD and SDSU just after the event and the creepmeter data (red star). Black dots are data points. The LOS deformation from interferometry is projected to a horizontal displacement vector parallel to the fault strike, based on the assumption of no vertical slip. (d) The surface crack was measured over a length of 8 km, about 1/2 of the total fault length. The lower amplitude of the field measurements with respect to the interferometry could indicate some creep was underestimated in the field because it occurred off of the main fault strand or rotation of en-echelon cracks occurred [*Bilham*, 2005].

Extensional stepovers were identified and a ruler was placed over the crack and aligned in the direction of the overall fault trace (302 degrees clockwise from North). Then the distance between conjugate piercing points was measured at 2-3 locations on each crack (Table 1). The averaged fault offsets are shown in Figure 3c.

ERS1/2 InSAR data covering a time period of more than 15 years constrain the long-term creep rate of the Superstition Hills fault, and 2 years of ENVISAT data constrain the displacement during the October 2006 event. Both ERS and ENVISAT data along track 356 were collected by the European Space Agency and obtained through the WINSAR archive (Figure 4). For the ERS data, we processed two frames, 2925 and 2943, together to better estimate the long wavelength error. ENVISAT data are used to image the 2006 creep event (ascending track 77, frame 657; descending track 356, frame 2943). The InSAR data was processed using SIOSAR software, and SRTM data were used to remove the topographic effect. Deformation along the southern-most end of the SHF was not fully recovered because all interferograms were decorrelated in the agricultural areas of the Imperial Valley.

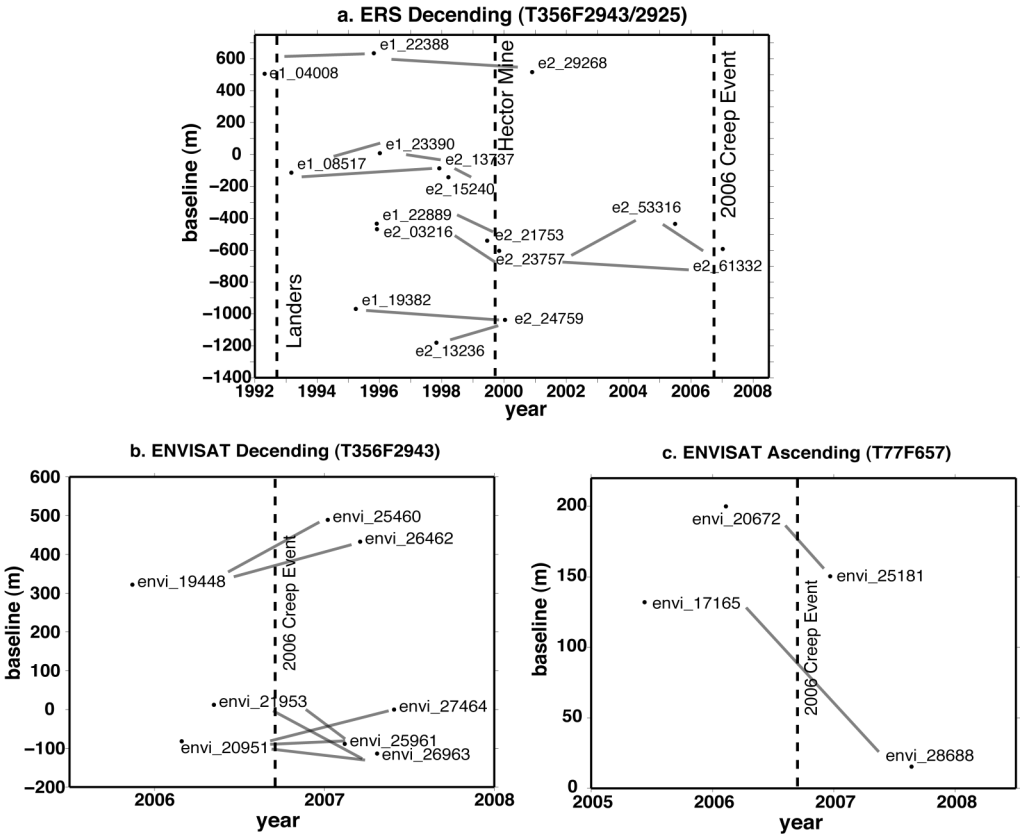

Figure 2-4. InSAR data used in this research. (a) ERS descending data for the long-term slip (Track 356 Frame 2943/2925). The dashed lines label the times of the Landers, Hector Mine earthquakes, and the 2006 creep event. (b) ENVISAT descending data (Track 356 Frame 2943) for the 2006 creep event. (c) ENVISAT ascending data (Track 77 Frame 657) for the 2006 creep event. The dashed line in b and c indicates the time of the 2006 creep event.

A combination of sparse GPS and dense InSAR is used to recover the surface deformation over the length scales needed to estimate slip versus depth. The field measurements only provide the slip on the trace of the fault. Estimation of the slip from the surface to the base of the seismogenic zone (10-14 km) requires deformation measurements extending between 0 and 14 km from the fault. This wide range of length scales requires both minimal smoothing of the interferograms as well as incorporating long-wavelength constraints from the GPS-derived SCEC V3.0 velocity model [*Shen et*

al., 1996]. We use a remove/restore method to combine the GPS and InSAR along with stacking to minimize the InSAR errors [*Lyons and Sandwell*, 2003b]. Deviations from the standard InSAR processing consisted in the following steps: (1) Compute the line-of-sight (LOS) model phase difference from the SCEC velocity model and map into radar co-ordinates using a topographic phase mapping function. (2) Compute the amplitude dispersion [*Ferretti et al.*, 2001] of all aligned SAR images to use as a weight function for the spatial filtering of the interferograms. (3) Low-pass filter each single-look interferogram using a Gaussian filter with a 0.5 gain at a wavelength of 100 m. (4) Stack the residual phase of the interferograms and remove a planar surface from the stack. (5) Restore the LOS phase from the SCEC velocity model.

2.4 Displacement along the fault

To begin the analysis we compared the fault slip measured in the descending stacked interferogram covering a time period of 2 years (Figure 3a) with the offsets measured in the field. The LOS displacement is measured by taking the difference of maximum and minimum value within 1 km from the fault after the profile is flattened. In this way, the LOS displacement won't be underestimated even though the interferograms are smoothed by the Gaussian filter. Atmospheric errors should be less than 3 mm, considering the fact that 7 images are stacked and the horizontal length scale is small [*Emardson et al.*, 2003]. In order to compare the InSAR measurements with the field measurements, pure strike slip is assumed, (as confirmed by data from the ascending orbit and three-dimensional modeling discussed below) and LOS measurements are

converted to strike-slip displacement based on satellite and fault geometry. The fault azimuth is 302 degrees clockwise from North and the local incidence angle of the satellite is 23 degrees. We use a local incidence angle for the finite fault inversion and a constant 23 degrees incidence angle for the anti-plane dislocation model.

Results from the creepmeter, InSAR, and field measurements are compared in Figure 3c. All three measurements are consistent at the location of the creepmeter where the displacement is 27 mm. In general there is good agreement between the field measurements and the InSAR data, which confirm that the creep has a negligible (if any) dip-slip component and is confined to a very narrow zone. The InSAR step appears smooth (~50 m) because of the low-pass Gaussian filter that was applied to reduce the phase noise. The dextral horizontal displacement along SHF shows two lobes with a minimum at the along-fault distance of ~13 km (Figure 3c). The along-fault variations in displacement for the 2006 event are very similar to the field measurements of fault creep made in 1999 just after the Hector Mine earthquake, and the fault offset for both the 2006 and 1999 creep events is similar in magnitude to events in 1968, 1979, and 1987 as compiled by *Rymer et al.* [2002].

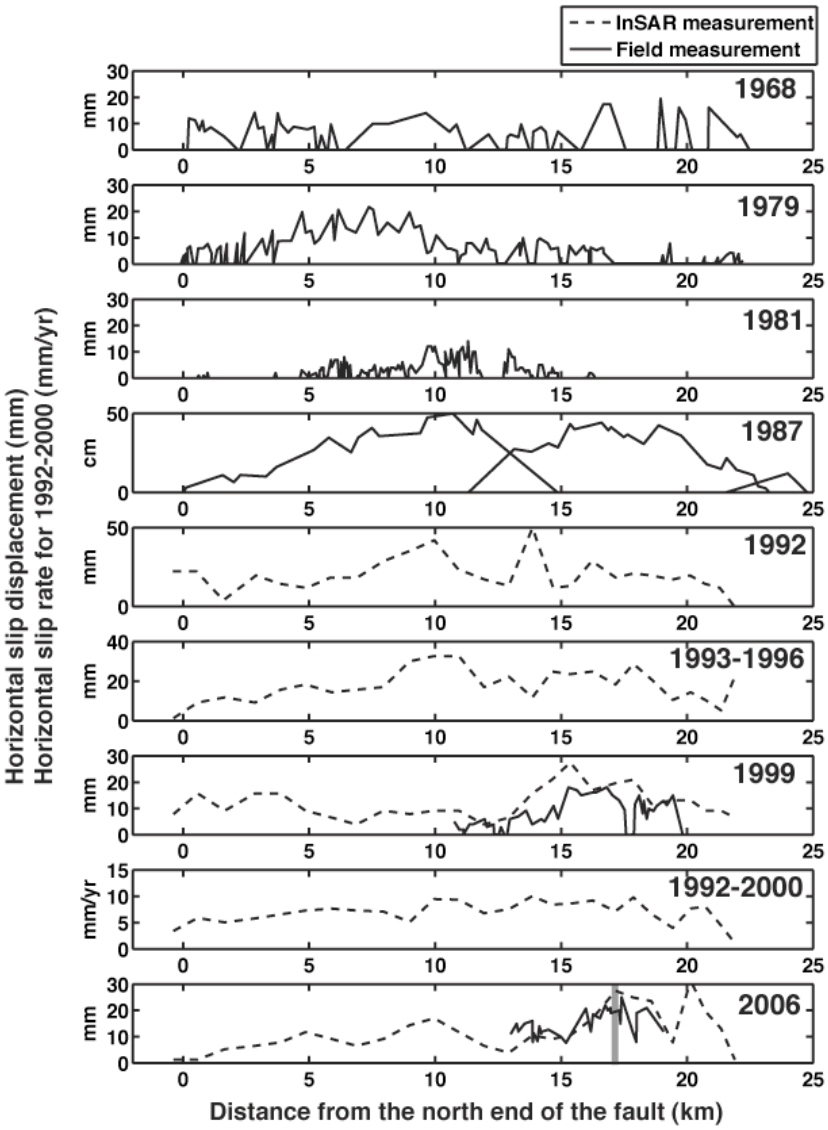

Figure 2-5. Slip distribution along the SHF during 7 slip events. The y-axis is displacement except the 1992-2007, which is slip rate. Solid lines are field measurements, while dashed lines are InSAR measurements. Field measurements of 1968, 1979, 1981, 1987 and 1999 are digitized from *Rymer* [2002]. No field measurements were made on the northern part of the fault (0-10 km) for the triggered event in 1999. Field measurement of the 2006 event and all InSAR measurements are from this study. There are no short-duration interferometric pairs spanning the 1992 Landers earthquake. So a residual interferogram is generated by subtracting e1_08517_e1_23390 from e1_04008_e1_223881009. Black dots are the data sampling of InSAR measurements. The 1987 displacement is measured 12 days after the earthquake. The vertical grey bar in 2006 event shows the location of the Caltech/CU creepmeter. The 0 km is at N32.023 W115.853.

In addition, we estimate the along-strike slip variation from 1992 to 2007 using both individual and stacked interferograms. The slip that accumulated between 1992 and 2007 is compared with the slip measured by *Rymer et al.* [2002] for the slip events (Figure 5). The InSAR result is consistent with field measurement for slip events in 1999 and 2006, which lends support to the validity of the method. Many of the slip inferred from the InSAR measurements for the 1999 event are significantly larger than the slip reported from the field measurements, probably because the deformation zone is wider than the cracks seen in the field, or additional displacement occurred shortly after the field measurements. The slip during 1993-1996 is substantial, with a maximum slip rate of 10 mm/yr, which exceeds the steady background slip rate between 1989 and 1992 [*Bilham and Behr*, 1992] derived from creepmeter data. We hypothesize that one or more creep events occurred between 1993 and 1996. Similarly the average slip between 1992 and 2007 is higher than the background slip rate and the slip is relatively uniform along the fault; both observations suggest slip occurred in multiple events and the stable creep and episodic creep events have a different spatial distribution along the fault. Next, we examine slip variations with distance from the fault to estimate the slip distribution with depth.

2.5 Estimates of slip versus depth using a finite fault model

Solutions for surface displacements due to dislocations in an elastic half-space are readily available for both homogeneous [*Okada*, 1985] and layered media [*Wang et al.*, 2003]. To model the displacement for the 2006 creep event, we use the finite fault homogeneous Greens function [*Okada*, 1985]. This finite fault model is appropriate for

a short-term event because, as we demonstrate below, most of the slip occurred in the shallow crust. However, to model the long-term slip from 1992 – 2007, we need to account for the fault slip below the brittle-ductile transition. Expecting less variation of slip along the fault during the interseismic period and trying to simplify the modeling of the interseismic slip, we use the Green's function for an anti-plane dislocation model for the long-term slip [*Savage et al.*, 1981]. Although the Superstition Hills fault cuts through thick sediments through overlying bedrock [*Fuis and Kohler*, 1986], the principal effect of increases in rock rigidity with depth is a small shift in the inferred slip distribution toward shallower depth [*Cohen*, 1999; *Fialko*, 2004]. So we ignore the effects of layering in our analysis. In order to do a direct comparison of the slip depth between the 2006 creep event and the long-term slip, we model the 2006 creep event using the anti-plane dislocation model as well.

Slip inversions using co-seismic and post-seismic deformation data are well established techniques [*Nielsen et al.*, 1995; *Murray and Segall*, 2002; *Fialko et al.*, 2005]. A homogeneous half-space elastic model is used to estimate the strike-slip and dip-slip components at depth by least-square fitting the surface deformation data (Figure 6,7,8). The detailed procedure and data reduction method can be found in *Fialko* [2004]. To stabilize the inversions in the presence of long-wavelength noise (mainly atmospheric noise), we perform an irregular spatial sampling of the data based on the distance from the fault (Figure 7). Since the displacement signal is near-field and low amplitude, it is crucial to describe the surface trace of the fault as accurately as possible. We use 26 segments, based on the USGS regional fault map and B4 Laser altimetry data [*Bevis et al.,* 2005] to model the 20-km-long SHF. Since the inversions are inherently non-

unique, additional constraints are added to regularize the inversion. We prohibited sinistral slip by using a Coleman algorithm, which is the default in MATLAB function "lsqlin" [*Coleman and Li*, 1996]. Wild spatial variations in slip were suppressed by using a Laplacian smoothness constraint. The smoothness weighting parameter controls the smoothness of the slip model. The Root Mean Square (RMS) misfit of the model is inversely related to the smoothness weighting parameter, which is a classic tradeoff, as shown in Figure 6. We use this tradeoff to seek the "smoothest" slip distribution with the lowest RMS misfit. RMS misfit is defined as $\chi = \sqrt{\frac{\sum_{i=1}^{N}\left(d_i - d_i^m\right)^2}{N}}$, where d_i is the LOS displacement on sampled InSAR data points (both ascending and descending), d_i^m is the modeled LOS displacement on the sampled points, and N is the total number of the sampled points.

The data and modeled interferograms are illustrated in Figure 7 for both descending and ascending LOS directions. The misfit is 1.0 mm LOS for ascending data and 0.9 mm LOS for descending data. The relatively large anomaly at the very southern end of the fault in the descending residual might be due to creep on a sub-fault in the irrigation area. Because it is only an edge effect for our inversion and no useful ascending data cover that sub-fault, we didn't include it in our model. The slip versus depth distribution shown in Figure 8 indicates that most slip is confined to depths less than 3 km and maximum slip occurs at the surface. The model has only a small component of vertical fault slip (<10%), which validates our assumption of pure horizontal slip. There are two patches of high slip along the fault. The north segment

slips less than the south segment, with an average dextral slip of about 9 mm and 13 mm respectively, which is consistent with the fault offset observed in the field (Figure 3). Using a "nominal" value of the shear modulus of 33 GPa [*Becker et al.*, 2005], the moment of this slip event is 1.3×10^{23} dyne-cm. This corresponds to a moment magnitude of M_w 4.7 earthquake [*Kanamori*, 1977]. Since the fault slipped slowly over a period of 9 days, no seismic waves were generated. No aftershocks were detected by the regional seismic arrays or local portable seismometers.

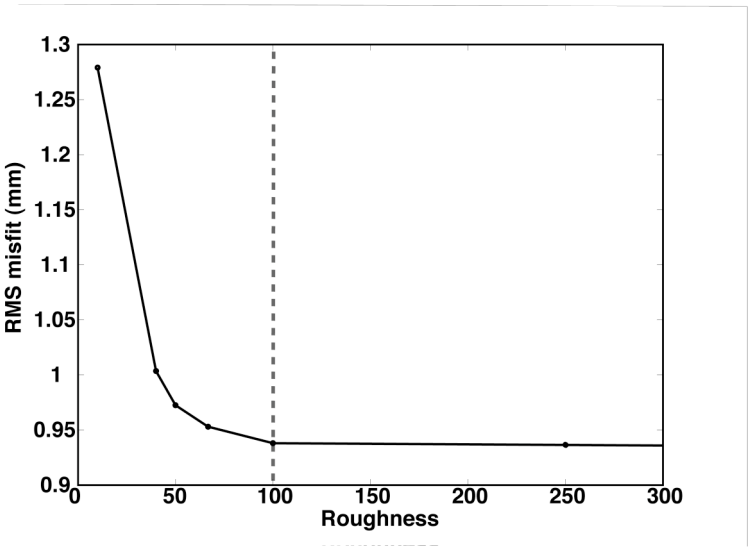

Figure 2-6. LOS RMS misfit versus roughness for the finite fault model inversion. The black dots are the sampling data. The dashed line indicates the value we use for roughness, 100.

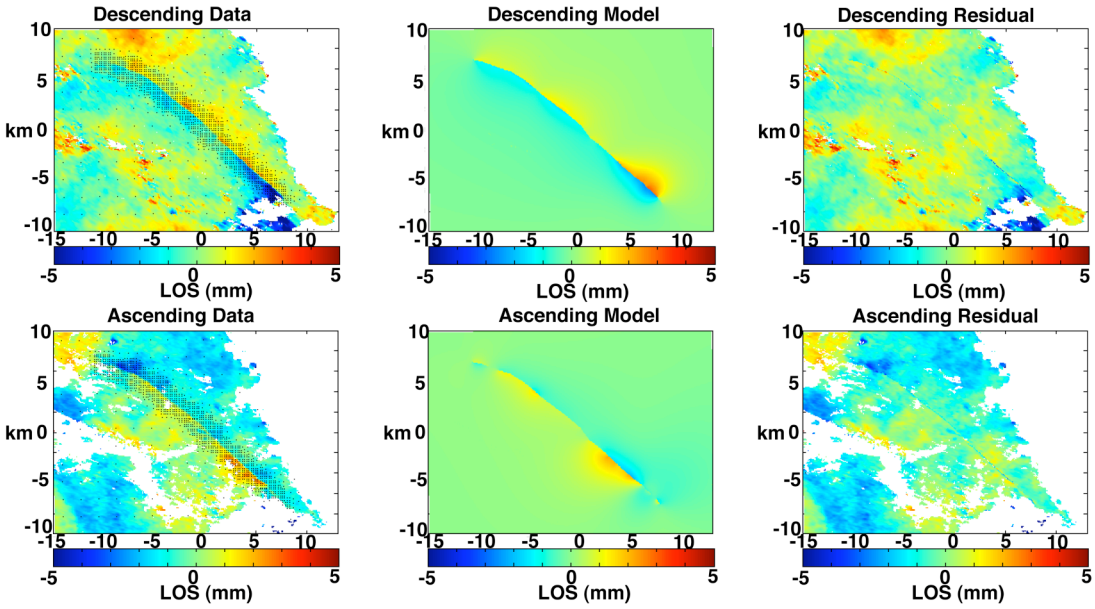

Figure 2-7. InSAR data (left column), the best fitting model (middle column), and the residual (right column) for the 2006 event. The black dots in InSAR data figures are sub-sample locations of data that are used in the inversion.

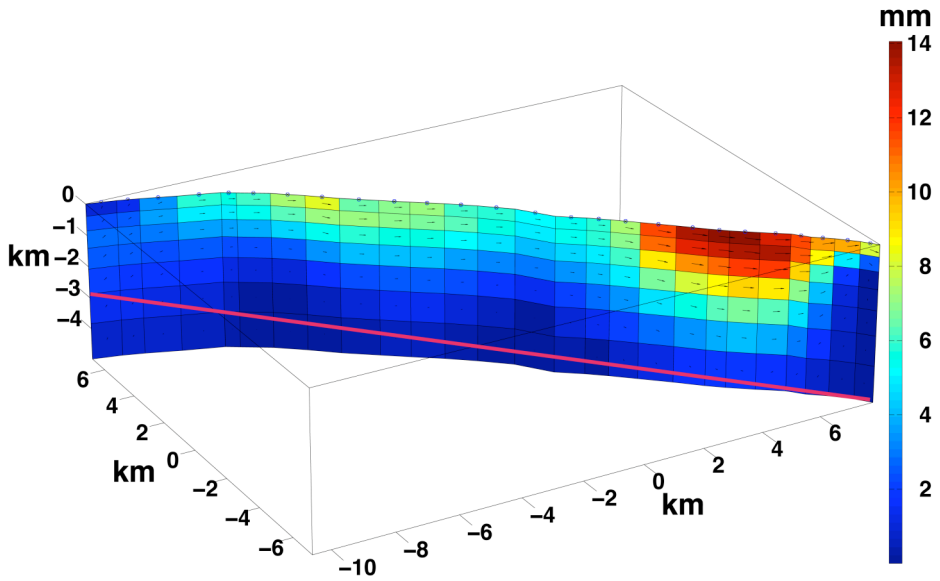

Figure 2-8. The slip distribution for the 2006 creep event using finite fault model. The patch size along the fault varies from 0.5 km to 0.9 km. The patch size in depth varies from 0.4 km to 1 km, increasing with depth. The arrow shows the relative size and direction of vertical and horizontal slip. The pink link is the sediment depth from seismic reflection data [*Kohler and Fuis,* 1986].

2.6 Anti-plane dislocation model for both the creep event and the long-term slip

Modeling the long-term slip requires consideration of the entire depth range from the surface to well below the brittle-ductile transition. The deep slip is most easily parameterized by an anti-plane dislocation extending from the locking depth to infinity. To compare the 2006 creep event to the long-term slip we repeat the event analysis of Section 4 using an anti-plane dislocation model. A discrete slip model has been used to compute the surface profile. However, the shallow locking depth estimated from the discrete slip model is not realistic and shouldn't be regarded as the true locking depth [*Savage*, 2006]. Therefore we use a model assuming piecewise constant variations in fault slip with depth based on the anti-plane dislocation model that consists of a dextral strike-slip dislocation in an elastic half space [*Weertman*, 1965; *Cohen*, 1999]. The surface displacement *v(x)* is given by

$$v(x) = \int_{-\infty}^{0} \frac{x}{x^2 + z^2}\, m(z)\, dz \qquad (1)$$

where *x* is the distance from the fault trace, *z* is the depth and *m(z)* is the slip distribution versus depth.

The model is parameterized in layers with uniform slip in each layer. In this case, the slip distribution *m(z)* in equation (1) can be set up as a linear programming problem with a smoothness constraint in the form of Laplacian operator ∇^2,

$$\min \| (Am - b) / \sigma \|^2 + \lambda \| \nabla^2 m \| \quad \text{subject to } m > 0 \qquad (2)$$

where b is the observed surface displacement as a function of distance from the fault trace, σ is the uncertainty in the observation, m is fault slip versus depth, λ is the weighting factor of smoothness, and A is a Matrix of the Green's function,

$$\begin{aligned} A_{ij} &= \int_{z_j}^{z_{j-1}} \frac{x_i}{x_i^2 + z^2} dz \\ &= \int_{z_{j-1}}^{0} \frac{x_i}{x_i^2 + z^2} dz - \int_{z_j}^{0} \frac{x_i}{x_i^2 + z^2} dz \qquad (3) \\ &= \tan^{-1} \frac{x_i}{z_j} - \tan^{-1} \frac{x_i}{z_{j-1}} \end{aligned}$$

where x_i is the distance from the fault, z_j is the depth of the top of a layer and z_{j-1} is the depth of the bottom of a layer.

The inversion is more sensitive to the shallow slip than to the deep slip so the layer thickness was adjusted to increase with depth from 200 m to 1800 m. The last layer extends from the maximum depth of seismicity in the region (14 km) to infinity. As a consequence, the entry in the matrix A that corresponds to the last layer is calculated with a single arctangent function. The 100-m wavelength spatial Gaussian filter that was applied to the interferogram was also applied to the Greens functions in the matrix A to make the model smoothness match the data smoothness.

Sixteen fault-perpendicular profiles were extracted from interferograms in rectangular boxes 400 m wide and up to 40 km long. Data near the ends of the fault were not used to avoid the 3-D edge effects. Profiles were binned at an even 100 meters spacing away from the fault [*Parker*, 1977; *Parker and Song*, 2005]. The smoothness parameter was selected as a tradeoff between model smoothness and RMS misfit. Because the east side of the SHF is close to farm land, where InSAR data are decorrelated, there is only 5 km of data on the east side of each profile, while data to the west of the fault provides much better coverage (> 30km). The model successfully reproduced the surface deformation for all 16 profiles, and the average root mean square (RMS) misfit is 6 mm (Figure 9). The sharp step near the fault is caused by the shallow slip. The magnitude of the slip varies along the fault (as seen from variations between different profiles). However, the decay pattern with depth is similar for all profiles. The far-field deformation vanishes away from the fault, suggesting there is no deep slip for the 2006 creep event. In all cases, the slip has a maximum at the surface and then decays rapidly to zero slip at 2-4 km depth. Many of the profiles show a high noise area about 1 km to the west of the fault. This is likely to be a consequence of stacking several interferograms with similar atmospheric error and less than optimal correlation. To the north of the SHF (Figure 1), a large range change in LOS is observed and is likely explained by ground subsidence due to the groundwater extraction [*Mellors and Boisvert*, 2003].

The same anti-plane dislocation inversions were performed on 16 profiles extracted from the long-term stack (1992-2007). These profiles generally have a lower noise level because more data are available for stacking. The anti-plane dislocation

model also shows a good fit to all the profiles with an average RMS misfit of 1.1 mm/yr (Figure 10). The slip versus depth models show shallow and deep slipping zones separated by a locked zone from 3-7 km deep. The shallow slip has a peak at the surface and decays rapidly to zero at 2-4 km depth. This is very similar to the slip versus depth distribution derived from the interferograms spanning the 2006 event. In addition, the long-term models all have a deep-slip component that matches the nearly linear trend in the data profiles far from the fault. As discussed above, this trend is constrained by the SCEC velocity model, which is based on GPS measurements. We find there is a trade off between the locking depth and the deep slip rate. Based on the maximum depth of the aftershocks following the 1987 earthquake, we chose the upper edge of the deepest layer to be 14 km [*Lin et al.*, 2007]. In the inversion, a deep slip rate of about 30 mm/yr from 1992 to 2007 is preferred. However, as discussed below, an unknown fraction of the linear trend could be due to interseismic slip on nearby faults such as the San Andreas/Brawley Seismic Zone, Superstition Mountain, or Imperial faults. Therefore, we cannot constrain the deep slip rate using the InSAR data.

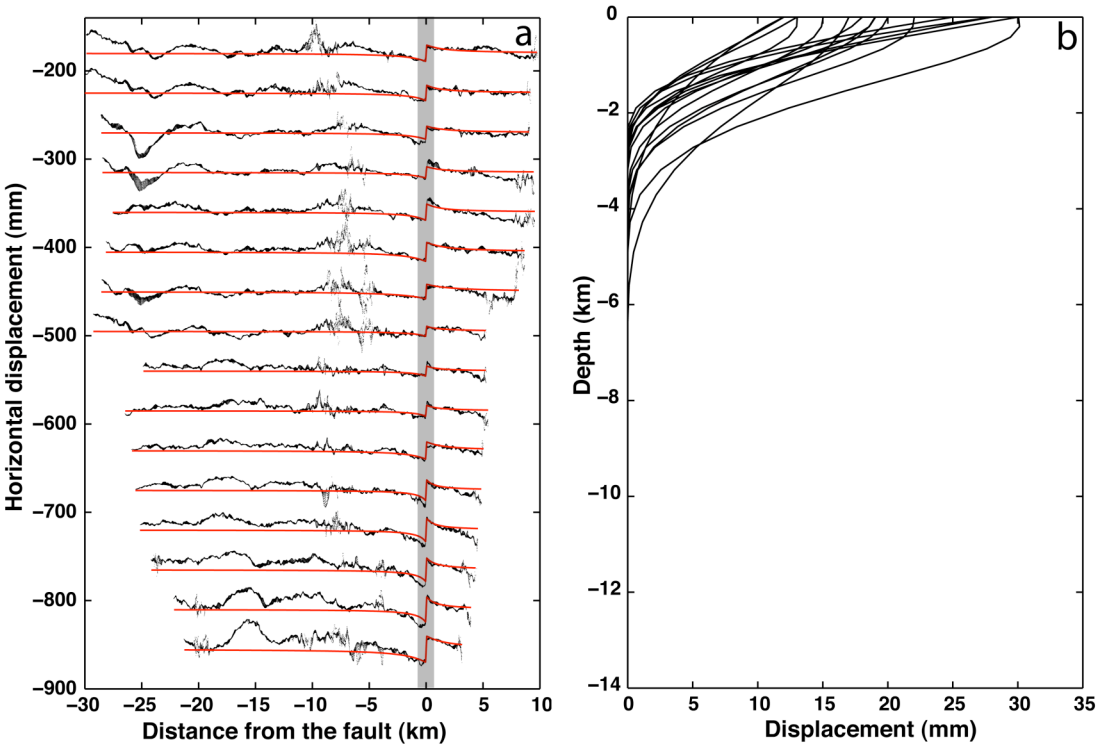

Figure 2-9. Profiles of the 2006 slip event on the SHF and the best fitting anti-plane dislocation models. (a) Profiles and best fitting anti-plane dislocations. The black dots are the InSAR data with boxes 400 m wide and 40 km long, and the red lines are the best fitting models. The y-axis is the relative slip displacement. (b) Slip in depth distribution of the best fitting models for the creep event. Smoothness constraint is chosen from the tradeoff between misfit and smoothness. The result shows that the creeping depth is about 2-4 km for the event. The sharp signal on 10 km left of fault (left Figure) is not aligned with Superstition Hills Mountain fault.

To estimate how deep slip from nearby faults might contribute to our inversion (without constructing a comprehensive interseismic model across the plate boundary), we re-ran the inversion on a representative profile (#11) and removed a linear trend from the data. As a consequence, the deep slip rate decreases as the linear trend is removed. When a linear trend of 0.2-0.3 mm/yr/km is removed, the deep slip rate is consistent with independent estimates for long-term slip rate on this fault, which ranges from 1.7 to 5.5 mm/yr, based on paleoseismic evidence [*Hudnut and Sieh*, 1989].

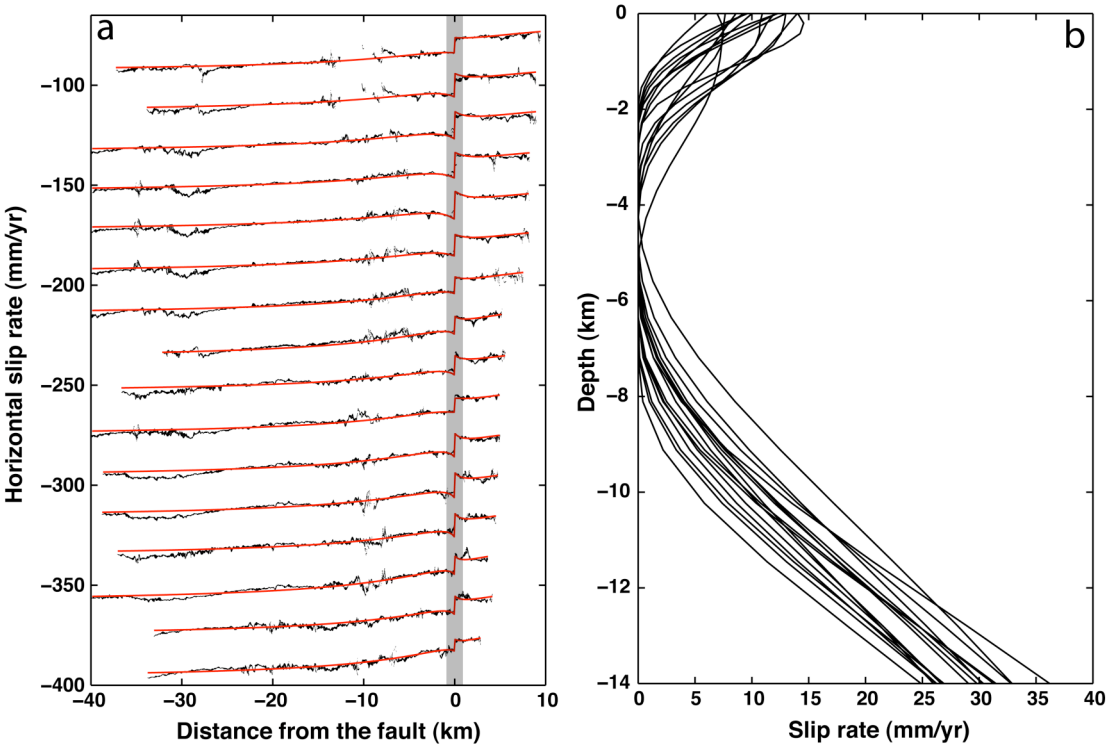

Figure 2-10. Profiles of the 1992-2007 interferograms on the SHF and the best fitting models. (a) Displacement profiles across the fault and the predicted slip displacement from the model. The black dots are the InSAR data with boxes 400 m wide and 40 km long, and the red lines are the best fitting model. The y-axis is the relative slip rate. (b) Slip in depth distribution of the best fitting models for the slip during 1992-2007. Smoothness constraint is chosen from the tradeoff between misfit and smoothness. The result shows that the shallow creeping depth is about 2-4 km. The slip in depth distribution pattern looks like a mirror image of the seismic moment distribution found for several large earthquakes around the world [*Fialko et al.*, 2005].

Despite the amount of linear trend that is removed all the inversions show similar patterns of shallow slip between 0 and 4 km deep (Figure 11); there is a maximum in slip rate at the surface that decreases to zero slip at 4 km depth, which is required to fit the sharp curvature in the horizontal displacement between 0 and 4 km from the fault on both sides. At depths greater than 5 km the estimates of slip rate are highly dependent on the removed linear trend. High linear trend removed (> 0.2 mm/yr/km) result in no slip in the seismogenic layer (at depths between 4 and 9 km). In contrast, low linear trend removed (< 0.2 mm/yr/km) result in low slip rate between 4 and 9 km. Understanding

the slip rate at greater depths will require a more complete regional analysis that includes a three-dimensional finite fault interseismic model of all major faults of the southern San Andreas system and the cross-faults which parallel to the Elmore Ranch fault.

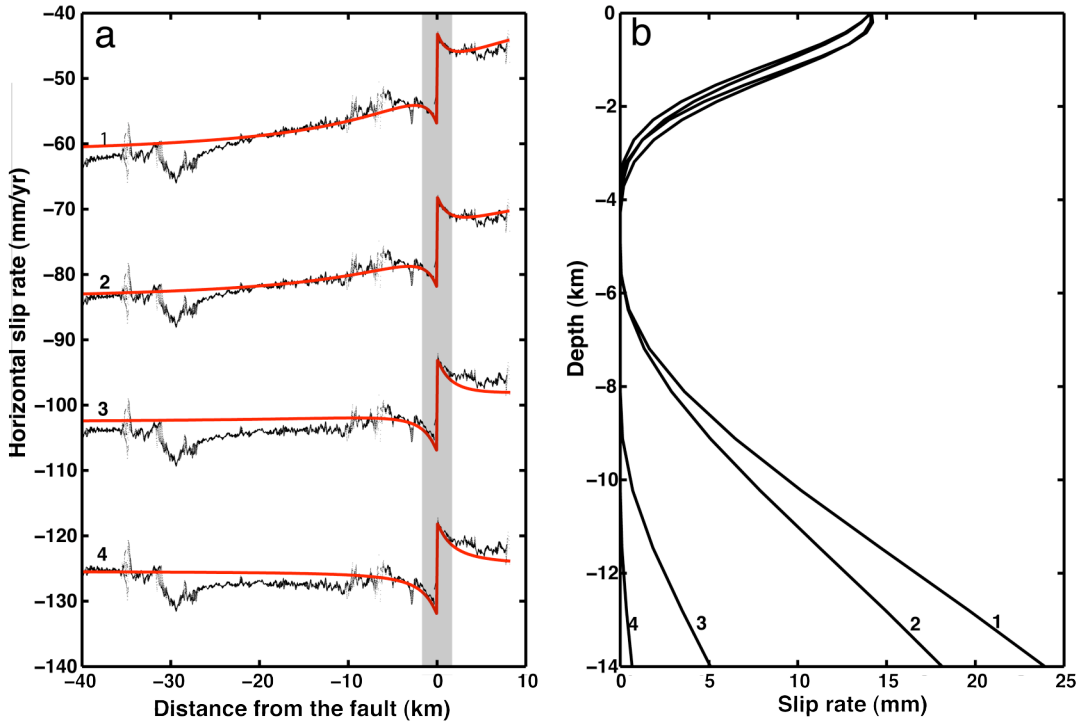

Figure 2-11. The effect of interseismic deformation on nearby faults on slip inversion. (a) InSAR profile #11 (see Fig.3a) and best fitting models for data with different linear trends removed: (1) No trend removed, , 24 mm/yr deep slip rate; (2) 0.1 mm/yr/km, 17 mm/yr deep slip rate; (3) 0.2 mm/yr/km, 5 mm/yr deep slip rate; (4) 0.3 mm/yr/km. .5 mm/yr deep slip rate. Black dots are InSAR data with different trend removed and red lines are the best fitting models. (b) Slip rate distribution along depth for the best fitting models (1-4). The high curvature near 4 km on both sides of the fault is a robust indication of a locked zone in the middle of the crust.

2.7 Discussion

Previously published data from creepmeter measurements have demonstrated that creep on the SHF consists of a secular background creep and a decaying post-

seismic transient that are punctuated by episodic creep events [*Bilham and Behr*, 1992]. The quasi-steady creep was highest just after the 1987 earthquake (28 mm/yr) and slowed to 2.4 mm/yr between May 1989 and July1991. Creepmeter data were unavailable from 1992 to 2004. One question is whether the post-seismic transient still affects the present-day deformation. We divided the average slip along the SHF fault for each interferogram by the time interval of the interferogram (Figure 12). To make sure that the result represents average slip, we excluded interferograms with a time interval shorter than 2 years. Usually one needs to stack several interferograms to reduce the atmospheric error. However, for our purpose, atmospheric error is negligible because the creep signal is localized within 1 km of the fault and changes in the atmospheric contribution are typically not large over this length scale. In the context of afterslip after the 1987 SHF earthquake, we compare our data with two afterslip models, both stemming from the rate and state friction formulation but in different ways. The first model (Figure 12, solid curve), a prediction of the rate-and-state theory [*Dieterich*, 1979; *Marone et al.*, 1991], is $S(t) = b\dfrac{1}{1 + t/(\frac{a}{b})}$, where *S(t)* is the slip rate, *t* is time after the earthquake, *a* and *b* are rate-and-state parameters estimated from creepmeter data on the SHF between 1987-1992 (*a* = 53.45 and *b* = 302.2 in Figure 12) [*Marone et al.* 1991*; Wennerberg and Sharp*, 1997]. The second model (Figure 12, dashed curve), a prediction from the generalized rate-and-state model [*Rice et al*., 2001; *Barbot et al.*, 2009], is $S(t) = A\dfrac{\coth(k/2)e^{kt/t_0}}{1-\left[\coth(k/2)e^{kt/t_0}\right]^2} + c$, where *A, k, t_0* and *c* are empirical constants (*A*=-20, *k*=5, t_0=25 and *c*=0.5 in Figure 12). Both models describe afterslip on a fault

plane driven by coseismic stress changes and have decaying velocity with time but have different asymptotic behavior; the first model doesn't have a well-defined limit of full relaxation, while the second model eventually returns to the background (interseismic) slip rate. The similarity between the two models during the early relaxation epoch as well as the large uncertainty in the InSAR data does not allow us to discriminate between them. Also we cannot conclude that the slip rate is decaying during 1992-2008 time interval. However, in the 11 years prior to the 1987 earthquake, the shallow creep rate was only 0.5 mm/yr [*Louie et al.*, 1985] which is much lower than any of the post earthquake measurements. This suggests that the post-seismic transient from the 1987 earthquake might be still occurring.

Sieh and *Williams* [1990] estimated the depth (0.6 – 2.7 km) of shallow creep and compared it with the sediment depth (1.3-3 km) of the Coachella Valley segment of the San Andreas Fault. They concluded that the high pore pressures in the sediments could produce a weak zone by reducing the effective normal stress in the upper 1 or 2 km of the fault, and the shallow creep is controlled by sediment depth, at least indirectly. Our study of the SHF is consistent with their conclusion. We find a maximum creep depth of 2-4 km where the sediment thickness varies between 3 km and 5 km [*Kohler and Fuis*, 1986].

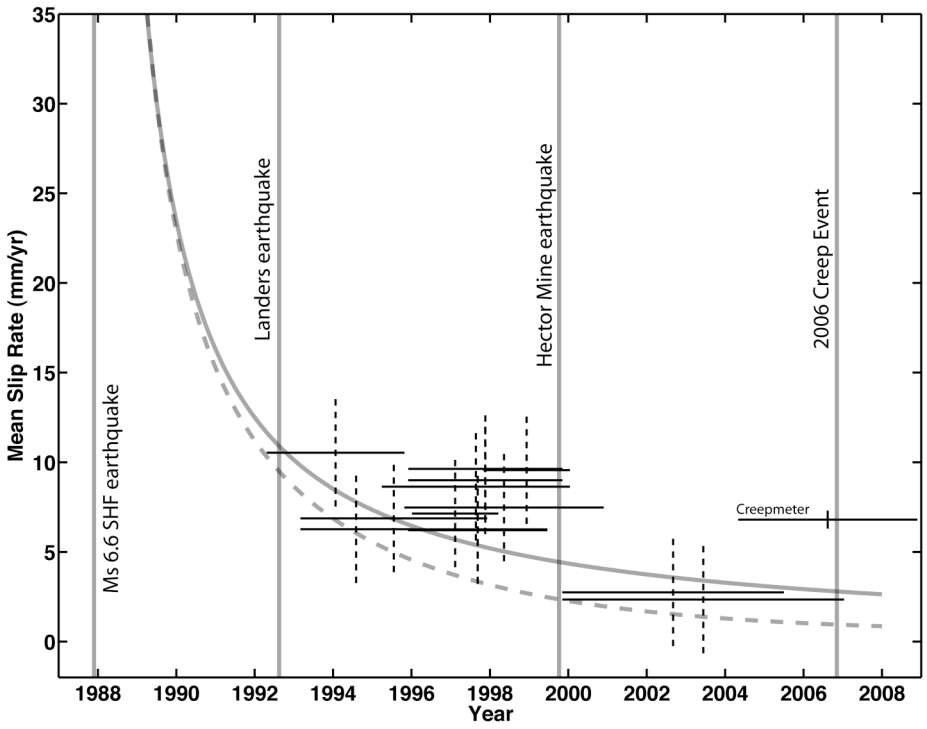

Figure 2-12. Slip history of the SHF from 1992 to 2008. The solid decay curve is the afterslip model based on table 3 of *Marone et al.* [1991]. The dashed decay curve is a model based on *Barbot et al.* [under review, 2009]. All slip rates are taken from InSAR data with a time interval greater than 2 years, except the solid cross, which is from creepmeter data, 6.8 mm/yr between March 2004 and October 2008. The range of horizontal solid line is the time span of the interferogram or the creepmeter. The slip rate is calculated by dividing average displacement on the fault by the time span of the interferogram. The vertical dashed bar is the uncertainty of the slip rate (+/-3 mm/yr, estimated from RMS of image). The uncertainty of the creepmeter data is set to 0.5 mm/yr.

Our results from the interseismic modeling show both shallow and deep aseismic slip with a locked zone at depths between 4 and 6 km. This interseismic distribution of slip with depth is nearly a mirror image of the co-seismic moment release versus depth inferred from several major strike-slip earthquakes (Landers, Mw 7.3, Hector Mine, Mw 7.1, Izmit Mw 7.6 and Bam Mw 6.5) for which high-quality geodetic data are available

[*Fialko et al.*, 2005]. All four earthquakes show shallow coseismic slip deficit. If the shallow coseismic slip deficit is a common feature of strike-slip faults, it must be compensated by post-seismic afterslip, episodic slip events, continuous interseismic creep, or off-fault yielding [*Bodin and Bilham*, 1994; *Fialko et al.*, 2005]. The Superstition Hills fault displays all three types of localized shallow slip.

We note that no seismic signal was detected by seismometers of the existing network during the 2006 creep event or by a seismometer installed on the fault after the creep event (*E. Cochran*, Personal communication). The closest operating seismometer, SWS of the Caltech/USGS regional seismic network, was about 5 km away from the SHF trace (Southern California Earthquake Center). These observations suggest that the 2006 creep event was a spontaneous slip event that was neither triggered by, nor produced any seismic activity. This event was also not detected by the existing continuous GPS network. The closest available continuous GPS station, CRRS in the SOPAC network, is 9.3 km to the northeast. The precision of the GPS station is 1.1 mm in north, 1.3 mm in east, and 3.0 mm in up component, and the sampling rate is 1 Hz. Based on our finite fault slip model, the expected signal from the 2006 creep event is 0.9 mm north and 0.6 mm east. We checked the data in the CRRS station and found no obvious signal around the time of the creep event. The lack of a resolvable signal at the closest GPS site is consistent with our inference that the creep occurred at a fairly shallow depth. It also illustrates difficulties associated with detection of shallow transient deformation using relatively sparse GPS arrays.

2.8 Conclusions

The InSAR data, field measurements, and creepmeter data well document the surface deformation due to the 2006 creep event on the SHF (Figure 3). The maximum slip occurred along the southern end of the fault. The slip distribution along the fault is similar to the surface slip of the triggered event in 1999. Using InSAR, we detect at least three creep events. The creep event in 1992 is triggered by the Landers earthquake, the event in 1999 is triggered by the Hector Mine earthquake, and the 2006 event has no obvious triggering mechanism. The maximum shallow slip rate in the SHF is about 10 mm/yr between 1992 and 2007, and the maximum surface displacement due to the 2006 event is about 27 mm. Both the 2006 creep event and the long-term slip, which includes several creep events, have maximum slip at the surface and decay to zero at depth of 2-4 km where the sediment thickness varies between 3 km and 5 km. Our results lend support to previous suggestions that the shallow creep is controlled by sediment depth, perhaps due to high pore pressures in the unconsolidated sediments.

2.9 Acknowledgements

We thank R. Bilham for providing the creepmeter data. We thank USGS grant for making the creepmeter measurements possible (USGS grant 04HQAG0008). We thank K. Luttrell, S. Barbot, D. Brothers, E. Cochran, R. Mellors and A. Van Zandt for participating in the field surveys on October 12, 2006. We thank D. Kilb for internal review of the paper. We thank R. Mellors, K. Hudnut, G. Peltzer, P. Bird and A. Yin for discussions. We also thank R. Bilham and an anonymous reviewer for their detailed and constructive reviews. The European Space Agency provided the InSAR data through

WInSAR Consortium. This research was supported by the National Science Foundation (EAR 0811772) and the Southern California Earthquake Center.

Text of Chapter 2, in full, is a reprint of the material as it appears in the Journal of Geophysical Research. The dissertation author was the primary investigator and author of this paper.

2.10 References

Allen, C. R., Wyss, M., Brune, J. N., Grantz, A., and Wallace, R. (1972), Displacement on the Imperial, Superstition Hills, and San Andreas faults triggered by the Borrego Mountain earthquake, in The Borrego Mountain Earthquake, *U.S. Geol. Surv. Profess. Pap.* 787, 87–104.

Barbot, S., Fialko, Y., and Bock, Y. (2009), Postseismic Deformation due to the Mw6.0 2004 Parkfield Earthquake: Stress-Driven Creep on a Fault with Spatially Variable Rate-and-State Friction Parameters, *Journal of Geophysical Research-Solid Earth,* 114, B07405, doi:10.1029/2008JB005748.

Becker, T. W., Hardebeck, J. L., and Anderson, G. (2005), Constraints on fault slip rates of the southern California plate boundary from GPS velocity and stress inversions, *Geophysical Journal International*, *160*(2), 634-650, doi:10.1111/j.1365-246X.2004.02528.x.

Bevis, M., et al. (2005), The B4 Project: Scanning the San Andreas and San Jacinto Fault Zones, *American Geophysical Union, Fall Meeting 2005, abstract #H34B-01.*

Bilham, R. (1989), Surface Slip Subsequent to the 24 November 1987 Superstition Hills, California, Earthquake Monitored by Digital Creepmeters, *Bulletin of the Seismological Society of America*, *79*(2), 424-450.

Bilham, R., and Behr, J. (1992), A 2-Layer Model for Aseismic Slip on the Superstition Hills Fault, California, *Bulletin of the Seismological Society of America*, *82*(3), 1223-1235.

Bilham, R., Suszek, N., and Pinkney, S. (2004), California creepmeters, *Seismological Research Letters*, *75*(4), 481-492.

Bilham, R. (2005), Coseismic strain and the transition to surface afterslip recorded by creepmeters near the 2004 Parkfield epicenter, *Seismological Research Letters*, *76*(1), 49-57, doi:10.1785/0120050823.

Boatwright, J., Budding, K. E., and Sharp, R. V. (1989), Inverting Measurements of Surface Slip on the Superstition Hills Fault, *Bulletin of the Seismological Society of America*, *79*(2), 411-423.

Bodin, P., Bilham, R., Behr, J., Gomberg, J., and Hudnut, K. W. (1994), Slip Triggered on Southern California Faults by the 1992 Joshua-Tree, Landers, and Big-Bear Earthquakes, *Bulletin of the Seismological Society of America*, *84*(3), 806-816.

Burford, R. O., and Harsh, P. W. (1980), Slip on the San-Andreas-Fault in Central California from Alignment Array Surveys, *Bulletin of the Seismological Society of America*, *70*(4), 1233-1261.

Burgmann, R., Schmidt, D., Nadeau, R. M., d'Alessio, M., Fielding, E., Manaker, D., McEvilly, T. V., and Murray, M. H. (2000), Earthquake potential along the northern Hayward fault, California, *Science*, *289*(5482), 1178-1182, doi:10.1126/science.289.5482.1178.

Cohen, S. C. (1999), Numerical models of crustal deformation in seismic zones, *Advances in Geophysics, Vol 41*, *41*, 133-231.

Coleman, T. F., and Li, Y. Y. (1996), A reflective Newton method for minimizing a quadratic function subject to bounds on some of the variables, *Siam Journal on Optimization*, *6*(4), 1040-1058.

Dieterich, J. H. (1979), Modeling of Rock Friction, 1. Experimental Results and Constitutive Equations, *J. Geophys. Res.,* 84, 2161–2168.

Emardson, T. R., Simons, M., and Webb, F. H. (2003), Neutral atmospheric delay in interferometric synthetic aperture radar applications: Statistical description and mitigation, *Journal of Geophysical Research-Solid Earth*, *108*(B5), 2231, doi:10.1029/2002JB001781.

Ferretti, A., Prati, C., and Rocca, F. (2001), Permanent scatterers in SAR interferometry, *Ieee Transactions on Geoscience and Remote Sensing*, *39*(1), 8-20.

Fialko, Y., Simons, M., and Agnew, D. (2001), The complete (3-D) surface displacement field in the epicentral area of the 1999 M(w)7.1 Hector Mine earthquake, California, from space geodetic observations, *Geophysical Research Letters*, *28*(16), 3063-3066, doi:10.1029/2001GL013174.

Fialko, Y. (2004), Probing the mechanical properties of seismically active crust with space geodesy: Study of the coseismic deformation due to the 1992 M(w)7.3 Landers (southern California) earthquake, *Journal of Geophysical Research-Solid Earth*, *109*(B3), B03307, doi:10.1029/2003JB002756.

Fialko, Y., Sandwell, D., Simons, M., and Rosen, P. (2005), Three-dimensional deformation caused by the Bam, Iran, earthquake and the origin of shallow slip deficit, *Nature*, *435*(7040), 295-299, doi:10.1038/nature03425.

Fialko, Y. (2006), Interseismic strain accumulation and the earthquake potential on the southern San Andreas fault system, *Nature*, *441*(7096), 968-971, doi:10.1038/nature04797.

Funning, G. J., Burgmann, R., Ferretti, A., and Novali, F. (2007), Creep on the Rodgers Creek fault, northern San Francisco Bay area from a 10 year PS-InSAR dataset, *Geophysical Research Letters*, *34*(19), L19306, doi:10.1029/2007GL030836.

Hudnut, K. W. and Clark, M. M. (1989), New Slip Along Parts of the 1968 Coyote Creek Fault Rupture, California, *Bulletin of the Seismological Society of America*, *79*(2), 451-465.

Hudnut, K. W., Seeber, L., and Pacheco, J. (1989a), Cross-Fault Triggering in the November 1987 Superstition Hills Earthquake Sequence, Southern-California, *Geophysical Research Letters*, *16*(2), 199-202, doi:10.1029/GL016i002p00199.

Hudnut, K. W., Seeber, L., and Rockwell, T. (1989b), Slip on the Elmore Ranch Fault during the Past 330 Years and Its Relation to Slip on the Superstition Hills Fault, *Bulletin of the Seismological Society of America*, *79*(2), 330-341.

Hudnut, K. W., and Sieh, K. E. (1989), Behavior of the Superstition Hills Fault during the Past 330 Years, *Bulletin of the Seismological Society of America*, *79*(2), 304-329.

Kanamori, H. (1977), Energy-Release in Great Earthquakes, *Journal of Geophysical Research*, *82*(20), 2981-2987, doi:10.1029/JB082i020p02981.

King, C. Y., Nason, R. D., and Tocher, D. (1973), Kinematics of fault creep, *Phil. Trans. Roy. Soc.*, 274(1239), 355-360.

Klinger, R. E. and Rockwell, T. K. (1989), Flexural-Slip Folding Along the Eastern Elmore Ranch Fault in the Superstition Hills Earthquake Sequence of November 1987, *Bulletin of the Seismological Society of America*, *79*(2), 297-303.

Kohler, W. M. and Fuis, G. S. (1986), Travel-Time, Time-Term, and Basement Depth Maps for the Imperial-Valley Region, California, from Explosions, *Bulletin of the Seismological Society of America*, *76*(5), 1289-1303.

Lienkaemper, J. J., Baker, B., and McFarland, F. S. (2006), Surface slip associated with the 2004 Parkfield, California, earthquake measured on alinement arrays, *Bulletin of the Seismological Society of America*, *96*(4), S239-S249, doi:10.1785/0120050806.

Lin, G. Q., Shearer, P. M., and Hauksson, E. (2007), Applying a three-dimensional velocity model, waveform cross correlation, and cluster analysis to locate southern California seismicity from 1981 to 2005, *Journal of Geophysical Research-Solid Earth*, *112*(B12), B12309, doi:10.1029/2007JB004986.

Lindvall, S. C., Rockwell, T. K., and Hudnut, K. W. (1989), Evidence for Prehistoric Earthquakes on the Superstition Hills Fault from Offset Geomorphic Features, *Bulletin of the Seismological Society of America*, *79*(2), 342-361.

Lohman, R. B., and Mcguire, J. J. (2007), Earthquake swarms driven by aseismic creep in the Salton Trough, California, *Journal of Geophysical Research-Solid Earth*, *112*(B4), B04405, doi:10.1029/2006JB004596.

Lorenzetti, E., and Tullis, T. E. (1989), Geodetic Predictions of a Strike Slip Fault Model - Implications for Intermediate-Term and Short-Term Earthquake Prediction, *Journal of Geophysical Research-Solid Earth and Planets*, *94*(B9), 12343-12361.

Louie, J. N., Allen, C. R., Johnson, D. C., Haase, P. C., and Cohn, S. N. (1985), Fault Slip in Southern-California, *Bulletin of the Seismological Society of America*, *75*(3), 811-833.

Lyons, S., and Sandwell, D. (2003a), Fault creep along the southern San Andreas from interferometric synthetic aperture radar, permanent scatterers, and stacking, *Journal of Geophysical Research-Solid Earth*, *108*(B1), -.

Lyons, S., and Sandwell, D. (2003b), Fault creep along the southern San Andreas from interferometric synthetic aperture radar, permanent scatterers, and stacking, *Journal of Geophysical Research-Solid Earth*, *108*(B1), 2047, doi:10.1029/2002JB001831.

Lyons, S. N., Bock, Y., and Sandwell, D. T. (2002), Creep along the imperial fault, southern California, from GPS measurements, *Journal of Geophysical Research-Solid Earth*, *107*(B10).

Malservisi, R., Furlong, K. P., and Gans, C. R. (2005), Microseismicity and creeping faults: Hints from modeling the Hayward fault, California (USA), *Earth and Planetary Science Letters*, *234*(3-4), 421-435, doi:10.1016/j.epsl.2005.02.039.

Marone, C., and Scholz, C. H. (1988), The Depth of Seismic Faulting and the Upper Transition from Stable to Unstable Slip Regimes, *Geophysical Research Letters*, *15*(6), 621-624, doi:10.1029/GL015i006p00621.

Marone, C. J., Scholtz, C. H., and Bilham, R. (1991), On the Mechanics of Earthquake Afterslip, *Journal of Geophysical Research-Solid Earth and Planets*, *96*(B5), 8441-8452, doi:10.1029/91JB00275.

Massonnet, D. and Feigl, K. L. (1998), Radar interferometry and its application to changes in the earth's surface, *Reviews of Geophysics*, *36*(4), 441-500, doi:10.1029/97RG03139.

Mavko, G. M. (1982), Fault Interaction near Hollister, California, *Journal of Geophysical Research*, *87*(NB9), 7807-7816, doi:10.1029/JB087iB09p07807.

Mcgill, S. F., Allen, C. R., Hudnut, K. W., Johnson, D. C., Miller, W. F., and Sieh, K. E. (1989), Slip on the Superstition Hills Fault and on Nearby Faults Associated with the 24 November 1987 Elmore Ranch and Superstition Hills Earthquakes, Southern-California, *Bulletin of the Seismological Society of America*, *79*(2), 362-375.

Mellors, R. J., and Boisvert, A. (2003), Deformation near the Coyote Creek fault, imperial county, california: Tectonic or groundwater-related?, *Geochemistry Geophysics Geosystems*, *4*, 1012, doi:10.1029/2001GC000254.

Murray, J. and Segall, P. (2002), Testing time-predictable earthquake recurrence by direct measurement of strain accumulation and release, *Nature*, *419*(6904), 287-291, doi:10.1038/nature00984.

Nason, R. D. (1971), Investigation of fault creep slippage in northern and central California, *Ph.D. Thesis*, UCSD.

Nielsen, S., Knopoff, L., and Tarantola, A. (1995), Model of Earthquake Recurrence - Role of Elastic-Wave Radiation, Relaxation of Friction, and Inhomogeneity, *Journal of Geophysical Research-Solid Earth*, *100*(B7), 12423-12430, doi:10.1029/95JB00714.

Okada, Y. (1985), Surface Deformation Due to Shear and Tensile Faults in a Half-Space, *Bulletin of the Seismological Society of America*, *75*(4), 1135-1154.

Parker, R. L. (1977), Understanding Inverse Theory, *Annual Review of Earth and Planetary Sciences*, *5*, 35-64, doi:10.1146/annurev.ea.05.050177.000343.

Parker, R. L. and Song, Y. Q. (2005), Assigning uncertainties in the inversion of NMR relaxation data, *Journal of Magnetic Resonance*, *174*(2), 314-324, doi:10.1016/j.jmr.2005.03.002.

Prescott, W. H., Lisowski, M., and Savage, J. C. (1981), Geodetic Measurement of Crustal Deformation on the San-Andreas, Hayward, and Calaveras Faults near San-Francisco, California, *Journal of Geophysical Research*, *86*(Nb11), 853-869.

Rice, J. R., Lapustaa, N., and Ranjitha, K. (2001), Rate and state dependent friction and the stability of sliding between elastically deformable solids, *J. Mech. Phys. Solids*, 49, 1865-1898, doi:10.1016/S0022-5096(01)00042-4

Rosen, P. A., Hensley, S., Zebker, H. A., Webb, F. H., and Fielding, E. J. (1996), Surface deformation and coherence measurements of Kilauea volcano, Hawaii, from SIR-C radar interferometry, *Journal of Geophysical Research-Planets*, *101*(E10), 23109-23125, doi:10.1029/96JE01459.

Rymer, M. J., Boatwright, J., Seekins, L. C., Yule, J. D., and Liu, J. (2002), Triggered surface slips in the Salton Trough associated with the 1999 Hector Mine, California, earthquake, *Bulletin of the Seismological Society of America*, *92*(4), 1300-1317, doi:10.1785/0120000935.

Savage, J. C., Prescott, W. H., Lisowski, M., and King, N. E. (1981), Strain Accumulation in Southern-California, 1973-1980, *Journal of Geophysical Research*, *86*(NB8), 6991-7001, doi:10.1029/JB086iB08p06991.

Savage, J. C. and Lisowski, M. (1993), Inferred Depth of Creep on the Hayward Fault, Central California, *Journal of Geophysical Research-Solid Earth*, *98*(B1), 787-793, doi:10.1029/2001GL012979.

Savage, J. C. (2006), Dislocation pileup as a representation of strain accumulation on a strike-slip fault, *Journal of Geophysical Research-Solid Earth*, *111*(B4), B04405, doi:10.1029/2005JB004021.

Schmidt, D. A., Burgmann, R., Nadeau, R. M., and d'Alessio, M. (2005), Distribution of aseismic slip rate on the Hayward fault inferred from seismic and geodetic data, *Journal of Geophysical Research-Solid Earth*, *110*(B8), B08406, doi:10.1029/2004JB003397.

Schulz, S. S., Mavko, G. M., Burford, R. O., and Stuart, W. D. (1982), Long-Term Fault Creep Observations in Central California, *Journal of Geophysical Research*, *87*(NB8), 6977-6982.

Sharp, R. V. (1989), Pre-Earthquake Displacement and Triggered Displacement on the Imperial Fault Associated with the Superstition Hills Earthquake of 24 November 1987, *Bulletin of the Seismological Society of America*, *79*(2), 466-479.

Sharp, R. V., et al. (1989), Surface Faulting Along the Superstition Hills Fault Zone and Nearby Faults Associated with the Earthquakes of 24 November 1987, *Bulletin of the Seismological Society of America*, *79*(2), 252-281.

Sharp, R. V. and Saxton, J. L. (1989), 3-Dimensional Records of Surface Displacement on the Superstition Hills Fault Zone Associated with the Earthquakes of 24 November 1987, *Bulletin of the Seismological Society of America*, *79*(2), 376-389.

Shen, Z. K., Jackson, D. D., and Ge, B. X. (1996), Crustal deformation across and beyond the Los Angeles basin from geodetic measurements, *Journal of Geophysical Research-Solid Earth*, *101*(B12), 27957-27980, doi:10.1029/96JB02544.

Sieh, K. E. and Williams, P. L. (1990), Behavior of the Southernmost San-Andreas Fault during the Past 300 Years, *Journal of Geophysical Research-Solid Earth and Planets*, *95*(B5), 6629-6645, doi:10.1029/JB095iB05p06629.

Simpson, R. W., Lienkaemper, J. J., and Galehouse, J. S. (2001), Variations in creep rate along the Hayward Fault, California, interpreted as changes in depth of creep, *Geophysical Research Letters*, *28*(11), 2269-2272, doi:10.1029/2001GL012979.

Steinbrugge, K. V. and Zacher, E. G. (1960), Creep on the San Andreas fault: fault creep and property damage, *Bulletin of the Seismological Society of America*, *50*, 389-396.

Thatcher, W. (1990), Order and Diversity in the Modes of Circum-Pacific Earthquake Recurrence, *Journal of Geophysical Research-Solid Earth and Planets*, *95*(B3), 2609-2623, doi:10.1029/JB095iB03p02609.

Tocher, D. (1960), Creep on the San Andreas Fault: creep rate and related measurements at Vineyard, California, *Bulletin of the Seismological Society of America*, *50*, 396-404.

Toda, S. and Stein, R. S. (2002), Response of the San Andreas fault to the 1983 Coalinga-Nunez earthquakes: An application of interaction-based probabilities for Parkfield, *Journal of Geophysical Research-Solid Earth*, *107*(B6), 2126, doi:10.1029/2001JB000172.

Wang, R. J., Martin, F. L., and Roth, F. (2003), Computation of deformation induced by earthquakes in a multi-layered elastic crust - FORTRAN programs EDGRN/EDCMP, *Computers & Geosciences*, *29*(2), 195-207, doi:10.1016/S0098-3004(02)00111-5

Weertman, J. (1965), Relationship between displacements on a free surface and the stress on a fault, *Bulletin of the Seismological Society of America*, 55(6), 945-953.

Wennerberg, L. and Sharp, R. V. (1997), Bulk-friction modeling of afterslip and the modified Omori law, *Tectonophysics*, *277*(1-3), 109-136, doi:10.1016/S0040-1951(97)00081-4.

Wesson, R. L. (1988), Dynamics of fault creep, *Journal of Geophysical Research-Solid Earth*, *93*(B8), 8929-8951, doi: 10.1029/JB093iB08p08929.

Williams, P. L. and Magistrale, H. W. (1989), Slip Along the Superstition Hills Fault Associated with the 24 November 1987 Superstition Hills, California, Earthquake, *Bulletin of the Seismological Society of America*, *79*(2), 390-410.

Wyss, M. (2001), Locked and creeping patches along the Hayward fault, California, *Geophysical Research Letters*, *28*(18), 3537-3540, doi:10.1029/2001GL013499.

3. CHAPTER 3: Triggered slip on faults in the Salton Trough by the 2010 Mw 7.2 El Mayor Earthquake revealed by InSAR

Earthquake safety tip 3:

Do you have a treasured childhood toy? Perhaps a stuffed animal, such as a teddy bear? Well, let's see Mr. Bear help you now.

3.1 Abstract

Radar interferometry (InSAR), field measurements and creepmeters reveal surface slip on multiple faults in the Imperial Valley triggered by the main shock of the 4 April 2010 El Mayor-Cucapah M_w 7.2 earthquake. Co-seismic offsets occurred on the San Andreas, Superstition Hills, Imperial, Elmore Ranch, Wienert, Coyote Creek, Elsinore, Yuha, and several minor faults near the town of Ocotillo at the northern end of the mainshock rupture. We documented right-lateral slip (< 40 mm) on northwest-striking faults and left-lateral slip (< 40 mm) on southwest-striking faults. Slip occurred on 15-km- and 20-km-long segments of the San Andreas Fault in the Mecca Hills (≤ 50 mm) and Durmid Hill (≤ 10 mm) respectively, and on 25 km of the Superstition Hills Fault (≤ 37 mm). Field measurements of slip on the Superstition Hills Fault agree with InSAR and creepmeter measurements to within a few millimeters. Dislocation models of the InSAR data from the Superstition Hills Fault confirm that creep in this sequence, as in previous slip events, is confined to shallow depths (< 3 km).

3.2 Introduction

Surface slip triggered by nearby earthquakes is common on faults in the Salton Trough region of Southern California [*Rymer et al.,* 2002], a regional pull-apart basin formed at a releasing step over between major right-lateral faults associated with the Pacific and the North American plate boundary (Figure 1) [*Elders et al.*, 1972]. The "trough" is filled with sediments mainly from the Colorado River and surrounded by Mesozoic basement rocks and Tertiary volcanic rocks [*Dorsey,* 2010]. Previous studies have documented triggered slip on faults in the Imperial Valley during more than 8 earthquakes in the last 50 years [*Hudnut et al.,* 1989; *Rymer et al.*, 2002]. Between earthquakes steady surface creep on these faults occurs at rates of a few mm/yr, interrupted by episodic creep events [*Rymer et al.*, 2002; *Wei et al*., 2009]. *Sieh and Williams* [1990] infer an association between shallow creep in unconsolidated sediments with inferred high pore pressures. *Marone et al.* [1991] and *Du et al.* [2005] provide a theoretical basis for both steady creep and episodic creep events along the respective faults. They show that in response to steady loading, a velocity-strengthening zone in the uppermost 3 km can host creep events, whose occurrence time may be advanced by shaking during the passage of seismic waves.

In this study we document triggered slip on faults in the Imperial Valley associated with the 4 April 2010 El Mayor-Cucapah Mw 7.2 earthquake using radar interferometry (InSAR) imagery, field surveys, and creepmeter data. Co-seismic offsets occurred on more than ten faults in this area. We estimate the depth of the triggered slip on the Superstition Hills Fault using dislocation modeling. We find that the results are consistent with previous inferences that slip extends only through the uppermost few

kilometers roughly corresponding to the basement depth (3-5 km) [*Wei et al.,* 2009]. The study illustrates that InSAR is an effective tool for measuring small fault offsets. Finally, we discuss the implications for the long-term slip budget. Comprehensive accounts of triggered slip are potentially important for slip budget analysis in the Imperial Valley region as well as seismic hazard assessment.

3.3 Data and Methods

We processed ENVISAT and ALOS InSAR data to study the spatial distribution of slip triggered by the main shock of the 2010 El Mayor-Cucapah earthquake. All InSAR data were processed using GMTSAR, a newly developed software package utilizing Generic Mapping Tools (GMT). The Shuttle Radar Topography Mission (SRTM) Digital Elevation Model [*Farr et al.,* 2007] was used to remove the topographic phase. The best measurements of triggered slip were obtained with 5.6 cm wavelength C-band ENVISAT data, which we found to be less noisy and yielding larger backscatter than the 23.6 cm wavelength L-band ALOS data, especially in the dry lakebed areas such as near the Superstition Hills Fault area. ALOS data were used where either ascending or descending ENVISAT data were unavailable. To maintain the best spatial resolution, all post-processing was done in the radar coordinates using minimal filtering (Gaussian filter with 0.5 gain at 100 m wavelength). Along each fault where we identified triggered slip from the InSAR data, we extracted phase profiles in several locations of the largest offsets. Each of these profiles is 400 meters wide and 4 km long.

We estimated the offset as the difference between the maximum and minimum value in the best fitting curve within 200 m of the fault.

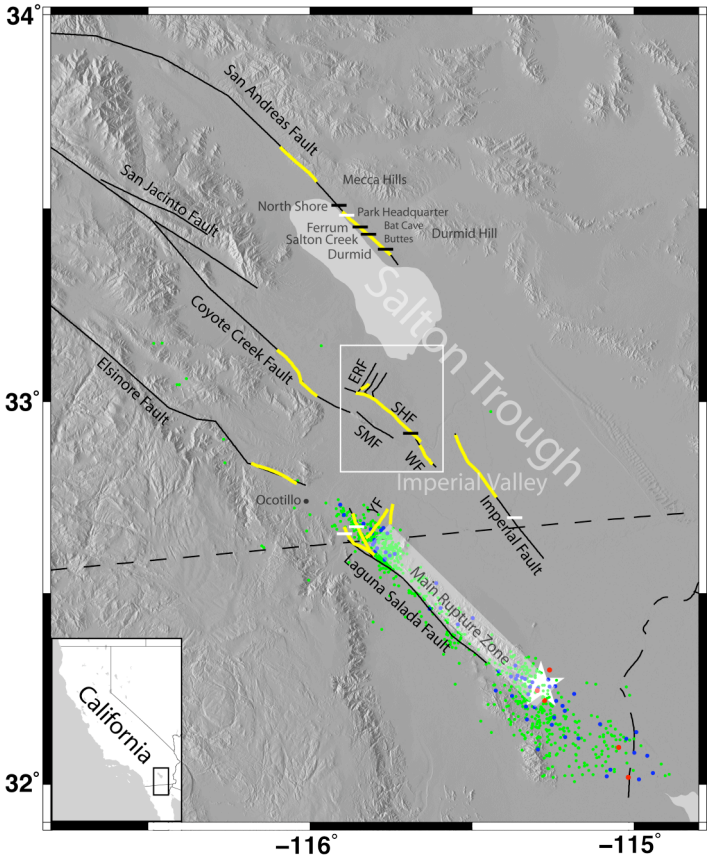

Figure 3-1. Map of Southern California and Northern Baja California. Black solid lines are major faults. Yellow solid lines are faults with observed offsets. Dashed black lines are National and State borders. Black horizontal bars indicate creepmeters operating before April 2010. White horizontal bars indicate creepmeters installed after the earthquake. White star is the epicenter of the 4 April 2010 El Mayor-Cucapah earthquake. Red dots are aftershocks within one month after the main rupture with magnitude greater than 5, blue 4-5, and green 3-4. Earthquake data are from the Southern California Earthquake Center. The mainshock rupture, as revealed by aftershocks and radar interferometry, occurred on largely unmapped faults east of the Laguna Salada Fault. The gray boxes show the locations of InSAR data in figure 2. Fault names are abbreviated as follows: ERF, Elmore Ranch fault; SHF, Superstition Hills fault; SMF, Superstition Mountains fault; WF, Wienert fault; YF, Yuha Fault.

In addition to InSAR observations, we measured offsets in the field on the Superstition Hills Fault (SHF), the San Andreas Fault (SAF) and the Imperial Fault (IF). Abrupt triggered slip with negligible afterslip was recorded by creepmeters on the SHF (23 mm) and the southern SAF (≈ 5 mm). In these creepmeter data, the slip occurred between two 5-minute samples and was complete by the next sample. The timing coincided with the passage of the seismic waves. Our field survey of the SHF on 9 April, 5 days after the mainshock, revealed surface offsets along more than 10 km of the fault, approximately coincident with the same areas that experienced surface slip during a spontaneous creep episode in 2006 (Figure 2) [*Wei et al.,* 2009]. We measured offsets up to 37 mm following the method described in *Rymer et al.* [2002] and *Wei et al*. [2009]. On 2 May, 28 days after the mainshock, we conducted a survey of the SAF and IF. Since a portion of the SAF had already been surveyed [*Michael Rymer*, personal communication], we searched for cracks along an un-surveyed area between the Salton Sea Park Headquarters and Bat Cave Buttes where the interferograms show small phase discontinuities, and where three creepmeters also indicate significant slip (~5mm). The search for fresh cracks was guided by the high-resolution topographic imagery (0.5 m resolution) of the fault trace from the B4 LiDAR survey [*Bevis et al.,* 2005]. We also searched for cracks along two segments of the IF, at E. Harris Road (W115.53905, N32.88366) and E. McCabe Road (W115.42576, N32.75197). Fresh cracks showing mostly extensional motion were observed on these paved roads, whereas-mostly right-lateral with minor extensional motion was mainly observed in the dirt on the sides of these roads (see supplemental Tables A1 and A2).

3.4 Results

InSAR data, field measurements and creepmeters revealed triggered slip on the San Andreas, Superstition Hills, Imperial, Elmore Ranch, Wienert, Coyote Creek, Elsinore, Yuha faults, and several minor faults near the northern end of the Laguna Salada Fault (Figure 1). For all but three of these faults the dominant fault motion is right-lateral strike-slip. The exceptions are sinistral slip on the northeast-striking Elmore and Yuha faults, and a northeast-striking fault about 10 km southeast of the Yuha Fault (Table 1). Because the sense of surface displacements agrees with the long-term fault motion, and the radar phase is essentially discontinuous across the fault trace, we concluded that the observed deformation is due to localized fault slip and not a broad response of compliant fault zones to static stress changes [*Fialko*, 2004]. Because no significant aftershocks occurred on fault segments that slipped during the time period of our observation (4 April – 2 May, 2010), we do not attribute any of the observed slip to aftershocks. Creepmeter data confirm that slip was an abrupt step without significant afterslip.

Table 3-1. InSAR derived slip amplitude and direction on major faults.

Profile ID	Latitude	Longtitude	LOS1 (mm) *	LOS2 (mm) *	Horizontal (mm) **	Vertical (mm) ***
San Andreas Fault						
1	33.603481	-116.018619	12.09±2.04	4.15±0.89	32.3±8.1	-8.8±3.8
2	33.582136	-115.991753	7.37±2.37	2.76±1.46	20.2±10.6	-4.8±5.1
3	33.485131	-115.889969	12.27±3.53	4.87±0.85	30.3±13.3	-6.7±5.5
North Laguna Salada Fault						
4	32.629236	-115.860837	4.80±1.11	7.51±1.33	19.1±2.7	0.6±0.9
5	32.673412	-115.85208	-9.09±2.28	22.96±3.58	41.9±12.9	13.9±2.1
Yuha Fault and an unkown northeast striking fault						
6	32.680794	-115.790124	21.83±3.01	6.72±1.88	-42.1±5.2	-8.0±1.9
7	32.69424	-115.75064	5.12±1.40	3.35±1.55	-33.4±8.2	-0.8±1.1
Superstition Hills Fault						
8	32.915935	-115.682689	9.15±5.10	8.07±1.40	29.6±4.0	-1.9±1.3
9	32.968969	-115.745803	5.84±1.56	4.71±0.75	18.6±3.1	-1.6±1.0
Elmore Ranch Fault						
10	33.037825	-115.830281	5.54±0.93	0.99±0.62	-9.4±1.6	-2.0±0.6
Coyote Creek Fault						
11	33.030892	-116.002016	1.68±0.98	2.33±0.59	6.9±2.0	-0.2±0.7
12	33.060105	-116.029755	2.03±0.91	1.23±0.87	17.9±6.9	-2.2±1.0
13	33.111056	-116.070245	8.13±1.06	6.03±1.09	26.3±2.8	-3.3±0.9
Elsinore Fault						
14	32.824217	-116.126643	8.35±1.58	2.93±0.65	15.9±2.4	-3.9±1.0

*Positive: increase in range direction

**Positive: right-lateral

***Positive: east side up

Note: Profile ID number matches the number in figure 2 and supplemental figures.

3.4.1 San Andreas Fault

The southern San Andreas Fault is believed to have a high potential for generating a future large earthquake [e.g. *Fialko,* 2006; *Field*, 2007]. The seismic moment of such a large earthquake could be reduced by the existence of shallow creep on the SAF triggered by a local or regional event. Triggered slip on this section of the SAF has been observed after numerous nearby earthquakes [*Rymer et al.*, 2002]. Triggered slip associated with the 2010 El Mayor-Cucapah was observed along 35 km of the southern SAF on the Mecca Hills (15 km) and the Durmid Hill (20 km) segments of the fault as defined by *Bilham and Williams* [1985]. Maximum slip of ~30 mm was observed in the Mecca Hills in 2010, where ~20 mm of triggered slip also occurred in association with the 1968 Borrego Mountain and 1992 Landers earthquakes [*Rymer*, 2000]. Comparable slip was also triggered in the Mecca Hills by the 1986 North Palm Springs, the 1987 Superstition Hills [*Williams et al.,* 1988], and the 1999 Hector Mine earthquakes [*Rymer et al.,* 2002]. Fault offsets between North Shore and Salt Creek are discontinuous and poorly expressed. In this area no triggered slip was reported due to the Landers [*Rymer*, 2000] or Hector Mine earthquakes [*Rymer et al.,* 2002]. Creepmeters at Ferrum, Salt Creek and 1 km south of Bat Cave Buttes (Figure 1) each recorded about 5 mm of slip, and minor surface cracking consistent with 5 mm of slip could be traced ±1 km of the southern most creepmeter.

We used ALOS descending data and ENVISAT descending data to distinguish horizontal from vertical triggered offsets on the SAF. ENVISAT ascending data was not used because the Mecca Hills, where the greatest slip occurred is out of the scene coverage (Supplemental Figure A1). Assuming no fault normal displacement, we

estimated 32.3 ± 8.1 mm of horizontal motion and 8.8 ± 3.8 mm of vertical motion (SW side down) on the SAF. The assumption of negligible fault-normal displacement is supported locally at two locations on Durmid Hill where experimental fault-normal creepmeters had been installed a few months earlier. At both locations fault-normal displacements were <10% of the horizontal slip, an estimate that is limited in accuracy by knowledge of the local strike of the fault.

3.4.2 Superstition Hills Fault

The SHF has a long history of triggered slip caused by nearby earthquakes in the last several decades [*Wei et al.*, 2009]. For the 2010 earthquake, field measurements and InSAR data show that the entire shallow portion of the Superstition Hills Fault slipped, with a maximum offset of about 37 mm near its southern end. This observation is inconsistent with a model postulating that triggered slip is enhanced at a more distant end of a fault with respect to the seismic source [*Fuis,* 1982; *Rymer et al.,* 2002]. Slip on the SHF was predominantly right-lateral with minor vertical motion (Table 1). The distribution of offsets along the fault strike is similar to the distribution mapped in 2006 [*Wei et al*., 2009] (Figure 2C) as well as to the afterslip following the 1987 event. The similarity of slip patterns in 1987, 2006, and 2010 suggests that all slip is in response to the shallow slip deficit produced by the 1987 earthquake.

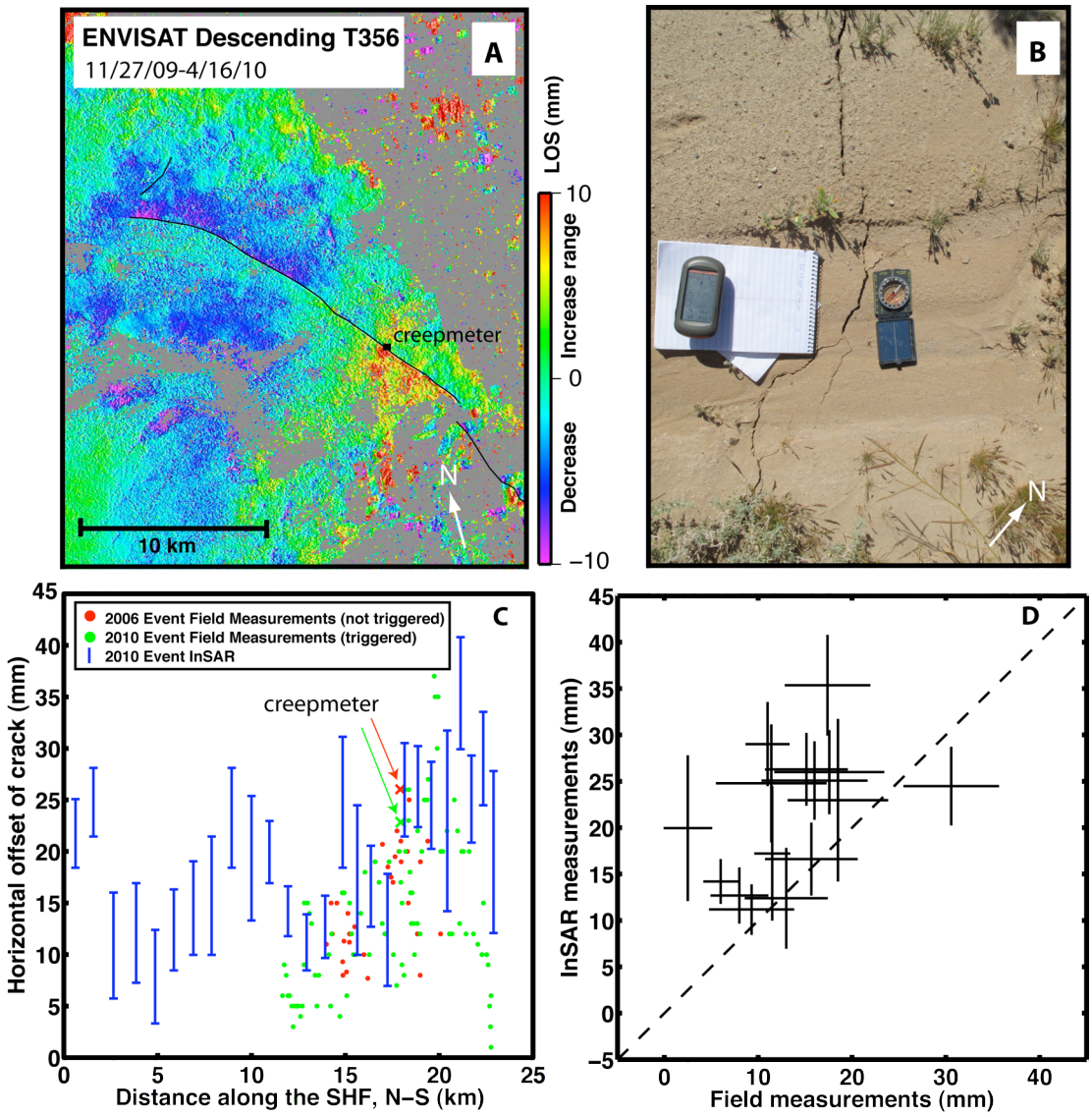

Figure 3-2. (A) InSAR data in radar coordinates show triggered slip on the Superstition Hills Fault and the Elmore Ranch Fault. Solid black lines are the fault traces. White arrow points to North. (B) A photo taken in the field. (C) Slip along the Superstition Hills Fault. (D) Comparison of InSAR measurements with field measurements for the 2010 triggered slip. Dashed line represents the line of ratio 1:1. Solid cross shows the InSAR and Field measurements with uncertainty in segments.

We extracted twenty-six InSAR profiles from interferograms across the 25-km-triggered segment of the SHF and converted them to horizontal slip using the known

radar incidence angles. The field measurements were binned in the same fashion as the InSAR profiles. The mean value and standard deviation of the binned field measurements provide an estimate of the uncertainties in the field data (Figure 2D). The comparison shown in Figure 2D illustrates that the InSAR measurements are on average 50% larger than the field measurements. This suggests that a fraction of deformation occurs away from the main trace and probably reflects greater slip on the fault in the subsurface. Overall the generally good agreement between InSAR and field measurements validates InSAR as a tool for measuring small fault offsets.

The broad coverage of the flanks of the fault provided by InSAR also allows one to estimate the depth of the triggered slip. A single profile was extracted and interpreted using an anti-plane dislocation model similar to that of *Wei et al.* [2009]. The model shows that creep extends to a depth of only 3-4 km (Figure A2), similar to the results obtained from slip data from the 2006 event [*Wei et al.,* 2009] and indicates that triggered slip is confined to the thick sedimentary cover imaged by seismic studies [*Fuis et al.,* 1984].

3.4.3 Other Faults

In addition to the SAF and SHF, we also quantified triggered slip on the Imperial , Elmore Ranch, Wienert, Coyote Creek, Elsinore, Yuha faults, and three minor faults at the northern end of the Laguna Salada Fault. As with the SAF and SHF, repeated slip occurred on the same sections on the Imperial, Weinert, and Coyote Creek faults (Figure A3). In contrast, this is the first report of triggered slip on the Elmore Ranch Fault

(Figure 2A, A1) and the Elsinore Fault (Figure A4). This may only be a consequence of these fault segments being remote and hardly accessible for field studies.

Slip was also observed on several minor faults near the town of Ocotillo (Figure 1) near the northern end of the 2010 surface rupture zone (Figure A1). These minor faults are in an area that shows small offsets in the interferograms. Two of these minor faults are northwest-striking and likely represent an extension of the Laguna Salada Fault. The two faults slip right-laterally. The one on the west has a horizontal-vertical ratio (HVR) of 33:1 and a maximum horizontal slip of 19.1 mm, whereas the other fault has a significant amount of vertical slip (HVR 3:1) with a maximum horizontal slip of 40 mm. The Yuha Fault and another northeast-striking fault are perpendicular to the Laguna Salada Fault, forming a cross-fault system similar to EF/SHF system. Both northeast-striking faults show left-lateral slip (< 40 mm). These two faults were previously unmapped and are not currently included in the USGS or SCEC databases.

3.5 Discussion

Surface afterslip on the SHF in the four years following the 1987 M_w 6.2 Superstition Hills earthquake amounted to 90 cm [*Bilham and Behr*, 1992]. Episodic creep events on the SHF in 2006 [*Wei et al.*, 2009] and the 2010 triggered slip observed in this study can be viewed as on-going afterslip because a surface slip deficit remains from the 130 cm co-seismic slip at depth inferred for the 1987 mainshock [*Larsen et al.,* 1992]. We note also that static stress changes due to the El Mayor-Cucapah rupture increased shear stress on the SHF fault. The recorded creep rate on the SHF in the year

preceding the 4 April earthquake (0.95 mm/yr) fell to 0.3 mm/yr in the six months following the earthquake, suggesting a complicated time-dependent behavior of shallow creep.

In addition to the 1987 earthquake, in the past 40 years triggered slip has been documented more than seven times on the Superstition Hills fault each with maximum amplitudes of 20-30 mm (Figure 5 in *Wei et al.*, 2009). The accumulated triggered slip on the SHF over the last 40 years thus exceeds 0.16 m, about 16% of the average coseismic slip (1 m) on the fault [*Rymer et al.,* 2002]. Prior to the 1987 earthquake few slip events were recorded and a Caltech creepmeter recorded negligible creep. We assume that creep and triggered slip will continue to release the remaining surface slip deficit on the fault in the interval before the next major earthquake.

A multi-institution study [*Rymer et al.*, in preparation] documents triggered slip on more than 30 faults in southern California, most of which are in the Yuha Desert. Slip on these faults was not detected by InSAR methods presumably because slip was below the InSAR detection threshold (less than a few mm).

3.6 Conclusions

Triggered slip occurred on numerous faults in the Imperial Valley due to the 4 April 2010 El Mayor-Cucapah earthquake: the San Andreas Fault, the Superstition Hills Fault, the Imperial Fault, the Elmore Ranch Fault, the Wienert Fault, the Coyote Creek Fault, the Elsinore Fault, the Yuha Fault, and several sub-faults near the Northern end of the Laguna Salada Fault. The northwest-striking faults all show mainly right-lateral slip. The northeast-striking Yuha Fault, an unnamed fault north of the Laguna Salada Fault,

and the Elmore Ranch Fault show predominantly left-lateral slip. The consistency between slip determined by InSAR and field measurements with minor exceptions shows that InSAR is a useful tool in measuring centimeter-scale fault offsets Also, the slip determined by InSAR is on average 50% larger than the slip determined from field measurements, suggesting a fraction of the deformation is away from the main trace. Dislocation modeling of InSAR data from the Superstition Hills Fault shows that triggered slip on the fault was confined to the uppermost 3 km as in previous documented slip events.

3.7 Acknowledgements

We thank Michael Rymer and John Caskey for reviewing this paper, and K. Luttrell and D. Kilb for their comments on an early version of the manuscript. We thank X. Tong, J. Means, X. Chen, D. Huang (UCSD), R. Mellors (SDSU) and G. Fisch for their help with the fieldwork. We thank M. Rymer (USGS) and his collaborators for the information about their field results in the same area. This work was supported in part by the NSF Geophysics Program (EAR 0811772), the NASA EarthScope Program (the InSAR and Geodetic Imaging Component NNX09AD12G), and SCEC. The creepmeters were funded by USGS grant G10AC0016 and 07HQAG0026 and NSF Rapid EAR-1039474.

Text of Chapter 3, in full, is a reprint of the material as it appears in the Geophysical Research Letters. The dissertation author was the primary investigator and author of this paper.

3.8 References

Bevis, M., et al. (2005), The B4 Project: Scanning the San Andreas and San Jacinto fault zones, *Eos Trans. AGU*, 86(52), Fall Meeting Suppl., Abstract H34B-01.

Bilham, R. and Behr, J. (1992), A two-depth model for aseismic slip on the Superstition Hills fault, California, *Bull. Seism. Soc. Amer.,* 82, 1223-1235.

Bilham, R. and Williams, P. (1985), Sawtooth segmentation and deformation processes on the southern San Andreas Fault, California, Geophys. Res. Lett., 12, 557-560, doi:10.1029/GL012i009p00557.

Du, W., Sykes, L. R., Shaw, B. E., and Scholz, C. H. (2003), Triggered aseismic fault slip from nearby earthquakes, static or dynamic effect? *J. Geophys. Res.,* 108, 2131, doi:10.1029/2002JB002008.

Dorsey, R. (2010), Sedimentation and crustal recycling along an active oblique-rift margin: Salton Trough and northern Gulf of California, *Geology*, May 2010; v. 38; no. 5; p. 443–446; doi: 10.1130/G30698.1.

Elders, W. A., Rex, R. W., Meidav, T., Robinson, P. T., and Biehler, S. (1972), Crustal spreading in southern California, *Science*, v. 178, p. 15–24.

Farr, T. G. et al. (2007), The Shuttle Radar Topography Mission, *Rev. Geophys.,* 45, RG2004, doi:10.1029/2005RG000183.

Fialko, Y. (2004), Probing the mechanical properties of seismically active crust with space geodesy: Study of the co-seismic deformation due to the 1992 Mw7.3 Landers (southern California) earthquake, *J. Geophys Res.*, 109, B03307, doi:10.1029/2003JB002756.

Fialko, Y. (2006), Interseismic strain accumulation and the earthquake potential on the southern San Andreas Fault system, *Nature,* 441, 968–971, doi:10.1038/nature04797.

Field, E. H. (2007), A Summary of previous working groups on California earthquake probabilities, *Bulletin of the Seismological Society of America,* Vol. 97, No. 4, pp. 1033–1053, August 2007, doi: 10.1785/0120060048.

Fuis, G. S., Mooney, W. D., Healy, J. H., McMechan, G. A., and Lutter, W. J. (1984), A seismic refraction survey of the Imperial Valley region, California, *J. Geophys. Res.* 89, no. B6, 1165–1189.

Fuis, G. S. (1982), Displacement on the Superstition Hills fault triggered by the earthquake, in The Imperial Valley, California, Earthquake of October 15, 1979, *U.S. Geol. Surv. Profess. Pap.* 1254, 145–154.

Hudnut, K., Seeber, L., Rockwell, T., et al. (1989), Surface Ruptures on Cross-Faults in the 24 November 1987 Superstition Hills, California, Earthquake Sequence, *Bulletin of the Seismological Society of America*, Vol. 79, pp. 282-296.

Larsen, S., Reilinger, R., Neugebauer, H., and Strange, W. (1992), Global Positioning System Measurements of Deformations Associated With the 1987 Superstition Hills Earthquake: Evidence for Conjugate Faulting, *J. Geophys. Res.,* 97(B4), 4885–4902, doi:10.1029/92JB00128.

Marone, C. J., Scholz, C. H., and Bilham, R. (1991), On the mechanics of earthquake afterslip, *J. Geophys. Res.*, 96, 8441 – 8452, doi:10.1029/91JB00275.

Rymer, M. J. (2000), Triggered Surface Slips in the Coachella Valley Area Associated with the 1992 Joshua Tree and Landers, California, Earthquakes. *Bull. Seismol. Soc. Am.*, 90, 4, pp. 832–848, doi: 10.1785/0119980130.

Rymer, M. J., Boatwright, J., Seekins, L. C., Yule, J. D., and Liu, J. (2002), Triggered surface slips in the Salton Trough associated with the 1999 Hector Mine, California, earthquake, *Bull. Seismol. Soc. Am.*, 92, 1300–1317, doi:10.1785/0120000935.

Sieh, K. E. and Williams, P. W. (1990), Behavior of the Southernmost San Andreas fault during the past 300 years, *J. Geophys Res.*, 95(B5) 6629-6645.

Wei, M., Sandwell, D., and Fialko, Y. (2009), A silent Mw 4.7 slip event of October 2006 on the Superstition Hills fault, southern California, *J. Geophys. Res.,* 114, B07402, doi:10.1029/2008JB006135.

Williams, P. L., McGill, S. F., Sieh, K. E., Allen, C. R., and Louie, J. N. (1988), Triggered slip along the San Andreas fault after the 8 July 1986 North Palm Springs earthquake, *Bull. Seismol. Soc. Am.,* v. 78; no. 3; p. 111.

3.9 Auxiliary materials.

Table 3-A1. Field survey result of the Superstition Hills Fault.

Lat	Lon	mm	Strike (NW)	Lat	Lon	mm	Strike (NW)
33.44875	-115.84392	0.5		32.92965	-115.70021	15	40
33.44850	-115.84370	4		32.92859	-115.69935	8	
33.44848	-115.84342	3		32.92850	-115.69892	26	
33.44837	-115.84317	4		32.92825	-115.69858	20	60
32.97378	-115.75420	6		32.92719	-115.69732	23	40
32.97323	-115.75343	9		32.92694	-115.69717	26	70
32.97265	-115.75255	8		32.92653	-115.69662	18	47
32.97205	-115.75173	6		32.92633	-115.69642	16	52
32.97153	-115.75103	6		32.92598	-115.69599	13	100
32.97082	-115.75003	5		32.92557	-115.69560	16	71
32.97017	-115.74943	3		32.92493	-115.69483	13	70
32.96957	-115.74865	5		32.92474	-115.69457	10	80
32.96900	-115.74780	5		32.92377	-115.69333	13	90
32.96843	-115.74702	5		32.92362	-115.69313	22	60
32.96782	-115.74615	4		32.92289	-115.69205	12	56
32.96723	-115.74532	5		32.92236	-115.69135	20	59
32.96660	-115.74443	9		32.92147	-115.69015	25	60
32.96603	-115.74437	15		32.92055	-115.68885	25	61
32.96542	-115.74287	15		32.92028	-115.68842	27	59
32.96480	-115.74203	14		32.91825	-115.68568	37	60
32.96407	-115.74110	13		32.91800	-115.68532	35	72
32.96270	-115.73947	8		32.91737	-115.68436	30	50
32.96207	-115.73868	5		32.91706	-115.68393	35	46
32.96132	-115.73783	8		32.91634	-115.68275	20	60
32.95625	-115.73328	10		32.91578	-115.68182	20	46
32.95532	-115.73257	5		32.91437	-115.67994	22	59
32.95433	-115.73198	12		32.91407	-115.67884	12	64
32.95097	-115.72832	4		32.91346	-115.67768	12	58
32.95033	-115.72723	16		32.91261	-115.67660	25	58
32.94983	-115.72638	16		32.91143	-115.67513	22	60
32.94903	-115.72515	6		32.91060	-115.67425	13	71
32.94819	-115.72392	15		32.90950	-115.67326	20	54
32.94756	-115.72303	12		32.90857	-115.67254	20	50
32.94694	-115.72217	10		32.90738	-115.67129	12	65
32.94617	-115.72114	10		32.90638	-115.66991	20	44
32.94453	-115.71889	14		32.90505	-115.66793	12	70

Table 3-A1. Continued

32.94311	-115.71703	18		32.90358	-115.66599	11	70
32.94147	-115.71503	10		32.90188	-115.66418	10	72
32.93936	-115.71239	19		32.90126	-115.66342	15	
32.93781	-115.71058	17		32.90019	-115.66206	10	
32.93683	-115.70917	13		32.89938	-115.66130	9	
32.93586	-115.70797	12		32.89876	-115.66065	5	
32.93436	-115.70611	19		32.89864	-115.66006	1	
32.93278	-115.70411	10		32.89845	-115.66022	3	
32.93219	-115.70272	7		32.89840	-115.66018	0	
32.93064	-115.70144	20		32.89840	-115.66014	0	
32.93008	-115.70072	17		32.89827	-115.66005	6	
32.92967	-115.70022	9	55				

Note: Several groups did the field survey. Not all groups measured the azimuth.

Table 3-A2. Field survey result of the San Andreas Fault and the Imperial Fault.

Survey on triggered slip on the SAF and Imperial Fault. May 2nd, Matt Wei and Xiaopeng Tong, SIO

Site	Note ID	Latitude	Longtitude	Elevation (feet)	Displacement (mm)	Azimuth(No true north correction)	Note
SAF10	A	33.48531	-115.89091	-162	5	NW50	
SAF11	B	33.48461	-115.89023	-152	5	NW40	
SAF12	C	33.48289	-115.88838	-153	6	NW50	
SAF13	D	33.48181	-115.88746	-147	15	NW40	
SAF14	F	33.48077	-115.88627	-144	5	NW50	
SAF15	G	33.47993	-115.8853	-141	9	NW50	
SAF16	H	33.47721	-115.88155	-134	8	NW50	200 feet north of SAF16
SAF16	I	33.47679	-115.88085	-135	3	NW60	
SAF17	J	33.46632	-115.86591	-139	6	NW50	

Table 3-A2. Continued

							Box Canyon. Found small cracks other than the measured one, but not extend more than 20 meters. Southern extention are harder surface, which could be the reason of missing surface expression. No cracks found in SAF2, about 300 feet south of SAF1. We didn't go to SAF4, 8, 9; We went to SAF3,5,6,7 but found no cracks.
SAF1	K	33.5726	-115.98153	100	5	NW40	
Imperial & Harris road		32.88366	-115.53905	-114	10	N	On concrete road, along strike
					16	NE80	South of road, hard soil. Not along strike
							Large cracks, several parallel, across the road. On the south of the road, much more opening, very little along strike offset.
S-Line	S	32.75197	-115.42576	-19	15	NW48	Concrete road
					18	NW60	Concrete road
					9	NW70	South of the road, hard soil.
					14	N	South of the road, hard soil.
							Multiple cracks on road, one on soil. Southern side still there, northern side is destroyed by walking or driving. More openings than along strike displacement.

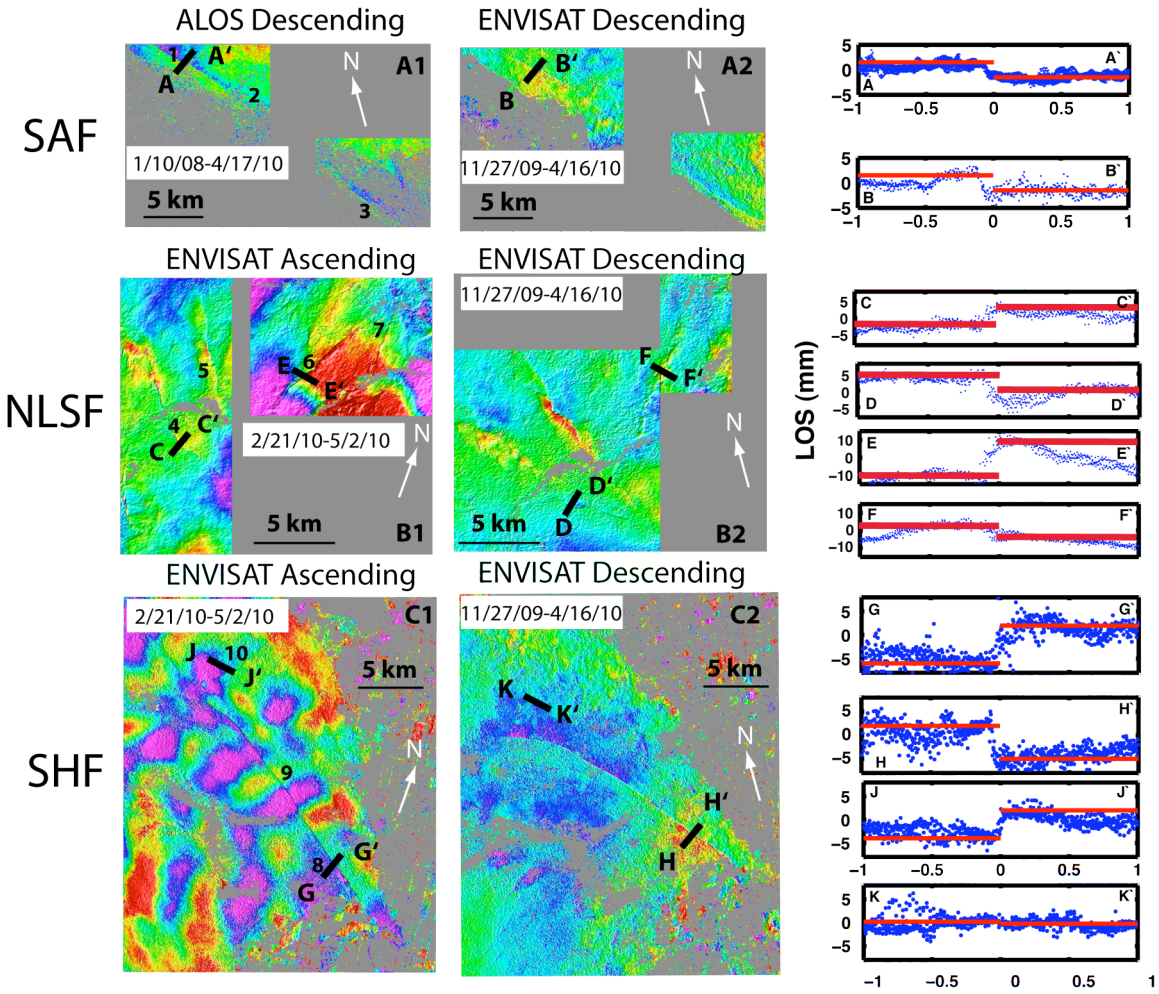

Figure 3-A1. (A-C) InSAR data in radar coordinates and profiles show triggered slip on multiple faults. Solid black lines are the locations of the profiles on the right. Black numbers show the location of profiles in table 1. Orientations of the images are different because we work in radar coordinates to avoid resolution lost due to projection to geographic coordinates. White arrows point to North.

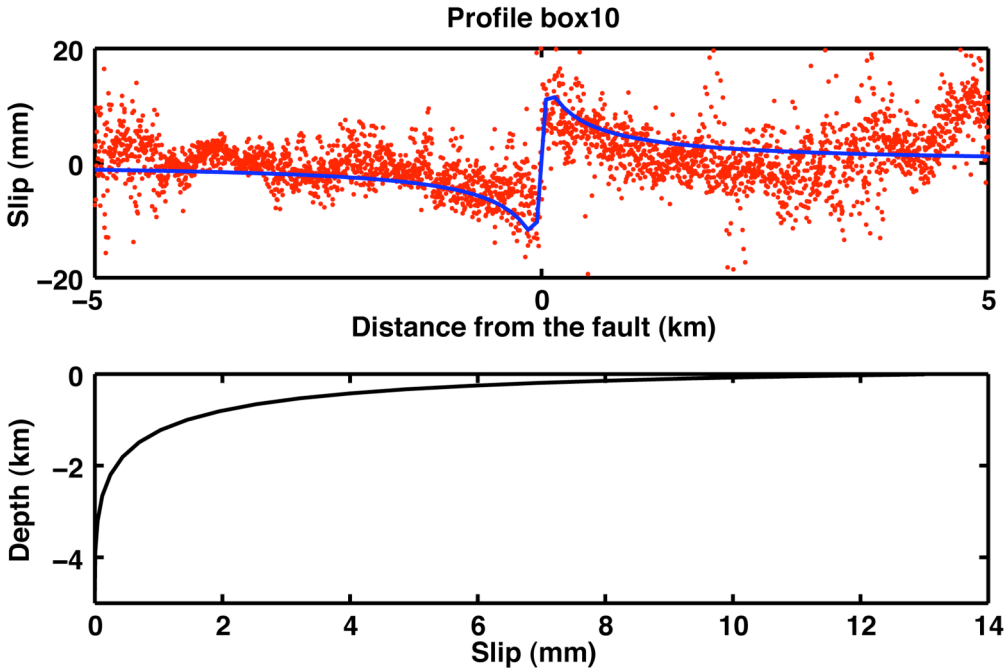

Figure 3-A2. An InSAR profile across the Superstition Hills Fault. Red dots are InSAR data and the blue line is the profile generated by the best fitting model below. The 100-m wavelength spatial Gaussian filter that was applied to the InSAR data was also applied to the model to make the model smoothness match the data smoothness. This profile is not across the location with maximum slip. This is why it has about 12 mm slip on the surface instead of 30 mm.

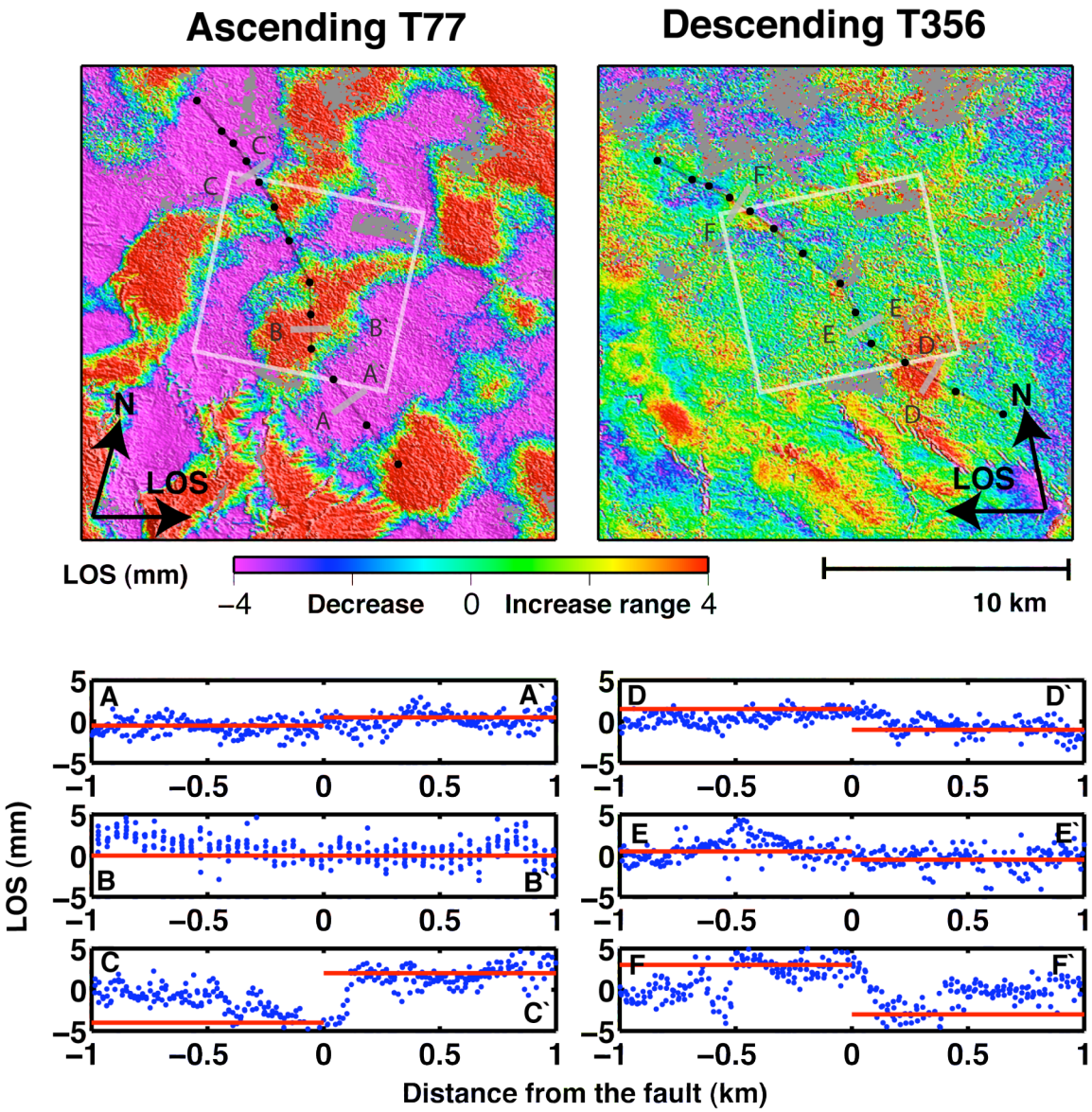

Figure 3-A3. Offset on the Coyote Creek Fault observed by InSAR. The top figures are in radar coordinates for the same fault. The slip on the Coyote Creek fault occurs on a 20-km-long section between highway 78 and the Superstition Mountain. The maximum offset is 26 mm at a location 2 km north of the highway 78. This section slipped up to 15 mm during the 1987 SHF earthquake [*Hudnut and Clark*, 1989].

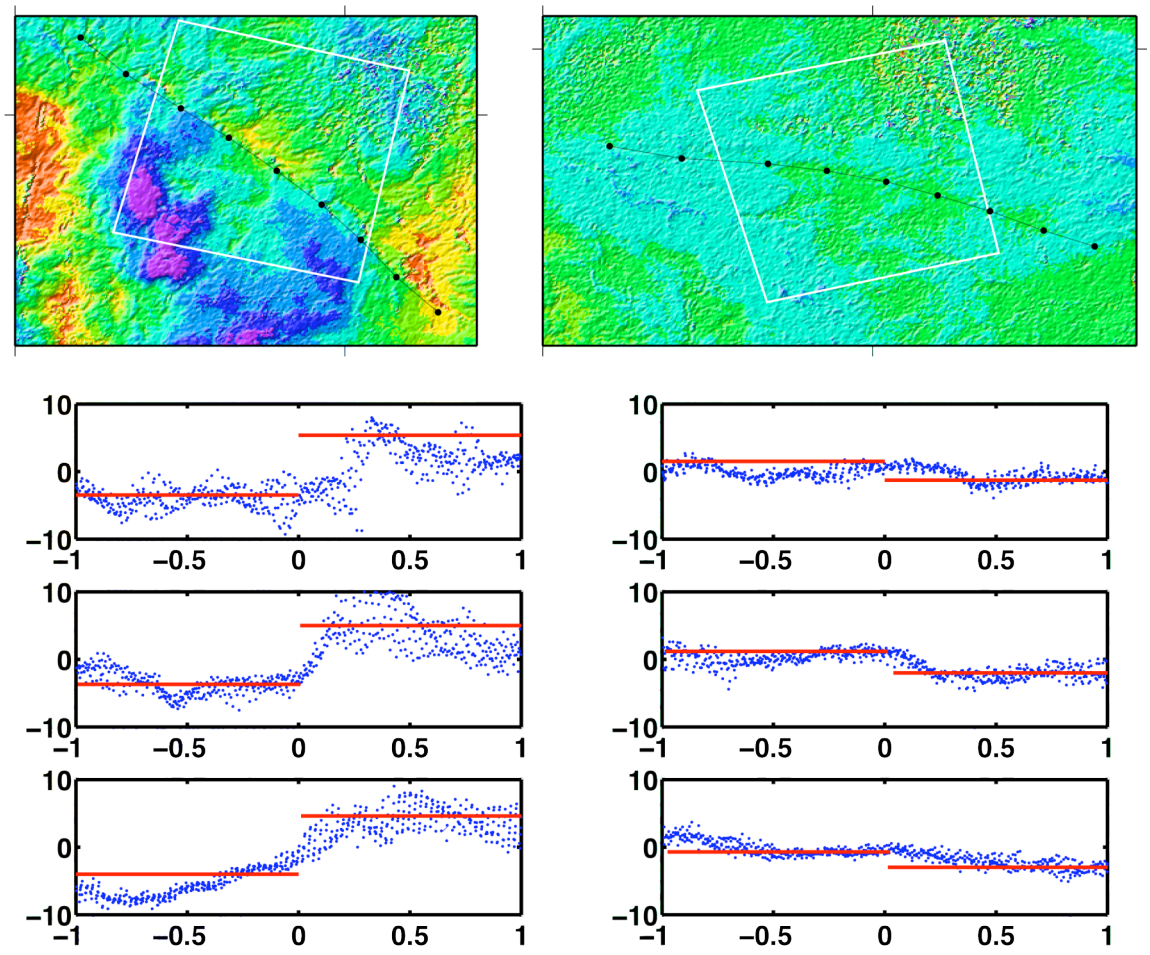

Figure 3-A4. Offset on the Elsinore Fault observed by InSAR. A 15-km long section of the Elsinore Fault shows slip with maximum amplitude of 16 mm. To our knowledge, this is the first time that triggered slip was reported on the Elsinore Fault, perhaps because this fault segment is remote and difficult to get to for field reconnaissance. A seismic analysis of this section of the fault shows low b-value [*Wyss et al.*, 2000], suggesting this segment is an asperity, which might rupture in future earthquakes.

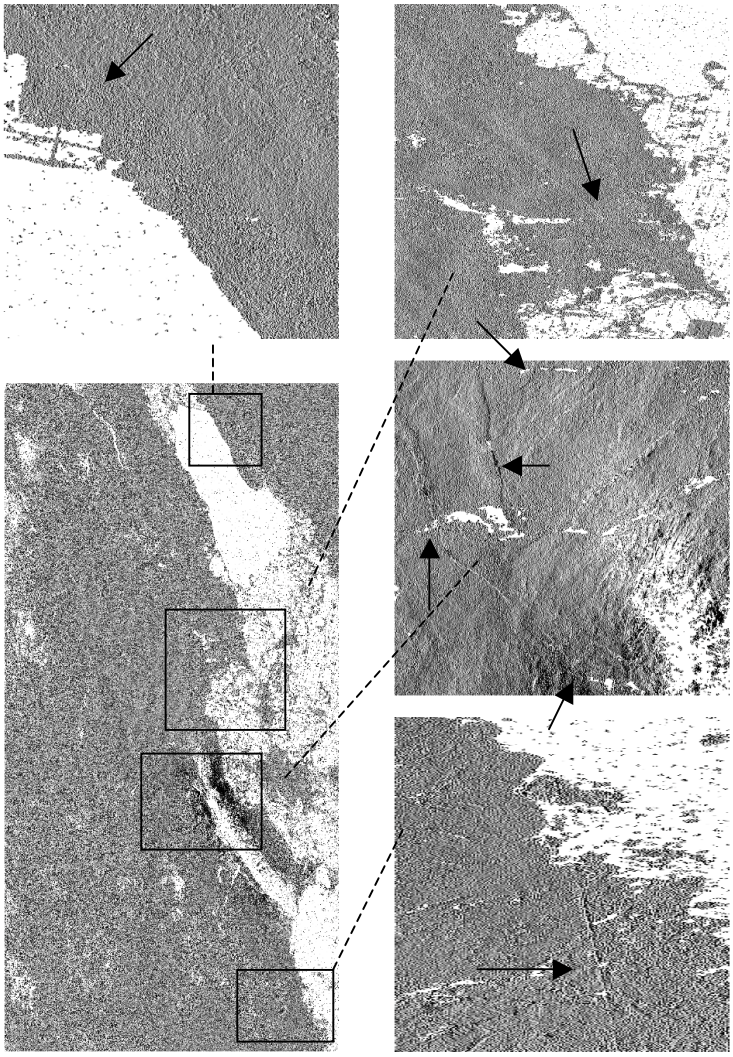

Figure 3-A5. Highlight offsets using phase gradient method. Left bottom figure is the ENVISAT InSAR observation of Frame 77. The other four smaller images are zoom-in in specific areas, in the order of north to south. Sharp linear features (pointed by black arrows) are the fault motion in the first three zoom-in figures or road subsidence in the bottom right figure. Small amplitude triggered slip (< 20 mm) is difficult to detect and measure when it is superimposed on large phase signals from the main earthquake rupture. We therefore used the phase gradient method [*Price and Sandwell*, 1998] to highlight and digitize the triggered slip. This technique is useful to extract short wavelength offsets by manipulating interferograms.

Elmore Ranch Fault

Slip is seen in the ENVISAT interferometry along one branch of the Elmore Ranch Fault system, which consists of several southwest-trending parallel faults, sometimes called cross-faults that intersect the northern end of the SHF. The last big event on this fault was the 1987 Mw 6.2 earthquake, when left lateral rupture was distributed on several branches across a zone 10 km wide [*Hudnut et al.,* 1989]. Subsequently, there have been no reports of slip on this fault until now, when the middle segment slipped about 10 mm. Importantly, this segment had the most co-seismic slip during the 1987 earthquake (Figure 2 in *Hudnut et al.,* 1989), showing similar pattern of preferred slip in certain segments.

Additional References

Hudnut, K., and Clark, M. (1989), New Slip Along Parts of the 1968 Coyote Creek Fault Rupture, California, *Bulletin of the Seismological Society of America*, Vol. 79, pp.451-465.

Price, E. J. and Sandwell, D. T. (1998), Small-scale deformation associated with the Landers 1992 California earthquake mapped by InSAR Phase Gradient, *J. Geophys. Res.*, 103, 27001-27016.

Wyss, M., Schorlemmer, D., and Wiemer, S. (2000), Mapping asperities by minima of local recurrence time: The San Jacinto-Elsinore fault zones, J. Geophys. Res., 105, 7829–7844.

4. CHAPTER 4: Relationship Between Fault Creep and Shallow Stress Accumulation Rate

Earthquake safety tip 4:

For those who fear earthquakes, it may comfort you to know that a majority of the damage during the 1906 San Francisco earthquake did not come from the tremors themselves. Instead, it was from the raging, out-of-control fires that consumed most of the city.

4.1 Abstract

Fault creep, which is non-seismic movement of a fault, is important for earthquake hazard assessment but the factors controlling fault creep are not well understood. Here we investigate the hypothesis that creep rate depends on the product of shallow stress accumulation rate and the creeping depth. Stress accumulation rate at 2 km depth along the San Andreas Fault System (SAFS) is estimated from a 3-D viscoelastic model constrained by GPS observations. The creeping depth is estimated with two approaches: i) assuming a uniform depth along the entire SAFS and ii) using a depth based on the balance between model stress and fault friction. The model with a uniform creeping depth shows a good correlation with observed creep rate while the correlation is poor for the model where creep rate depends on accumulated stress. This paper is still in preparation because more data are needed to complete this project.

4.2 Introduction

Aseismic creep is the measurable surface displacement along a fault in the absence of notable earthquakes. Both geological and geodetic observation methods have found evidence of creep along many segments of the San Andreas Fault System (SAFS) [*Burford and Harsh*, 1980; *Prescott et al.*, 1981; *Schulz et al.*, 1982; *Burgmann et al.*, 2000; *Lyons et al.*, 2002; *Lyons and Sandwell*, 2003]. Aseismic creep usually ranges from 0 to 30 mm/yr [*Thatcher,* 1990; *Wisely et al.,* 2008]. The presence of creep could release elastic energy and delay the occurrence of future earthquakes [*Burgmann et al.,* 2000], so it is an important part of seismic hazard estimation, especially in actively creeping areas, such as the Hayward fault, the central San Andreas fault and the Imperial fault [*Bilham et al.*, 2004]. Various groups have studied fault creep along San Andreas and Hayward fault, where best available data exist [*Malervisi et al.*, 2005; *Schmidt et al.,* 2005; *Galehouse and Lienkaemper,* 2003]. While there are many studies of fault creep, the dominant physical mechanism controlling creep is uncertain. The candidate mechanisms include:

1) Low normal stress and mature fault gouge in the upper 3 km of the crust that causes the frictional properties of the fault to undergo velocity strengthening [*Marone and Scholz*, 1988; *Linker and Dieterich*, 1992]. This model predicts that all mature faults have near-surface creep during the interseismic period.

2) The creep behavior depends on the rock type and pore pressure [e.g. *Sieh and Williams*, 1990; *Moore and Lockner*, 2008]. This model predicts that creep will be correlated with rock type.

3) The creep behavior depends on the shallow stress accumulation rate, which in turn depends on the deep locking depth *D* [*Savage and Lisowski*, 1993]. This model predicts that fault creep will be proportional to shallow stress accumulation rate.

Here we investigate the third hypothesis to better understand the role of stress accumulation rate and locking depth on fault creep. Moreover, our comparisons reveal areas where new creep rate observations would be useful for model discrimination.

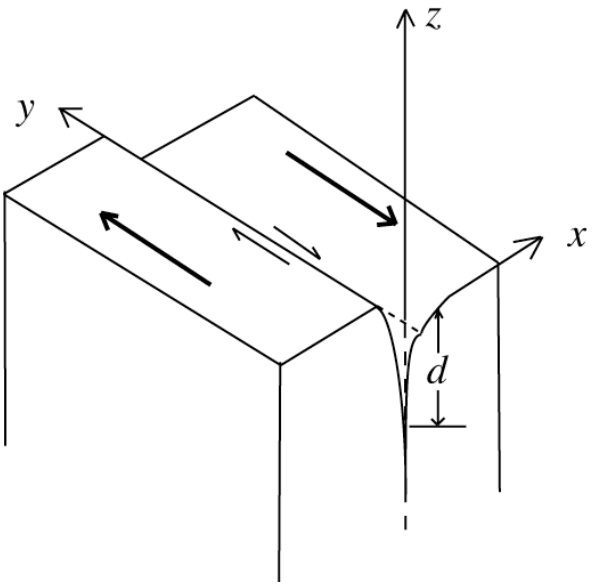

Figure 4-1. Diagram showing the displacement rate (creep) associated with the stress accumulation rate applied to a frictionless crack with a creeping depth of *d*, the depth of the shallow creep zone.

4.3 Creep rate modeling

The basic physical model used in this study is illustrated in Figure 1. An anti-plane stress rate $\dot{\tau}$ is applied to a frictionless crack extending from the surface of the

Earth to some creeping depth *d*. The creep rate $\dot{s}$ at the surface of the Earth across the crack is given by the following formula [*Knopoff* , 1958 ; *Sieh and Williams*, 1990]

$$\dot{s} = 2d\frac{\dot{\tau}}{\mu} \qquad (1)$$

where μ is the shear modulus and *d* is the creeping depth. This model differs from the regular locked fault model [*Savage,* 1990] by adding a creeping section on top of the locked section. This model is equivalent to equation 7 of *Savage and Lisowski* [1993] as the stressing rate includes both that from adjunct faults and tectonic loading and that from aseismic slip below the seismogenic zone on the same fault.

According to this model, the creep rate depends on two unknown parameters, the shallow stress accumulation rate and the creeping depth. The distribution and amplitude of shallow stress accumulation rate is adequately resolved by the current GPS array at SAFS [*Feigl and Dupre*, 1999; *Freymueller et al.*, 1999; *Murray et al.*, 2001; *Segall*, 2002; *Smith and Sandwell*, 2003]. The creeping depth *d* can be estimated two ways. First, one could assume a constant creeping depth or have *d* based on depth to basement; we call this Model A. Second, one could derive the creeping depth by balancing the frictional strength of the fault with the applied absolute tectonic stress [*Savage and Lisowski*, 1993]; we call this Model B. In Model B the creeping depth is calculated by

$$d = \frac{\pi\tau}{2k} \qquad (2)$$

(see derivation in Appendix) where τ is the depth averaged total stress on the fault and k is frictional strength of the fault. One model for frictional strength of the fault is Byerlee's law [*Byerlee*, 1978], $k = fg\Delta\rho$, where f is the coefficient of friction, g is the acceleration of gravity and $\Delta\rho$ is the effective density. The effective density is the difference between the rock density and the water density, if water is present within the rock and under hydrostatic pressure within the fault. Using Byerlee's law for fault frictional strength, the creep rate ($\dot{s}$) is the product of the depth averaged total stress (τ) and the stress accumulation rate ($\dot{\tau}$) (Appendix)

$$\dot{s} = \frac{\pi}{\mu f \Delta\rho g}\tau\dot{\tau} \qquad (3)$$

The stress accumulation rate $\dot{\tau}$ is primarily dependent on the long-term slip rate and deep locking depth D and is relatively insensitive to the earthquake history and viscoelastic rheology [*Smith and Sandwell*, 2003; *Smith and Sandwell*, 2006]. The uncertainties of the estimation [*Smith-Konter et al*., 2008] are as follows: stress accumulation rate uncertainties, derived from a range of geodetically- and seismically driven locking depth estimates, are roughly +3/-0.5 MPa/100 years; uncertainties derived from realistic slip rate variations are roughly +1/-0.5 MPa/100 years. In contrast to the stress accumulation rate, estimates of total accumulated stress τ on fault segments spanning multiple earthquake cycles are highly dependent on the prescribed slip history

of each fault segment [*Freed and Burgmann*, 2004]. Uncertainties in accumulated stress can range from 0.5-3.0 MPa for various slip history scenarios. Despite these uncertainties, we calculate the accumulated stress by assuming complete slip (or stress) release following each earthquake event [*Smith and Sandwell*, 2006]. This assumption results in a lower bound on the accumulated stress at a given time. Moreover, it should be emphasized that these are estimates of stress change and do not reflect the absolute level of stress, which is dependent on the non-linear rheology of the crust and mantle [*Hetland and Hager*, 2005]. However, we use these estimates to constrain the absolute stress in Model B. Both stress rate and stress estimation on the creeping section of the San Andreas Fault is invalid. As high creep rate in this section, very little stress should be accumulated. The relative high stress rate is a result of the 1 km pixel size of the model to meet the computer speed and memory limitations. Therefore, we excluded data from the creeping section in our analysis.

Based on published data, mainly from creepmeters, *Wisely et al.* [2008] compiled a dataset of shallow creep rate in California mainly based on the analysis of *Louie et al.* [1985] and *Galehouse and Lienkaemper* [2003]. To minimize the influence of nearby seismic events, observations within a few years following a major event are omitted from the analysis. In cases where there are multiple measurements at the same location, the measurement with the smallest uncertainty is used. Measurements of zero creep rate are also included. Uncertainties are included when they are available. We adopted their results in this study.

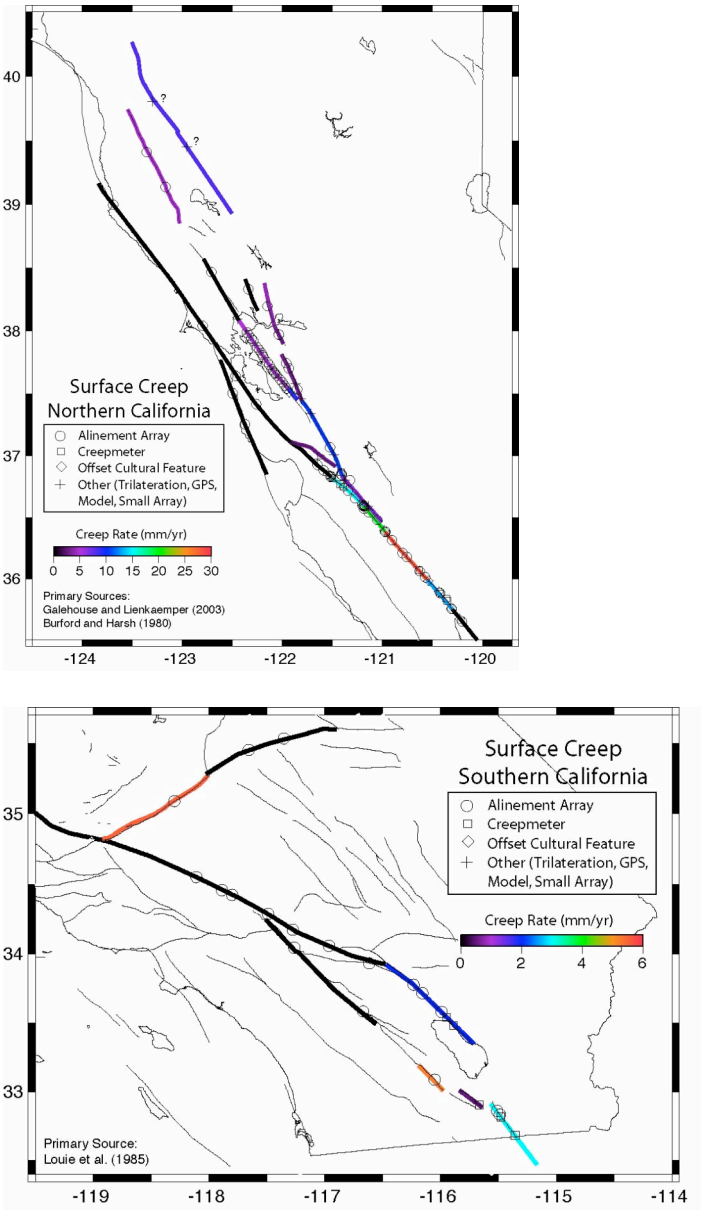

Figure 4-2. Creep rate on faults in California (Reproduced from *Wisely et al.*, 2008 with the permission of the authors). The color bars in the two figures are different. Most measurements are from creepmeters and alignment array.

For southern California, new measurements from InSAR and GPS suggested different value of creep rate at several locations from the dataset that *Wisely et al.* [2008] compiled. *Louie et al.* [1985], the main resource of creep rate data in their dataset, are

based on observations with temporal interval of 3-14 years during 1970s and 1980s. At some locations, the creep rate seems inaccurate due to the short length of recording period or timing in the seismic cycle. For example, a 5 mm/yr creep rate on Western Garlock fault was based on one measurements between 1971-1984. However, InSAR data for the last 20 years show no creep at the same location. So even if the 5 mm/yr during 1971-1984 is from creep, the rate should be decreased, as longer measurements from InSAR suggest no creep for the last 20 years. Another example is on the Superstition Hills Fault. The measurements of *Louie et al.* [1985] cover the end of the interseismic period because an earthquake occurred on the Fault at the end of the recording. After the event, the SHF creeps fast as afterslip. The average creep rate during 1992-2007 is about 10 mm/yr. Thirdly, a repeated GPS survey on the San Andreas Fault near Painted Canyon shows 5 mm/yr creep rate. So, we updated these three measurements in our analysis.

In this study, we compare our predictions of creep rate based on our two models (A and B) with two datasets: dataset 1, Wisely et al. dataset and new observations from InSAR and GPS; dataset 2, dataset 1 excludes zero creep rate measurements. Dataset 2 are also used because we suspect both model A and B are not valid on the faults segments that do not creep. Please note that data on the creeping section of the San Andreas Fault are excluded in both datasets. In addition, we estimated the creeping depth for all segments in California and compared them with other studies.

4.4 Data Analysis and Results

We used the model of *Smith and Sandwell* [2006] (now referred to as SS06) to calculate the stress accumulation rate and the accumulated stress due to earthquake cycle effects at 2 km depth along the entire SAFS (Figure 3). The model simulates 1000 years of the earthquake cycle along the SAFS by convolving best estimates of interseismic and coseismic slip with the Green's function for a point dislocation in an elastic plate overlying a viscoelastic half-space. Interseismic slip rate is based on long-term geological estimates while the fault locking depths are derived from horizontal GPS measurements. Stress magnitude is largely independent of assumed rheology, but it is very sensitive to the slip history on each fault segment.

Based on the SS06 model results (τ and $\dot{\tau}$), we developed two models for creep rate. First, assuming a constant creeping depth (Model A, equation 1) we used the stress accumulation rate model (Figure 3b) to calculate the creep rate along all of the SAFS and found the best estimate of the creeping depth by fitting observations (Figure 4). For the second model, we calculated the creeping depth using the accumulated stress. Then we calculated the creep rate (equations 2 and 3, Model B) and found the best estimate of the coefficient of the friction (Figure 5). Effective density is assumed to be a constant with a value of 1.7×10^3 kg/m^3 with respect to hydrostatic water content present in the rocks. The shear modulus is set to 30 GPa [*Becker et al.,* 2004].

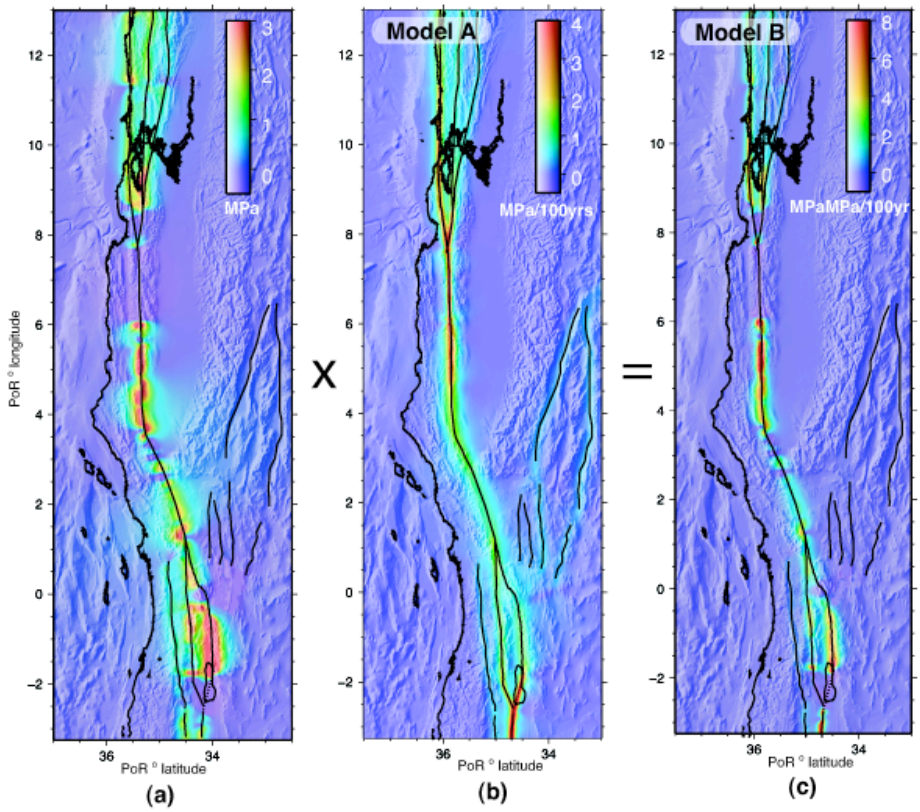

Figure 4-3. (a) Estimates of accumulated stress (τ, MPa) following the SS06 method, (b) Estimates of stress accumulation rate ($\dot{\tau}$, MPa/100yr), (c) Product of accumulated stress and stress accumulation rate. All stress estimates are calculated at a depth of 2 km along the SAFS. Model A is a scaled version of b, derived from equation 1. Model B is a scaled version of c, derived from equation 3. Note that the creeping section in central SAF is set to zero because the accumulated stress and stress accumulation rate are uncertain.

To validate these models, we compare them with a compiled database of published creep rate measurements for the SAFS [*Wisely et al.*, 2008] and new observation from InSAR and GPS in Southern California. Note that the distribution of measurement locations (Figure 2) reflects a higher density of measurements made in northern and central California. This implies a need for measurements on some critical

segments where the model suggests creep but no observations exist. We fit Models A and B to the creep rate observations, data 1 and data 2, using a least-squares approach (Figure 4 and 5).

Both modeled creep rate estimates were fit to the observed data using a standard linear regression analysis [*Bevington,* 1969]. Our objective was to determine if the observations are correlated with Models A and B. In other words, could one generate the observed creep rates with the observed mean and standard deviation that is completely uncorrelated with these models? For both models we performed two linear regressions by swapping the dependent and independent variables and calculated the linear correlation coefficient. When using data 1, Model A has a correlation of 0.55, while the correlation is much lower for Model B (0.23). To test the influence of sample size, we did Student t-test for both cases. With 82 observations, the probability of the observed creep being uncorrelated with the stress accumulation rate (Model A) is very small ($1x10^{-7}$). In contrast, the probability of being uncorrelated in Model B is much larger, 0.038. These results show that Model A is much more consistent with the data than model B.

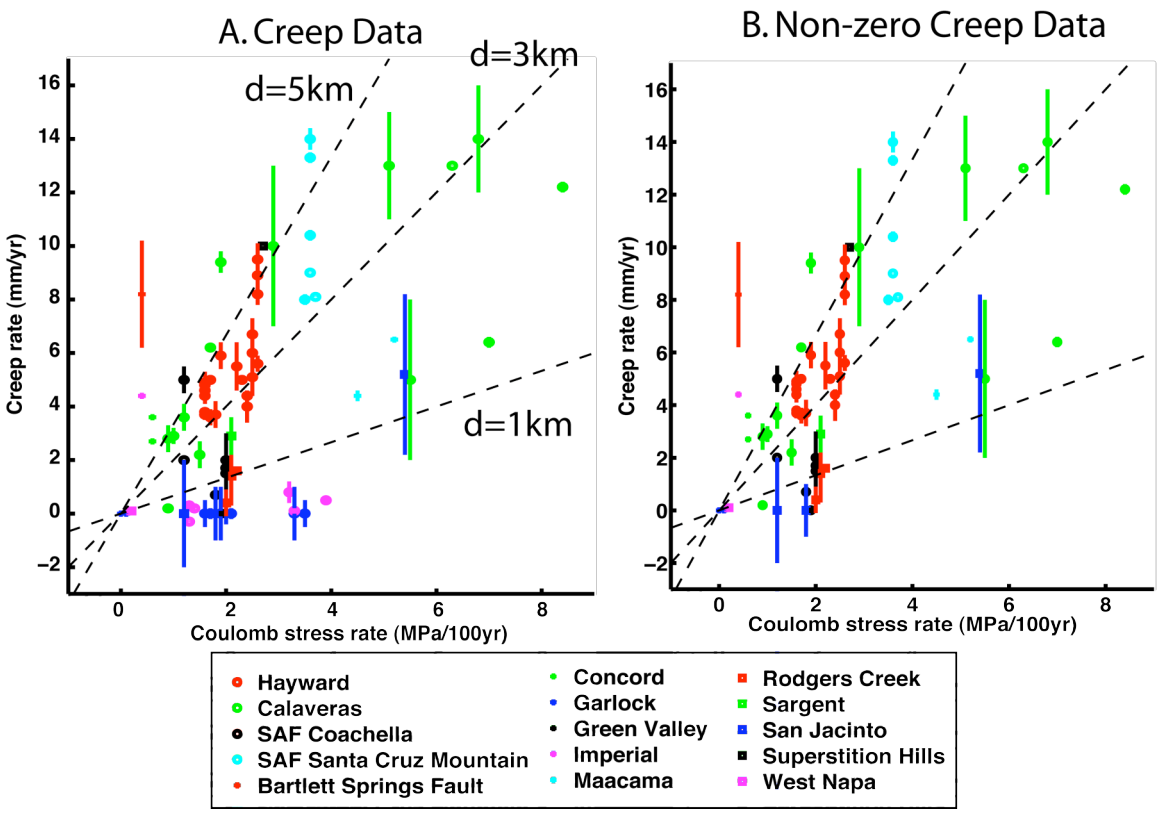

Figure 4-4. Model A. (A) Stress accumulation rate versus measured creep rate with all data including *Wisely et al.*, 2008 and updated data in this study: 5 mm/yr creep rate on the West Garlock Fault was removed. Creep rate on the Superstition Hills Fault is modified to 10 mm/yr. One data point at the SAF Coachella is modified to 5 mm/yr based on new data. Color and shape labels different fault segments in California. (B) Same plot as A with zero creep rate data removed.

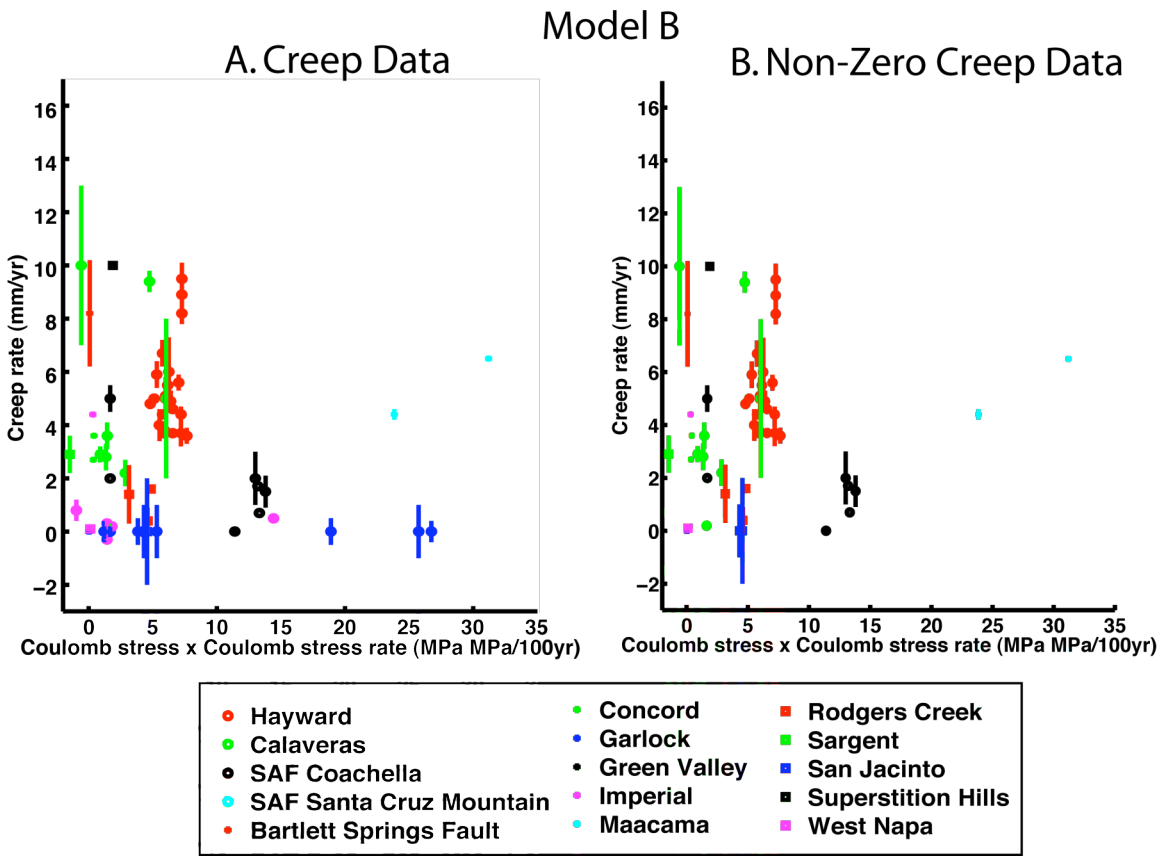

Figure 4-5. Model B. (A) Stress accumulation rate versus measured creep rate with all data including *Wisely et al.*, 2008 and updated data in this study: 5 mm/yr creep rate on the West Garlock Fault was removed. Creep rate on the Superstition Hills Fault is modified to 10 mm/yr. One data point at the SAF Coachella is modified to 5 mm/yr based on new data. Color and shape labels different fault segments in California. (B) Same plot as A with zero creep rate data removed.

As an additional test, we removed data where the creep rate was zero, forming data 2. Removal of the zero creep data significantly improved the correlation for model A, from 0.55 to 0.64 and also slightly improved the correlation for Model B from 0.23 to 0.25. The t-tests also showed improvements. The probability of the observed creep being uncorrelated with the stress accumulation rate (Model A) is very small for the three

cases of all data, updated with InSAR and GPS and excluding zero creep to $1x10^{-7}$, and $0.3x10^{-7}$, respectively; while for Model B the probability were is 0.038, and 0.044, respectively.

Model A has a best fit slope (assuming zero intercept, best fitting slope is $k = \sum_{i=1}^{n} x_i y_i / \sum_{i=1}^{n} x_i x_i$ for minimum misfit) that corresponds to an average creeping depth of 2.48 km using data 1. For data 2, the corresponding average creeping depth is 2.86 km. Model B has a best-fit slope of 1.3 km/MPa^2, which through equation 3 corresponds to a frictional coefficient of 0.08, using data 1. For data 2, the corresponding frictional coefficient is 0.09. The extremely low friction coefficient suggests that Model B is invalid.

4.5 Discussions

Based on Model A, our best estimate for the average creeping depth along the entire SAFS is 2.86 km. While this depth seems rather large, we note that this is the average depth and there is a bias in the compilation of the creep rate data because faults that are known not to creep are usually not studied and therefore they are not included in our compiled creep database (Table 1). It is interesting to compare this average creeping depth to the average basement depth along these faults under the working hypothesis that creeping depth is controlled by rock lithology. In southern California, *Kohler and Fuis* [1986] constructed a basement depth map of the Imperial fault using seismic refraction data. They found the basement depth to be about 5 km at the Imperial fault and 4 km at the Superstition Hills fault which is in good agreement with our model average of 5 km.

In contrast, the basement depth at SAFOD (central California) is lower - from 0.8 to 2.5 km [*Hole et al.*, 2001]. Considering that sediments are not present everywhere, 2.86 km is a reasonable value for the average basement depth. Indeed, it would be instructive to adjust the basement depth on each fault segment so that the model creep rate matched the observed creep rate. This could be compared with a more complete basement depth map of the SAFS when it becomes available.

The analysis using Model B, implies a low friction coefficient of 0.08. Although model B does not fit the data, there are two possible implications of our analysis. First, the SAFS is a weak fault zone, (i.e. the coefficient of friction is low). Whether the strength of the SAF is low is still under debate [*Zoback*, 2000]. While laboratory experiments suggest a high fault friction [*Byerlee,* 1978], stress orientation observations [*Mount and Suppe*, 1987] and heat flow data [*Lachenbruch and Sass*, 1992] prefer a weak fault. A second possibility is that our estimates of stress are low, implying a low stress drop during an earthquake, only a fraction of the absolute stress. The estimates of the stress in SS06 are in agreement with the 1-7 MPa stress drops measured during major earthquakes [*Kanamori and Anderson*, 1975; *Fletcher and Mcgarr*, 2006; *Shearer et al.*, 2006; *Allmann and Shearer*, 2007]. According to equation 3, if the accumulated stress level increased by a factor of 10, then the best fitting value for the friction coefficient would be 0.4, which is a more reasonable value. However, the relationship between stress drop and the absolute stress is controversial and relates to the strength of the fault zone [*Scholz*, 2000; *Zoback*, 2000; *Hardebeck and Hauksson*, 2001]. An obvious solution is to obtain measurements of the stress levels and physical conditions from within the fault. However, these measurements are difficult, resource intensive and time

consuming. Theoretical work can be done before more measurements are collected. For example, we can use Model B in an opposite way, in that we can use the creep rate measurements and stress accumulation rate estimates to estimate the absolute stress level.

If model A is valid, we can estimate creep depth using the creep rate and stress rate (Figure 6). The creep depth we calculated is consistent with some previous studies at the Calaveras Fault [*Manaker et al.,* 2003], the Hayward Fault [*Schmidt et al.,* 2005; *Malservisi et al.* 2005], the Superstition Hills Fault [*Wei et al.*, 2009] and the Imperial Fault [*Lyons et al.,* 2002]. Our estimations of creep depth on many other faults are reasonable, such as the Coachella section of the San Andreas Fault, the Maacama Fault and the Rogers Creek Fault. Our result is inconsistent with the creeping section of the San Andreas Fault because the stress rate estimated in this section is incorrect. Extremely high values of creeping depth (> 10 km) are found on the Bartlett Springs Fault, the Concord fault and the Green Valley Fault. The extremely high values might be due to the limited available measurements on these faults. When more data available, our new estimation of creep rate and stress rate might generate a reasonable creeping depth.

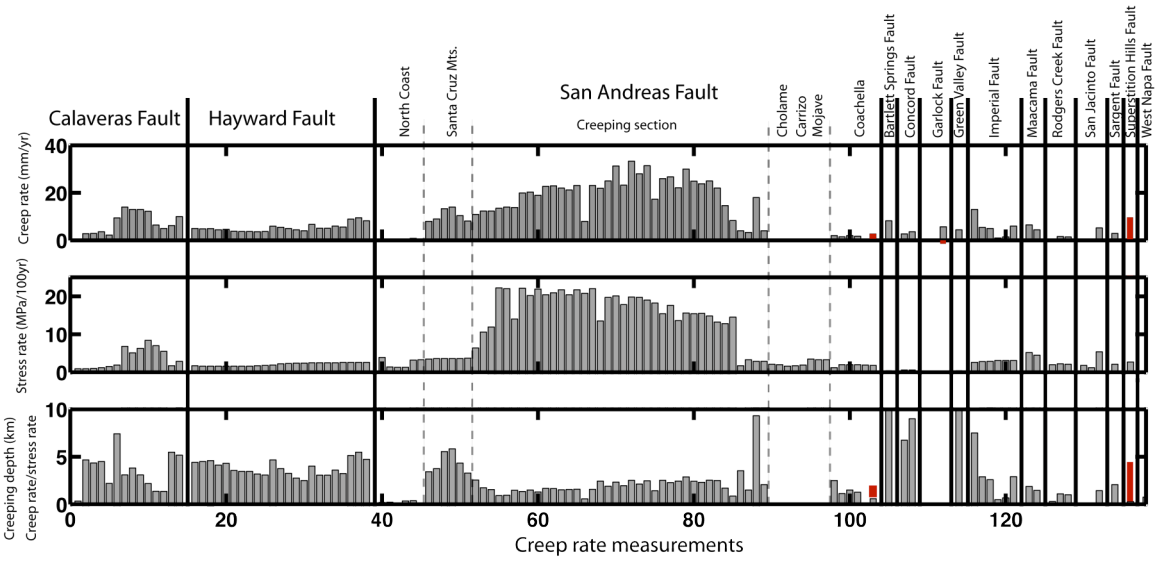

Figure 4-6. Estimation of shallow creeping depth based on creep rate and stress accumulation rate on faults in California. The upper panel is the creep rate data from *Wisely et al.*, 2008. The stress accumulation rate data is from this study. The creeping depth is calculated based on equation 1, assuming constant shear modulus of 30 GPa. Red bars label the data points using updated data.

One of the more important results from this analysis is that it reveals many segments of the SAFS where no creep observations exist. Indeed, observations of zero-creep rate could place much better constraints on the models. *Galehouse and Lienkaemper* [2003] also note some important faults, such as the northern Green Valley, central Calaveras, Greenville, and southern Maacama, which lack creep observations. Constraining the creep rate along the entire SAFS to an accuracy of a few mm/yr would provide much stronger constraints on the model. Moreover, understanding the across-fault velocity variations could better constrain the creeping depth. Over short distances of 0.1 to 3 km, InSAR measurements are not plagued by systematic errors and atmospheric artifacts. Strike-slip motion of 10 mm or more maps into 3 mm of line-of-sight signal in InSAR measurements and is detectable if the coherence is adequate

[*Burgman et al.,* 2000; *Lyons and Sandwell,* 2003; *Schmidt et. al.,* 2005]. Therefore interferograms must span at least three years to provide new creep rate/depth information in many areas. Unfortunately along most of the SAFS north of San Bernardino, C-band interferometry becomes decorrelated after two years [*Rosen et al*., 1998]. Decorrelation times may be much longer for L-band interferometry [*Rosen et al.,* 1996]. The new ALOS L-band InSAR satellite may provide the needed creep rate measurements in the upcoming years.

4.6 Appendix

Here we re-derive of the relationship between the creeping depth and the absolute stress. This derivation includes some of the steps that were not included in the appendix of *Savage and Lisowski* [1993]. Following their model, we assume the effective normal stress is proportional to the lithostatic pressure. According to Byerlee's law, [*Byerlee*, 1978] the frictional strength τ_f increases linearly with depth z

$$\tau_f = \tau_o + kz \qquad \text{(A1)}$$

where τ_o is the limiting resisting stress (cohesion) at the free surface, k is a coefficient (discussed later) and z is the depth. We assume that the stress drops to zero during an earthquake. Following the earthquake, the absolute stress at shallow depth increases with time. Creep occurs when the absolute stress on the fault plane exceeds the Byerlee

strength criterion (A1). Assuming the absolute stress is constant at shallow depth where creep occurs, the stress relieved by the creep (τ_c) is

$$\tau_c(z) = \tau_f(z) - \tau_{xy}(z) = \tau_o + kz - \tau \qquad \text{(A2)}$$

where τ_{xy} is the absolute stress and τ is the depth averaged absolute stress at shallow depth.

If slip is resisted only by friction, then the creeping depth *d* is determined by the condition [*Weertman, 1964*, eq. 6]

$$\int_{-d}^{d} \frac{\tau_c(|u|)}{\sqrt{d^2 - u^2}} du = 0 \qquad \text{(A3)}$$

The integration of equation (A3) can be calculated by

$$\int_{-d}^{d} \frac{\tau_c(|u|)}{\sqrt{d^2 - u^2}} du = (\tau_o - \tau) \int_{-d}^{d} \frac{1}{\sqrt{d^2 - u^2}} du + 2k \int_{0}^{d} \frac{u}{\sqrt{d^2 - u^2}} du \qquad \text{(A4)}$$

The integration can be calculated by variable change ($\cos\alpha = u/d$). The result is

$$\int_{-d}^{d} \frac{\tau_c(|u|)}{\sqrt{d^2 - u^2}} du = 2kd + (\tau_o - \tau) = 0 \qquad \text{(A5)}$$

From (A5) and assume the limiting resisting stress at the free surface is low relative to the total stress ($\tau_o = 0$), the creeping depth is related to the total stress by

$$d = \frac{\pi\tau}{2k} \qquad \text{(A6)}$$

One model of k is $k = fg\Delta\rho$, where f is the coefficient of friction, g is the acceleration of gravity and $\Delta\rho$ is the effective density. Substituting k into A6, we get

$$d = \frac{\pi \ \tau}{2f(\rho - \rho_w)g} \qquad \text{(A7)}$$

4.7 Acknowledgements

We thank Glenn Ierley and Bruce Bills for help with developing the mathematical equations used for this study. We thank Yuri Fiako, Howard Zebker, Ray Weldon and David Schmidt for their discussions. We thank Karen Luttrell and Debi Kilb for internal review.

Text of Chapter 4, in part is currently being prepared for submission for publication of the material. The dissertation author was the primary investigator and author of this paper.

4.8 References

Allmann, B. P. and Shearer, P. M. (2007), Spatial and temporal stress drop variations in small earthquakes near Parkfield, California, *J. Geophys. Res., 112*, doi:10.1029/2006JB004395.

Becker, T.W., Hardebeck, J., and Anderson, G. (2004), Constraints on fault slip rates of the southern California plate boundary from GPS velocity and stress inversions, *Geophys. J. Int.* 160, doi: 10.1111/j.1365-246.

Bevington, P. R. (1969), *Data Analysis and Error Analysis for the Physical Sciences, McGraw-Hill, New York, 336 pp.*

Bilham, R., Suszek, N., and Pinkney, S. (2004), California creepmeters, *Seismological Research Letters*, *75*, 481-492.

Burford, R. O. and Harsh, P. W. (1980), Slip on the San-Andreas-Fault in Central California from Alignment Array Surveys, *Bulletin of the Seismological Society of America*, *70*, 1233-1261.

Burgmann, R., Schmidt, D., Nadeau, R. M., d'Alessio, M., Fielding, E., Manaker, D., McEvilly, T. C., and Murray, M. H. (2000), Earthquake potential along the northern Hayward fault, California, *Science*, *289*, 1178-1182.

Byerlee, J. (1978), Friction of Rocks, *Pure and Applied Geophysics*, *116*, 615-626.

Feigl, K. L. and Dupre, E. (1999), RNGCHN: a program to calculate displacement components from dislocations in an elastic half-space with applications for modeling geodetic measurements of crustal deformation, *Computers & Geosciences*, *25*, 695-704.

Fletcher, J. B. and McGarr, A. (2006), Distribution of stress drop, stiffness, and fracture energy over earthquake rupture zones, *J. Geophys. Res.*, *111*, B03312, doi:10.1029/2004JB003396.

Freed, A. M., and Burgmann, R. (2004), Evidence of power-law flow in the Mojave desert mantle, *Nature*, *430*, 548-551.

Freymueller, J. T., Murray, M. H., Segall, P., and Castillo, D. (1999), Kinematics of the Pacific North America plate boundary zone, northern California, *Journal of Geophysical Research-Solid Earth*, *104*, 7419-7441.

Galehouse, J. S., and Lienkaemper, J. J. (2003), Inferences drawn from two decades of alinement array measurements of creep on faults in the San Francisco Bay Region, *Bulletin of the Seismological Society of America*, *93*, 2415-2433.

Hardebeck, J. L., and Hauksson, E. (2001), Crustal stress field in southern California and its implications for fault mechanics, *Journal of Geophysical Research-Solid Earth*, *106*, 21859-21882.

Hetland, E. A. and Hager, B. H. (2005), Postseismic and interseismic displacements near a strike-slip fault: A two-dimensional theory for general linear viscoelastic rheologies, *J. Geophys. Res.*, *110*, B10401, doi:10.1029/2005JB003689.

Hole, J. A., Catchings, R. D., St. Clair, K. C., Rymer, M. J., Okaya, D. A., and Carney, B. J. (2001), Steep-Dip Seismic Imaging of the Shallow San Andreas Fault Near Parkfield, *Nature, V. 294,* 1513-1515

Kanamori, H. and Anderson, D. L. (1975), Theoretical Basis of Some Empirical Relations in Seismology, *Bulletin of the Seismological Society of America*, *65*, 1073-1095.

Lachenbruch, A. H. and Sass, J. H. (1992), Heat-Flow from Cajon Pass, Fault Strength, and Tectonic Implications, *Journal of Geophysical Research-Solid Earth*, *97*, 4995-5015.

Linker, M. F. and Dieterich, J. H. (1992), Effects of Variable Normal Stress on Rock Friction - Observations and Constitutive-Equations, *Journal of Geophysical Research-Solid Earth*, *97*, 4923-4940.

Louie, J. N., Allen, C. R., Johnson, D. C., Haase, P. C., and Cohn, S. N. (1985), Fault Slip in Southern-California, *Bulletin of the Seismological Society of America*, *75*, 811-833.

Lyons, S. and Sandwell, D. (2003), Fault creep along the southern San Andreas from interferometric synthetic aperture radar, permanent scatterers, and stacking, *J. Geophys. Res., 108(B1)*, 2047, doi:10.1029/2002JB001831.

Lyons, S. N., Bock, Y., and Sandwell, D. T. (2002), Creep along the Imperial Fault, southern California, from GPS measurements, *J. Geophys. Res., 107(B10),* 2249, doi:10.1029/2001JB000763.

Malservisia, R., Furlongb, K. P., and Gansb, C. R. (2005), Microseismicity and creeping faults: Hints from modeling the Hayward fault, California (USA), *Earth and Planetary Science Letters*, 234(3-4), 421-435, doi:10.1016/j.epsl.2005.02.039.

Manaker, D. M., Burgmann, R., Prescott, W. H., and Langbein, J. (2003), Distribution of interseismic slip rates and the potential for significant earthquakes on the Calaveras fault, central California, *J. Geophys. Res.*, 108(B6), 2287, doi:10.1029/2002JB001749.

Marone, C., and Scholz, C. H. (1988), The Depth of Seismic Faulting and the Upper Transition from Stable to Unstable Slip Regimes, *Geophysical Research Letters*, *15*, 621-624.

Moore, D.E. and Lockner, D.A. (2008), Slow-Speed Weakening of Serpentinite Sheared Against Quartzofeldspathic Rocks: Implications for Fault Creep in the San Andreas System, American Geophysical Union, Fall Meeting 2008, abstract #S41A-1829.

Mount, V. S. and Suppe, J. (1987), State of Stress near the San-Andreas Fault - Implications for Wrench Tectonics, *Geology*, *15*, 1143-1146.

Murray, J. R., Segall, P., Cervelli, P., Prescott, W., and Svarc, J. (2001), Inversion of GPS data for spatially variable slip-rate on the San Andreas Fault near Parkfield, CA, *Geophysical Research Letters*, *28*, 359-362.

Prescott, W. H., Lisowski, M., and Savage, J. C. (1981), Geodetic Measurement of Crustal Deformation on the San-Andreas, Hayward, and Calaveras Faults near San-Francisco, California, *Journal of Geophysical Research*, *86*, 853-869.

Prescott, W. H., and Lisowski, M. (1983), Strain Accumulation Along the San-Andreas Fault System East of San-Francisco Bay, California, *Tectonophysics*, *97*, 41-56.

Savage, J. C., Prescott, W. H., Lisowski, M., and King, N. E. (1981), Strain Accumulation in Southern-California, 1973-1980, *Journal of Geophysical Research*, *86*, 6991-7001.

Savage, J. C., Equivalent strike-slip earthquake cycles in half-space and lithosphere-asthenosphere earth models, J. Geophys. Res., 95, 4873–4879, 1990.

Savage, J. C., and Lisowski, M. (1993), Inferred Depth of Creep on the Hayward Fault, Central California, *Journal of Geophysical Research-Solid Earth*, *98*, 787-793.

Schmidt, D. A., Burgmann, R., Nadeau, R. M., and d'Alessio, M. (2005), Distribution of aseismic slip rate on the Hayward fault inferred from seismic and geodetic data, *J. Geophys. Res., 110*, B08406, doi:10.1029/2004JB003397.

Scholz, C. H. (2000), Evidence for a strong San Andreas fault, *Geology*, *28*, 163-166.

Schulz, S. S., G. M. Mavko, R. O. Burford and W. D. Stuart (1982), Long-Term Fault Creep Observations in Central California, *Journal of Geophysical Research*, *87*, 6977-6982.

Segall, P. (2002), Integrating geologic and geodetic estimates of slip rate on the San Andreas fault system, *International Geology Review*, *44*, 62-82.

Shearer, P. M., Prieto, G. A., and Hauksson, E. (2006), Comprehensive analysis of earthquake source spectra in southern California, *J. Geophys. Res., 111*, B06303, doi:10.1029/2005JB003979.

Sieh, K. E. and Williams, P. L. (1990), Behavior of the Southernmost San-Andreas Fault during the Past 300 Years, *Journal of Geophysical Research-Solid Earth and Planets*, *95*, 6629-6645.

Smith, B. and Sandwell, D. (2003), Coulomb stress accumulation along the San Andreas Fault system, *J. Geophys. Res., 108*, 2296, doi:10.1029/2002JB002136.

Smith, B. R. and Sandwell, D. T. (2006), A model of the earthquake cycle along the San Andreas Fault System for the past 1000 years, *J. Geophys. Res., 111*, B01405, doi:10.1029/2005JB003703.

Smith-Konter, B., Solis, T., and Sandwell, D.T. (2008), Data-derived stress uncertainties of the San Andreas Fault System, EOS Trans. AGU, 89 (53), Fall Meet. Suppl., U51B-0029.

Wei, M. and Sandwell, D. T. (2009). A silent Mw 4.7 slip event of October 2006 on the Superstition Hills fault, southern California. *Journal of Geophysical Research*, 114, B07402.

Wisely, B. A., and Schmidt., D. A. (2008). Appendix P: Compilation of Surface Creep on California Faults and Comparison of WGCEP 2007 Deformation Model to Pacific-North American Plate Motion. *USGS Open File Report*, 2007-1437p.

Zoback, M. D. (2000), Earth science - Strength of the San Andreas, *Nature*, *405*, 31-32.

5. CHAPTER 5: Decorrelation of L-band and C-band interferometry over vegetated areas in California

Earthquake Safety tip 5

A doorway is the safest place to be during a quake. Eat, sleep and work in doorways.

5.1 Abstract

Temporal decorrelation is one of the main limitations for recovering interseismic deformation along the San Andreas Fault system using interferometric Synthetic Aperture Radar. To assess the improved correlation properties of L-band with respect to C-band, we analyzed L-band ALOS interferograms with a range of temporal and spatial baselines over three vegetated areas in California and compared them with corresponding C-band ERS interferograms. Over the highly vegetated Northern California forests in the Coast Range area, ALOS remains remarkably well correlated over a two-year period, while an ERS interferogram with a similar temporal and spatial baseline lost correlation. In Central California near Parkfield, we found a similar pattern in decorrelation behavior, which enabled the recovery of a fault creep and a local uplifting signal at L-band that was not apparent at C-band. In the Imperial Valley of Southern California, both ALOS and ERS have low correlation over farmlands. ALOS has lower correlation over some sandy surfaces than ERS, probably due to low signal-to-noise ratio. In general L-band interferograms with similar seasonal acquisitions have higher correlation than those with dissimilar season. For both L- and C-band, correlation over vegetated areas decreases with time for intervals

less than 1 year and then remains relatively constant at longer time intervals. L-band has a decorrelation time of more than 2 years in the forest in California while C-band less than 6 months. Overall these results suggest that L-band interferograms will reveal near-fault interseismic deformation once sufficient data become available.

5.2 Introduction

Interferometric Synthetic Aperture Radar (InSAR) has become an important tool for measuring slow surface deformation associated with natural hazards such as earthquakes and volcanoes [*Massonnet and Feigl*, 1998; *Burgmann et al.,* 2000, *Rosen et al.,* 2000]. One of the main limitations of the InSAR technique is temporal decorrelation due to surface change, especially in vegetated areas, because the low correlation prevents the recovery of the phase measurement. The Advanced Land Observation Satellite (ALOS) launched by the Japanese Aerospace Exploration Agency (JAXA) in January 2006 uses a longer-wavelength, L-band 236 mm, compared to the C-band radars 56 mm (ERS, Radarsat, and Envisat), which should enable coherent phase recovery over much longer time intervals in vegetated areas [*Zebker and Villasenor*, 1992; *Rosen et al.,* 1996; *Sandwell et al.,* 2008], such as the creeping section of the San Andreas Fault (SAF). Key parameters of ALOS and ERS satellites are listed in Table 1. Although previous theoretical and limited experimental studies suggest this advantage of the longer wavelength SAR over vegetated areas, here we perform a more extensive and quantitative analysis using ALOS and ERS data over a variety of surfaces, temporal baselines, and spatial baselines. Our main objective is to provide a quantitative measure

of temporal decorrelation at L- and C-band. Our results provide insights and suggestions for future SAR mission such as the U.S. satellite DESDynl, Japanese satellite ALOS2, and German satellite TanDEM-L.

Table 5-1. Comparison of satellites.

	ERS	ALOS
Wavelength	56 mm	236 mm
Altitude	790 km	700 km
Look angle*	23 degrees	34.3 degrees
Bandwidth	15.55 MHz	FBS: 28 MHz FBD: 14 MHz
Critical Baseline	1.1 km	FBS: 13 km FBD: 6.5 km

***Other look angles are available for ALOS, but 34.3 degrees is the main one.**

Correlation, or sometimes called coherence, is a measure of the similarity of the phase of two synthetic aperture radar images. Theoretically, correlation ranges between [0,1], where 0 denotes no correlation and 1 corresponds to perfect correlation. In practice, a number of pixels are weighed to estimate the correlation [*Touzi et al.,* 1999]. In our case, correlation is measured from 49 independent pixels, equivalent to 7 looks in each direction [*Burgmann et al.,* 2000], and the detectable correlation is slightly different with the minimum being 0.12 and the maximum being 0.96 in our calculation. A correlation of 0.5 marks a signal to noise ratio of 1 in linear scale [*Bendat and Piersol*, 2000]. As shown in previous studies [*Sandwell et al*., 2008] and in our study, there is a critical range of correlation between 0.15 and 0.20 that determines whether an interferogram is usable. When the correlation is larger than 0.25, phase information can be retrieved, when correlation is between 0.2-0.25, it is possible but hard to retrieve

some phase information, and when the correlation is below 0.15 no phase information can be retrieved. Please note that this means, if no other decorrelation effects are relevant, one doesn't need SNR greater than 1 in linear scale to get useful phase information, as correlation of 0.25 corresponds to a SNR of 1/3 in linear scale. Generally, high correlation (> 0.25) is expected in areas where the surface condition doesn't change much with time, such as in urban areas, and low correlation is expected where vegetation is present. Techniques such as permanent scatters can be used to extract phase information in areas where a few local stable reflection points are imbedded in an area of generally low correlation [*Ferretti et al.,* 2001]. Correlation is also important for topography measurements [*Hoen and Zebker*, 2000]. In this paper, we analyzed L-band ALOS interferograms over three vegetated areas in California and compared them with corresponding C-band ERS interferograms. Our results are consistent with previous suggestion that L-band has higher correlation over vegetated areas than C-band and correlation depends on the type of surface.

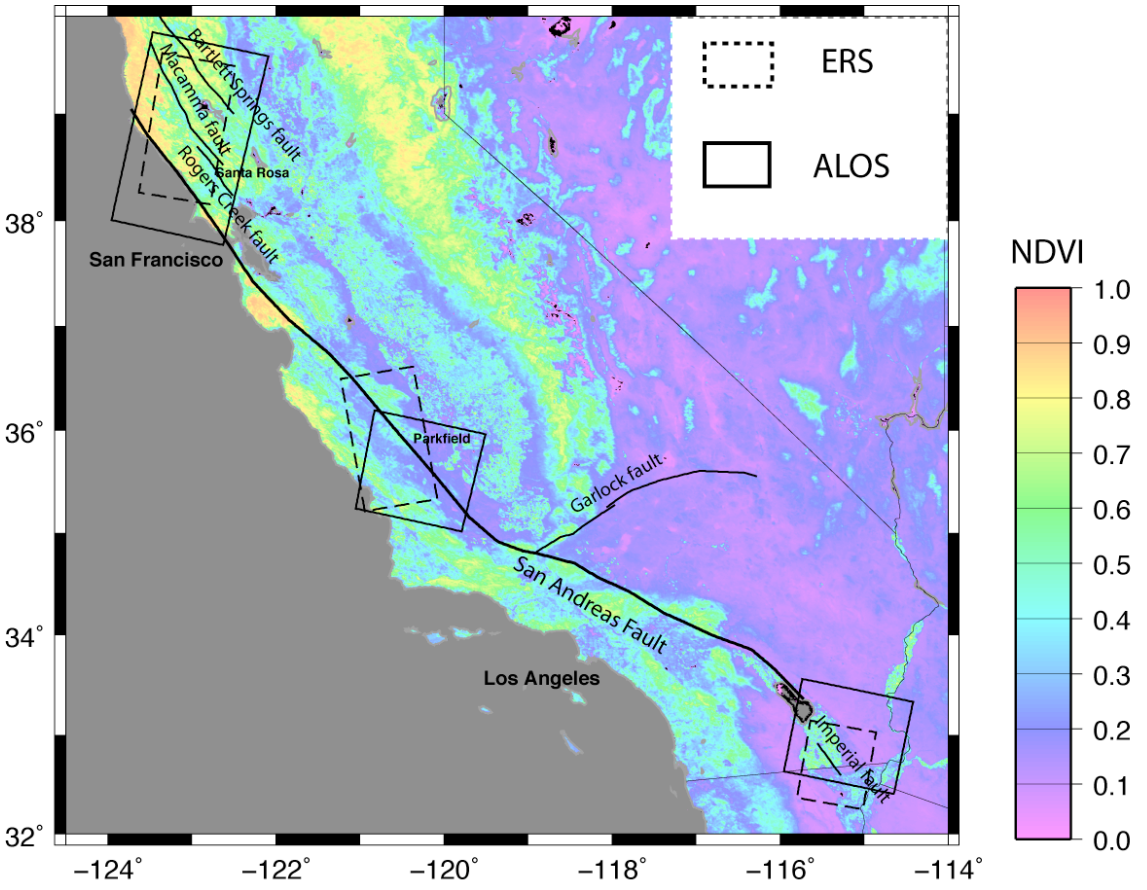

Figure 5-1. Three research areas in California: (1) the Coast Ranges of northwestern California, (2) the creeping section of the San Andreas Fault near Parkfield in Central California, and (3) the Imperial Valley in Southern California. The color background indicates Normalized Difference Vegetation Index (NDVI) acquired by MODIS satellite in October 2006. The purple background means no or little vegetation while the green means high vegetation. The solid lines show the main fault traces. The solid and dashed boxes show the coverage of InSAR images used in this study.

5.3 Theory

Most InSAR satellites are designed as repeat-pass, which means a single radar acquires images of the same area at two different times, usually with a repeat time of 10-50 days. The detailed theory and mathematical derivation of correlation can be found in several previous studies [*Hoen and Zebker*, 2000; *Rosen et al.,* 2000]. We present the

relevant equations here. Assume pixels of the complex radar images for first and second acquisition are

$$\begin{aligned} s_1 &= c + n_1 \\ s_2 &= c + n_2 \end{aligned} \qquad (1)$$

where c is correlated part of the signal and n_1 and n_2 are the uncorrelated noise caused by baseline, temporal, thermal, rotation, and other unknown factors.

One measure of the correlation between two images is:

$$\gamma = \frac{\left|\left\langle s_1 s_2^* \right\rangle\right|}{\sqrt{\left\langle s_1 s_1^* \right\rangle \left\langle s_2 s_2^* \right\rangle}} \qquad (2)$$

where $s*$ is the complex conjugate of s and $\langle \bullet \rangle$ denotes ensemble average. When the two radar images are exactly the same, correlation equals one and when they are completely different, the correlation approaches zero. The total correlation mainly consists of three parts, thermal decorrelation $\gamma_{thermal}$, baseline $\gamma_{baseline}$, and temporal $\gamma_{temporal}$ decorrelation [*Zekber and Villasenor,* 1992; *Rosen et al.*, 1996; *Hoen and Zebker*, 2000].

$$\gamma = \gamma_{thermal}\gamma_{spatial}\gamma_{temporal} \qquad (3)$$

where γ is total correlation. The thermal decorrelation is related to the signal-to-noise ratio of the radar signal as,

$$\gamma_{thermal} = \frac{1}{1 + SNR^{-1}}$$

In most cases, the SNR ratio for ERS and ALOS is high enough to ignore this effect in correlation [*Hoen and Zebker*, 2000]. Exceptions include special cases such as L-band over sandy surface where the SNR is significant lower [*Rosen et al.,* 2000]. The spatial decorrelation is caused by the non-zero perpendicular baseline between the reference and repeat images [*Li and Goldstein*, 1990; *Rodriguez and Martin*, 1992; *Zebker and Villasenor*, 1992; *Hajnsek et al.,* 2009]. There are two effects of spatial decorrelation, volumetric and surface decorrelation. For area with high penetrating, such as pine forests [*Garestier et al.,* 2008] and ice [*Langley et al.,* 2007], volume decorrelation dominants. However in our case, no significant volume decorrelation is observed, so we only consider spatial decorrelation related to surface scatters. There are two ways to estimate the spatial decorrelation. One is using a range spectral filter [*Gatelli et al.,* 1994] and the other way is using the following model [*Zebker and Villasenor*, 1992]. If the satellite has a perpendicular baseline of *B*, the baseline correlation between the two radar images is

$$\gamma_{baseline} = 1 - \frac{2 \mid B \mid R_y \cos^2(\theta - \alpha)}{\lambda \rho} \qquad (4)$$

where R_y is the range resolution, θ is the incidence angle, α is the local surface slope in

range direction, λ is the wavelength, and ρ is the distance between the satellite sensor and the target on surface. This equation is used to isolate the temporal decorrelation from the measured decorrelation in the following analysis. When correcting spatial decorrelation using this equation, we need to make sure that no band-pass filtering is done during the processing. The temporal decorrelation is caused by surface changes between the two acquisitions. Generally, temporal decorrelation increases with the amount of vegetation cover because the scatters on the plants change with time [*Rosen et al.*, 1996]. With sufficiently high SNR and low volumetric decorrelation, temporal decorrelation can be isolated after removing the spatial decorrelation.

5.4 Data and Method

To compare the correlation of interferograms of ERS and ALOS, we processed interferograms over three vegetated areas in California (Figure 1): (1) the Coast Ranges of northwestern California, (2) the creeping section of the San Andreas Fault near Parkfield in Central California, and (3) the Imperial Valley in Southern California. The ERS data was provided by the European Space Agency and obtained through the Western North America Interfeometric Synthetic Aperture Radar Consortium (WINSAR) archive. ALOS data was provided by JAXA and obtained through Alaska Satellite Facility as well as the ALOS User Interface Gateway (AUIG).

Since ALOS has limited acquisition in California and the baseline has been drifting by more than 10 km after launch, although the baseline is controlled within 3 km tube after early 2008, we found only one interferogram in each area that was suitable for

direct comparison (Table 2). To focus on temporal decorrelation we search for long time intervals (>10 months) and short baselines (< 200 m for ERS; < 2 km for ALOS). Since the number of ALOS acquisitions is much smaller than the number of ERS acquisitions, we first selected the best ALOS interferogram and found an ERS interferogram with corresponding baseline, time interval, and season(s). Even within a single interferogram, the correlation can be highly spatially variable depending on the type of surface and degree of vegetation. So we selected several corresponding sub-areas within the overlapping ALOS and ERS frames corresponding to no vegetation, light vegetation, and heavy vegetation. The size of the patches were small enough to cover one particular kind of surface but large enough to provide meaningful statistics; the chosen patch size (lengths/widths of a rectangle) varies from 3 km to 7 km depending on the surface condition.

The Normalized Difference Vegetation Index (NDVI) provides an overview of the vegetation along the San Andreas Fault system (Figure 1). The NDVI data was collected by MODIS satellite and obtained through NASA WIST website. The NDVI indicates the concentrations of green leaf vegetation quantitatively. Although many possible perturbing factors exist, the NDVI can be used to identify the surface vegetation. Comparing the NDVI with the correlation in Figures 2-4, we observe that when the NDVI is less than 0.3, both ERS and ALOS interferograms have high correlation.

All interferograms are processed following standard procedure of InSAR processing using SIOSAR software [*Wei et al.,* 2009]. SRTM data [*Farr et al.,* 2007] were used to remove the topographic effect from the single-look complex interferograms prior to ensemble averaging. All interferograms were ensemble averaged using a

Gaussian filter with a 0.5 gain at 100 m wavelength before computing the phase and correlation, which is equivalent to 7 looks in more popular InSAR processors such as ROI-PAC [*Burgmann et al.,* 2000]. Based on this filter width, we find the minimum detectable correlation is 0.12 based on ocean data where the correlation should be zero.

Table 5-2. Interferograms used for direct compare correlation.

	intf	1st_date	2nd_date	dt (days)	Baseline (m)	Correlation				
Northern California						Heavy Vegetated Mountain	Light Vegetated Mountain	Urban		
ALOS T549F2830	4357_15093 (FBS-FBS)	11/18/06	11/23/08	736	252	0.35	0.27	0.35		
ERS T113F2817/2835	e1_22646_e2_13995	11/13/95	12/23/97	770	110	0.14	0.13	0.23		
Creeping Section of the SAF						Mountain 1	Mountain 2	Urban		
ALOS T220F700	5969_16705 (FBS-FBS)	3/9/07	3/14/09	735	905	0.25	0.28	0.34		
ERS T256F2889	e2_05621_e2_17144	5/17/96	7/31/98	804	68	0.14	0.25	0.24		
Imperial fault						light cultivation area	Heavy cultivation area	desert 1	desert 2	urban
ALOS T532F2960	4167_14903 (FBS-FBS)	11/5/06	11/10/08	736	17	0.16	0.13	0.30	0.17	0.53
ERS T84F2943	e2_03445_e2_12463	12/17/95	9/7/97	629	55	0.15	0.14	0.34	0.46	0.28

5.5 Result

The correlation results for the three areas are shown in Figures 2, 3 and 4 along with the local NVDI and topography. Although the value of correlation can theoretically range between 0 (uncorrelated) to 1 (perfectly correlated), our analysis is focused on the range of 0.15 to 0.25. In all three areas, ALOS remains correlated over longer time intervals than ERS does over vegetated area. In urban areas, ALOS tends to have higher correlation. In farmlands, neither ALOS nor ERS has high correlation because of the cultivation activity. However, the details are different for each area.

1) *The Coast Ranges of Northwestern California*. Major faults in this area

include the San Andreas Fault, the Maacama fault, the Rodgers Creek fault, and the Bartlett Spring fault. This area is studied less extensively than the other two areas because it is far from major cities and is in mainly mountainous area. Limited previous studies used GPS (13) and creepmeter (14) measurements. Because of this sparse geodetic coverage, the contribution to our understanding of these fault systems from ALOS could be significant. Over 90% of the area is covered with trees except the farmlands and urban areas near the city of Santa Rosa. To compare the correlation of ALOS and ERS, two interferograms are selected (Table 2). The ALOS interferogram has a two-year November-to-November time interval and a perpendicular baseline of 252 m. The ERS interferogram has a two-year November-to-December time interval and a perpendicular baseline of 110 m. As Figure 2 shows, the ALOS interferogram has high correlation (> 0.27) over most of the land area, while ERS interferogram has generally low correlation except the urban area near Santa Rosa. The values of correlation for the three sub areas are provided in Table 2. The ALOS interferogram has better correlation not only in the vegetated areas but also in the urban areas.

2) *The creeping section of the San Andreas Fault near Parkfield in central California*. This area is particularly scientifically interesting because of its regular pattern of magnitude 5-6 earthquakes and a transition from creeping in the northern section to locked fault in the southern section [*Johanson and Burgmann*, 2005; *Titus et al.*, 2006]. Previous studies show that InSAR can measure the continuous slip distribution and magnitude of fault motion along the SAF [*Wei et al.*, 2009]. However, because of the temporal decorrelation, the previous C-band interferograms can't provide a long time (> 2 years) measurement of deformation in this area [*Rosen et al.*, 1998]. The

two interferograms we chose for direct comparison are: an ALOS interferogram with a two-year March-to-March time interval and a perpendicular baseline of 905 m; and an ERS interferogram with a two-year May-to-July time interval and a perpendicular baseline of 68 m (Table 2). As shown in Figure 3, ERS has generally low correlation over the vegetated mountains while ALOS is generally well correlated. The detailed comparison of correlation over different surface is provided in Table 2. One important feature of the ALOS phase is that there is a correlation between residual phase and topography. The large-scale (> 5 km) residual is probably due to atmospheric error while the small-scale (< 1 km) residual is probably due to either DEM error or small mis-registration between topography and interferogram.

3) *The Imperial Valley in Southeastern California*. The Imperial Valley between the Colorado River and the Salton Sea contains some of the most seismically active faults along the SAF system including those with well-documented instances of surface rupture and triggered slip [*Wei et al.*, 2009]. Much of the Imperial Fault is covered by farmlands, which makes it difficult to measure interseismic deformation using InSAR, although clear signs of slip such as cracks on roads are observed [*Lyons et al.,* 2002]. The interferograms selected for direct comparison are: an ALOS interferogram with a two-year November-to-November time interval and a perpendicular baseline of 17 m; and an ERS interferogram with a two-year December-to-September time interval and a perpendicular baseline of 55 m (Table 2). As shown in Figure 4, both ALOS and ERS have generally low correlation over the farmlands. A detailed comparison of correlation over a variety of surfaces is provided in Table 2. ALOS has higher correlation over urban areas while the ERS has higher correlation over the sandy surface to the east of the

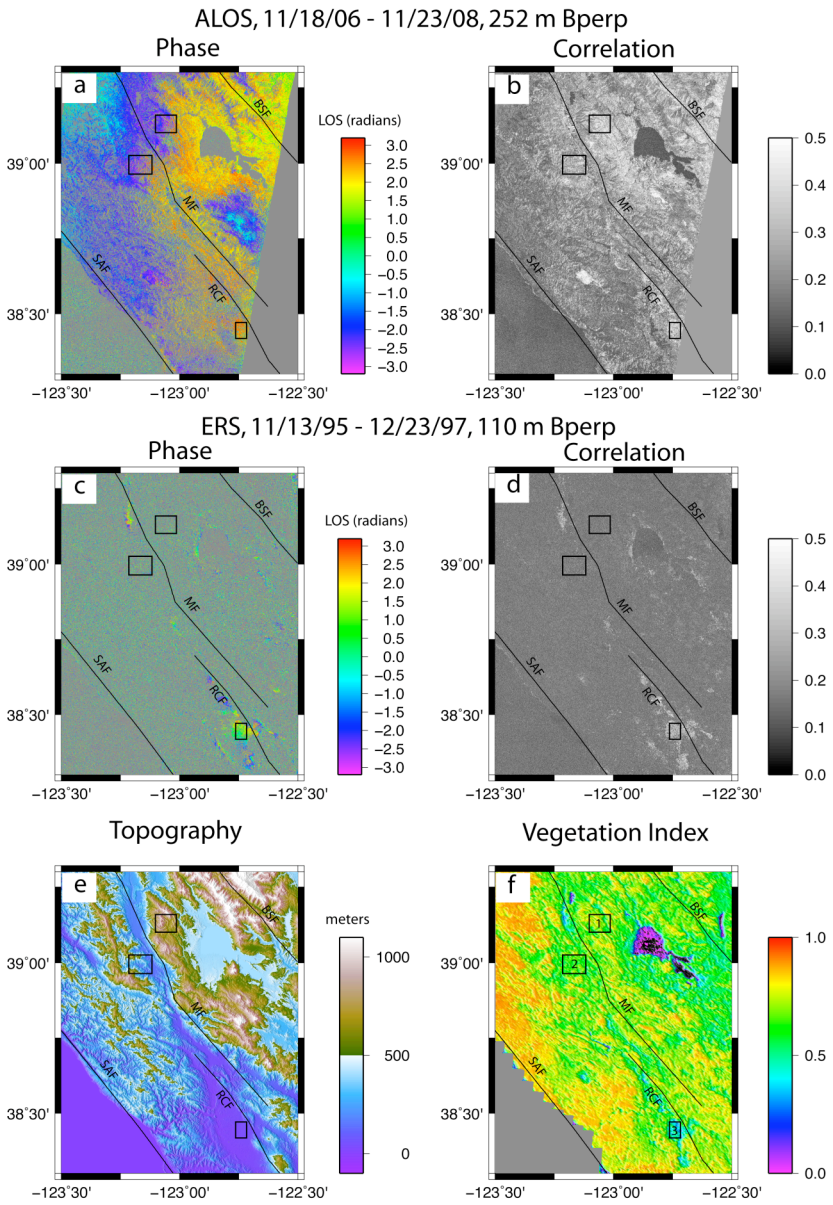

Figure 5-2. Comparison between ERS and ALOS interferograms in the Coast Range area in Northern California. The details of the interferograms are shown in table 2. The solid lines are the major faults in this area. Fault names are abbreviated as follows: SAF, San Andreas Fault; MF, Maacama Fault; RCF, Rogers Creek Fault; BSF, Bartlett Springs Fault. The boxes are the areas that correlation is extracted in table 2, 3 and figure 5. The box number in (f) indicates the corresponding areas in figure 5: (1) Vegetated mountain 1; (2) Vegetated mountain 2; (3) Urban areas. The phase images are masked based on the correlation (< 0.15 is masked out). White in (b) and (d) means high correlation while black means low correlation. The red and green in (f) means high vegetation while purple means low vegetation.

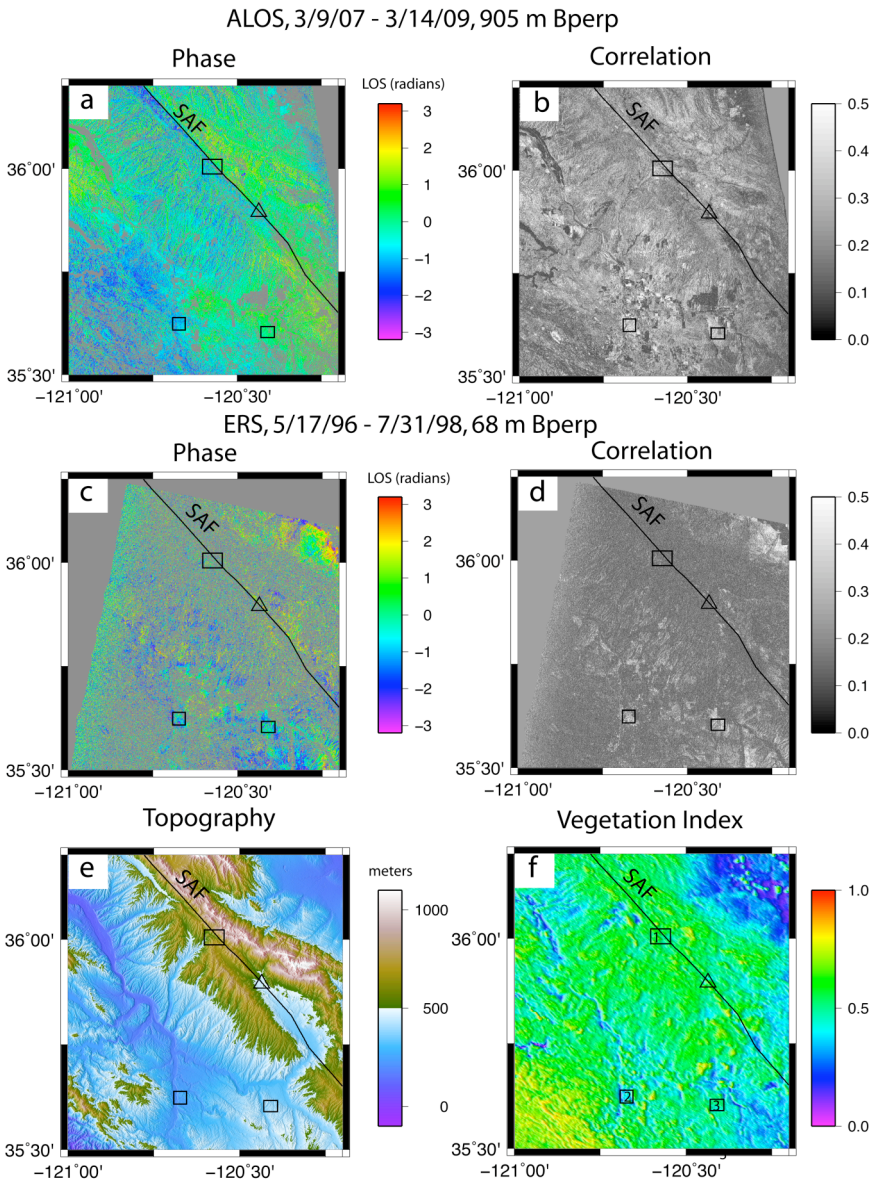

Figure 5-3. Comparison between ERS and ALOS interferograms near Parkfield in Central California. The details of the interferograms are shown in table 2. The solid line is the fault trace of the San Andreas Fault in this area. The triangle is the city of Parkfield. The boxes are the areas that correlation is extracted in table 2 and 3 and figure 6. The box number in (f) indicates the corresponding areas in figure 6: (1) Vegetated mountain 1; (2) Vegetated mountain 2; (3) Urban areas. The phase images are masked based on the correlation (< 0.15 is masked out).

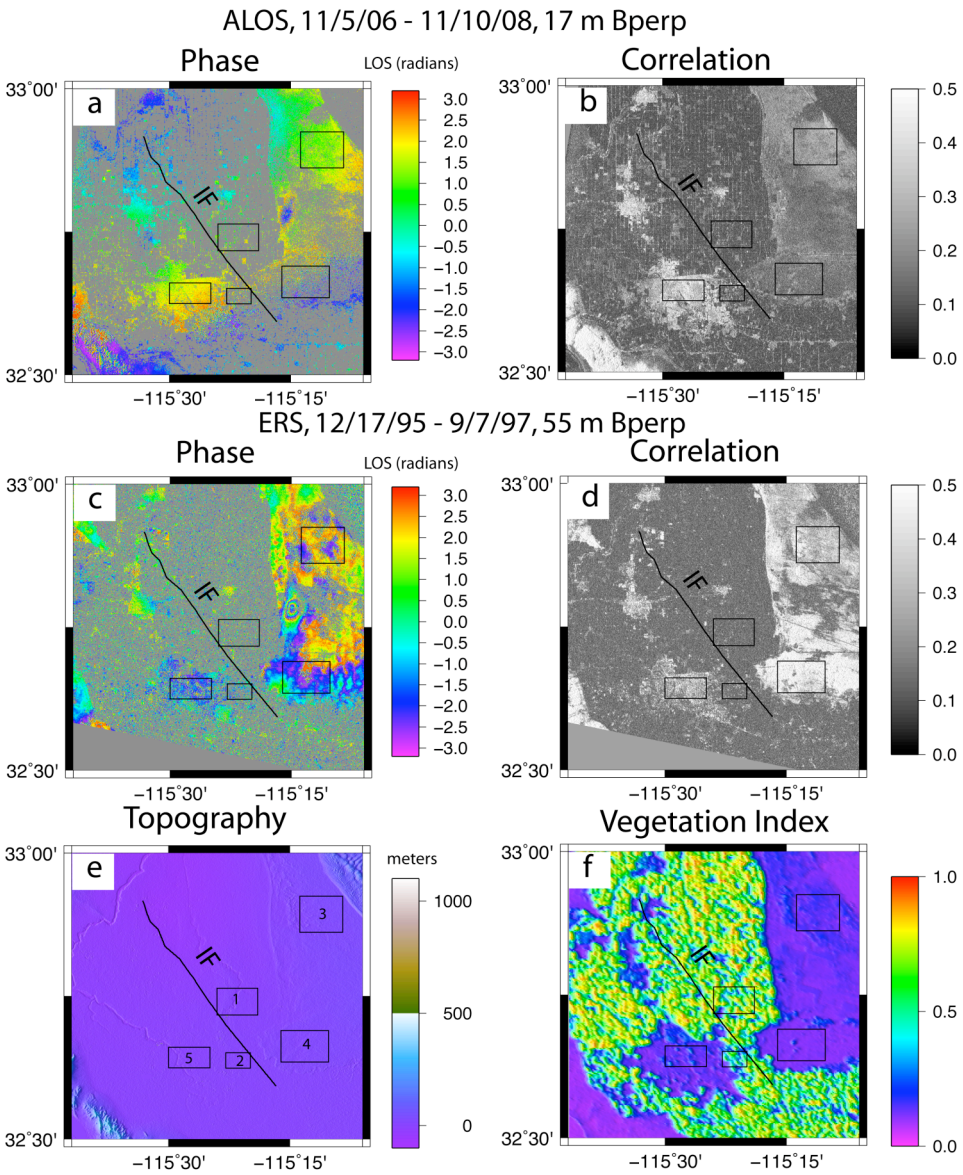

Figure 5-4. Comparison between ERS and ALOS interferograms in Imperial Valley in Southern California. The details of the interferograms are shown in table 2. The solid line is the fault trace of the Imperial Fault. The boxes in (e) are the areas that correlation is extracted in figure 7. The phase changing area in the middle right on both phase images are due to subsidence caused by underground water extraction. The box number in f indicates the corresponding areas in figure 7: (1) Light cultivation; (2) Heavy cultivation; (3) desert 1; (4) desert 2; (5) Urban areas. The phase images are masked based on the correlation (< 0.15 is masked out).

valley, probably due to low SNR for L-band over sandy surface. Although ALOS is decorrelated over the irrigated farmlands, the correlation remains high on some roads between farmlands; this makes it possible to recover some deformation signal across the Imperial Fault. We also note that the correlation over farmlands in the US (northern side of the US-Mexico border) is generally higher than the correlation in Mexico (southern side). This could be due to differences in cultivation methods of these different countries.

5.6 Spatial and Temporal decorrelation

To focus on the seasonal effect of the correlation, we processed data acquired during various seasons and analyzed the result for both ALOS and ERS. As expected, the interferograms with similar season for both acquisitions have better correlation compared with those with dissimilar seasons. However, we don't have enough data spanning all the seasons to identify a preferred season.

To focus on the temporal decorrelation and its relationship to surface type, we processed interferograms and chose four surface types including urban area, mountain, farmlands, and sandy area. For each interferogram, we extracted the mean and standard deviation of correlation in small sub areas (3 km - 7 km in lengths/widths). Since baseline decorrelation is related to the slope of the surface, we selected these areas to be as flat as possible except in mountainous areas. We included the local slope effect when we estimated the baseline decorrelation. With sufficiently high SNR and low volumetric decorrelation, we isolated temporal decorrelation after removing the spatial decorrelation (Figures 5, 6, 7). To check whether volumetric decorrelation exists, we plotted the spatial corrected correlation versus perpendicular baseline. We also plotted the temporal correlation versus time interval. The boundary between partial (>0.2) and poor (<0.15)

correlation is highlighted in Figure 5-7 in grey lines.

For the ERS cases, the spatial corrected correlation doesn't change much with spatial baseline over all the surface types in the three areas, which means spatial decorrelation correction works well and confirms our assumption of low volume decorrelation for C-band. A high correlation anomaly for ERS exists in the creeping section (see left panel in Figure 6) might simply due to short time interval (35 days). The correlation over vegetation decreases with time when the time interval is less than 6 months in both Central California and Southern California (see Figure 6-7) and becomes uniform for intervals greater than 1 year. In Northern California (see Figure 5), all samples over forests are below critical line and the minimum time interval of the sample is 6 months. In the urban area, the correlation stays above the critical line and shows the buildings are good stable scatters.

For the ALOS cases, no volumetric decorrelation is observed. Although Figure 5 shows decreasing trends of correlation with increasing baseline in the northern California case, this might be due to season effect more than volumetric. All the pairs with low correlation cover the winter season. In Northern California and Central California, correlation over vegetation decreases with time when time interval is less than 1 year. For time intervals greater than 1 year, the correlation remains constant and sometimes increases with time interval. In Northern California, one interferogram with two-year interval has higher correlation than several interferograms with only 2-3 months interval over vegetation. This illustrates the scattered nature of the temporal effects perhaps due to rainfall and soil moisture. The ability of ALOS to remain correlated above the 0.2 threshold for multi-year intervals is critical for measuring slow

interseismic deformation, which ranges from several mm/year to cm/year. Indeed as more short-baseline ALOS interferograms become available over the next few years, we expect that ALOS will become the primary tool for resolving the near-fault interseismic strain rate that is not resolved by the relatively sparse (~10 km) GPS measurements.

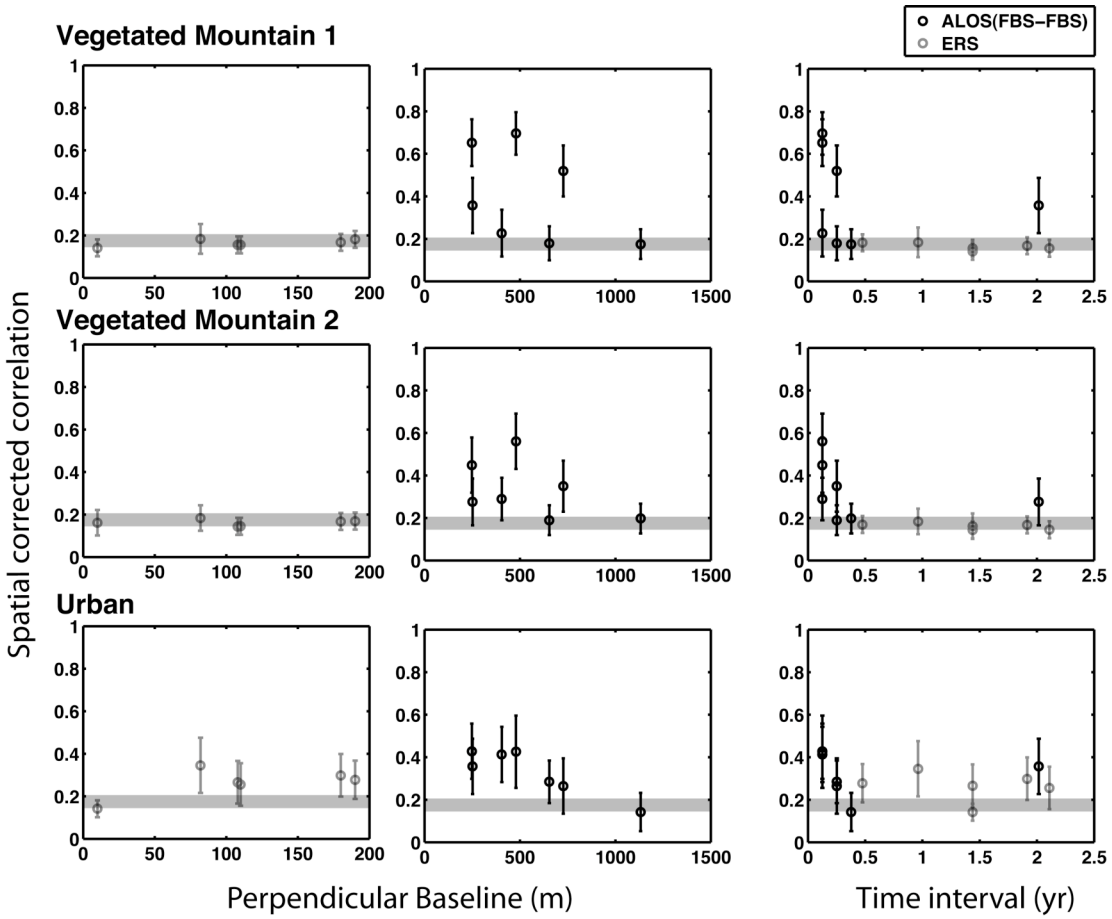

Figure 5-5. Spatial corrected correlation changes with baseline and time on three types of surface in the Coast Range area in Northern California. All ALOS data is FBS-FBS mode. The horizontal grey line labels the range 0.15-0.2 correlation. Data above the grey line is well correlated and almost all the phase information can be used. Data in the grey line is partially correlated and it is possible to retrieve some phase information. Data below the grey line is decorrelated and no phase information can be retrieved. Each row shows data over the same area. Each column shows data with same kind but in different areas.

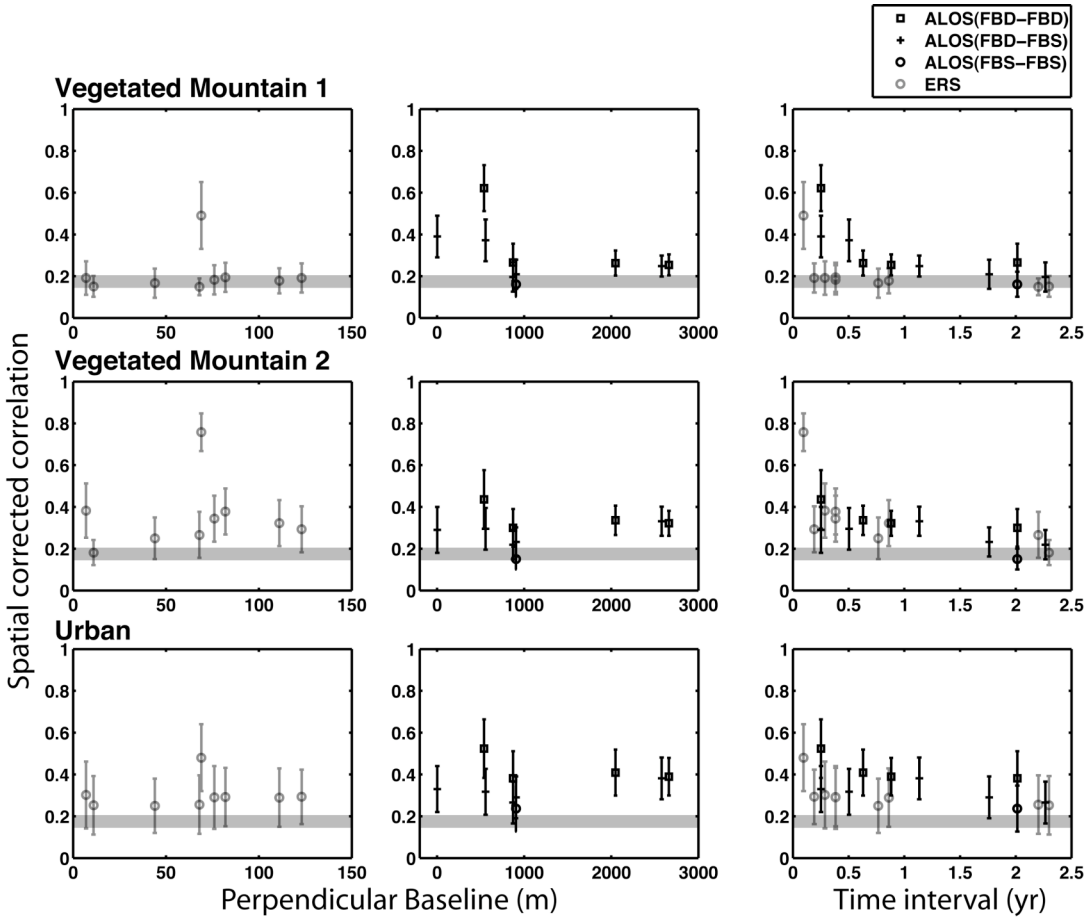

Figure 5-6. Spatial corrected correlation changes with baseline and time on three types of surface near Parkfield in Central California. ALOS data is either same mode or mix mode, e.g. FBS-FBD or FBD-FBS. The horizontal grey line labels the range 0.15-0.2 correlation.

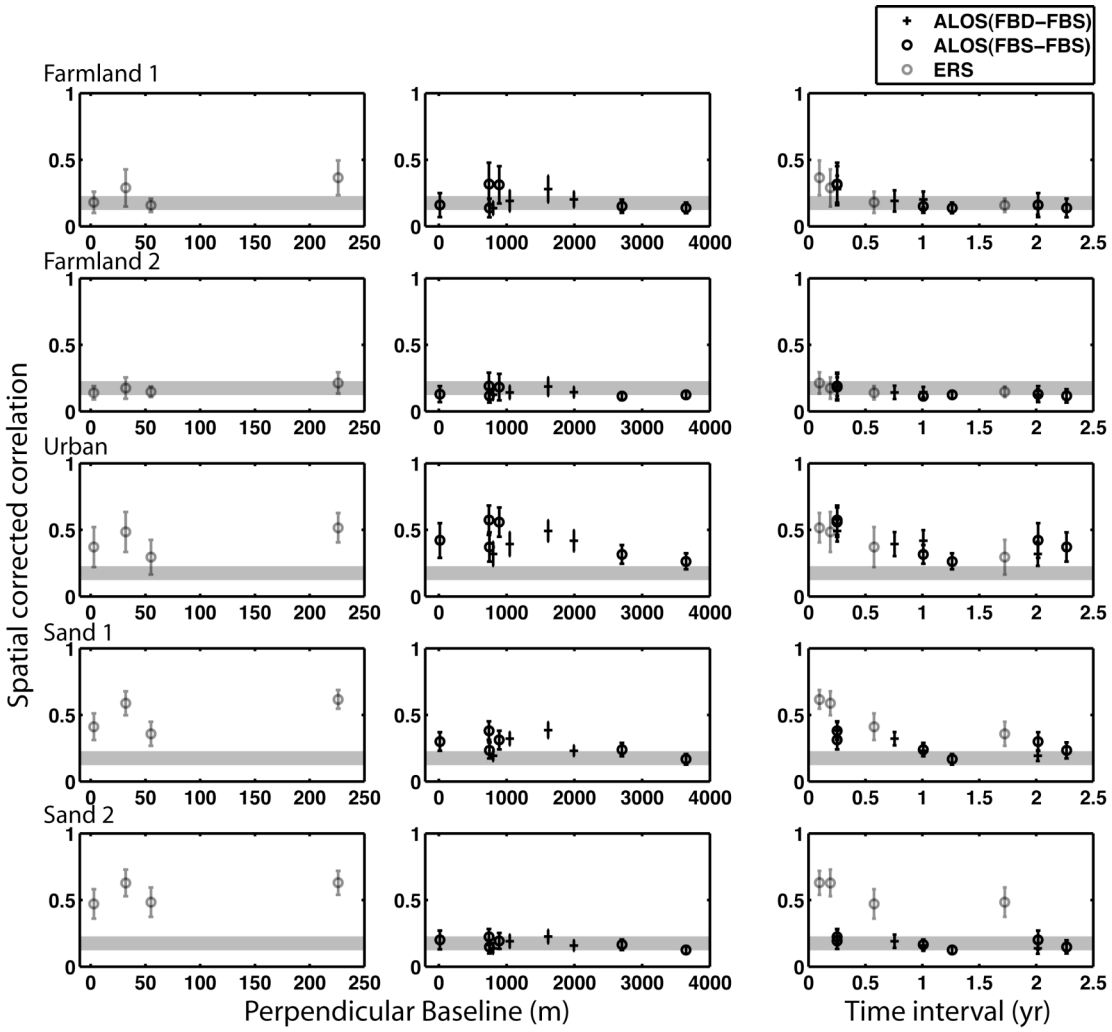

Figure 5-7. Spatial corrected correlation changes with baseline and time on five types of surface in the Imperial Valley in Southern California. ALOS data is either FBS-FBS mode or mix mode, e.g. FBS-FBD or FBD-FBS. The horizontal grey line labels the range 0.15-0.2 correlation.

One feature of ALOS is that it is operated at two different range resolutions (i.e. 1/radar bandwith). The fine-beam single polarization (FBS-HH, 28-MHz bandwidth) has 2 times better range resolution than ERS and the fine-beam dual polarization (FBD-HH and HV, 14 MHz) has the same range resolution than ERS. ALOS interferograms can be made between either same modes or mix modes although conversion from FBD

to FBS is required. In some cases the correlation of FBS-FBS interferograms, was slightly higher than that of mixed-mode interferograms, i.e. FBD-FBS. For example, in Figure 7, FBS-FBS interferograms with time interval longer than 6 months have significantly higher correlation than the mix-mode interferograms, especially in the urban area. However, there is not much difference for interferograms with FBD-FBD compared to mix-mode interfergrams in Central California. This probably is due to the fact that FBS has higher resolution than FBD.

As figure 7 shows, ALOS has lower correlation than ERS over some sandy areas. This has been observed before by *Rosen et al.* [2000]. This is likely due to the low SNR for L-band over sandy area. We checked the amplitude image of the data, which confirm this idea. In addition, both ALOS and ERS lost coherence over farmlands in the Imperial Valley within 6 months, which shows L-band has no advantage over C-band over farmlands. However, we notice that L-band stay well correlated on the roads between farmlands while C-band lost coherence. With sufficient dataset, it is possible to extract deformation data across the fault using the phase recovered on the roads in ALOS.

5.7 Conclusions

In conclusion, correlation decreases with time especially for intervals between 0 and 1 year. The decorrelation time for ALOS is more than 2 years while ERS less than 6 months. Seasonal effects are also important. We also found in some cases, for example, in the desert and urban areas in the Imperial Valley (Figure 7), that the correlation of FBS-FBS interferograms was slightly better than that of mix-mode interferograms (i.e.

FBD-FBS) and FBD-FBD, probably due to higher resolution of FBS.

The conclusions for each of the three areas are as follows: (1) In the highly vegetated Northern California forests of the Coast Range area, ALOS remained remarkably well correlated over a two-year winter-to-winter interferogram (~0.27), while an ERS interferogram with a similar temporal and spatial baseline was below the threshold correlation (<0.13). (2) In central California near Parkfield, we found similar pattern. Four ALOS interferograms with a two-year temporal baseline all had adequate correlation (0.16-0.25) over vegetated mountain areas, while the ERS interferogram had inadequate correlation (0.13-0.16). This improvement in correlation at L-band revealed creep and a local uplifting along the San Andreas Fault that was not apparent at C-band (Figure 3). (3) In the Imperial Valley of Southern California, ALOS had higher correlation in both the urban area (0.4 versus 0.3) and lightly irrigated area (0.18 versus 0.16). However, it had lower correlation over some sandy surfaces (0.2 versus 0.4).

Overall these results demonstrate that ALOS remains correlated much longer than ERS over forest areas but not farmlands in California. To date the primary limitation for using ALOS for recovering interseismic strain along the San Andreas Fault is that there are too few acquisitions along the descending passes, which have better geometry for measuring strike-slip motion. Nevertheless the archive of ALOS images from ascending passes is growing rapidly and they will be important for constraining the vertical motions along the fault system. We look forward to the more systematic L-band observations from ALOS-2 (2014 launch), DESDynI (2016-2020 launch), and German satellite TanDEM-L (TBD).

Table 5-3. Interferograms used in this research.

	intferograms	Frist_date	Second_date	dt (days)	Baseline (m)	Correlation				
Northern California (Maacama fault)						Urban	Heavy Vegetated Mountain	Light Vegetated Mountain		
ALOS T549F2830	4357_15093 (FBS-FBS)	11/18/06	11/23/08	736	252	0.35	0.35	0.27		
	8383_9054 (FBS-FBS)	8/21/07	10/6/07	46	479	0.41	0.67	0.54		
	8383_9725 (FBS-FBS)	8/21/07	11/21/07	92	727	0.25	0.49	0.33		
	8383_10396 (FBS-FBS)	8/21/07	1/6/08	138	1132	0.13	0.16	0.18		
	9054_9725 (FBS-FBS)	10/6/07	11/21/07	46	248	0.42	0.64	0.44		
	9054_10396 (FBS-FBS)	10/6/07	1/6/08	92	654	0.27	0.17	0.18		
	9725_10396 (FBS-FBS)	11/21/07	1/6/08	46	405	0.40	0.22	0.28		
ERS T113F2817/2835	e1_21644_e2_06981	9/4/95	8/20/96	351	82	0.32	0.17	0.17		
	e1_21644_e2_09486	9/4/95	2/11/97	525	108	0.24	0.14	0.13		
	e1_22646_e2_13995	11/13/95	12/23/97	770	110	0.23	0.14	0.13		
	e2_06981_e2_09486	8/20/96	2/11/97	174	190	0.23	0.15	0.14		
	e2_06981_e2_17001	8/20/96	7/21/98	699	180	0.25	0.14	0.14		
	e2_09486_e2_17001	2/11/97	7/21/98	525	10	0.14	0.14	0.16		
Creeping Section of the SAF						Mountain 1	Mountain 2	Urban		
ALOS T220F700	7311_8653 (FBD-FBD)	6/9/07	9/9/07	92	540	0.57	0.40	0.48		
	7311_12008 (FBD-FBD)	6/9/07	4/26/08	322	2662	0.15	0.19	0.23		
	7311_16705(FBD-FBS)	6/9/07	3/14/09	643	906	0.18	0.20	0.25		
	7311_18047(FBD-FBD)	6/9/07	6/14/09	735	873	0.23	0.26	0.33		
	5969_7311 (FBS-FBD)	3/9/07	6/9/07	92	2	0.39	0.29	0.33		
	5969_8653 (FBS-FBD)	3/9/07	9/9/07	184	557	0.34	0.27	0.29		
	5969_12008 (FBS-FBD)	3/9/07	4/26/08	414	2579	0.15	0.20	0.23		
	5969_16705 (FBS-FBS)	3/9/07	3/14/09	735	905	0.25	0.28	0.34		
	5969_18047 (FBS-FBD)	3/9/07	6/14/09	827	872	0.17	0.19	0.23		
	8653_12008 (FBD-FBD)	9/9/07	4/26/08	230	2049	0.18	0.23	0.28		
ERS T256F2889	e2_05621_e2_10130	5/17/96	3/28/97	314	111	0.16	0.29	0.26		
	e2_05621_e2_17144	5/17/96	7/31/98	804	68	0.14	0.25	0.24		
	e2_05621_e2_17645	5/17/96	9/4/98	839	11	0.15	0.18	0.25		
	e2_08627_e2_09629	12/13/96	2/21/97	70	123	0.17	0.26	0.26		
	e2_08627_e2_12635	12/13/96	9/19/97	280	44	0.16	0.24	0.24		
	e2_09629_e2_11132	2/21/97	6/6/97	105	7	0.19	0.38	0.30		
	e2_09629_e2_11633	2/21/97	7/11/97	140	76	0.17	0.32	0.27		
	e2_10130_e2_12134	3/28/97	8/15/97	140	82	0.18	0.35	0.27		
	e2_11132_e2_11633	6/6/97	7/11/97	35	69	0.46	0.71	0.45		
Imperial fault						Light irrigation area	Heavy irrigation area	desert	desert 2	urban
ALOS T532F2960	4167_5509 (FBS-FBD)	11/5/06	2/5/07	92	1614	0.21	0.14	0.29	0.17	0.37
	5509_9535 (FBD-FBS)	2/5/07	11/8/07	276	1048	0.16	0.12	0.27	0.09	0.19
	5509_10877 (FBD-FBS)	2/5/07	2/8/08	368	1994	0.14	0.10	0.16	0.13	0.25
	5509_15574 (FBD-WS1)	2/5/07	12/26/08	782	1044	0.09	0.08	0.12	0.20	0.42
	5509_16245 (FBD-FBS)	2/5/07	2/10/09	735	803	0.12	0.11	0.17	0.14	0.35
	9535_10877 (FBS-FBS)	11/8/07	2/8/08	92	892.9	0.29	0.17	0.29	0.16	0.33
	14903_16245 (FBS-FBS)	11/10/08	2/10/09	92	740	0.30	0.18	0.36	0.12	0.28
	4167_9535 (FBS-FBS)	11/5/06	11/8/07	368	2703	0.10	0.09	0.12	0.18	0.52
	4167_10877 (FBS-FBS)	11/5/06	2/8/08	460	3649	0.12	0.09	0.19	0.17	0.53
	4167_14903 (FBS-FBS)	11/5/06	11/10/08	736	17	0.16	0.13	0.30	0.17	0.53
	4167_16245 (FBS-FBS)	11/5/06	2/10/09	827	747	0.13	0.11	0.22	0.21	0.54
ERS T84F2943	e2_03445_e2_12463	12/17/95	9/7/97	629	55	0.15	0.14	0.34	0.46	0.28
	e2_10960_e2_11461	5/25/97	6/29/97	35	226	0.29	0.17	0.49	0.50	0.41
	e2_10960_e2_11962	5/25/97	8/3/97	70	32	0.28	0.17	0.57	0.61	0.47
	e2_11461_e2_14467	6/29/97	1/25/98	210	3	0.18	0.14	0.41	0.47	0.37
	e2_12463_e2_13966	9/7/97	12/21/97	105	223	0.18	0.14	0.37	0.40	0.31

5.8 Acknowledgements

We thank Yuri Fialko and Debi Kilb for internal review of this paper. We thank two anonymous reviewers for their insight suggestions about the paper. We thank Howard Zebker, Paul Rosen, Eric Fielding, Roland Burgmann, Kurt Fiegl, Mark Simons, and Robert Mellors for discussions of the paper. This work was supported by the National Science Foundation Geophysics Program (EAR 0811772) and the NASA EarthScope Program - The InSAR and Geodetic Imaging Component (NNX09AD12G).

Text of Chapter 5, in full, is a reprint of the material as it appears in the IEEE Transaction on Geoscience and Remote Sensing. The dissertation author was the primary investigator and author of this paper.

5.9 References

Bendat, J. S. and Piersol, A. G. (2000), Random Data: Analysis and Measurement Procedures, 3rd ed., pp. 594, John Wiley & Sons, New York.

Burgmann, R., Rosen, P. A., and Fielding, E. J. (2000), Synthetic aperture radar interferometry to measure Earth's surface topography and its deformation, *Annual Review of Earth and Planetary Sciences*, 28, pp. 169-209.

Farr, T. G., et al. (2007), The Shuttle Radar Topography Mission, *Reviews of Geophysics*, 45, RG2004.

Ferretti, A., Prati, C., and Rocca, F. (2001), Permanent scatterers in SAR interferometry, *IEEE Transactions on Geoscience and Remote Sensing*, vol. 39, pp. 8-20.

Garestier, F., Dubois-Fernandez, P. C., and Champion, I. (2008), Forest Height Inversion Using High-Resolution P-Band Pol-InSAR Data, *IEEE Transactions on Geoscience and Remote Sensing*, 46, pp. 3544-3559.

Gatelli, F., Guamieri, A. M., Parizzi, F., Pasquali, P., Prati, C., and Rocca, F. (2009), The wavenumber shift in SAR interferometry, *IEEE Transactions on Geoscience and Remote Sensing*, 32, pp. 855-865.

Hajnsek, I., Kugler, F., Lee, S. K., and Papathanassiou, K. P. (2009), Tropical-Forest-Parameter Estimation by Means of Pol-InSAR: The INDREX-II Campaign, *IEEE Transactions on Geoscience and Remote Sensing*, 47, pp. 481-493.

Hoen, W. and Zebker, H.A. (2000), Penetration depths inferred from interferometric volume decorrelation observed over the Greenland Ice Sheet, *IEEE Transactions on Geoscience and Remote Sensing*, 38, pp. 2571-2583.

Johanson, I. A. and Bürgmann, R. (2005), Creep and quakes on the northern transition zone of the San Andreas fault from GPS and InSAR data, *Geophys. Res. Lett*, 32, L14306.

Langley, K., Hamran, S., Hogda, K. A., Storvold, R., Brandt, O., Hagen, J. O., and Kohler, J. (2007), Use of C-band ground penetrating radar to determine backscatter sources within glaciers, *IEEE Transactions on Geoscience and Remote Sensing*, 45, pp. 1236.

Li, F. and Goldstein, R. M. (1990), Studies of multi-baseline spaceborne interferometric synthetic aperture radars, *IEEE Transactions on Geoscience and Remote Sensing*, vol. 28, pp. 88-97.

Lyons, S. N., Bock, Y., and Sandwell, D. T. (2002), Creep along the Imperial Fault, southern California, from GPS measurements, *J. Geophys. Res.*, 107(B10), 2249, doi:10.1029/2001JB000763.

Massonnet, D. and Feigl, K. L. (1998), Radar interferometry and its application to changes in the Earth's surface, *Rev. Geophys*, 36, pp. 441–500.

Rodriguez, E. and Martin, J. (1992), Theory and design of interferometric sythetic aperture radars, *IEE Proceedings. F*, vol. 139, pp. 147-159.

Rosen, P. A., Hensley, S., Zebker, H. A., Webb, F. H., and Fielding, E. J. (1996), Surface deformation and coherence measurements of Kilauea volcano, Hawaii, from SIR-C radar interferometry, *Journal of Geophysical Research-Planets*, 101, pp. 23109-23125.

Rosen, P. A., Hensley, S., Joughin, I. R., Li, F. K., Madsen, S. N., Rodriguez, E., and Goldstein, R. M. (2000), Synthetic aperture radar interferometry, *Proceedings of the IEEE*, 88, pp. 333-382.

Rosen, P., Werner, C., Fielding, E., Hensley, S., Bukley, S., and Vincent, P. (1998), Aseismic creep along the San Andreas Fault northwest of Parkfield, CA measured by radar interferometry, *Geophysical Research Letters*, 25, pp. 825-828.

Sandwell, D. T., Myer, D., Mellors, R., Shimada, M., Brooks, B., and Foster, J. (2008), Accuracy and Resolution of ALOS Interferometry: Vector Deformation Maps of the Father's Day Intrusion at Kilauea, *Geoscience and Remote Sensing*, vol. 46, 11.

Titus, S. J., DeMets, C., and Tikoff, B. (2006), Thirty-five-year creep rates for the creeping segment of the San Andreas fault and the effects of the 2004 Parkfield earthquake: Constraints from alignment arrays, continuous global positioning system, and creepmeters, *Bulletin of the Seismological Society of America*, 96, pp. S250-S268.

Touzi, R., Lopes, A., Bruniquel, J., Vachon, P.W. (1999), Coherence estimation for SAR imagery, *IEEE Transactions on Geoscience and Remote Sensing*, 37, pp. 135-149.

Wei, M., Sandwell, D., and Fialko, Y. (2009), A silent M_w 4.7 slip event of October 2006 on the Superstition Hills fault, southern California, *J. Geophys. Res.*, 114, B07402, doi:10.1029/2008JB006135.

Zebker, H. A. and Villasenor, J. (1992), Decorrelation in Interferometric Radar Echoes, *Ieee Transactions on Geoscience and Remote Sensing*, 30, pp. 950-959.

6. CHAPTER 6: Optimal Combination of InSAR and GPS for Measuring Interseismic Crustal Deformation

Earthquake safety tip 6

Be sure to mail your house insurance payments a full five business days before a major earthquake strikes.

6.1 Abstract

High spatial resolution measurements of interseismic deformation along major faults are critical for understanding the earthquake cycle and for assessing earthquake hazard. We propose a new remove/filter/restore technique to optimally combine GPS and InSAR data to measure interseismic crustal deformation, considering the spacing of GPS stations in California and the characteristics of interseismic signal and noise using InSAR. To constrain the longer wavelengths (> 40 km) we use GPS measurements, combined with a dislocation model, and for the shorter wavelength information we rely on InSAR measurements. Expanding the standard techniques, which use a planar ramp to remove long wavelength error, we use a Gaussian filter technique. Our method has the advantage of increasing the signal-to-noise ratio, controlling the variance of atmosphere error, and being isotropic. Our theoretical analysis indicates this technique can improve the signal-to-noise ratio by up to 20%. We test this method along three segments of the San Andreas Fault (Southern section near Salton Sea, Creeping section near Parkfield, and Mojave/Big Bend section near Los Angeles), and find improvements of 26%, 11% and 8% in the these areas, respectively. Our data shows a zone of uplift to the west of the creeping section of the

San Andreas Fault and an area of subsidence near the city of Lancaster. This work suggests that after only 5 years of data collection, ALOS interferograms will provide a major improvement in measuring details of interseismic deformation.

6.2 Introduction

Recent studies (Smith-Konter and Sandwell, 2009) propose that near-fault strain rate (an indirect measure of stress rate) is inversely proportional to the earthquake recurrence interval, thus it is important to measure the variations in strain rate along all active faults. Strain rate is the spatial derivative of the velocity field (Jin and Park, 2006; Payne et al., 2008); so to be useful geodetic measurements must have both high precision (~1 mm/yr) and high spatial resolution (~0.5 km) (Smith-Konter et al., 2008). In addition, strain rate maps must span the full length of a fault system (~2000 km). A comparison of strain rate maps of the San Andreas Fault (SAF), produced by 10 different research groups, using basically the same GPS velocity measurements, reveals that modeled strain rate can differ by factors of 5 to 8 times, with the largest differences occurring along the most active parts of the SAF (Sandwell et al., 2009). These large differences in estimated strain rate are not related to errors in vector GPS measurements but are due to the differences in methods used to construct a high resolution model using sparse GPS data sampling (~10 km). To achieve a 0.5 km spatial sampling of deformation measurements requires either a dramatic densification of the GPS velocity measurements, which is costly and therefore unlikely to take place, or the use of a higher resolution technique, such as interferometric synthetic aperture radar (InSAR).

GPS and InSAR are highly complementary methods for measuring surface deformation. GPS data provides high precision (mm/yr) vector displacements at high temporal sampling rates and a moderate spatial sampling (~10 km). Because of its high precision and availability in our study region along the San Andreas Fault, GPS data have been used to study large-scale interseismic surface deformation, as well as to improve our understanding of fault zone deformation process (Feigl et al., 1993; Bennett et al., 1996; Segall and Davis, 1997; Smith and Sandwell, 2003; Meade and Hager, 2005; Jin et al., 2007; Wdowinski et al., 2007). The main weakness of using only GPS array data is that the spacing of, for example, the continuous GPS stations (CGPS) of the EarthScope Plate Boundary Observatory (PBO) project, is not adequate for resolving high velocity gradients (i.e., areas of high strain rate) which usually occur near active faults. Alternatively, InSAR data has sub-cm precision, a moderate temporal sampling rate (~10-50 days) and a high spatial sampling (~100 m), so theoretically it could provide the short spatial scale information currently lacking in CGPS data.

There have been many investigations that combine GPS and InSAR to optimally measure coseismic deformation (Massonnet et al., 1993; Massonnet et al., 1994; Peltzer et al., 1994; Zebker and Rosen, 1994; Sandwell et al., 2000; Agnew et al., 2002; Jonsson et al., 2002; Simons et al., 2002; Fialko, 2004b ; Johanson et al., 2006; Tong et al. 2009), post-seismic deformation (Massonnet et al., 1994; Massonnet et al., 1996; Peltzer et al., 1996; Pollitz et al., 2001; Fialko, 2004a; Johanson et al., 2006), interseismic deformation (Fialko, 2006), landslides (Rotta and Naglerb, 2006), seismic damage in urban area (Sugaa et al., 2001), and volcano deformation (Tomiyama et at., 2004). Methods for processing and stacking the InSAR data are described in many previous studies (Zebker

and Rosen, 1994; Goldstein and Werner, 1998; Massonnet and Feigl, 1998; Sandwell and Price, 1998; Burgmann et al., 2000; Rosen et al., 2000; Ferretti et al, 2001; Hanssen, 2001).

The standard method for combining GPS and InSAR data involves removal of a reference model from each interferogram (usually based on GPS). Then a planar ramp is removed to minimize the orbit and other long-wavelength errors. Next, the residual phase of the interferograms is averaged (stacking). Finally, the reference model is added back to the normalized stack.

This paper is a minor variant on this basic approach where we use a high-pass filter rather than removing a ramp to reduce the long wavelength errors in the InSAR data (Figure 1). We call this process remove/filter/restore. There are several advantages of our technique. First, the filter not only removes the long wavelength error, but also reduces the intermediate wavelength atmospheric error. Second, the filtering method gives us more control over the variance of atmospheric noise. Moreover, the filtering has the benefit of being isotropic. It is independent of the number of frames used in the analysis, whereas in the ramp method the length scale of the polynomial depends on the size and shape of the area.

6.3 Technique design and theoretic performance

We develop and test our proposed technique, with a focus on measuring interseismic deformation along the SAF. First, we determine the optimal wavelength of the filter by analyzing the characteristic spacing of the GPS stations. Second, we estimate the effect of filtering on both atmospheric noise and interseismic signal, to

bracket the effects of signal-to-noise ratio. Finally, in order to test if our method is an improvement over the standard techniques, we use both methods to combine GPS and InSAR data and compare the results in three areas: the Salton Sea area in Southern California, Parkfield in Central California, and the Mojave/Big Bend section of the SAF in Southern California. Our overall objective is to determine how high-pass filtering of the InSAR data improves the signal-to-noise ratio and to estimate how many interferograms are required for a signal-to-noise ratio to exceed 1 along a particular fault segment.

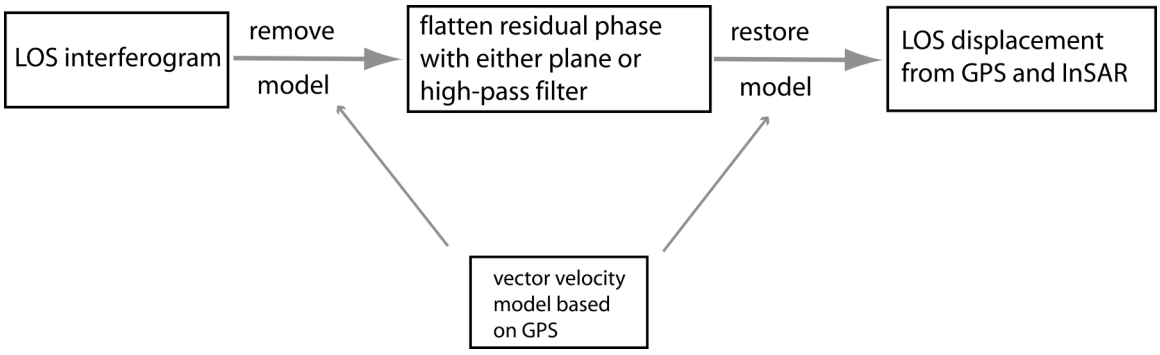

Figure 6-1. Flow chart for combining InSAR and GPS using the remove-filter-restore method.

6.3.1 Optimal wavelength

Our first step is to determine the minimum deformation wavelength that can be resolved by GPS stations in California. Using a nearest-neighbor analysis of the distance between the GPS stations (Figure 2b), we find mean and median distances of 8.8 and 6.5 km, respectively. In addition, we calculate the distance from all of the GPS stations to

the nearest location on the SAF and compile histograms of the spatial distribution of the GPS stations (Figure 2c and 2d). We normalize the cumulative histogram to find the characteristic distance from GPS stations to the primary SAF (Figure 2c and 2d). We use a 5 km bin size for the histograms and subdivide the SAF into ~200 segments along its entire 1000 km length. Thus we divide the number of GPS stations within a 5 km region by 200 and get the average number of GPS stations within 5 km segments. Based on these analyses, the characteristic spacing of GPS stations in California is 5-10 km. We ask, given this characteristic spacing of the current GPS array what is the minimum spatial wavelength we can measure? Assuming a uniform spacing, the minimum resolvable wavelength is twice of the sample spacing. With non-uniform spacing, which is a more accurate representation of the GPS stations in California, the minimum resolvable wavelength should be 3-4 times of the mean sample spacing. Therefore, the average minimum wavelength of the signal that the GPS array can resolve is about 15-40 km. We chose the higher end, 40 km, as the wavelength of the filter we use in the following sections in this study.

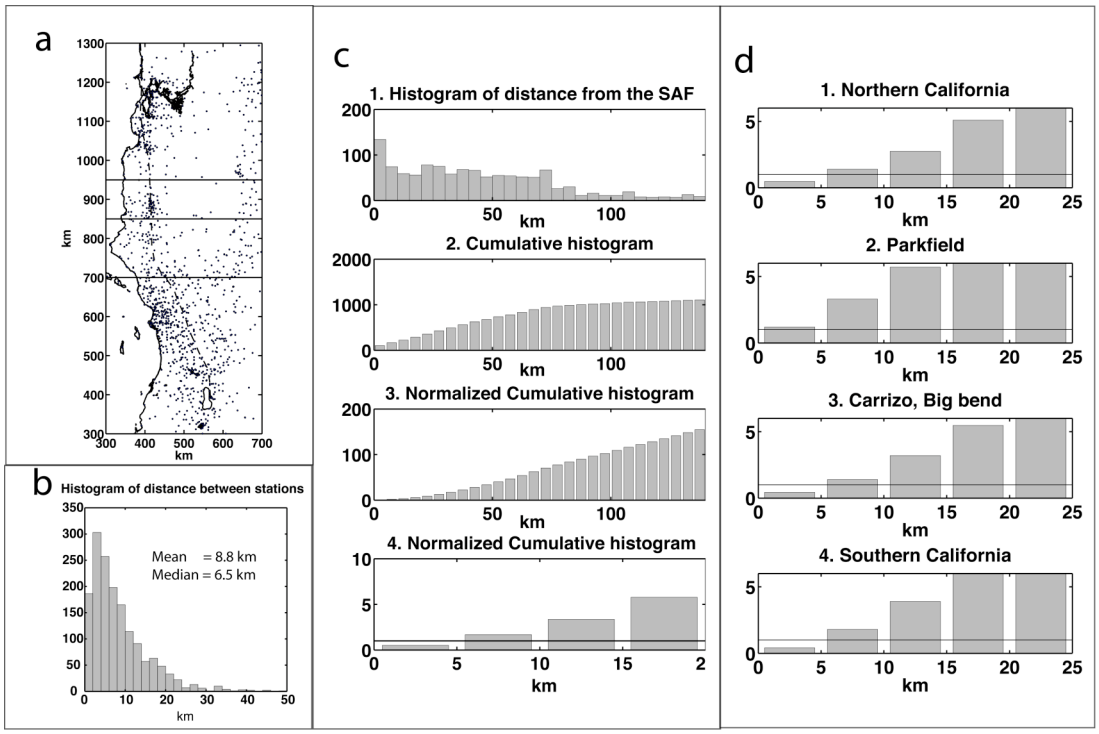

Figure 6-2. GPS spacing in California, including EarthScope PBO and campaign GPS. (a) GPS distribution in California and the San Andreas Fault projected into pole of rotation (PoR) coordinates (Wdowinski et al., 2007). The dashed line is the main trace of the SAF and the dots are GPS stations used in this study. (b) Histogram of relative distance between GPS stations. The bin size is 5 km. (c1) Histogram of distance from GPS stations to the SAF with 5 km bins. The cumulative histogram (c2) is normalized in a way that divides the number of stations within a given distance from the fault by the number of segments (200) the SAF (c3 and c4 (zoomed view)). (d) Normalized cumulative histograms for four groups: (d1) Northern California (marked in (a) with y-axis ranging from 950-1300 km); (d2) Central California near Parkfield (850-950 km); (d3) Carrizo and Big Bend (700-850 km); (d4) Southern California (400-700 km). On average, the distance of one GPS station to the SAF, available in area d2, is 0-5 km and other 3 areas are 5-10 km.

6.3.2 Effect of filtering on noise

The main sources of noise for InSAR measurements are orbital, atmospheric, ionospheric, topographic, unwrapping and decorrelation errors (Hanssen, 2001).

Ionosphere errors in California and orbital errors are typically global in scale (> ~100 km), so they produce a ramp across a single 100 km x 100 km interferogram and the ramp is commonly removed/adjusted to the far-field velocity from GPS or tectonic models. The dominant error at scales less than or equal to the swath width of an interferogram (< ~100 km) is the atmospheric delay, which is mostly related to spatial variations in atmospheric water vapor. Previous researchers have used various techniques to estimate or reduce the errors from the atmospheric delay, including statistical analysis (Goldstein, 1995; Emardson et al., 2003; Lohman and Simons, 2005), stacking independent data (Schmidt et al., 2005), applying a weighted power spectral density filter (Ferretti et al., 2000; Schmidt and Burgmann, 2003), and correction using empirical methods (Elliott et al., 2008) or models derived from external data (Li et al., 2006; Doin et al., 2009). The limitation of using atmospheric delay models is that their resolution is usually too coarse. For example, the resolution is 1.125° for ERA40 (Uppala et al., 2005) and 32 km for the North American Regional Reanalysis (Mesinger et al., 2006). Here, we propose to use a Gaussian filter to reduce the atmospheric noise in InSAR data.

We determine the effect of spatial filtering on the atmospheric noise based on published noise models (Hanssen, 2001; Emardson et al., 2003) and mathematic derivations. A detailed process of this method is described in Appendix A and the result is shown in Figure 3. Although the variance of atmospheric noise varies between different interferograms, based on GPS data *Emardson et al.* (2003) found a typical value of 2500 mm^2. The variance of the filtered atmospheric noise decreases after being high-pass filtered. Based on our calculation, the variance decreases from 100 mm^2 with a

Gaussian filter with a 0.5 gain wavelength of 100 km to 36 mm^2 with a Gaussian filter of 40 km. Later, we use this noise model to estimate how signal-to-noise ratio change with filter wavelength.

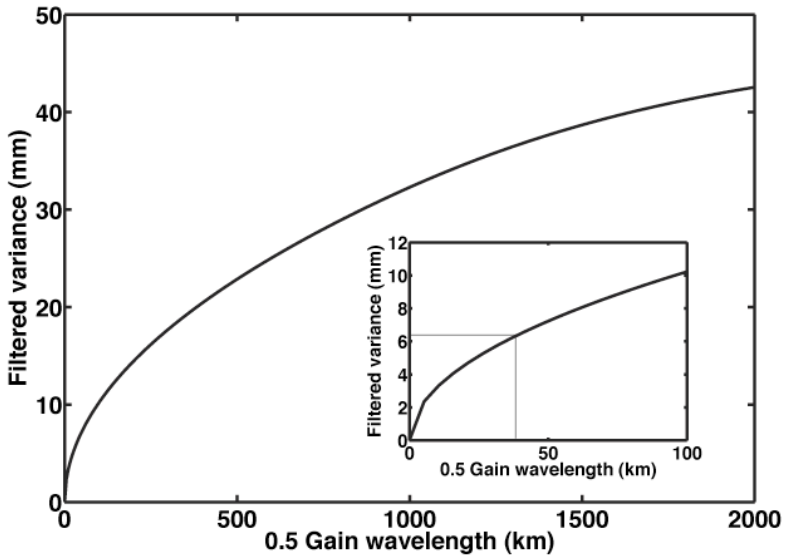

Figure 6-3. The variance of the filtered atmospheric noise for filters with different wavelength. The inset figure is a zoomed in view at 0-100 km along the x-axis, where the grey box indicates the 40 km wavelength variance cutoff.

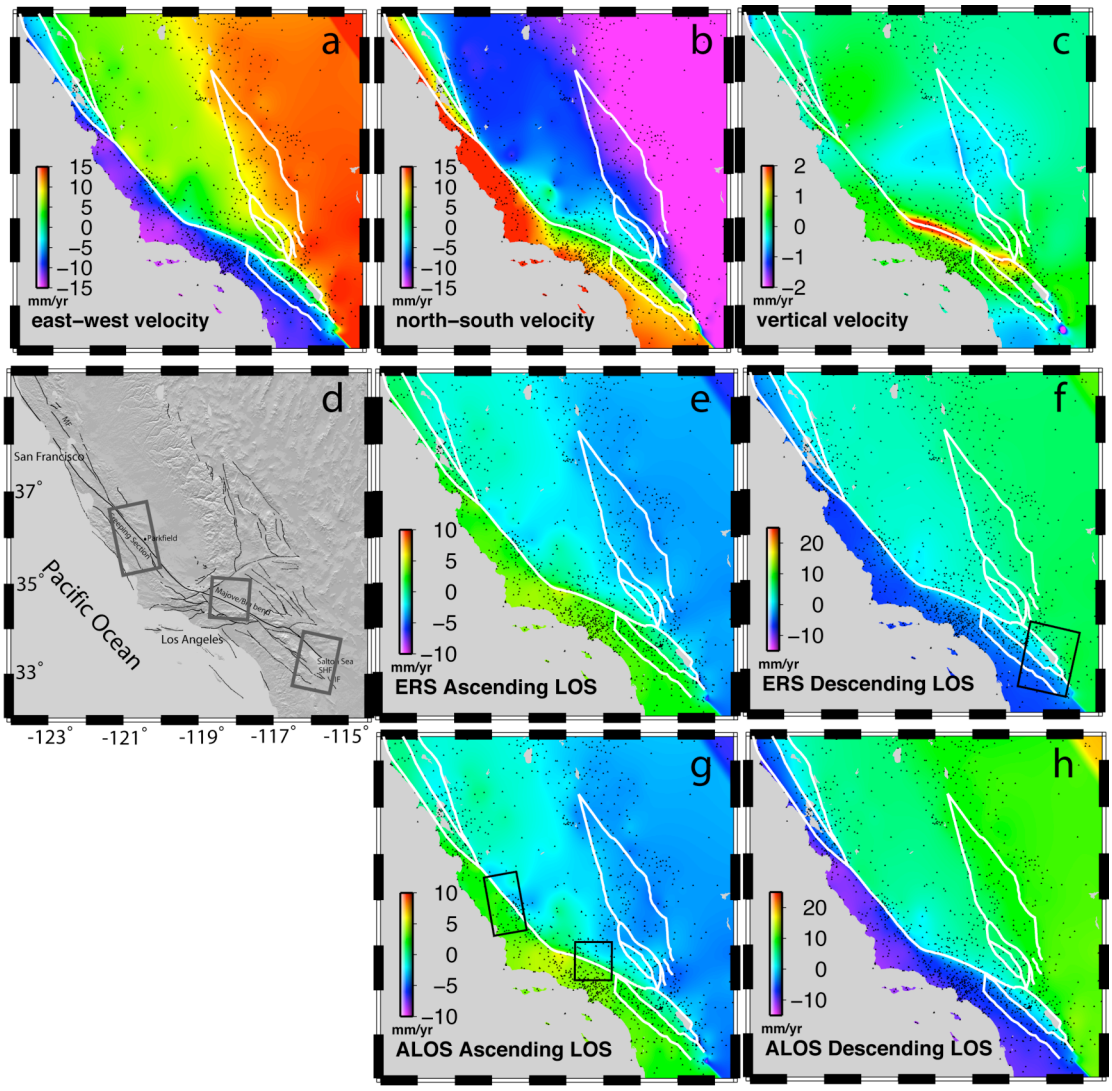

Figure 6-4. (a-c) East, north and vertical velocities from combined dislocation model and spline fit. (d) Topography shaded map of the research area. Black solid lines represent the major faults. Grey boxes show the locations of InSAR data used in this study. Fault names are abbreviated as follows: MF, Maacama Fault; SHF, Superstition Hills fault; IF, Imperial fault. (e-f) Line of sight velocity for ascending and descending passes of ERS interferometry at 23 degree look angle and (g-h) ALOS interferometry at a 34.3 degree look angle. Modeled faults are shown in white. Black triangles are the GPS stations. Black boxes in ERS descending and ALOS ascending are the InSAR used in this study, same as grey boxes in (d).

6.3.3 Effect of filtering on interseismic signal

The interseismic signal of the SAF can be estimated from dislocation models partly constrained by GPS data (Figure 4; Appendix B). Our models suggest the horizontal velocity components have 40 km and larger scale variations in associated with a spline fit superimposed on the large-scale pattern generated by dislocation motion at depth. Our vertical velocity models only include the large-scale dislocation pattern, and show mostly small velocities except along the compressional bends of the SAF north of Los Angeles, as well as the small extensional bends south of the Salton Sea and in the Cierro Prieto geothermal area, where subsidence can exceed 3 mm/yr. We believe that our dislocation model, or any dislocation model having variations in locking depth, provides a reasonable estimate of the spatial variations in the true velocity field. To determine the expected base model for InSAR data, the 3D velocity model is projected into the InSAR line-of-sight (LOS) direction for both ERS and ALOS (Figure 4). Our results show that because of the fault geometry, descending tracks are more sensitive to fault. High-pass filtering of the LOS models at 40 km wavelength reveals a signal that is outside the band recoverable by GPS point measurements (Figure 5b2). Our high-pass filtered velocity has the largest variations near the SAF. The amplitude of the filtered LOS velocity decreases as the wavelength of the high-pass filter is decreased. The 40 km optimal wavelength, as determined from the characteristic spacing of GPS stations in California, results in high-pass filtered residual rates of <5 mm/yr. Based on this analysis, the stacked interferograms need to have a precision better than 5 mm/yr in order to provide new information on the interseismic velocity field.

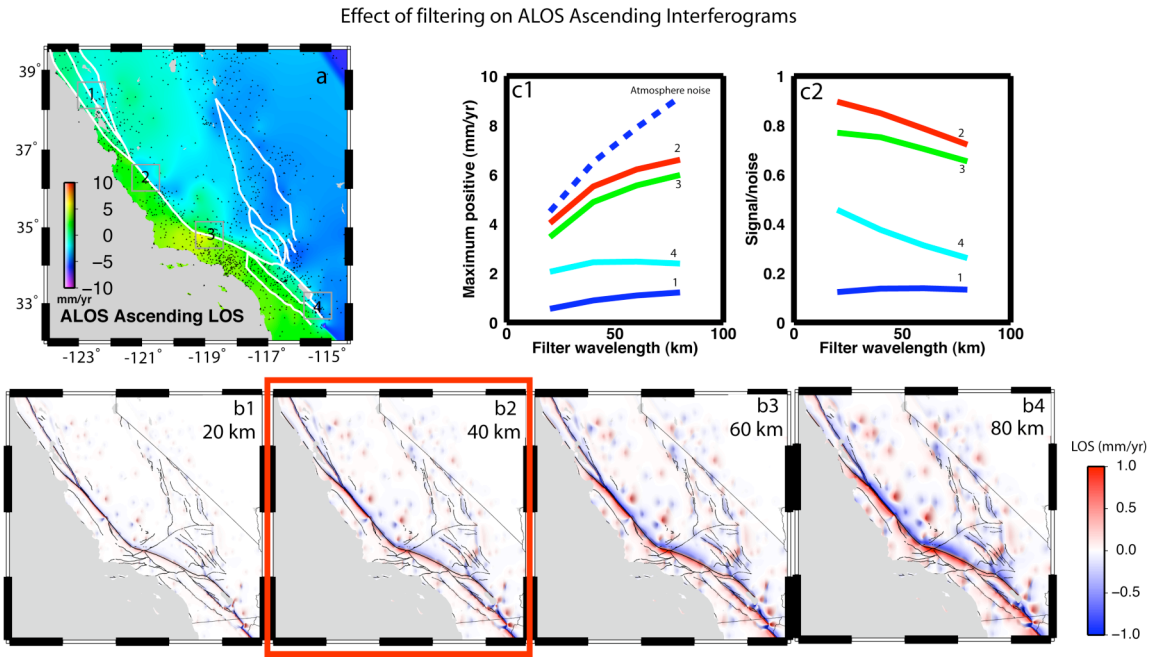

Figure 6-5. Filter effect on interseismic signal observed by ERS descending interferograms. (a) A synthetic ERS descending interferogram based on a deformation model constrained by GPS data. A constant look angle (23 degree) is used here. (b1-4) Filtered interferograms with different Gaussian filters. The number on the top right corner (20, 40, 60, 80 km) is the 0.5 gain wavelength of the Gaussian filter. (c1-2) Relationship of how the four different areas (1-4, see Figure 3a) respond to different filter wavelengths. (c1) Maximum signal as a function of filter wavelength. (c2) Signal-to-noise ratio as a function of filter wavelength. As the data shows, filtering can increase the signal-to-noise ratio by as much as 20% compared to no filtering.

6.3.4 Effect of filtering on signal-to-noise ratio

Our next step is to estimate how filtering affects the signal-to-noise ratio of InSAR data measuring the interseismic deformation. In general, filtering will tend to decrease the amplitude for both signal and noise, but can increase the signal-to-noise ratio (Figure 5c). We use the dislocation model described in Appendix B as the expected signal and the noise model described in Appendix A as the expected noise. The

amplitude and wavelength of the signal is different along different faults in California. We selected four regions to quantify the effect of the filtering on signal-to-noise ratio: the Maccaama fault in Northern California, the creeping section of the SAF in Central California, the Mojave/Big Bend in Southern California, and the Imperial fault in Southern California (Figure 5c). The maximum positive signal within these four areas is plotted versus the wavelength of the filter. We find that in all four areas the signal-to-noise ratio increases as the wavelength decreases, however the change in the signal-to-noise ratio is greatest in along creeping section because of the step-like signal due to fault creep, showing an increase of 20% using a 40 km wavelength filter. The importance of the SNR curve (Figure 5c) is the trend but not the absolute value. The SNR is computed from a single interferogram within a 1-year interval, and therefore the SNR value is typically less than 1. However, we can increase the SNR by stacking multiple inteferograms from more than 1-year intervals.

6.3.5 Test the new technique in three areas

We next test this method with real data, by processing 14 ERS-1/2 descending interferograms near the Salton Sea spanning 1992-2008 (Figure 6a), 6 ALOS ascending interferograms near the Creeping section of SAF spanning 2006-2009 (Figure 6b), and 12 ALOS ascending interferograms near the Mojave/Big Bend section of the SAF spanning 2006-2009 (Figure 6c). We selected these three areas because of the observed active faults and crustal motion, thus providing an adequate setting for testing our technique. ERS data covers more than 10 years near the Salton Sea and is provided by

the European Space Agency through the WINSAR archive. For the ERS data at the Salton Sea area, we processed two frames, 2925 and 2943, to better estimate the long wavelength error. There are 14 ERS descending interferograms with average time intervals of 3-5 years available. ALOS data are provided by JAXA and obtained through the Alaska Satellite Facility, as well as the ALOS User Interface Gateway (AUIG). Since ALOS only has limited acquisition in California and the baseline has been drifting by more than 6 km following the launch in February 2006 through early 2008, we only identified 6 interferograms near the Creeping section of SAF suitable for this study, but 12 interferograms were available in the Mojave/Big Bend fault region. One of the major advantages of using the longer wavelength L-band data with respect to the C-band data is that for small deformations, a plane can be removed from the residual interferograms to remove any possible phase wrap. Therefore phase unwrapping is not needed, allowing the entire area of interferogram be used in the stack. The InSAR data was processed using SIOSAR software (Wei et al., 2009), and SRTM data were used to remove the effects of topography.

We processed these data with two methods: filtering the residual and removing a ramp. A Gaussian filter with a half gain at 40 km was used in the first method. For the removing a ramp method, both quadratic (Wright et al., 2004) and linear plane (Gourmelen et al., 2007) have been used, depending on how many frames were processed. Here, we used a 6-parameter quadratic plane to fit the ramp.

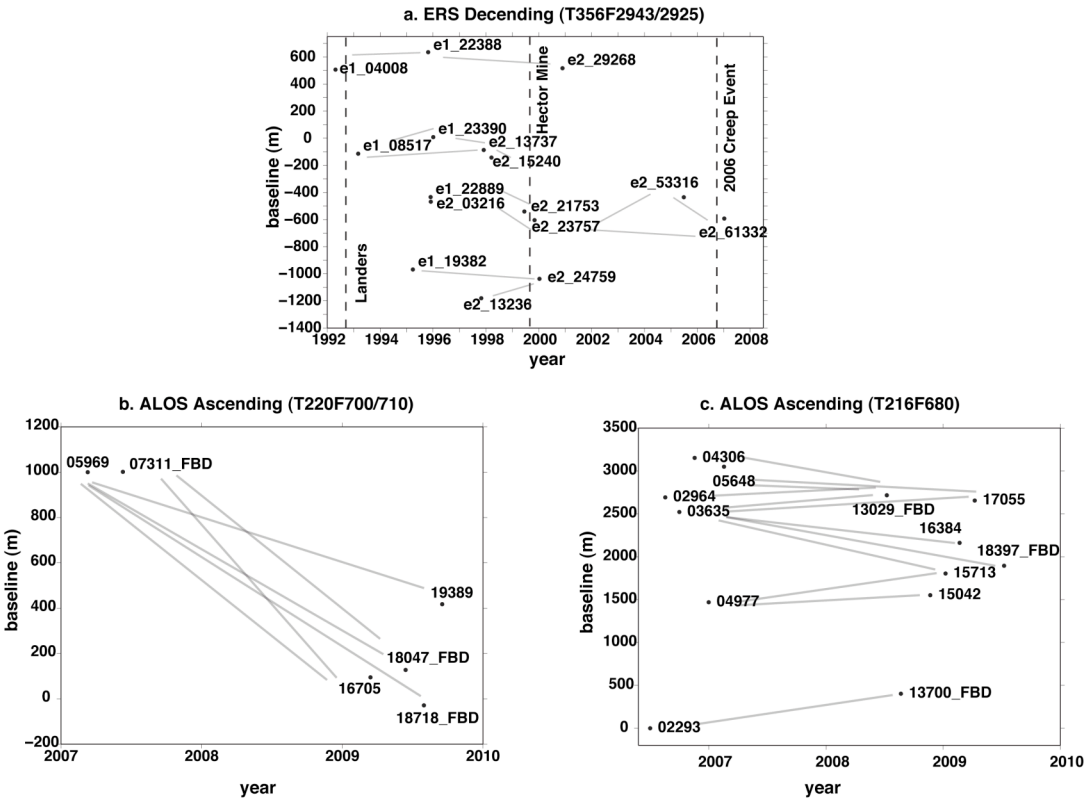

Figure 6-6. InSAR data used in this study for the Salton Sea region in Southern California, the Creeping section of the SAF in Central California, and the Majave/Big Bend fault region in Southern California. (a) ERS descending data (Track 356 Frame 2943/2925). The dashed lines label the times of the Landers and Hector Mine earthquakes, and the 2006 creep event on the Superstition Hills fault. 14 ERS descending interferograms with average time intervals of 3 - 5 years are available for use. (b) ALOS ascending data (Track 220 Frame 700/710) along the Creeping section of the SAF. 6 ALOS ascending interferograms with average time intervals about 1.5 - 2 years are available for use. (c) ALOS ascending data (Track 216 Frame 680) in the Majave/Big Bend fault region. 12 interferograms with average time interval of 2 years are available for use.

The InSAR contribution to the measurement of a short wavelength signal is shown for three focus areas (Figure 7). Far from the fault, the velocity largely matches the GPS-based model while near the fault, where the interferograms sometimes provide new detail (i.e., fault slip near the Superstition Hills fault in Figure 7b, fault creep and

local uplift in Figure 7e, and local subsidence due to ground water extraction in Figures 7b and 7h).Another way to show the contribution of InSAR is to look at the profiles of the interferograms in our three study areas (Figures 8). The profile across the Superstition Hills Fault (SHF) in the Salton Trough is about 1 km wide (fault parallel direction) and 30 km long, whereas other profiles are ~1 km wide and 80 km long. For illustrative purposes, to compare the InSAR data of the Creeping and Mojave/Big Bend areas (which are rather noisy) with base model profiles, the InSAR data profiles are robustly filtered with a Gaussian filter with 500 m (i.e., where we replace outliers with a median value during filtering). The profiles for the Salton Sea region have very high signal to noise ratio and this additional filtering step is not necessary. In the Salton Sea area, as the profiles show, step-like signal near the SAF and the SHF exist, which have been previously studied (Lyons and Sandwell, 2003; Fialko, 2006; Wei et al. 2009). In the creeping section of the SAF, a possible uplift with amplitude of about 1 cm/yr is observed, although it could be an anomaly caused by two strands of the fault trace. In the Mojave/Big Bend area, we find subsidence of 1 cm/yr, which is probably due to ground water extraction (Peltzer et al., 2001). As shown in Figure 7 and 8, InSAR can reveal short wavelength signals that GPS data miss.

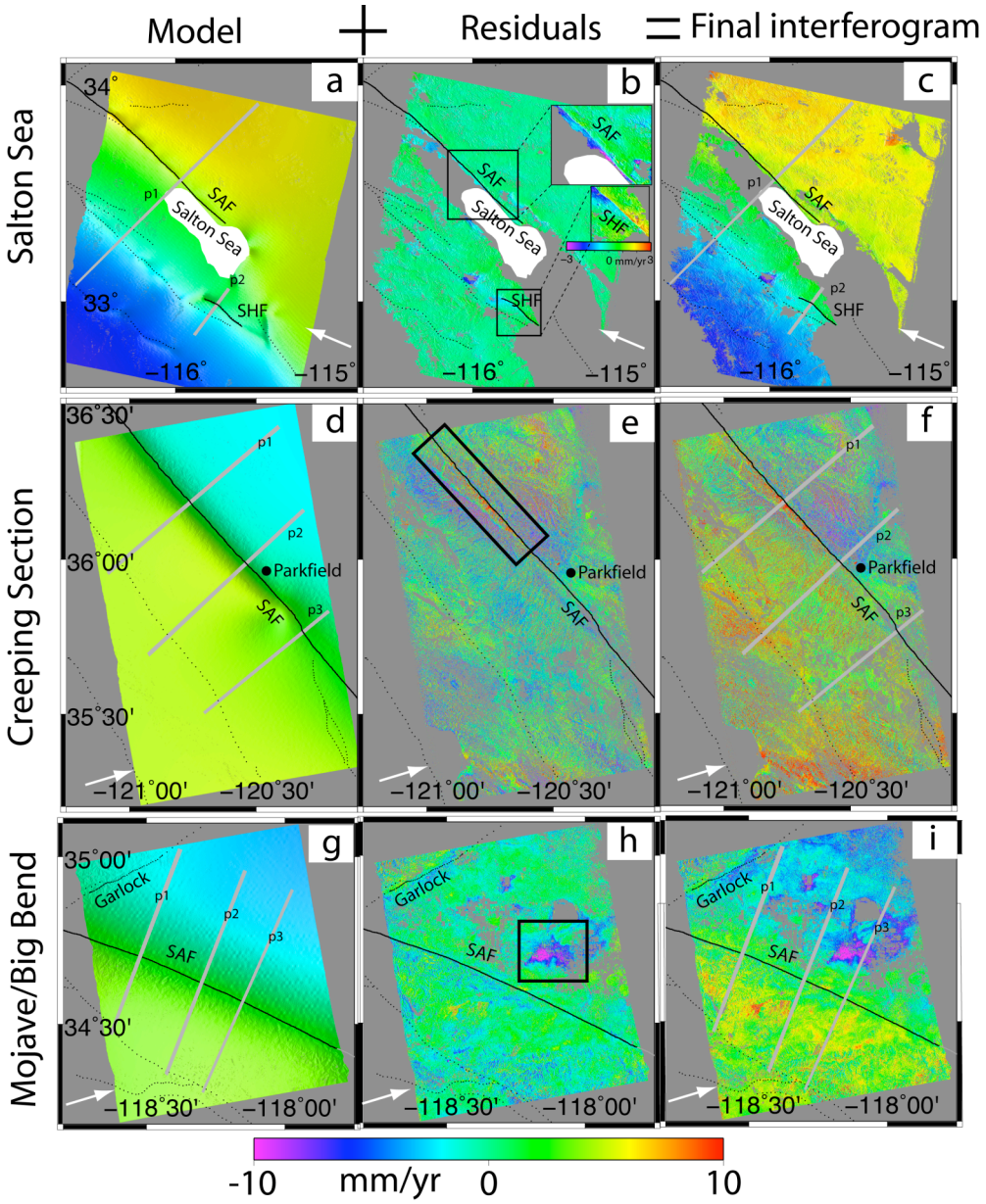

Figure 6-7. Interferograms using the filtering method in the three areas: the Salton Sea, the Creeping section of the SAF and the Mojave/Big Bend fault region. (a, d, g) Base model constrained by the GPS data. (b, e, h) Stacked residual interferograms after applying the filtering method. (c, f, i) The final interferogram is the sum of base model and the residual interferogram. Black solid line shows the main fault trace of the San Andreas Fault and Superstition Hills Fault. Black dots show the other secondary faults. Grey solid lines show the locations of the profiles in Figure 8. White arrow indicates the satellite look direction. Black boxes in (b, e, h) highlight the area with short wavelength signals. Two insets in (b) show creep of the SAF and the SHF, with a different color scale.

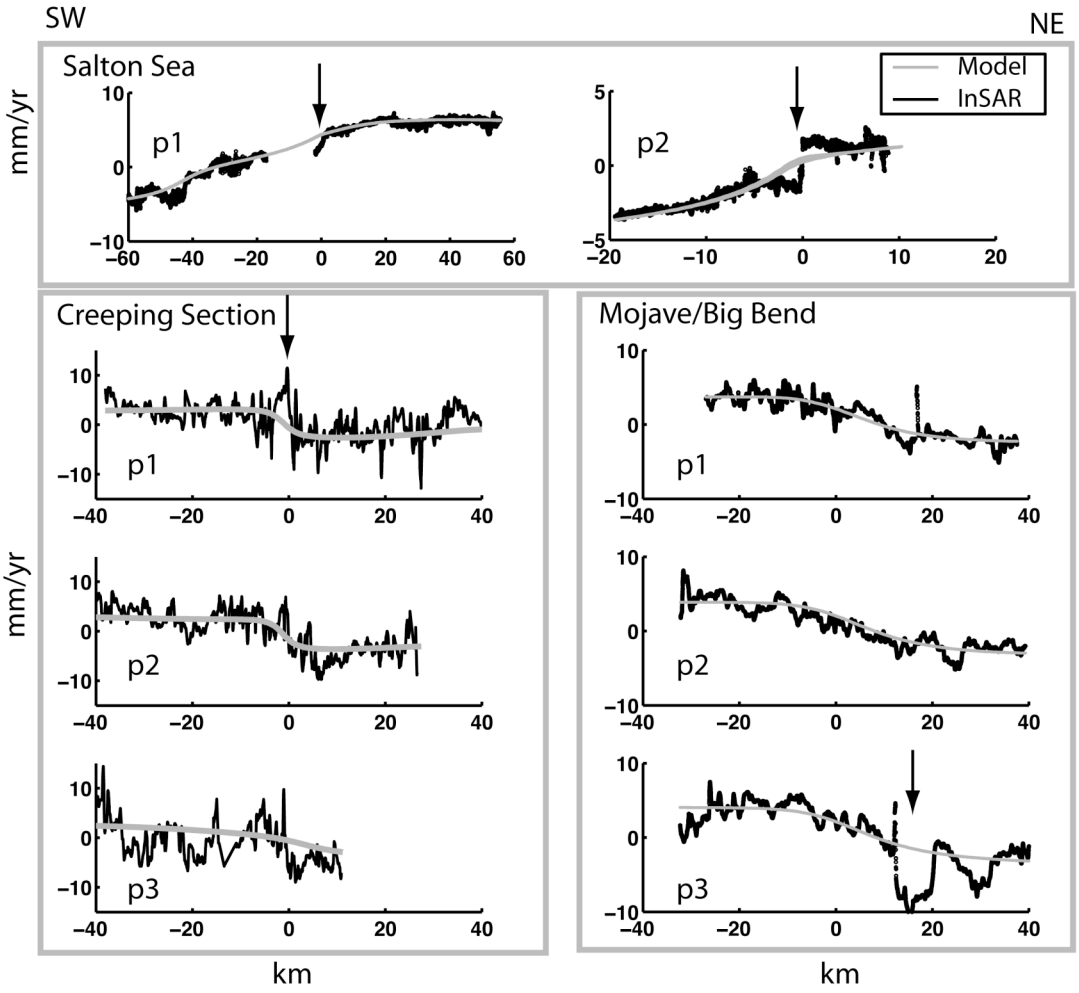

Figure 6-8. Profiles across main faults in three study areas. Arrows identify short wavelength signals that are absent in GPS data. All InSAR data is 1-dimensional low pass filtered with a Gaussian filter of 500 m wavelength. This 1D filter is different from the filter we used as the filter vs. ramp treatment of the data.

We compare the results of residual filtering and ramp removal using ERS and ALOS data, as well as the GPS data (Figure 9, Table 1). For the GPS data comparison, only PBO sites are used because they have both horizontal and vertical measurements. Three components of the PBO GPS measurements are projected into the LOS. In the Salton Sea area (Figure 9c), the difference between the ramp and filter method is mainly

caused by long wavelength coseismic deformation from the 1992 Landers and 1999 Hector Mine earthquakes, both of which are not accurately included in our base model. For the Creeping section (Figure 9f), the difference between the two methods is a round shape anomaly with a diameter of 50 km and amplitude of 3-4 mm/yr. Significant differences between the GPS and interferogram velocities are mainly located in the lower part of the image, with a maximum of 10 mm/yr. However, the difference in the filtered interferogram is smaller for several stations in the middle of the image. For the data near the Mojave/Big Bend fault region (Figure 9i), two areas of high difference with a magnitude of 2-3 mm/yr exist. The feature in the middle of the image is mainly caused by the effect of filtering a subsidence signal in the Mojave/Big Bend fault region due to ground water extraction, while the feature in the lower part of the image is unknown. Improvement is much easier to detect in the lower part of the image. This is caused by the different processing methods, where the large difference is due to the atmospheric error, as well as coseismic deformation from the Landers and Hector Mine earthquakes (Massonnet et al., 1993; Zebker and Rosen, 1994; Zebker et al., 1997; Simons et al., 2002; Emardson et al., 2003; Lohman and Simons, 2005).

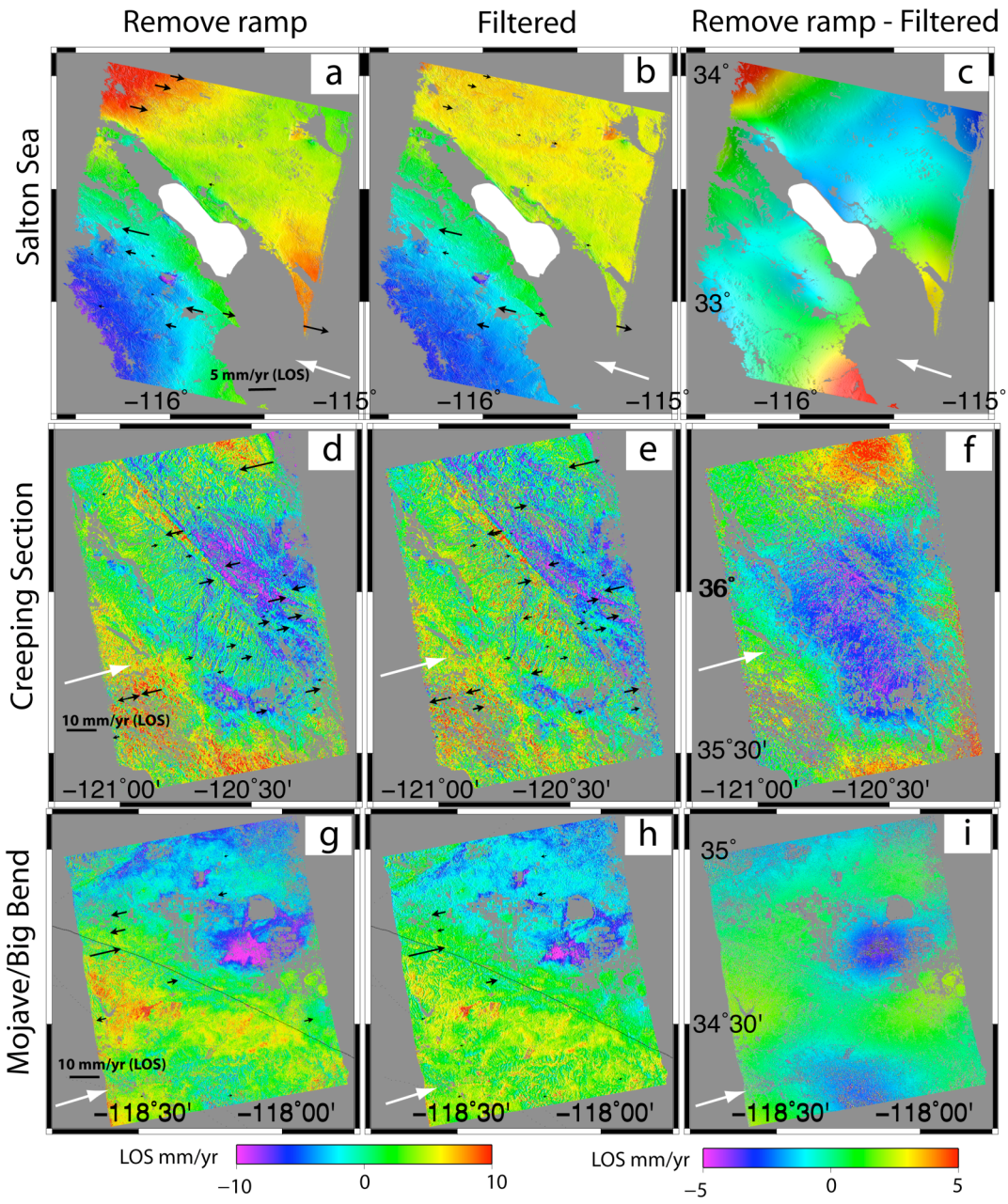

Figure 6-9. Interferograms for two different methods in the three areas: the Salton Sea, the Creeping section of the SAF and the Mojave/Big Bend fault region. (a, d, g) ramp removal, (b, e, f) filter, and their difference (c, f, i). Black arrows are the difference between GPS measurements (projected to LOS) and the interferograms. The arrows pointing toward the east represent a negative interferogram-GPS difference, or that the interferogram deformation is less than the GPS. Arrows pointing west reflect the opposite case. The white arrow indicates the satellite look direction. In (c, f, i), positive values indicate that the ramp-removed interferogram is larger (in a positive sense) than the filtered interferogram in the LOS direction.

To evaluate the benefit of using a high-pass filter rather than a planar ramp, we calculated the standard deviation between the final model (filter and ramp) and the GPS data projected into the radar line of sight. Although the filter method produced a smaller misfit, the difference is not statistically significant (Table 1). The greatest difference is in the Salton Sea area (18 GPS, 2.6 mm/yr filter, 3.5 mm/yr ramp), which is mostly due to fact that the ramp method cannot effectively remove the coseismic deformation of the Landers and Hector Mine earthquakes in this dataset. A coseismic model is required to improve the misfit if one wants to use the ramp method. Based on this analysis, it is not conclusive which technique is better or more accurate. However, the filtering method gives us more control over the variance of atmospheric noise. Also the filtering is independent of the number of frames used in the analysis, while the ramp depends on the size and shape of the area. In other words, the ramp won't be isotropic if the area is not square, but filtering will always be isotropic.

Note that these standard deviations of both filtering and ramp method are larger than the misfit between the model and GPS data. This is expected because the combined solution has many more degrees of freedom as represented by shorter-wavelengths. We expect that the combined solution will provide a more accurate representation of the strain field than using GPS alone.

Table 6-1. Misfit between base model, filtered insar, ramp removed insar and PBO GPS stations. Three components of GPS velocity are projected to the satellite line-of-sight direction.

	Number of interferograms	Number of PBO GPS Stations	Misfit to GPS (LOS mm/yr)			
			Base model	InSAR filter	InSAR ramp	Improvement (filter versus ramp)
Salton Sea	14	18	2.5	2.6	3.5	26%
Creeping Section	6	35	2.7	3.4	3.8	11%
Mojave/Big Bend	12	13	3.7	4.0	4.3	8%

6.4 Discussion

The spatial covariance parameter σ_e in the model we adopted from Emardson et al. (2003) has variability, which is reflected as different atmospheric noise level in interferograms. The range of the variability is not provided in Emardson et al. (2003). As shown in equation (A17), the variability of σ_e will affect the number of interferograms required to resolve small interseismic signals. However, it will not affect the advantage of the filtering technique as long as the spatial characteristics of atmosphere are the same.

The technique we outline in this work can be used to improve our estimation and understanding of interseismic deformation, especially along the section of the SAF north of Los Angeles in the next few years. In the arid areas of Southern California, previous C-band InSAR satellites, ERS1/2 and ENVISAT, have acquired numerous datasets now that are available for analysis. However, temporal decorrelation due to vegetation has

severely limited this type of analysis along the northern section of the SAF. The improved temporal decorrelation from the Japanese L-band satellite ALOS will allow us to apply InSAR in Northern California (Wei and Sandwell, 2010). However, the acquisition of ALOS in California is infrequent, at ~ 2-4 images per year. At the time of this manuscript preparation (March, 2010), the ALOS dataset is not large enough to provide better constraints on the interseismic deformation. Based on our present calculations of the deformation signal and noise of ALOS data, we estimate that 5-years of ALOS data will be needed to improve the interseismic models using InSAR. The greatest improvements will be in Northern California where GPS measurements are sparse. All processing and model codes utilized here are publicly available (http://topex.ucsd.edu).

6.5 Conclusions

We have developed a remove/filter/restore technique to combine GPS and InSAR data optimally. This technique is based on the analysis of the spacing of EarthScope PBO and campaign GPS. We estimate the improvements of signal-to-noise ratio in InSAR data for measuring interseismic deformation in California. Because the residual interseismic signal and noise have different scale dependencies, filtering an interferogram can increase the signal-to-noise ratio by as much as 20%. Applying this procedure to a large stack of ERS1/2 interferograms in the Salton Sea, Southern California and ALOS interferograms near Parkfield, Central California and Mojave Desert/Big Bend, Southern California, we find improvements in all three areas using the

new technique, although they are not statistically significant. Our analysis shows that ALOS data will be able to make major contributions toward measuring interseismic deformation after collecting data for 5 years in orbit.

6.6 Acknowledgements

The authors would like to thank Debi Kilb and Karen Luttrell for the internal review of this paper, Shuanggen Jin and two anonymous reviewers for the insightful suggestions about this paper, and Yuri Fialko, Gilles Peltzer and Mark Simons for the discussions of this paper. This work was supported by the National Science Foundation Geophysics Program (EAR 0811772) and the NASA EarthScope Program - The InSAR and Geodetic Imaging Component (NNX09AD12G).

Text of Chapter 6, in full, is a reprint of the material as it appears in the Advances in Space Research. The dissertation author was the primary investigator and author of this paper.

6.7 Appendix A: The effect of high-pass filtering on atmospheric error

Assume the phase of the interferogram $p(\vec{x})$ has two parts:

$$p(\vec{x}) = s(\vec{x}) + n(\vec{x}) \tag{A1}$$

where $\vec{x}$ is two-dimensional spatial vector, $s(\vec{x})$ is the deformation signal and $n(\vec{x})$ is the atmospheric noise. Here we focus on the atmospheric noise, which is assumed stationary, random, and isotropic with zero mean.

The autocovariance of the noise is

$$C(\vec{x}) = \iint n(\vec{x}_o)n(\vec{x} - \vec{x}_o)d^2\vec{x}_o, \tag{A2}$$

where the integrals are performed over the area A of the interferogram.

By definition, the variance of the noise is

$$\delta^2 = C(0,0) = \iint n^2(\vec{x})d^2\vec{x} \tag{A3}$$

and the standard deviation of the noise is

$$\sigma_{noise} = \sqrt{\frac{\delta^2}{A}} \tag{A4}$$

Now suppose that we filter the noise using an isotropic filter. What is the new filtered autocovariance function and variance? The filtered noise is

$$\hat{n}(\vec{x}) = \iint f(\left|\vec{x} - \vec{x}_o\right|)n(\vec{x}_o)d^2\vec{x}_o \tag{A5}$$

where $f(|\vec{x}|)$ is a real valued isotropic filter. Note that the Fourier transform of the autocovariance function is the power spectrum and is given by

$$C(\vec{k}) = N(\vec{k})N^*(\vec{k}) \tag{A6}$$

where $N(\vec{k}) = \iint n(\vec{x})e^{-2\pi i(\vec{k}\bullet\vec{x})}d^2\vec{x}$.

Now we want to compute the autocovariance function and the variance of the filtered noise. The power spectrum of the filtered autocovariance is

$$\begin{aligned}\widehat{C}(\vec{k}) &= \widehat{N}(\vec{k})\widehat{N}^*(\vec{k}) \\ &= \left(N(\vec{k})F(|\vec{k}|)\right)\ \left(N(\vec{k})F(|\vec{k}|)\right)^* \\ &= F^2(|\vec{k}|)N(\vec{k})N^*(\vec{k})\end{aligned} \tag{A7}$$

where $F(|\vec{k}|)$ is the Fourier transform of the filter which is real-valued and isotropic.

Using the convolution theorem, we can rewrite this as

$$\widehat{C}(\vec{x}) = \iint_A g(|\vec{x} - \vec{x}_o|)C(\vec{x}_o)d^2\vec{x}_o \tag{A8}$$

where $g(|\vec{x}|) = \Im_2^{-1}(F^2(|\vec{k}|))$. Then we assume that $C(\vec{x}_o)$ is an isotropic function, so the integration can be partly completed in cylindrical co-ordinates, where $d^2\vec{x} = rdrd\theta$. The integration becomes

$$\hat{C}(r) = 2\pi \int_0^\infty g(|r - r_o|) C(r_o)\, r_o\, dr_o \tag{A9}$$

Next we use an autocovariance function of atmospheric noise based on signal delays in the GPS data from Southern California (Emardson et al., 2003). Their one-way noise variance model is:

$$\sigma = cL^\alpha + kH \tag{A10}$$

where σ is the square root of variance in mm, L is the distance between two points in km and H is the height difference in km. c, α and k are constants with value of 2.5, 0.5 and 4.8, respectively, derived from the neutral atmospheric delays in GPS data in Southern California. This model is valid over a range of 10-800 km for L and 0-3 km for H. While α is basically site-independent, c depends on the location on the Earth.

If e_1 and e_2 are the observation errors corresponding to the observations d_1 and d_2, which are any two pixels within a given interferogram, the autocovariance between these two errors are

$$Cov(e_1,e_2) = \frac{1}{2}Var(e_1) + \frac{1}{2}Var(e_1) - \frac{1}{2}Var(e_1 - e_2)$$
$$= \sigma_e{}^2 - \frac{1}{2}\sigma^2 \tag{A11}$$

where $\sigma_e{}^2$ is defined as $Var(e) = \frac{1}{2}Var(e_1) + \frac{1}{2}Var(e_1)$. Based on the GPS data, *Emardson et al.* (2003) find σ_e is about 50 mm and σ is described as in equation (A10). Usually, the dependence of height difference can be dropped because it is much smaller than the distance dependence. Then the autocovariance function is

$$Cov(e_1,e_2) = \sigma_e{}^2 - \frac{c^2}{2}L^{2\alpha}. \tag{A12}$$

Next, we use this function to calculate the covariance of the noise in a high-pass filtered interferogram. The Gaussian filter we use is

$$f(|\vec{x}|) = \frac{1}{2\pi\eta^2}e^{-\frac{|\vec{x}|^2}{2\eta^2}} = \frac{1}{2\pi\eta^2}e^{-\frac{x^2+y^2}{2\eta^2}} \tag{A13}$$

where η is the standard deviation of the Gaussian distribution and a characteristic wavelength. The Fourier transform of the Gaussian filter is

$$\Im_2\left[f(\vec{x})\right] = \iint \frac{1}{2\pi\eta^2}e^{-\frac{x^2+y^2}{2\eta^2}}e^{-2\pi i(\vec{k}\bullet\vec{x})}d^2\vec{x} = e^{-2\pi^2\eta^2(k_x^2+k_y^2)}. \tag{A14}$$

The inverse Fourier Transform of the squared Fourier Transform of the Gaussian filter is

$$\Im_2^{-1}\left[\Im_2\left[f(\vec{x})\right]^2\right] = \iint (e^{-2\pi^2\eta^2(k_x^2+k_y^2)})^2 e^{2\pi i(\vec{k}\bullet\vec{x})} d^2\vec{k} = \frac{1}{4\pi\eta^2} e^{-\frac{x^2+y^2}{4\eta^2}} \tag{A15}$$

We substitute equation (A15) and (A12) into (A9). Then the filtered autovariance function is

$$\widehat{C}(r) = 2\pi \int_0^{L_{\max}} \frac{1}{4\pi\eta^2} e^{-\frac{|r-r_o|^2}{4\eta^2}} \left(\sigma_e^2 - \frac{c^2}{2}\left(r-r_o\right)^{2\alpha}\right) r_o \, dr_o . \tag{A16}$$

where $L_{\max}$ is the maximum distance that equation (A10) is valid, which equals 800 km in Southern California (Emardson et al., 2003). We are most interested in the variance, which is equation (A16) at *r = 0.* Since $\alpha = 0.5$ based on GPS data, the integration is simplified to

$$\widehat{C}(0) = 2\pi \int_0^{L_{\max}} \frac{1}{4\pi\eta^2} e^{-\frac{r_o^2}{4\eta^2}} (\sigma_e^2 - \frac{c^2}{2} r_o) \, r_o \, dr_o = \sigma_e^2 - \frac{c^2\eta\sqrt{\pi}}{2} erf(\frac{L_{\max}}{2\eta}) . \tag{A17}$$

This is the result of the low-pass filter. To get the high-pass result, we need to subtract equation (A17) from the original variance,

$$\sigma_f^2 = \sigma_e^2 - \hat{C}(0) = \frac{c^2 \eta \sqrt{\pi}}{2} erf(\frac{L_{\max}}{2\eta}). \quad \text{(A18)}$$

We substitute parameters in equation (A17) with values, $\sigma_e = 50, L_{\max} = 800, c = 2.5$, then the standard deviation of the noise in the high-pass filtered data is

$$\sigma_f = \sqrt{3.125 \eta \sqrt{\pi} erf(\frac{800}{2\eta})}. \quad \text{(A19)}$$

6.8 Appendix B: Dislocation model

The vector velocity field cannot be completely resolved with point GPS measurements, so we use a dislocation model (1 km resolution), constrained by GPS velocities, to provide a complete vector field. We expect the model to be accurate at large scales especially away from the faults, but less accurate at smaller scales. We model the North American-Pacific plate boundary as a series of vertical connected fault dislocations imbedded in an elastic plate overlying a viscoelastic half-space (Smith and Sandwell, 2006). The dislocation model simulates interseismic strain accumulation, coseismic displacement, and post-seismic viscous relaxation of the mantle. However when considering the recent average EarthScope PBO velocity field (2004-2009), the interseismic part of the model dominates. Three types of data are used to estimate the

parameters of the model: 1) Long-term slip rates (i.e. over many earthquake cycles) are initially constrained by geologic estimates (WGCEP, 1995; 1999; 2003; 2007) and then adjusted to ensure that the sum of the slip across the plate boundary is equal to the far-field estimate of 45 mm/yr. Slip rates are further adjusted to match contemporary geodetic estimates of far-field slip (e.g., Bennett et al., 1996; Freymeuller et al., 1999; Becker et al., 2004; Meade and Hager, 2005; Fay and Humphreys, 2005; Fialko, 2006). 2) Rupture history on each fault segment is based on historical accounts and paleoseismic recurrence intervals (e.g., WGCEP 1995; 1999; 2003; 2007; Grant and Lettis, 2003; Weldon et al., 2004; 2005). We assume that the amount of coseismic slip for each event is equal to the accumulated slip deficit on that segment. 3) Present-day crustal velocities are derived from 1709 GPS estimates from EarthScope PBO, as well as campaign GPS compiled by Corne Kreemer (Kreemer et al., 2009). An iterative least squares approach is used to adjust the locking depth along each segment (Smith-Konter et al., 2009 in preparation). For this model, we included interseismic slip on 41 fault segments over variable locking depths (ranging from 1-23 km), and assume the following model parameters: shear modulus (30 GPa), mantle viscosity (1e19 Pa s), and elastic plate thickness (60 km). Best-fit models have an RMS residual velocity misfit of 2.02 mm/yr in the E-W direction, 2.69 mm/yr in the N-S direction, and 2.73 mm/yr in the vertical direction.

Since the dislocation model with over 45 parameters cannot capture all of the tectonic and non-tectonic motions, especially in areas away from model fault segments, we fit the horizontal GPS residuals (using a 40 km block median) to a biharmonic spline using a tension factor of 0.45 (Wessel and Bercovici, 1998) weighted by the uncertainty

in each GPS data point. The spline represents un-modeled fault motion at scales greater than 40 km wavelength. After fitting the residual GPS velocities, the horizontal data-model misfits are 1.47 mm/yr in the E-W direction and 1.56 my/yr in the N-S direction.

6.9 References

Agnew, D.C., Owen, S., Shen, Z.K., Anderson, G., Svarc, J., Johnson, H., Austin, K.E., Reilinger, R. Coseismic displacements from the Hector Mine, California, earthquake: results from survey-mode GPS measurements, Bull. Seism. Soc. Am., 92, pp. 1355-1364, 2002.

Bendat, J. S., and A. G. Piersol, Random data analysis and measurement procedures. Second ed. New York: John Wiley & Sons, 1986.

Bennett, R.A., Rodi, W., Reilinger, R.E. Global Positioning System constraints on fault slip rates in southern California and northern Baja, Mexico, J. Geophys. Res., 101, pp. 21,943–21,960, 1996.

Burgmann, R., Rosen, P.A., Fielding, E.J. Synthetic aperture radar interferometry to measure Earth's surface topography and its deformation, Annu. Rev. Earth Planet. Sci., 28, pp. 169-209, 2000.

Doin, M.P., Lasserre, C., Peltzer, G., Cavalie, O., Doubre, C., C Corrections of stratified tropospheric delays in SAR interferometry: Validation with global atmospheric models, Journal of Applied Geophysics, 69, pp. 35-50, 2009.

Elliott, J.R., Biggs, J., Parsons, B., Wright, T.J. InSAR slip rate determination on the Altyn Tagh Fault, northern Tibet, in the presence of topographically correlated atmospheric delays, Geophys. Res. Lett, 35, pp. L12309, 2008.

Emardson, T.R., Simons, M., Webb, F.H. Neutral atmospheric delay in interferometric synthetic aperture radar applications: statistical description and mitigation, J. Geophys. Res, 108, pp. 2231, 2003.

Fay, N.P., Humphreys, E.D. Fault slip rates, effects of elastic heterogeneity on geodetic data, and the strength of the lower crust in the Salton Trough region, southern California, J. Geophys. Res, 110, 2005.

Feigl, K.L., Agnew, D.C., Bock, Y., Dong, D., Donnellan, A., Hager, B.H., Herring, T.A., Jackson, D.D., Jordan, T.H., King, R.W. Space geodetic measurement of crustal deformation in central and southern California, 1984-1992, J. Geophys. Res., 98, pp. 21,677–21,712, 1993.

Ferretti, A., Prati, C., Rocca, F. Nonlinear subsidence rate estimation using permanent scatterers in differential SAR interferometry, IEEE Trans. Geosci. Remote Sensing, 38, pp. 2202-2212, 2000.

Ferretti, A., Prati, C., Rocca, F. Permanent scatterers in SAR interferometry, IEEE Trans. Geosci. Remote Sensing, 39, pp. 8-20, 2001.

Fialko, Y. Evidence of fluid-filled upper crust from observations of postseismic deformation due to the 1992 Mw7. 3 Landers earthquake, J. Geophys. Res., 109, pp. B08401, 2004a.

Fialko, Y. Probing the mechanical properties of seismically active crust with space geodesy: Study of the coseismic deformation due to the 1992 M w 7.3 Landers (southern California) earthquake, J. Geophys. Res., 109, pp. B03307, 2004b.

Fialko, Y. Interseismic strain accumulation and the earthquake potential on the southern San Andreas fault system, Nature, 441, pp. 968-971, 2006.

Goldstein, R.M., Werner, C.L. Radar interferogram filtering for geophysical applications, Geophys. Res. Lett., 25, pp. 4035–4038, 1998.

Gourmelen, N., Amelung, F., Casu, F., et al. Mining-related ground deformation in Crescent Valley, Nevada: Implications for sparse GPS networks, Geophys. Res. Lett., 34, L09309, doi:10.1029/2007GL029427, 2007.

Hanssen, R.F. Radar Interferometry: Data Interpretation and Error Analysis, Dordrecht: Kluwer Academic Publishers, 2001.

Jin, S.G., and Park, P.H. Strain accumulation in South Korea inferred from GPS measurements, Earth Planets Space, 58(5), 529-534, 2006.

Jin, S.G., Park, P.H., Zhu, W. Micro-plate tectonics and kinematics in Northeast Asia inferred from a dense set of GPS observations, Earth Planet. Sci. Lett., 257, pp. 486-496, doi: 10.1016/j.epsl.2007.03.011, 2007.

Johanson, I.A., Fielding, E.J., Rolandone, F., Burgmann, R. Coseismic and postseismic slip of the 2004 Parkfield earthquake from space-geodetic data, Bull. Seismol. Soc. Am., 96, pp. 269-282, 2006.

Jonsson, S., Zebker, H., Segall, P., Amelung, F. Fault slip distribution of the 1999 M w 7.1 Hector Mine, California, earthquake, estimated from satellite radar and GPS measurements, Bull. Seismol. Soc. Am., 92, pp. 1377-1389, 2002.

Kreemer, C., Blewitt, G., Hammond, W.C., Plag, H.A. High-Resolution Strain Rate Tensor Model for the Western U.S, Presentation at the EarthScope Annual Meeting, Boise, Idaho, 2009.

Lohman, R.B., Simons, M. Some thoughts on the use of InSAR data to constrain models of surface deformation: Noise structure and data downsampling, Geochem. Geophys. Geosyst., 6, pp. Q01007, 2005.

Massonnet, D., Feigl, K., Rossi, M., Adragna, F. Radar interferometric mapping of deformation in the year after the Landers earthquake, Nature, 369, pp. 227-230, 1994.

Massonnet, D., Feigl, K.L. Radar interferometry and its application to changes in the Earth's surface, Rev. Geophys, 36, pp. 441–500, 1998.

Massonnet, D., Rossi, M., Carmona, C., Adragna, F., Peltzer, G., Feigl, K., Rabaute, T. The displacement field of the Landers earthquake mapped by radar interferometry, Nature, 364, pp. 138-142, 1993.

Massonnet, D., Thatcher, W., Vadon, H. Detection of postseismic fault-zone collapse following the Landers earthquake, Nature, 382, pp. 612-616, 1996.

Meade, B.J., Hager, B.H. Block models of crustal motion in southern California constrained by GPS measurements, J. Geophys. Res, 110, pp. B03403, 2005.

Mesinger, F., DiMego, G., Kalnay, K. et al. North American regional reanalysis. Bull. Am. Meteol. Soc., 87, pp. 343–360, 2006.

Payne, S. J., McCaffrey, R., and King, R.W. Strain rates and contemporary deformation in the Snake River Plain and surrounding Basin and Range from GPS and seismicity, Geology, 36, 647-650, 2008.

Peltzer, G., Hudnut, K.W., Feigl, K.L. Analysis of coseismic surface displacement gradients using radar interferometry: New insights into the Landers earthquake, J. Geophys. Res., 99, pp. 21,971–21,981, 1994.

Peltzer, G., Rosen, P., Rogez, F., Hudnut, K. Postseismic rebound in fault step-overs caused by pore fluid flow, Science, 273, pp. 1202, 1996.

Pollitz, F.F., Wicks, C., Thatcher, W. Mantle flow beneath a continental strike-slip fault: Postseismic deformation after the 1999 Hector Mine earthquake, Science, 293(5536), pp. 1814-1818, 2001.

Rosen, P.A., Hensley, S., Joughin, I.R., Li, F.K., Madsen, S.N., Rodriguez, E., Goldstein, R.M. Synthetic aperture radar interferometry, Proceedings of the IEEE, 88, pp. 333-382, 2000.

Rotta, H., and Naglerb, T. The contribution of radar interferometry to the assessment of landslide hazards, Advances in Space Science, 37, pp. 710-719, 2006.

Sandwell, D.T., Bird, P., Freed, A., et al. Comparison of strain-rate maps of western North America, Presentation at the EarthScope Annual Meeting, Boise, Idaho, 2009.

Sandwell, D.T., Myer, D., Mellors, R., Shimada, M., Accuracy and Resolution of ALOS Interferometry: Vector Deformation Maps of the Father's Day Intrusion at Kilauea, IEEE Trans. Geosci. Remote Sensing, 46, pp. 3524-3534, 2008.

Sandwell, D.T., Price, E.J. Phase gradient approach to stacking interferograms, J. Geophys. Res, 103, pp. 30183-30204, 1998.

Sandwell, D.T., Sichoix, L., Agnew, D., Bock, Y., Minster, J.B. Near real-time radar interferometry of the Mw 7.1 Hector Mine Earthquake, Geophys. Res. Lett, 27, pp. 3101-3104, 2000.

Schmidt, D.A., Bürgmann, R. Time-dependent land uplift and subsidence in the Santa Clara valley, California, from a large interferometric synthetic aperture radar data set, J. Geophys. Res, 108, pp. 2416, 2003.

Schmidt, D.A., Burgmann, R., Nadeau, R.M. Distribution of aseismic slip rate on the Hayward fault inferred from seismic and geodetic data, J. Geophys. Res, 110, pp. B08406, 2005.

Segall, P., Davis, J.L. GPS applications for geodynamics and earthquake studies, Annu. Rev. Earth Planet. Sci., 25, pp. 301-336, 1997.

Simons, M., Fialko, Y., Rivera, L. Coseismic deformation from the 1999 M w 7.1 Hector Mine, California, earthquake as inferred from InSAR and GPS observations, Bull. Seismol. Soc. Am., 92, pp. 1390-1402, 2002.

Smith, B., Sandwell, D. Coulomb stress accumulation along the San Andreas Fault system, J. Geophys. Res, 108, pp. 2296, 2003.

Smith, B.R., Sandwell, D.T. A model of the earthquake cycle along the San Andreas Fault System for the past 1000 years, J. Geophys. Res, 111, pp. B01405, 2006.

Smith-Konter, B., and D. T. Sandwell (2009), Stress evolution of the San Andreas Fault System: Recurrence interval vs. locking depth, *Geophys. Res. Lett.*, 36, doi:10.1029/2009GL037235.

Smith-Konter, B., T. Solis, and D.T. Sandwell (2008), Data-derived stress uncertainties of the San Andreas Fault System, EOS Trans. AGU, 89 (53), Fall Meet. Suppl., U51B-0029.

Sugaa, Y., Takeuchia, S., Oguroa, Y., et al. Application of ERS-2/SAR data for the 1999 Taiwan earthquake, Advances in Space Science, 28, pp. 155-163, 2001.

Tomiyama, N., Koike, K., and Omura, M. Detection of topographic changes associated with volcanic activities of Mt. Hossho using D-InSAR, Advances in Space Science, 33, pp. 279-283, 2004.

Tong, X., Sandwell, D.T., Fialko, Y. Coseismic deformation of Wenchuan earthquake, submitted to J. Geophys. Res., 2009.

Uppala, S., Kållberg, P., Simmons, A., Andrae, U. The ERA-40 re-analysis. Q. J. R. Meteorol. Soc., 131, pp. 2961–3012, 2005.

Wdowinski, S., Smith-Konter, B., Bock, Y., Sandwell, D.T. Spatial characterization of the interseismic velocity field in southern California, Geology, 35, pp. 311-314, 2007.

Wei, M., Sandwell, D. Decorrelation of L-band and C-band interferometry over vegetated areas in California, IEEE Trans. Geosci. Remote Sensing, in press, 2010.

Wei, M., Sandwell, D., Fialko, Y. A silent Mw 4.7 slip event of October 2006 on the Superstition Hills fault, southern California, J. Geophys. Res., 114, pp. B07402, 2009.

Wright, T.J., Parsons, B., England, P.C., Fielding, E.J. InSAR Observations of Low Slip Rates on the Major Faults of Western Tibet.Science,305, pp. 236 - 239, 2004.

Zebker, H.A., Rosen, P. Atmospheric artifacts in interferometric SAR surface deformation and topographic maps, J. Geophys. Res., 102, pp. 7547–7563, 1997.

Zebker, H.A., Rosen, P., Goldstein, R., Gabriel, A., Werner, C.L. On the derivation of coseismic displacement fields usingdifferential radar interferometry: The Landers earthquake, Geoscience and Remote Sensing Symposium, 1994. IGARSS'94. Surface and Atmospheric Remote Sensing: Technologies, Data Analysis and Interpretation., International, 1, 1994.

7. CHAPTER 7: Conclusions

Earthquake safety tip 7

In the event of a quake, get under something heavy, such as a desk, a table or your uncle.

7.1 Using InSAR and GPS to measure shallow fault creep

So far, geodetic data is the best way to measure shallow fault creep. GPS and InSAR are highly complementary methods for measuring surface deformation. GPS data provides high precision (mm/yr) vector displacements at high temporal sampling rates and a moderate spatial sampling (10 km). The main weakness of using only GPS array data is that the spacing of is not adequate for resolving high velocity gradients (i.e., areas of high strain rate) which usually occur near active faults. Alternatively, InSAR data has sub-cm precision, a moderate temporal sampling rate (10–50 days) and a high spatial sampling (100 m), so theoretically it could provide the short spatial scale information currently lacking in GPS data. We propose a new method, called remove/filter/restore, to optimal combine InSAR and GPS to measure interseismic deformation. Because the residual interseismic signal and noise have different scale dependencies, filtering an interferogram can increase the signal-to-noise ratio by as much as 20%. The optimal wavelength of the Gaussian filter is determined based on the spacing of continuous GPS stations in California. We test this method in the Salton Sea, Southern California and ALOS interferograms near Parkfield, Central California and Mojave Desert/Big Bend, Southern California using. Comparison between this

method and the traditional ramp-removal method shows that our method improves the final measurements in all three cases.

Temporal decorrelation is one of the main limitations for recovering interseismic deformation along the San Andreas Fault system using interferometric synthetic aperture radar. To assess the improved correlation properties of L-band with respect to C-band, we analyzed L-band Advanced Land Observation Satellite (ALOS) interferograms with a range of temporal and spatial baselines over three vegetated areas in California and compared them with corresponding C-band European Remote Sensing Satellite (ERS) interferograms. The three areas are: the highly vegetated northern California forests of the Coast Range area, central California near Parkfield, the Imperial Valley of Southern California. In forest area, ERS decorrelated in less than 6 months whereas ALOS kept correlated after 2 years. In farmlands, both ERS and ALOS lose correlation in a few months. In urban area, both ERS and ALOS kept correlation for more than 2 years. Our result shows that L-band ALOS data is better for measuring creep in forest area, because creep rate is slow and long time interval between SAR acquisitions is required to get enough signal-to-noise ratio.

To date the primary limitation for using ALOS for recovering interseismic strain along the San Andreas Fault is that there are too few acquisitions along the descending passes, which have better geometry for measuring strike-slip motion. Nevertheless the archive of ALOS images from ascending passes is growing rapidly and they will be important for constraining the vertical motions along the fault system. We look forward to the more systematic L-band observations from ALOS-2 (2013 launch), DESDynI (2016-2020 launch), and German satellite TanDEM-L (TBD).

7.2 New creep observations in the Salton Trough

As previous and our research show, fault creep in the Salton Trough are mainly triggered by nearby earthquakes, such as the Landers, Hector Mine and El Mayor-Cucapah earthquakes. Our main observations are: 1) the magnitude of triggered slip is on the order of a few centimeters. Triggered slip was found repeatable on certain segments, such as the Superstition Hills Fault and San Andreas Fault. 2) Not all earthquakes triggered fault slip the same time and same way. For example, Landers and Hector Mine earthquakes only triggered slip on the San Andreas Fault and the Superstition Hills Fault. The 2010 El Major earthquake triggered more than 12 faults. 3) The triggered slip on the Superstition Hills Fault has similar along-fault pattern to the 1987 co-seismic deformation. The accumulated fault slip on the surface is still less than the co-seismic slip in depth estimated in 1987 earthquake. These imply that after 23 years, this fault is still undergoing afterslip. 4) The depth of shallow fault creep is mainly 2-4 km, similar as the sedimentary depth. 5) In addition to triggered slip, the fault creep in the Salton Trough can also occur spontaneously.

7.3 Implications for creep mechanisms

In chapter 2 and 3, I studied the creep event on the Superstition Hills Fault in October 2006 and triggered slip on the 2010 El Mayor-Cucapah Earthquake. Modeling of the InSAR data shows the depth of fault creep in the Salton Trough, specifically the Superstition Hills Fault, is similar to the sedimentary depth, which is probably due to high pore-pressure in unconsolidated sediments in this area. This observation is consistent with the rate-and-state theory that the sediments are velocity strengthening.

In chapter 4, we studied the relationship between the fault creep rate and the shallow stress-accumulating rate. Data shows that although linear correlation is valid, the scatters of the data represent that there are more factors control the shallow creep rate. For example, rock type might be an important factor.

7.4 Future research

First, it is important to continue to measure fault creep along faults in California. Even though creep observations are abundant in areas like the Hayward Fault and Salton Trough, none of the observations exceeds even one seismic cycle. Continuing observation will provide complete temporal coverage of the seismic cycle and may provide new insights in the future. In areas that observations are not abundant, such as Macamma Fault in the Northern California, it is more important to acquire L-band InSAR observation to improve our knowledge of these faults. Actually, the later one can be done much sooner using the planned L-band InSAR satellites.

Second, new instruments might provide more accurate observations of fault creep. For example, other than C-band (5.6 cm) and L-band (24 cm), there are also satellites using shorter wavelength signal (X band, 31 mm), such as TerraSAR-X, launched on June 15, 2007 and a companion satellite TanDEM-X on 21 June 2010. The shorter wavelength should give more precise observation, which is very important in creep study. In addition, using airborne SAR measurements can also improve the resolution of fault creep. The Jet Propulsion Laboratory (JPL) operates UVASAR, which is designed for interferometric applications. It has finer pixel resolution than the satellite systems so can reveal details that are missing in satellite InSAR. For example, in the

2010 El Major-Cucapah earthquake, UVASAR data reveal fault creep on the Imperial fault, which is not visible in ENVISAT or ALOS. The disadvantages of the UVASAR are that raw data is not yet useful to others because the phase connections for the irregular aircraft trajectory can only be done at JPL. Another drawback to UVASAR is that it needs an image before and after the event in order to make observations. Obtaining a recent image immediately preceding an event is problematic since it would require regular flights over the area being monitored. In addition, JPL is not allowed to collect data outside the U.S. This also limits the use of this technique.

Third, observations other than geodesy might help to constrain the deformation model. In this thesis, only geodetic data was used to constrain the model. Observations from other methods, including seismic, geological and geochemical data should help reduce the number of possible models. Actually, some researchers have already used micro-seismic data to constraint their model.

Finally, fault creep has also been observed in subduction zones, such as the Cascade in Pacific Northwest of the U.S. Numerous studies focused on this area. A number of studies show evidence that shallow part of the subduction zone also show creep, although it is generally hard to observe because the creeping section occurs in the deep ocean. However, as technology progresses, similar modeling can be done when data become available.

Creep research continues to be an important area of study. There are fault segments that we know little about. For example, decorrelation prevents detailed analysis of creep along the Macamma Fault in the northern California. I would like to end this thesis by quoting from a report of the 2002 Working Group on California

Earthquake Probabilities, “we need more and better GPS and INSAR data to resolve the extent to which creep is occurring at depth and the partition of slip on the different, closely spaced faults in the region.” [WGCEP, 2002].

8. CHAPTER 8: Estimates of Ridge-Axis Heat Flow from Depth and Age Data

Earthquake safety tip 8

Those living in areas not prone to earthquakes can respond quickly to the plight of disaster victims in quake zones by complacently smirking and saying, "I told you so."

8.1 Abstract

The total heat output of the Earth constrains models of mantle and core dynamics. Previously-published estimates (42 - 44 TW) have recently been questioned because the measured conductive heat flow on young oceanic lithosphere is about a factor of 2 less than the expected heat flow based on half-space cooling models. Taking the ocean heat flow values at face value reduces the global heat flow from 44 to 31 TW, which has major implications for geodynamics and Earth history. To help resolve this issue, we develop a new method of estimating oceanic heat flow from depth and age data. The overall elevation of the global ridge system, relative to the deep ocean basins, provides an independent estimate of the total heat content of the lithosphere. Heat flow is proportional to the measured subsidence rate times the heat capacity divided by the thermal expansion coefficient. The largest uncertainty in this method is due to uncertainties in the thermal expansion coefficient and heat capacity. Scalar subsidence rate is computed from gradients of depth and age grids. The method cannot be applied over very young seafloor (< 3 Ma) where age gradient is discontinuous and the assumption of isostasy is invalid. Between 3 and 66 Ma the new estimates are in excellent agreement with half-space cooling model. Our

independent estimate of the total heat output of Cenozoic seafloor is 18.6 to 20.5 TW, which leads to a global output of 42 to 44 TW in agreement with previous studies.

8.2 Introduction

The total heat output of the Earth is comprised of heat flow from the core, radiogenic heat production in the mantle, secular cooling of the Earth, and radiogenic heat production in the continental crust. While the magnitude of the individual components is highly uncertain, the total surface heat output has been estimated at 42 - 44 TW [*Sclater et al*., 1980; *Pollack et al*., 1993]. Recently this estimate has been questioned [*Hofmeister and Criss*, 2005] mainly because the measured conductive heat flow on young oceanic lithosphere is about a factor of 2 less than the expected heat flow based on conductive cooling models. Taking ocean heat flow measurements at face value leads to a global heat output of only 31 TW. A reduction of this magnitude has important implications for heat flow across the core/mantle boundary, which is believed to drive mantle plumes. Moreover *Hofmeister and Criss* [2005] argue that this lower value of global heat flux is more consistent with the isotope chemistry and cooling history of the Earth.

The origin of 9 TW of this difference in global heat output is related to how one assesses heat flow over young oceanic lithosphere. Lithospheric cooling models, based primarily on the increase in seafloor depth with age, but also on conductive surface heat flow over older lithosphere (> 40 Ma) predict a high value of heat flow at the ridges [*McKenzie*, 1967; *Davis and Lister*, 1974; *Parsons and Sclater*, 1977; *Stein and Stein*, 1992]. Moreover, in the case of a one-dimensional approximation to the heat conduction

equation, the models have an infinite heat flow at zero age. While the integrated heat flow for these models is non-singular [*Oldenburg,* 1975] it is nevertheless a factor of 2 greater than the integrated measured heat flow. There are two ways to understand this discrepancy.

A) The true heat flow out of the top of the plate matches the predictions of the cooling models but conductive heat flow probes cannot "see" the true value because much of the heat is advected by hydrothermal circulation [*Lister*, 1972; *Williams et al.,* 1974; *Sleep and Wolery*, 1978, *Anderson and Hobart*, 1976]. In this case, the discrepancy between the measured and predicted heat flow has been thought to be the primary constraint on how the hydrothermal flux is divided between near-ridge and off-ridge environments [*Stein and Stein*, 1994].

B) The true heat flow out of the top of the plate is nearly equal to the measured heat flow. *Hofmeister and Criss* [2005] provide a number of theoretical and observational arguments in favor of this case. They claim that that hydrothermal circulation cannot cause the huge discrepancy because the MOR magma system is too small and hydrothermal systems are weak movers of heat.

In this paper we use the observed subsidence of the spreading ridges and physically realistic bounds on thermal expansion coefficient and heat capacity to resolve this issue. As shown in previous studies, elevation of ridges reflects total heat content of lithosphere [*Parsons and McKenzie*, 1978; *Doin and Fleitout*, 1996]. Therefore, the

scalar subsidence rate is a direct measure of the difference between surface heat flow and heat flow into the base of the plate [*Sandwell and Poehls*, 1980]. We re-derive this direct relationship between subsidence rate by using conservation of energy and local isostasy. The relationship does not rely on a particular cooling model and is therefore independent of the thermal conductivity of the lithosphere. Using gridded topography and age data, we estimate surface heat flow and show it is consistent with the half-space cooling model between ages of 3 and 66 Ma. The method fails to provide reliable heat flow estimates directly at the ridges because the assumption of local isostasy is not valid; ridge-axis topography is partly supported by dynamics and flexure. Overall the results are in agreement with a global heat output of 42-44 TW [*Sclater et al., 1980*; *Pollack et al*., 1993].

Theory

The theory is based on energy conservation, thermal contraction, and isostasy and does not rely on any particular heat transfer model [*Parsons and McKenzie*, 1978]. Assuming steady-state spreading and no internal heat generation, the conservation of energy is given by the time independent equation of heat transport where horizontal advection is balanced by the divergence of the heat flux.

$$\rho_m C_P \mathbf{v} \bullet \nabla T = \nabla \bullet \mathbf{q} \qquad (1)$$

where T is temperature, $\mathbf{q}$ is the heat flux vector, ρ_m the density, C_p the specific heat, and $\mathbf{v}$ is the horizontal velocity of the plate. We use the principles of thermal

contraction and isostasy to determine the increase in seafloor depth with increasing age $d(t)$. A reduction in temperature will cause an increase in density ρ as

$$\rho(T) = \rho_m[1 - \alpha(T - T_m)] \tag{2}$$

where ρ_m is the density of the lithosphere at a temperature of T_m and α is the coefficient of thermal expansion. For thermal isostasy, the seafloor depth depends on the integrated temperature as

$$d(t) = \frac{-\alpha\rho_m}{\rho_m - \rho_w} \int_d^L (T - T_m)dz \tag{3}$$

where ρ_w is the density of seawater and L is the depth to the bottom of the thermal boundary layer and also the depth of compensation. Taking the gradient of both sides of equation 4 and then the dot product with the plate velocity results in

$$\mathbf{v} \bullet \nabla d(t) = \frac{-\alpha\rho_m}{\rho_m - \rho_w} \int_d^L \mathbf{v} \bullet \nabla T dz \tag{4}$$

Next we use conservation of energy (equation 1) to re-write equation (4) as

$$\mathbf{v} \bullet \nabla d = \frac{-\alpha}{(\rho_m - \rho_w)C_P} \int_d^L \nabla \bullet \mathbf{q} dz \tag{5}$$

Finally by neglecting lateral heat transport on the right side of equation (5) and integrating, we arrive at

$$\int_d^L \frac{\partial}{\partial z} q(z)dz = q(L) - q(d) = q_b - q_s \tag{6}$$

where q_b and q_s are the surface heat flow and basal heat flow, respectively. Substitution equation (6) into equation (5), it gives

$$\mathbf{v} \bullet \nabla d = \frac{-\alpha}{(\rho_m - \rho_w)C_p}(q_b - q_s) \tag{7}$$

This equation relates the scalar subsidence rate to the difference between the surface and basal heat flow and it depends only on the thermal expansion coefficient, the heat capacity and the densities of mantle and seawater. Given a grid of seafloor age $A(\mathbf{x})$ [*Mueller et al.*, 1997], the local fossil spreading velocity is $\mathbf{v} = \frac{\nabla A}{\nabla A \bullet \nabla A}$. The final expression becomes

$$q_s - q_b = \frac{(\rho_m - \rho_w)C_p}{\alpha} \frac{\nabla A \bullet \nabla d}{\nabla A \bullet \nabla A} \tag{8}$$

Equation (8) provides a way to calculate heat flow based only on depth and age data sets. Note that the result is independent of thermal conductivity and its possible depth variations so the objection of *Hofmeister and Criss* [2005] that the temperature variations in thermal conductivity have been overlooked is now irrelevant.

While the final result is independent of the vertical heat transport mechanism, it does depend on two unknown parameters - heat capacity and thermal expansion coefficient. It would be circular reasoning to estimate the heat flow by adopting values of these parameters based on modeling depth and heat flow versus age data (e.g., from *Parsons and Sclater*, [1977]). Therefore, we must use parameter values developed independently from experimental data. As discussed in *Doin and Fleitout* [1996], these parameters are temperature and pressure dependent. However, *Doin and Fleitout* [1996] demonstrate that using temperature-averaged values provides a good approximation to the numerically-integrated depth and heat-flow models which use the full temperature dependence. *Doin and Fleitout* [1996] use data from *Kajiyoshi* [1986] to compute temperature-averaged values of heat capacity and thermal expansion coefficient. They arrive at the following values that we will initially adopt for our analysis ($\alpha = 3.85 \times 10^{-5\,o}C^{-1}$; $C_p = 1124 J \cdot kg^{-1} \cdot {}^{o}C^{-1}$; $\rho_m = 3330 kg \cdot m^{-3}$; $\rho_w = 1025 kg \cdot m^{-3}$). Uncertainties in our estimates of heat flow based on subsidence rate will depend in a first-order way on the values of these parameters and we discuss possible physical bounds on their values.

8.3 Mid-Atlantic ridge

The theory is first applied at Mid-Atlantic ridge to illustrate the strengths and weaknesses of the method. The result is shown in Figure 1 where we have plotted the surface heat flow minus the basal heat flow out to an age of 66 Ma using thermal parameters and densities provided above. Over Cenozoic seafloor, the basal heat flow is believed to be less than about 38 mWm^{-2}, [*Dion and Fleitout*, 1996] and therefore is a minor component of the surface heat flow. We initially ignore this contribution but later consider how basal heat flux effects the estimate of global heat flow. Most depth versus age analyses requires sediment-corrected depth before comparisons with models [*Renkin and Sclater,* 1988]. We have not applied this correction because sediments are generally thin on young seafloor and we are interested in the depth gradient, which is independent of sediment thickness as long as the sediments are locally uniform thickness. However, if the thickness of the sediments increases systematically with age along age corridors, we will underestimate the subsidence rate and thus the heat flow.

There are two practical problems that should be considered when computing the scalar subsidence rate $\frac{\nabla d \bullet \nabla A}{\nabla A \bullet \nabla A}$. First the age gradient ∇A should not be computed across ridges or transform faults because the denominator can go to zero in this case. Second $\frac{\partial d}{\partial t}$ can have the wrong sign in areas where there is an axial valley. The axial valley is not in isostatic equilibrium it should not be included in the analysis. To solve these two problems, we omit seafloor younger then 0.5 Ma from the analysis and additionally mask seafloor within a 20 km distance of the ridge/transform plate

boundary. The masked area is shown as a grey area in Figure 1. We also find that raw computation of data on a 0.1 degree grid leads to large oscillations in the scalar subsidence rate. This is caused by two effects, short wavelength topography and sharp variations in the age gradient due to fracture zones and other processes. To suppress these noise processes, we smooth the scalar subsidence rate with a 2-D Gaussian filter with a 0.5 gain at a wavelength of 265 km. This filter has no effect on the average of the heat flow over age bins (Figure 2), however the smoothing provides a realistic heat flow map as shown in Figure 1.

To compare these heat flow estimates with lithospheric cooling models, we average the surface minus basal heat flow into 3 Ma age bins (Figure 2, bottom). The first age bin (0.5 - 3.5 Ma) is sometimes partly masked over the youngest seafloor so estimates may be biased low but at greater ages we believe these estimates of heat flow are reliable. The uncertainty in each bin is the square root of the variance divided by the number of linearly-independent measurements which depends on the band-width of the low-pass filter. The statistical uncertainties are quite small because the depth versus age relation is well behaved. However, these statistical uncertainties do not reflect the true uncertainty in the heat flow estimates because, as discussed above, the uncertainties in our knowledge of the temperature-average thermal expansion coefficient and heat capacity are much larger. Our surface heat-flow versus age estimates is in basic agreement with the theoretical curve $q = 480/\sqrt{t}$, but only after adding a basal heat flow of 38 mWm^{-2}. The important conclusion is that the estimated heat flow is significantly greater than the average of the conductive heat flow measurements. Even without this

largely unknown basal heat flow contribution, the heat flow estimates are more than 200 mWm^{-2} on 5 Ma seafloor.

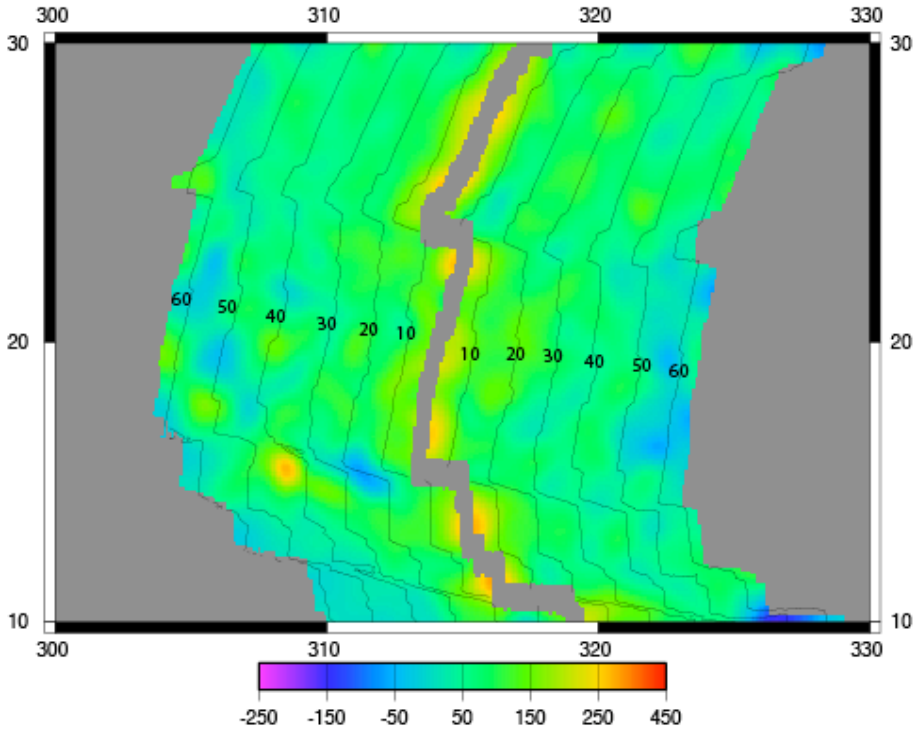

Figure 8-1. Surface minus basal heat flow based on equation 9 using depths from a 2-minute global grid [*Smith and Sandwell*, 1997] and ages from a global grid at 0.1 degree spacing [*Mueller et al.*, 1997]. Heat is highest on young seafloor > 250 mW m^{-2} and decreases systematically with age out to 66 Ma. Spatial variations in heat flow could be either be due to Airy-compensated topography which produces depth gradients at scales greater than the flexural wavelength (~300 km) or perhaps real variation in surface or basal heat flow.

In addition to estimating the heat flow versus age we also calculate depth versus age (Figure 2, top). Depth-age estimates are consistent with the empirical model $d = 2500 + 350\sqrt{t}$ [*Parsons and Sclater*, 1977] although we find the observed depth is

systematically too shallow at older ages. This could be due to neglecting the sediment correction or including areas that are anomalously shallow because of crustal thickening [*Hillier and Watts*, 2005].

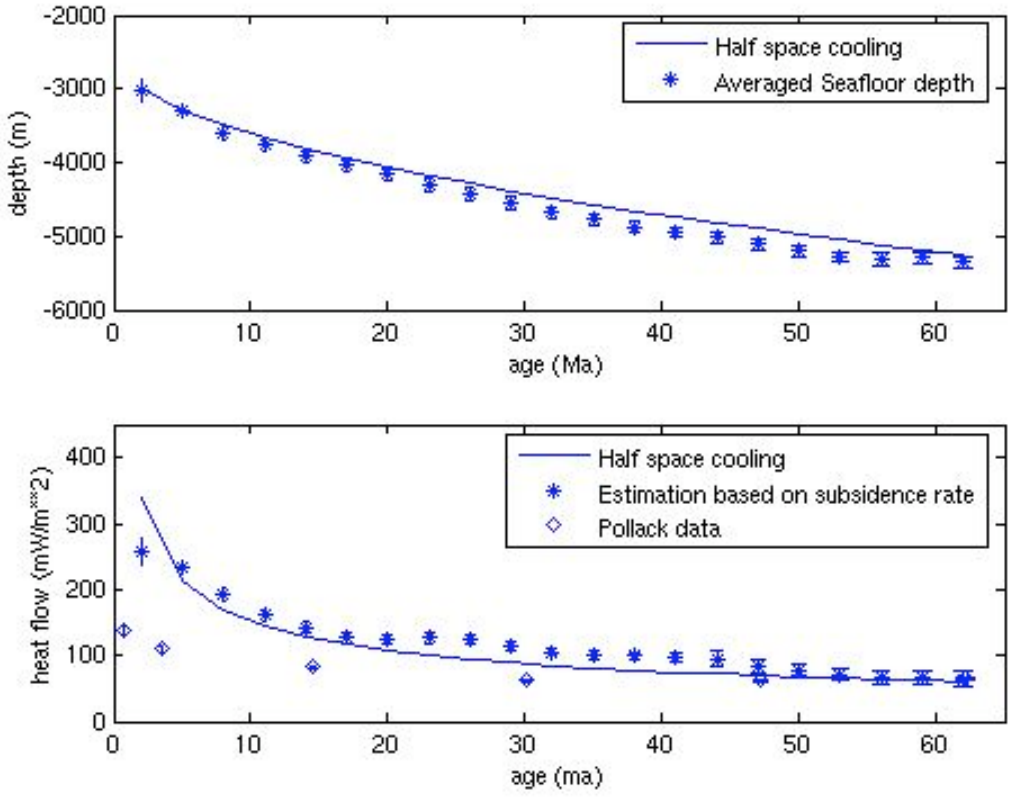

Figure 8-2. (top) Seafloor depth versus age of mid-Atlantic compared with prediction of half-space cooling model $d = 2500 + 350\sqrt{t}$. (bottom) Heat flow of mid-Atlantic inferred from subsidence rate (equation 8) compared with actual conductive heat flow measurements [*Pollack et al.*, 1993] and half-space cooling model $q = 480/\sqrt{t}$. A constant heat flow of 38 mW/m^2 was added to the estimated heat flow to account for the unobserved basal heat input *Doin and Fleitout* [1996]. This new estimate is consistent with the half-space cooling model and inconsistent with the conductive measurements.

8.4 **Global analysis**

The same analysis was performed on global depth and age data to estimate the Cenozoic heat output of the Earth. A global map of surface minus basal heat flow is shown in Figure 3 (top) along with a surface heat flow based on the half space cooling model (Figure 3, bottom). There is good qualitative agreement although the estimated heat flow still has considerable spatial variation even after low-pass filtering. Some of the large positive and negative spatial variations in heat flow are associated with topographic features that are Airy compensated. Consider a local bathymetric high; the gradient of the topography in the direction of increasing age will be sharply positive on the younger side and sharply negative on the older side. If the base level around the feature is the same on both sides and the fossil spreading rate is also the same, the false positive and negative estimated heat flow will cancel. We could attempt to mask these areas of anomalous depth; however, this cancellation effect will results in an overall unbiased estimate of heat flow. A similar argument does not apply to recovery of seafloor depth versus age because seamounts and plateaus can only make the depth shallower (thicker crust) and there is no compensating crustal thinning mechanism. This is why it is critical to remove seamounts and plateaus prior to analysis of depth versus age [*Hillier and Watts*, 2005]. There are also spatial variations in heat flow apparently associated with ridge jumps and fossil microplates. This is to be expected because the age gradient can be discontinuous leading to small values in the denominator of the scalar subsidence rate.

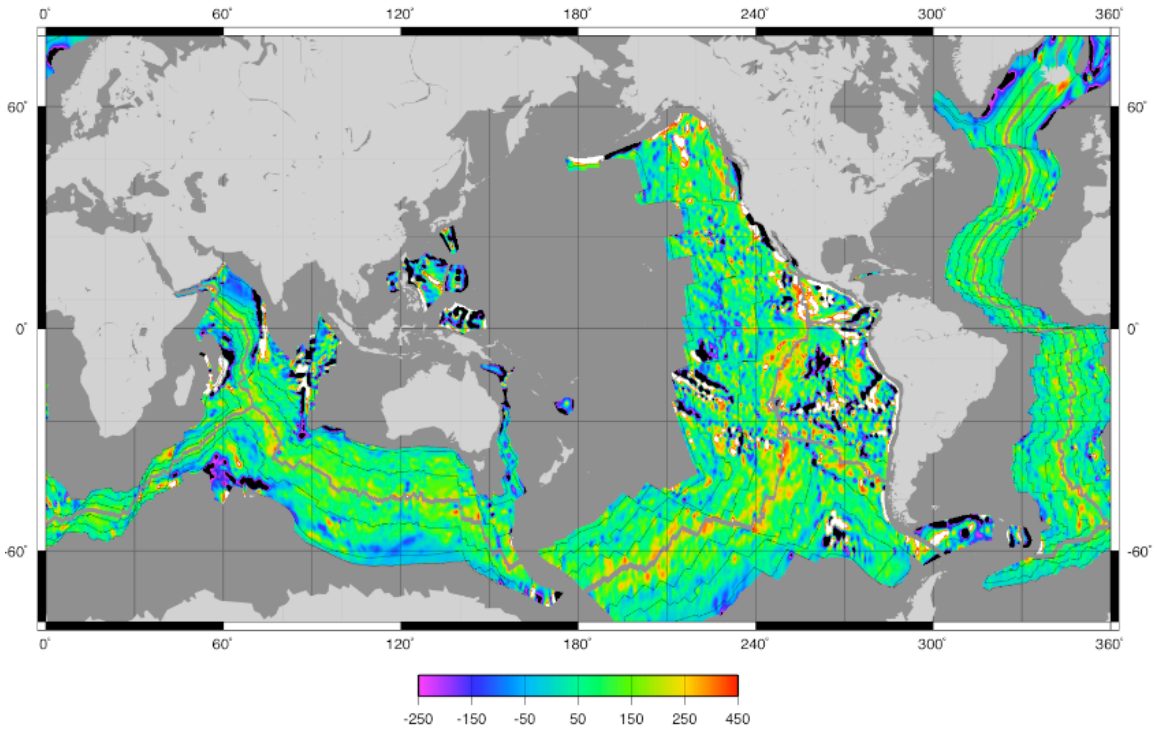

Figure 8-3. (top) Global heat flow based on subsidence rate. (bottom) Global heat flow based on space cooling model, $q = 480/\sqrt{t}$ **.**

As in the case of the mid-Atlantic Ridge, we average the depth and heat flow data into 3 Ma age bins between 0 and 66 Ma as shown in Figure 4. The depth versus age data show progressive disagreement with the theoretical curve. We believe this is mostly a depth bias caused by seamounts and plateaus, which become more prominent on 40 - 60 Ma seafloor. Nevertheless the fit is good for seafloor with age less than 30 Ma.

Heat flow estimated from scalar subsidence rate shows excellent agreement with the half-space cooling model when a basal heat flux of 38 mWm^{-2} is added (Figure 4, bottom). This basal heat flux is needed to match the measured conductive heat flow at

41 and 62 Ma [*Pollack et al*., 1993]. As in the case of the mid-Atlantic ridge, there is disagreement in the first age bin where we have been unable to estimate subsidence rate within 20 km of the ridge axis. The agreement is remarkably good between 3 and 66 Ma. The agreement would be poor if a basal heat flux was not added suggesting this is required, at least for ages greater than 40 Ma where measured conductive heat flow approaches the true value.

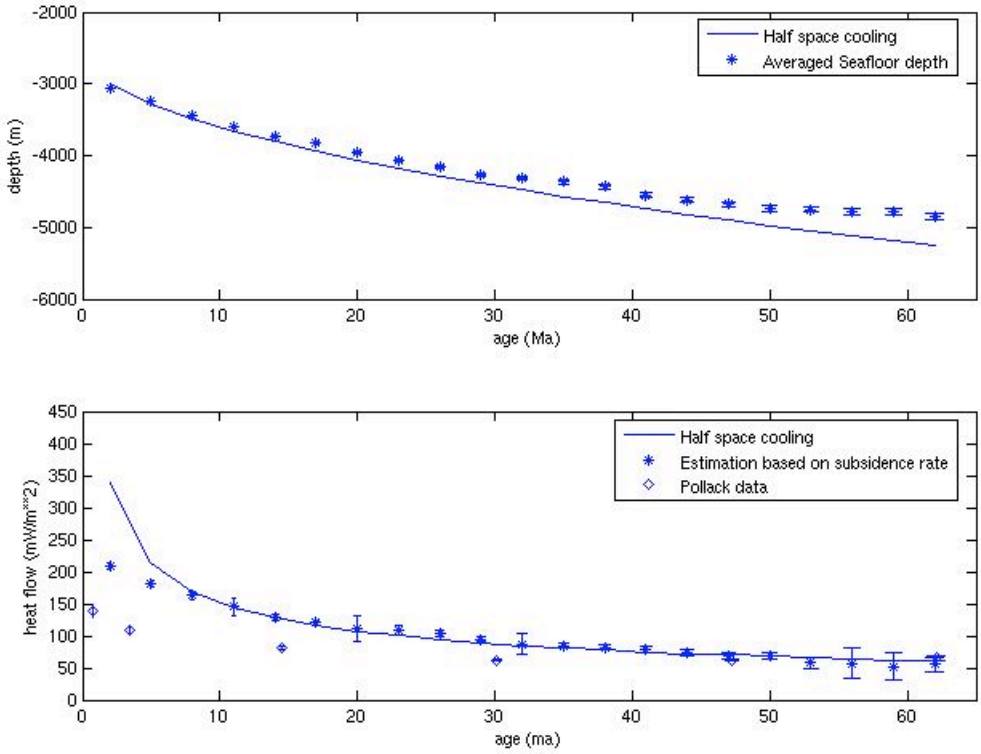

Figure 8-4. (top) Global seafloor depth versus age compared with prediction of half-space cooling model $d = 2500 + 350\sqrt{t}$. (bottom) Global heat flow inferred from subsidence rate (equation 9) with 38 mWm^{-2} basal heat flux added compared with actual conductive heat flow measurements [*Pollack et al*., 1993] and half-space cooling model $q = 480/\sqrt{t}$.

Heat output of Cenozoic seafloor and the heat output of the Earth

Using our new estimates of surface minus basal heat flow we can estimate the global heat output of the Cenozoic seafloor. A first approach is to integrate our surface minus basal heat flow (plus 38 mWm^{-2}) from 3 - 66 Ma. This results in a total of 14.4 TW resulting in a global heat output of 37.6 TW. This estimate may be a lower bound because we are missing two contributions: we cannot estimate the heat flow within 20 km of the ridge axes, and we do not estimate heat flow in the Arctic ocean where depth and age are poorly constrained. Indeed we show next that these contributions are 5.1 TW.

A second approach to estimating Cenozoic heat output is based on our good fit to the half-space cooling (HSC) model (Figure 4, bottom). If we assume the HSC model is correct and use the new age grid to estimate the total we arrive at an estimate of 20.4 TW in agreement with *Pollack et al*., [1993]. The results are shown in Figure 5 and numerical values are provided in Table 1. The upper plot is the area of seafloor divided into 3 Ma age bins from 0-66 Ma. The calculation of this area versus age relation out to 180 Ma approximately follows a linear decrease as proposed by *Parsons* [1982]. The heat flow in each age bin times the area of the bin is shown in Figure 5 (middle) where the theoretical heat flow over the age range t_1 to t_2 as

$$\bar{q}(\bar{t}) = \frac{1}{t_2 - t_1} \int_{t_1}^{t_2} C t^{-1/2} dt = \frac{2C}{t_2 - t_1} \left(t_2^{1/2} - t_1^{1/2} \right) \tag{9}$$

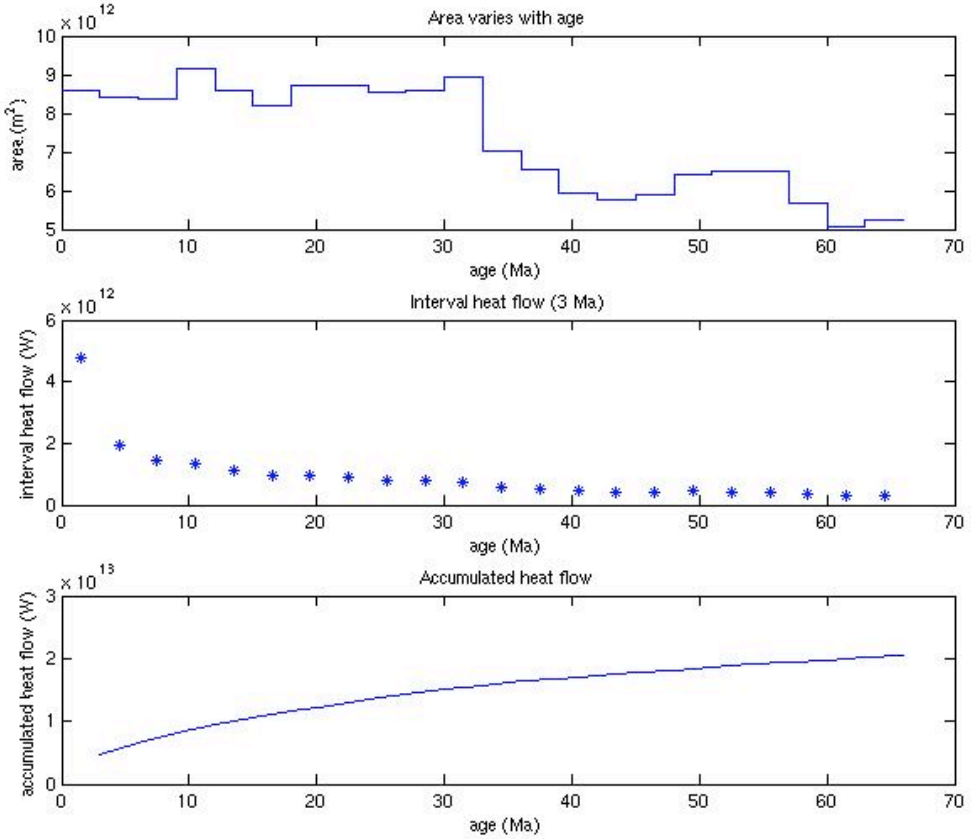

Figure 8-5. Global oceanic heat flow from 0 - 66 Ma crust based on HSC model. (top) Seafloor area versus age in 3 Ma bins based on the age grid of *Mueller at al.*, [1997]. (middle) Total heat flow in for each age bins is the product of the integrated model heat flux (equation 9) times the area of seafloor. The first age bin has 5 TW. (bottom) Age-integrated heat flow provides a total of 20.4 TW at 66 Ma.

Note that 5 TW of the global heat flow is produced in the first 3 Ma (Figure 5, middle). Since this is the age range where we are unable to estimate heat flow, our integrated estimate will be ~5 TW too low. The lower plot in Figure 5 shows the cumulative sum of the oceanic heat flow from 0 to 66 Ma. Again, the first age bin contributes 5 TW and the remainder 15.4 TW for a total of 20.4 TW in agreement with previous estimates. It

is interesting to note that *Pollack et al.,* [1993] arrive at the same value but use a model with a higher overall heat flow of $q = 510/\sqrt{t}$. We have used a lower value of 480 for the heat flow coefficient so we suggest that the more complete age grid has provided an increase in global heat flow to offset the lower heat flow coefficient.

The agreement between our estimates and the half-space cooling model suggests that the total heat output of the Earth is close to the 44 TW value. However, there are two large uncertainties in our calculations. First we have added an unknown basal heat flux of 38.0 mWm^{-2}. All lithospheric cooling models require some basal heat flux to explain the flattening of the depth vs. age relation in combination with the relatively high heat flow observed on very old seafloor of 45 mWm^{-2}. If we remove this basal heat contribution we obtain an integrated heat flow of 13.5 TW resulting in a global output of only 37.1 TW. The second large uncertainty is our estimate of the heat capacity and the thermal expansion coefficient. The temperature-averaged heat capacity has a rather narrow range between 1094 and 1124 J $kg^{-1}°C^{-1}$ depending on the dominant minerals (Figure 6, top). However, the temperature-averaged thermal expansion coefficient has a much larger range between 2.9 and $4.2x10^{-5}$ $°C^{-1}$ (Figure 6, bottom).

Given these uncertainties in thermal expansion coefficient and basal heat flux we can only place bounds on the Cenozoic heat output (Table 1 and Figure 7). The possible range of heat capacity is small so we set this value to 1124 J kg^{-1} $^{o}C^{-1}$. Next we vary the thermal expansion coefficient over the possible range of 2.9 to $4.2x10^{-5}$ $°C^{-1}$ and calculate the surface minus basal heat flux. Finally, we estimate the basal heat flux by varying this parameter so the heat flow in the 45 to 66 Ma age range matches the values of the HSC model. We use the HSC model rather than the two estimates from *Pollack et*

al. [1993] because the HSC model also provides a good fit to heat flow data on older seafloor 66-180 Ma. The results (Table 1 and Figure 7 (top)) provide integrated heat flow (3-66 Ma) ranging between 13.5 and 15.4 TW. To this we add the 5.1 TW that is predicted from the HSC model on young seafloor (0 - 3) to obtain the Cenozoic heat output and ultimately the global estimate range based on the non-Cenozoic estimates from *Pollack et al.*, [1993]. The global heat flux ranges between 42.2 and 44.1 TW; a likely thermal expansion of 3.5×10^{-5} °C^{-1} provides a global heat estimate of 43.1 TW.

The main weakness of our method is that it relies on the HSC cooling model to estimate the 5-TW contribution to the heat flow over the spreading ridges (0 - 3 Ma). If the heat flow out of the ridges is zero then our estimates are 5 TW too large and the true Cenozoic heat flow ranges between 37.1 and 39. Of course, high heat flow at spreading ridges is well documented in terms of both conductive heat flow measurement and heat coming from hydrothermal vents so this case is not possible [*Von Herzen et al.*, 2005]. Another weakness of our method is that we rely on a poorly known value of the lithospheric-averaged thermal expansion coefficient. It is possible to match the *Pollock et al* [1993] heat flow data with subsidence rate data although this requires an unrealistically high thermal expansion coefficient of 7.0×10^{-5} °C^{-1} (Figure 7, bottom). The highest thermal expansion of any naturally occurring mineral is 5.1×10^{-5} °C^{-1} (*Anderson and Isaak*, 1995) so this situation is also not possible.

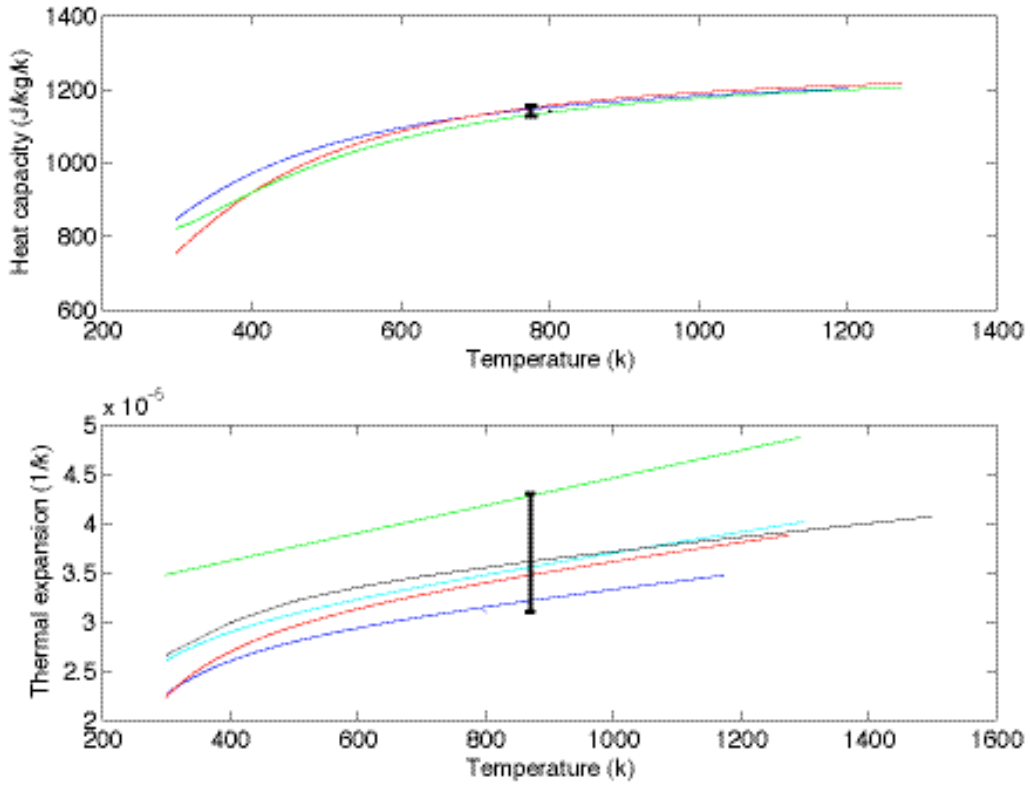

Figure 8-6. (top) Heat capacity of candidate minerals in the lithosphere [*Fei and Saxena*, 1986]. blue: olivine; red: spinel; green: Cpx. The range of temperature-integrated heat capacity of 1094 to 1124 J $kg^{-1}°C^{-1}$ is illustrated by the vertical bar. (bottom) Thermal expansion coefficient for olivine from different experiments involving slightly different minerals. blue: Mg2SiO4, [*Suzuki* 1975]; green:Mg2SiO4, [*Hazen*, 1976]; red: Mg2SiO4, [*Matsui*, 1985]; cyan: Mg2SiO4, [*Kajiyoshi*, 1986]; black: (Mg.9Fe.1)2SiO4, [*Anderson and Isaak*, 1995]. The range of temperature-integrated thermal expansion coefficient of 3.0 to 4.2x10^{-5} $°C^{-1}$ is illustrated by the vertical bar.

Table 8-1. Cenozoic and global heat flow totals

model		Q (TW)		Q_T(TW)
$\alpha(10^{-5}\ ^\circ C^{-1})$	q_b (W m^{-2})	0 - 66	3 - 66	global
2.9	28.9	-	15.4	44.1
3.5	**35.2**	**-**	**14.4**	**43.1**
3.85	38.0	-	14.0	42.7
4.2	40.0	-	13.5	42.2
7.0	50.2	-	12.0	35.6 (note the 0 -3 Ma HSC is not included)
HSC, $q(t) = 960\frac{\sqrt{t_2}-\sqrt{t_1}}{t_2-t_1}$				
lat -70˚ to 90˚		20.4	15.5	44.0
lat -70˚ to 70˚		20.14	15.3	43.7

Note global heat Q_T is the sum of integrated contribution (3 - 66 Ma), the 5.1 estimated from HSC (0 - 3 Ma), and the 23.6 from continents and older oceans [*Pollack et al.,* 1993].

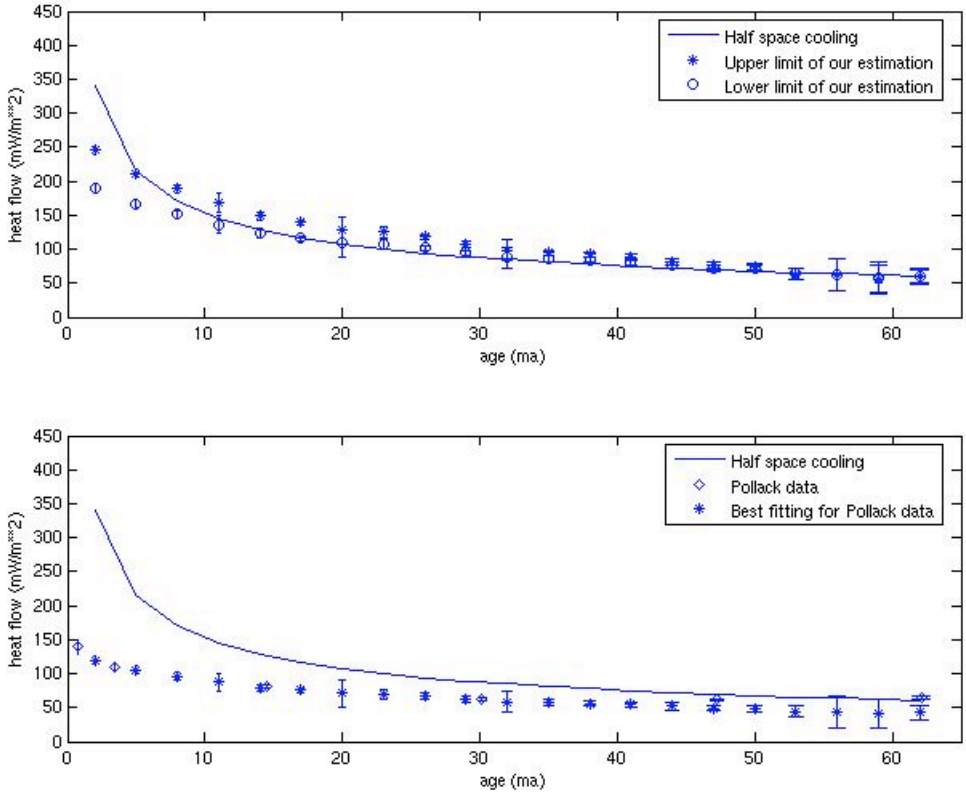

Figure 8-7. (top) The lower and upper bounds on estimated heat flow compared with the HSC model $q = 480/\sqrt{t}$ using thermal expansion coefficient of 2.9 and $4.2 \times 10^{-5\circ} C^{-1}$, respectively. (bottom) Our estimates of heat flow match the data of *Pollock et al*, [1993] but only if an unrealistically high value of thermal expansion coefficient is used ($7.0 \times 10^{-5\circ} C^{-1}$).

8.5 Conclusion

Conductive heat flow measurements over young oceanic lithosphere are significantly less than the prediction of lithospheric cooling models. This has led to a debate concerning the total heat output of the Earth. Model-based estimates of global heat flux provide an upper bound of 42-44 TW [*Sclater et al., 1980*; *Pollack et al*., 1993]

while measurement-based estimates (conductive only) provide a lower bound of ~35 TW [*Hofmeister and Criss*, 2005]. We propose that the overall elevation of the global ridge system, relative to the deep ocean basins, provides an independent estimate of the total heat content of the lithosphere. We re-derive an expression relating heat flow to local scalar subsidence rate and show that this relationship is independent of the vertical heat transport mechanism. The derivation relies only on conservation of energy, thermal expansion, and local isostasy. Heat flow out of the top of the plate minus the heat flow into the bottom of the plate is proportional to the measured subsidence rate times the heat capacity divided by the thermal expansion coefficient.

We develop a method of estimating scalar subsidence rate directly from depth and age gradients. Since the age gradient is discontinuous across a plate boundary, the method fails over very young seafloor. Additionally, the model assumes local isostatic balance so the flexure and dynamic topography within 20 km of the ridge axis must also be avoided. This zone includes the first 3 Ma of seafloor where half-space cooling models predict 5 TW of power escapes. Therefore our method cannot see this 0 - 3 Ma contribution. The estimates of the different heat flow between the upper and lower surface of the plate over the 3 - 66 Ma age range are robust, though a basal heat flow value must be added.

We compute global maps of surface minus basal heat flow that show qualitative agreement with heat flow based on the inverse square root of age relation. Averaging these estimates over 3 Ma age bins shows excellent agreement with the heat flow based on the *Parsons and Sclater* [1977] cooling model but only if a basal heat flux of 38 mWm^{-2} is added. This extra contribution is needed to fit observed heat flow in the 45 -

66 Ma age range. Our results are 9 TW larger than the observations of conductive heat flow for ages less than 40 Ma suggesting that another heat transport mechanism must operate (e.g. hydrothermal circulation). A major uncertainty in our estimate of global heat flux is related to the uncertainties in the temperature-averaged heat capacity and thermal expansion coefficient. We use values based on laboratory experiments, which provide a possible range of global heat output between 42 and 44 TW. A value of ~43 is most consistent with the experimental values of heat capacity and thermal expansion coefficient. We conclude that the observed elevation of the ridges, with respect to the deep oceans, is a first-order measure of the heat content of the cooling lithosphere and that the inferred ocean heat flow is in accordance with conductive cooling models.

8.6 Acknowledgements

We thank the editor, Hans Thybo and reviewers, Andrew Fisher and an anonymous reviewer for their excellent suggestions on improving the paper. The paper benefited from discussions with Norm Sleep and Guy Masters. This research was supported by NASA Solid Earth and Natural Hazards Program (NAG-5-13673) and the National Science Foundation, Marine Geology and Geophysics Program (OCE 0326707).

Text of Chapter 8, in full, is a reprint of the material as it appears in the Tectonophysics. The dissertation author was the primary investigator and author of this paper.

8.7 References

Anderson, O.L., Hobart, M.A., 1976. The relation between heat flwo, sediment thickness, and age in the eastern Pacific. . J. Geophys. Res., Vol. 81, 2968-2989.

Anderson, O.L., Isaak, D.G., 1995. Elastic constants of mantle minerals at high temperature. Mineral Physics and Crystallography, a handbook of Physical Constants, AGU reference shelf 2, 64-97.

Davis, E.E., Lister, C.R.B., 1974. Fundamentals of ridge crest topography. Earth and Planet. Sci. Let. Vol. 21, Issue 4, 405-413.

Doin, M.P., Fleitout, L., 2005. Thermal evolution of the oceanic lithosphere: an alternative view. Earth and Plan. Sci. Letters 142, 121-136.

Elderfield, H., Schultz, A., 1996. Mid-Ocean ridge hydrothermal fluxes and the chemical composition of the ocean. Annu. Rev. Earth Planet. Sci. 24, 191-224.

Fei, Y., 1995. Thermal Expansion. Mineral Physics and Crystallography, a handbook of Physical Constants, AGU reference shelf 2, 29-44.

Fei,Y., Saxena, S.K., 1986(?). An equation for the heat capacity of solids. Geochimica et Cosmochimica Acta Vol. 51, 251-254.

Hazen, R.M., 1976. Effects of temperature and pressure on the crystal structure of forsterite. Amer. Mineral, 61, 1280-1293.

Hillier, J.K., Watts, A.B., 2005. Relationship between depth and age in the North Pacific Ocean. J. Geophys. Res., Vol. 110, B02405.

Hofmeister, A.M., Criss, R.E., 2005. Earth's heat flux revised and linked to chemistry. Tectonophysics 395, 159-177.

Kajiyoshi, K., 1986. High temperature equation of state for mantle minerals and their anharmonic properties. Ph.D. Thesis, Okayama Univ.

Lister, C.R.B., 1972. On the thermal balance of a mid-ocean ridge. Geophys. J.R. Astron. Soc. 26, 515-535.

Matsui, T., Manghnani, M.H., 1985. Thermal expansion of single-crystal forsterite to 1023 K by Fizeau interferometry. Phys. Chem. Minerals, 12, 201-210.

McKenzie, D.P., 1967. Some remarks on heat flow and gravity anoamalies. J. Geophys. Res. 72, 6261-6273.

Mueller, R.D., Roest, W.R., Royer, J.-Y., Gahagan, L.M. & Sclater, J.G., 1997. Digital isochrons of the world's ocean floor. J. Geophys. Res., 102: 3211-3214.

Oldenburg, D.W., 1975. A physical model for the creation of the lithosphere. Geophys. J. R. astr. Soc. 43, 425-451.

Parsons, B., 1982. Causes and consequences of the relation between area and age of the ocean floor. J. Geophys. Res., Vol. 87, No. B1, 289-302.

Parsons, B., McKenzie, D., 1978. Mantle convection and the thermal structure of the plates. J. Geophys. Res. 83, 4485-4496.

Parsons, B., Sclater, J.G., 1977. An analysis of the variation of ocean floor bathymetry and heat flow with age. J. Geophys. Res. 82, 803-827.

Pollack, H.N., Hurter, S.J., Johnson, J.R., 1993. Heat flow from the Earth's interior: analysis of the global data set. Rev. Geophys. 31, 267-280.

Renkin, M.G., Sclater, J.G., 1988. Depth and age in the North Pacific. J. Geophys. Res. Vol. 93, Issue B4, 2919-2935.

Sandwell, D.T., Poehls, K.A., 1980. A compensation mechanism for the central pacific. J. Geophys. Res. 85, 3751-3758.

Sclater, J.G., Jaupart, C., Galson, D., 1980. The heat flow through oceanic and continental crust and the heat loss of the earth. Rew. Geophys and Space Physics. Vol. 18, 269-311.

Sleep, N.H., Wolery, T.J., 1978. Egress of hot water from midocean ridge hydrothermal systems: some thermal constraints. J. Geophys. Res. Vol. 83, 5913-5822.

Smith, W.H., Sandwell, D.T., 1997. Global sea floor topography from satellite altimetry and ship depth soundings. Science. Vol. 277, Issue 5334, 1956-1962.

Stein, C.A., Stein, S.A., 1992. A model for the global variation in oceanic depth and heat flow with lithospheric age. Nature 359, 123-128.

Stein, C.A., Stein, S.A., 1994. Constraints on hydrothermal heat flux through the oceanic lithosphere from global heat flow. J. Geophys. Res. 88, 3081-3095.

Suzuki, I., 1975. Thermal expansion of periclase and olivine and their anharmonic properties. J. Phys. Earth, 23, 145-159.

Von Herzen, R., Davis, E.E., Fisher, A.T. Stein, C. and Pollack, H.N., Comment on "Earth's heat flux revised and linked to chemistry" by A. M. Hofmeister and R.E. Chris, *Tectonophysics*, in press, 2005.

Williams, D.L., Von Herzen, R.P., Sclater, J.G., Anderson, R.R., 1974. The Galapagos spreading centre: Lithospheric cooling and hydrothermal circulation. Geophys. J. Roy. Astron. Soc., 38, 587-608.